Nanoindentation testing of soft polymers:

Computation, experiments and parameters identification

Dissertation

zur Erlangung des Grades

Doktor der Ingenieurwissenschaften (Dr.-Ing.)

der Naturwissenschaftlich-Technischen Fakultät III

Chemie, Pharmazie, Bio- und Werkstoffwissenschaften
der Universität des Saarlandes

vorgelegt von

Zhaoyu Chen M. Sc.

Saarbrücken

2013

Tag des Kolloquiums: 30.01.2014

Dekan: Prof. Dr. Volkhard Helms
Gutachter: Prof. Dr.-Ing. Stefan Diebels
                      Prof. Dr.rer.nat. Wulff Possart
Vorsitz: Prof. Dr. Michael Springborg
Akad. Mitarbeiter: Dr.-Ing. Frank Aubertin

Saarbrücker Reihe

Materialwissenschaft und Werkstofftechnik

Band xx

Nanoindentation testing of soft polymers: Computation, experiments and parameters identification

Zhaoyu Chen

Die Professoren der Fachrichtung Materialwissenschaft
und Werkstofftechnik Saarbrücken

Herausgeber:
Prof. Dr.-Ing. Stefan Diebels

PREFACE

Zhaoyu Chen
Saarbrücken, Germany

I

ABSTRACT

Since nanoindentation technique is able to measure the mechanical properties of extremely thin layers and small volumes with high resolution, it also became one of the important testing techniques for thin polymer layers and coatings.

This dissertation is focusing on the characterization of polymers using nanoindentation, which is dealt with numerical computation, experiments and parameters identification. An analysis procedure is developed with the FEM based inverse method to evaluate the hyperelasticity and time-dependent properties. This procedure is firstly verified with a parameters re-identification concept.

An important issue in this dissertation is to take the error contributions in real nanoindentation experiments into account. Therefore, the effects of surface roughness, adhesion force, friction and the real shape of the tip are involved in the numerical model to minimize the systematic error between the experimental responses and the numerical predictions. The effects are quantified as functions or models with corresponding parameters to be identified.

Finally, data from uniaxial or biaxial tensile tests and macroindentation tests are taken into account. The comparison of these different loading situations provides a validation of the proposed material model and a deep insight into nanoindentation of polymers.

ZUSAMMENFASSUNG

Da Nanoindentation die Messung der mechanischen Eigenschaften von dünnen Schichten und kleinen Volumen mit hoher Auflösung ermöglicht, hat sich diese Messmethode zu einer der wichtigsten Testmethoden für dünne Polymerschichten und -beschichtungen entwickelt.

Diese Dissertation konzentriert sich auf die Charakterisierung von Polymeren mittels Nanoindentation, die in Form von numerischen Berechnungen, Experimenten und Parameteridentifikationen behandelt wird. Es wurde ein Auswertungsverfahren mit einer FEM basierten inversen Methode zur Berechnung der Hyperelastizität und der zeitabhängigen Eigenschaften entwickelt. Dieses Verfahren wird zunächst mit einem Konzept der Parameter Re-Identifikation verifiziert.

Fehlerquellen wie Oberflächenrauheit, Adhäsionskräfte, Reibung und die tatsächlichen Form der Indenterspitze werden in das numerische Modell eingebunden, um die Abweichungen der numerischen Vorhersagen von den experimentellen Ergebnissen zu minimieren. Diese Einflüsse werden als Funktionen oder Modelle mit dazugehörigen, zu identifizierenden Parametern, quantifiziert.

Abschließend werden Messwerte aus uni- oder biaxialen Zugversuchen und Makroindentationsversuchen betrachtet. Der Vergleich dieser verschiedenen Belastungszustände liefert eine Bestätigung des vorgeschlagenen Materialmodells und verschafft einen tieferen Einblick in die bei der Nanoindentation von Polymeren ablaufenden Mechanismen.

LIST OF APPENDED PAPERS

This thesis consists of a summary and six appended papers:

Paper A   Z. Chen, S. Diebels, Nanoindentation of Hyperelastic Polymer Layers at Finite Deformation and Parameter Reidentification, *Archive of Applied Mechanics* 82 (2012) 1041-1056

Paper B   Z. Chen, S. Diebels, Parameter Re-identification in Nanoindentation Problems of Viscoelastic Polymer Layers: Small Deformation, *Zeitschrift für Angewandte Mathematik und Mechanik (ZAMM)* 93 (2012) 88-101

Paper C   Z. Chen, S. Diebels, J. Schmitt, Frictional Nanoindentation of Hyperelastic Polymer Layers: A Numerical Study, *Proceedings of the 3rd ECCOMAS Thematic Conference on the Mechanical Response of Composites* (2011) 229-236

Paper D   Z. Chen, S. Diebels, Modelling and Parameter Reidentification of Nanoindentation of Soft Polymers Taking into Account Effects of Surface Roughness, *Computers and Mathematics with Applications* 64 (2012) 2775-2786

Paper E   Z. Chen, S. Diebels, N. J. Peter, A. S. Schneider, Identification of Finite Viscoelasticity and Adhesion Effects in Nanoindentation of a Soft Polymer by Inverse Method, *Computational Materials Science* 72 (2013) 127-139

Paper F   Z. Chen, T. Scheffer, H. Seibert, S. Diebels, Macroindentation of a Soft Polymer: Identification of Hyperelasticity and Validation by Uni/Biaxial Tensile Tests, *Mechanics of Materials* 64 (2013) 111-127

CONTRIBUTIONS FROM CO-AUTHORS

The appended papers were prepared in cooperation with co-authors. The author of this thesis was in charge of the major work in all of the papers. The work of the co-authors is described in detail as following.

For **Paper A, Paper B and Paper D**, the sole co-author Prof. Dr.-Ing Stefan Diebels, who is my Ph.D supervisor, guided me to organize the ideas at the beginning. During the numerical computations, he supported me to develop the numerical model and the optimization procedure. Afterwards, he took part in planning the papers and correcting the English writing, which resulted in a qualitative improvement of these papers.

For **Paper C**, the co-authors, Prof. Dr.-Ing Stefan Diebels and Dr.-Ing Joachim Schmitt, supported me to implement the numerical model of nanoindentation taking into account the friction effects. The discussion of the simulation results with the co-authors is useful to organize the structure of the paper.

Paper E was prepared with three co-authors. My Ph.D supervisor Prof. Dr.-Ing Stefan Diebels supported me to develop a numerical model to simulate nanoindentation of viscoelastic polymers considering adhesion effects. He guided me to choose a suitable viscoelastic model and a contact model with a traction-separation interaction. B. Sc Nicolas Peter and Dr.-Ing Andreas Schneider performed the SEM and nanoindentation with in situ SPM tests to characterize the surface of the specimens and wrote the corresponding part to describe the experimental procedure. A qualitative improvement of the paper cannot be reached without useful suggestions of the co-authors and without their correction of my English writing.

For **Paper F**, Prof. Dr.-Ing Stefan Diebels brought forward the idea to characterize polymers with macroindentation and to compare the results to uni/biaxial tensile tests. Dipl.-Ing Tobias Scheffer and Dipl.-Ing Henning Seibert supported me to perform macroindentation tests and uni/biaxial tensile tests. They wrote the parts describing the experimental devices and prepared the illustrated sketches of the experimental devices and specimens. Fruitful discussion of the experimental data with all of the co-authors and their strategic suggestions lead to a qualitative improvement of the paper.

Zhaoyu Chen
Saarbrücken, Germany

X

Contents

I

A REVIEW AND SUMMARY OF THE THESIS

Nanoindentation testing is a fairly mature technique for hard metals, which uses the continuously sensed indentation depth combined with the measured applied force to determine the elastic modulus and the hardness of the test specimen. Since this technique is able to measure the local properties of extremely small volumes with high resolution, it also became one of the primary testing techniques for the mechanical characterization of polymers and biological tissues. The experimental setup and analysis methods of nanoindentation on soft polymers are developed to spread a wide adaption in polymers.

This thesis consists of a summary and six appended papers. A review and summary of the thesis are presented in this part. The primary problems existing in experiments and analysis about nanoindentation of soft polymers are discussed. The motivation and main works of the thesis are illustrated. Summaries of the appended papers A-F are also included.

1   Introduction and motivation

This section provides a description of the nanoindentation instrument and its measurement method. A review of the primary problems with wide adaption in polymers has motivated our research work in this field. A description of the objectives is also included in this part.

1.1   Nanoindentation instrument

Wide application of nanoindentation has spawned a number of nanoindentation instruments that compete on a world market. The instruments typically monitor the depth of penetration using either an inductance or capacitance displacement sensor. A load can be applied by the expansion of the piezoelectric element, the movement of a coil in a magnetic field. A typical nanoindentation test instrument, or "nanoindenter", has a depth resolution of less than a tenth of a nm and a force resolution of several nN. Maximum loads are usually limited to the mN range. The minimum load is usually less than a μN. The goal of majority of nanoindentation tests is to determine elastic modulus and hardness of the specimen material from the load-displacement curve.
Hysitron TriboIndenter® is a fully automated and powerful indentation instrument because it is a quantitative system with internal analysis procedure and it can provide in-situ topographical images of the sample surface before and after a test. All nanoindentation experiments in this study have been performed by using the Hysitron TriboIndenter®. The TriboIndenter® system contains three main components: the XYZ axes staging system, the Triboscanner and the transducer assembly. The coarse control of samples and tip positions is performed by the XYZ axes staging system. The samples are mounted directly to the XY stage via magnetic attraction or the optional vacuum stage. The Triboscanner and optics are mounted to the Z stage. The Triboscanner is designed to provide fine scale positioning of the probe tip before and after conducting the tests. The positioning is monitored by a three-axis piezo scanner using a tandem piezoelectric ceramic scanning tube. The top half of the Triboscanner tube is composed of four separate quarter cylinders. Each quarter of the tube controls the motion in a different direction: +X, +Y, -X, and -Y. When the lower tube is energized, it lengthens to provide motion along the Z-axis. The Triboscanner together with the Scanning Probe Microscopy mode can provide in-situ topographical images of the sample surface before or after a test is performed. Images are created by raster-scanning the probe across the sample surface while maintaining a constant normal force or setpoint. They can be used to determine the surface roughness and to present phenomenons such as cracking, delamination, or excessive pile-up. The TriboIndenter® uses a transducer

based on revolutionary three-plate capacitor technology providing simultaneous actuation and measurement of force and displacement with a range of 1 nN to 30 mN. The transducer system consists of two fixed outer plates (the drive plates) and one pickup electrode (the middle plate) which is spring mounted. Therefore, the middle plate is free to move up and down in the region between the two drive plates. The indenter is attached on the middle plate with a screw. To perform an indentation, an electrostatic force is generated between the drive plates and the pickup electrode when a voltage is applied to the drive plates. The electrostatic attraction between the pickup electrode and the bottom plate will pull the middle plate down. The force can be calculated from the magnitude of the voltage applied. The displacements are measured by changes in the capacitance of the stack of plates.

The indenter tip is a very important part of the nanoindentation test. The geometry and the material it is made from can dramatically influence the raw data. The material is important because its stiffness may influence the reduced modulus and because local adhesion might occur between the sample and the tip. The most often used indenter tips are made from diamond with a modulus about 1000 GPa and a Poisson's ratio of 0.07. The most common shapes of indenters are sphere, flat punch, cone and pyramid. The Berkovich indenter has the advantage that the edges of the pyramid are more easily constructed to meet at a single point even in the nano- or micro-scale. Therefore, it is generally used in nanoindentation, especially in the case of shallow penetration of hard metals. The conical indenter has the advantage of possessing axial symmetry. It is convenient to treat the pyramidal indenters as conical indenters with a cone angle that provides the same projected contact area to depth relationship as the actual indenter in question. This allows the use of axisymmetric numerical simulation models and axisymmetric elastic equations. The flat punch has an advantage that the contact area is constant. But in small scale, a contact angle may exist between the sample surface and the punch, which has strong influence on the measurements and such an influence is not easy to exclude. Spherical indenters are increasingly popular, as they can provide a smooth transition from elastic to elastic-plastic contact. They are particularly suitable for measuring soft materials and for replicating contact damage in in-service conditions.

1.2   Primary problems with adaption in polymers

Since nanoindentation has the considerable advantage to measure the local properties of extremely small volumes with sub-μm and sub-μN resolution, it also became one of the primary testing techniques for the mechanical characterization of thin polymer layers or coatings. However, a lot of questions still need to be answered in order to make a wide adaption of nanoindentation in polymers.

First of all, nanoindentation was originally designed to measure the hardness and mod-

ulus of hard metals. If this instrument is applied to soft polymers or some ultra-soft biomaterials, the experiment is going to be really tricky. It is required that a nanoindenter must have a very high force resolution as well as high precision over a large range of depth. Because nanoindentation on soft polymers results in a deep penetration depth with a low value of force. The noise of the force at this low level has an extremely strong influence on the accurate measurement if the force resolution is not high enough. Normally, indentation with a larger force is able to resolve this problem. However, in this case, the experiment may be terminated because of the insufficient depth range of the nanoindenter. Besides, detection of the initial contact point is another important issue of nanoindentation of soft materials, which will be described in details in the section of "Initial contact point". Moreover, most of the polymeric materials show highly elastic and viscous material behavior at the same time, called viscoelasticity. In the past decades, investigations of viscoelastic effects of polymeric materials using experimental testing, constitutive modeling and numerical computation have been published in e. g. [35, 36, 39, 31, 57, 58, 59]. Therefore, polymers creep during nanoindentation, which has the same effect on the measured force-displacement data as thermal drift, details are included in the section 3.1. It is difficult to quantify the thermal drift as a linear function of time. A pronounced error may be included in the force-displacement data if a long testing time is required in creep or relaxation loading histories.

Secondly, there is some problem about the analysis method to characterize the viscoelasticity of a polymer from nanoindentation still need to resolve. The analysis procedure, which is used in most indentation instruments to determine hardness and elastic modulus, is based on the Oliver & Pharr method [65, 66]. This analysis method assumes that the material behaves in an elastic-plastic manner and does not exhibit any time-dependent behavior or load rate dependence, details are included in section 2.2. This method is not applicable to a viscoelastic polymer. Furthermore, the measured hardness and the elastic modulus are not enough to represent the rate-dependent properties. In order to identify the viscoelastic behavior of polymers by nanoindentation, two ways have been documented in literature instead of the Oliver & Pharr method. The first method is based on analytical or semi-analytical solutions. These solutions are based on parameters of the respective viscoelastic model and represent the relationship between indentation force and displacement. The model parameters are then obtained by fitting the experimental force-displacement data with the analytical functions, details about viscoelastic solutions are included in section 2.3. Since the linear viscoelastic contact solutions are derived from the Hertz elastic contact theory by the correspondence principle, this method is restricted by yielding accurate identification only for specific linear viscoelastic models under fixed experimental processes. Furthermore, effects like non-linear friction, adhesion and surface roughness in nanoindentation experiments are not taken into account in the analytical solutions. The second method, the so called inverse method, is performed by combining finite element method (FEM) modeling and numerical optimization. In this method, the objective function, which is the difference between experimental and numerical data,

is minimized with respect to the model parameters using numerical optimization. The parameters of the constitutive models are identified as the optimized solution. Huber et al. [38, 40, 48, 82] have been the first to apply this method in indentation. They used neural networks to identify the material parameters from indentation experiments on metals. However, the inverse method is still a new topic regarding nanoindentation problems of polymeric materials. Hartmann [32] identified the viscoplastic model parameters with uniaxial tests and validated them using indentation tests. Rauchs [72, 71] employed a gradient-based numerical optimization method to identify viscous hyperelastic and elasto-viscoplastic material parameters. Guessasma [28] determined viscoelastic properties of biopolymer composite materials using the finite element calculation and nanoindentation experiments. Saux et al. [54] identified the constitutive model for rubber-like elasticity from micro-indentation tests. As the inverse method permits us to handle any material model with non-linear properties and to include additional effects in the numerical model, it is a useful new method to deal with the problems of identifying rate-dependent material properties from nanoindentation.

Thirdly, as mentioned at the beginning, nanoindentation has a considerable advantage to determine local properties from continuously measured force-displacement data with high resolution. Unfortunately, there are various problems that influence the actual material response during indentation, e. g. friction, adhesion, surface roughness and the indentation process associated factors. These problems result in a systematic error between the numerical and the experimental results that often leads to even larger errors in the parameter identification [71, 6, 60, 83]. Therefore, a certain knowledge about the influence of these factors and basic investigations are indispensable to characterize the material accurately by the inverse method.

1.3 Aims of our work

It is the aim of this work to develop a robust and reliable methodology of characterizing the viscoelastic properties of polymers from nanoindentation based on the inverse method.

In the first stage, a virtual laboratory for studying nanoindentation is developed. The boundary value problem describing the indentation test is simulated by a finite element computation in ABAQUS®. The influence of the rate-dependent behavior, of non-linearity due to large deformations, of friction, adhesion and surface roughness, is investigated. The involved model parameters are re-identified using a computer-based numerical optimization routine performed by ABAQUS® in combination with MATLAB®.

In the second stage of the work, the developed methodology and the obtained knowledge of the first stage are applied to real nanoindentation experiments. In addition, taking into account data from uniaxial or biaxial tension tests and from multiaxial

compressive loading as applied during indentation, this allows a deep insight into the material's behavior. The comparison of these different loading situations is able to validate the proposed material model and model modifications, respectively.

2 Analysis of nanoindentation test data

It is well known that the principal goal of nanoindentation testing technique is to determine elastic modulus and hardness of the specimen from experimental measurement of indenter's depth of penetration and the applied force. Since the spatial dimensions are nanometers, the readings of the indentation depth and the indenter geometry give an indirect measure of the contact area at full load. The mean contact pressure, and thus the hardness, can be determined from the contact area. The elastic modulus is estimated from the relationship of the force and the corresponding penetration depth. The stress and the deformation arising from the contact mechanics between two solids are of particular interest to understand indentation testing. The existing semi-analytical and analytical analysis methods in nanoindentation, e. g. Sneddon's solution, the Oliver & Pharr method and viscoelastic analytical solutions, are mostly derived from the elastic contact theory that is pioneered by Heinrich Hertz.

2.1 Elastic contact theory

First of all, we have to distinguish between conforming and non-conforming contacts according to [43].

> *A contact is said to be conforming if the surfaces of the two bodies 'fit' exactly or even closely together without deformation. Bodies which have dissimilar profiles are said to be non-conforming. When brought into contact without deformation they will touch first at a 'point-point contact'-or along a 'line-line contact'.*

> *—K. L. Johnson*

The contact area in the non-conforming contact is generally small compared with the dimensions of the two considered bodies. The contact pressures are highly concentrated in the region close to the contact zone and such a distribution is not greatly influenced by the shape of the bodies themselves. Indentation contains a typical non-conforming contact between the indenter and the specimen surface.

The first satisfactory analysis about the pressure and area of non-conforming contact and how they grow with increasing load between two elastic bodies is due to Hertz [34]. Two solids of spherical shape are shown in crosssection after deformation in Fig. I.1
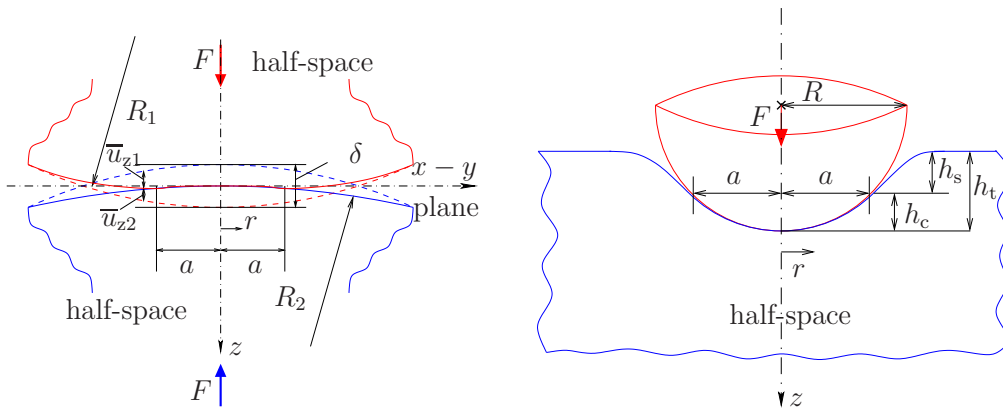
Figure I.1: Schematics of contact between two elastic deformable half-spaces (left) and indentation on an elastic half-space by a rigid spherical indenter (right)

(left) under a load F. The contact area could be circular, having a radius a. The boundary condition for normal displacements within contact can be written as

$$\overline{u}_{z1} + \overline{u}_{z2} = \delta - \frac{r^2}{2R}, \tag{I.1}$$

where $1/R = (1/R_1 + 1/R_2)$ is the relative curvature, δ is the distance of mutual approach, r $(0 \leq r \leq a)$ is the lateral coordinate along the contact area. Hertz then introduced the assumptions for the simplification to calculate the local deformation [34, 43]:

- Each solid in contact can be considered as an elastic half-space: $a \ll R_{1,2}$;

- The surface is continuous and non-conforming;

- The strain is small: $a \ll R$;

- The surfaces in contact are frictionless.

A distribution of contact pressure, proposed by Hertz with the maximum pressure p_0 can be written as

$$p(r) = p_0\{1 - (r/a)^2\}^{1/2}.$$ (I.2)

The total load F, which compresses the solids, is determined as an integration of the contact pressure over the contact area

$$F = \int_0^a p(r)2\pi r \ \mathrm{d}r = \frac{2}{3}p_0\pi a^2.$$ (I.3)

Hence the maximum pressure p_0 is $3/2$ times the mean pressure p_m. The normal displacements of both solids are given by

$$\overline{u}_{zi} = \frac{1 - \nu_i^2}{E_i}\frac{\pi\, p_0}{4a}(2a^2 - r^2), \quad i = 1, 2,$$ (I.4)

submitting the expressions for $\overline{u}_{z1}$ and $\overline{u}_{z2}$ into Eq. (I.1) one obtains

$$\frac{\pi\, p_0}{4aE^*}(2a^2 - r^2) = \delta - (1/2R)\, r^2.$$ (I.5)

The effective elastic modulus E^* is defined as

$$\frac{1}{E^*} = \frac{(1 - \nu_1^2)}{E_1} + \frac{(1 - \nu_2^2)}{E_2},$$ (I.6)

E_1, ν_1, E_2, ν_2 are the Young's modulus and the Poisson's ratio of the first and the second solid, respectively. Setting $r = 0$ and $r = a$ in Eq. (I.5), the radius of the contact area a and the mutual approach of distant points in the two solids δ are given by

$$a = \left(\frac{3FR}{4E^*}\right)^{1/3}, \quad \delta = \frac{a^2}{R} = \left(\frac{9F^2}{16RE^{*2}}\right)^{1/3}.$$ (I.7)

If $R_2 \rightarrow +\infty$, the Hertz contact, illustrated in Fig. I.1 (left), is equivalent to the indentation of a half-space with a non-rigid spherical indenter. Furthermore, if the second solid is assigned with a modulus of E^*, then the contact can be treated as taking place between a rigid indenter of radius R and a half-space, as shown in Fig. I.1 (right). The mutual approach of distant points δ in the second term of Eq. (I.7) becomes the total depth of penetration h_t beneath the specimen's free surface [26]. The deflection h of the specimen's original free surface in the vicinity of the indenter is derived from Eq. (I.5) as

$$h = \frac{1}{E^*}\frac{3}{2}\frac{F}{4a}\left(2 - \frac{r^2}{a^2}\right).$$ (I.8)

In the case of $r = 0$, the deflection h is the total elastic displacement h_t. If $r = a$, h is the depth of the circle of contact beneath the specimen's free surface h_s. Hence, it can be easily shown that $h_s = h_c = h_t/2$, h_c is the contact depth, which is the distance from the bottom of the contact to the contact circle. The relationship between the total load and the depth of penetration can be written as

$$F = \frac{4}{3} E^* \sqrt{R} \, h_t^{3/2}. \tag{I.9}$$

The mean contact pressure p_m, which has an actual physical significance as stress, is given by

$$p_m = \frac{F}{\pi a^2} = \left(\frac{4E^*}{3\pi}\right) \frac{a}{R}. \tag{I.10}$$

The second term in Eq. (I.10) is defined as an indentation stress-strain relationship similar to that more commonly obtained from conventional uniaxial tension and compression tests. Therefore, the mean contact pressure p_m is often referred to as the "indentation stress" and the term a/R as the "indentation strain".

For the Boussinesq problem of a rigid axisymmetric body indenting into a half-space composed of a homogeneous, linearly elastic and isotropic material, Sneddon derived an expression for the indentation load with an axisymmetric indenter of arbitrary shape [76, 77]

$$F = 2E^* a \int_0^1 \frac{x^2 f'(x)}{\sqrt{1 - x^2}} \, dx, \tag{I.11}$$

where $f(x)$ is the smooth shape function of the indenter with the dimensionless coordinate $x = r/a$ ($0 \leq x \leq 1$). For a spherical indenter of radius R, the Sneddon's solution of load is equivalent to Eq. (I.9). For a conical indenter, the relationship between the load and the contact radius a is expressed in terms of the indenter cone half-angle α as

$$F = \frac{\pi a}{2} E^* a \cot\alpha. \tag{I.12}$$

The displacement of the specimen free-surface beneath the indenter is given by:

$$h = \left(\frac{\pi}{2} - \frac{r}{a}\right) a \cot\alpha, \quad r \leq a. \tag{I.13}$$

Hence, the relationship between the load and the penetration depth h_t ($r = 0$) is found from

$$F = \frac{2}{\pi} E^* h_t^2 \tan\alpha. \tag{I.14}$$

For a cylindrical punch indenter of radius R, a simple relationship between the load and the penetration depth reads $F = 2RE^* h_t$.

The pyramidal indenters are generally treated as conical indenters with an effective

cone angle that provides the same contact area to the contact depth relationship as the considered one. This allows the Sneddon's elastic solutions of axisymmetric indenter, Eqs. (I.12) to (I.14), to be applied to indentation involving pyramidal indenters. The contact areas, as a function of the contact depth for some common indenters, are given in the following, where θ is the semi-angle of the pyramidal indenters and α is the effective cone angle.

Conical indenter

$$A = \pi\, h_{\mathrm{c}}^2 \tan^2\alpha$$

Berkovich indenter

$$A = 3\sqrt{3}\, h_{\mathrm{c}}^2 \tan^2\theta = 24.49 h_{\mathrm{c}}^2 \qquad\qquad \theta = 65.27°, \quad \alpha = 70.30°$$

Vickers indenter

$$A = 4\, h_{\mathrm{c}}^2 \tan^2\theta = 24.50 h_{\mathrm{c}}^2 \qquad\qquad \theta = 68°, \quad \alpha = 70.30°$$

Cube corner indenter

$$A = 3\sqrt{3}\, h_{\mathrm{c}}^2 \tan^2\theta = 2.60 h_{\mathrm{c}}^2 \qquad\qquad \theta = 35.26°, \quad \alpha = 42.28°$$

Knoop indenter

$$A = 2\, h_{\mathrm{c}}^2 \tan\theta_1 \tan\theta_2 \qquad\qquad \theta_1 = 86.25°, \ \theta_2 = 65°,$$
$$\quad = 108.21 h_{\mathrm{c}}^2 \qquad\qquad\qquad \alpha = 77.64°$$

2.2 Oliver & Pharr method

The Oliver & Pharr method was introduced in 1992 [65] and refined in 2004 [66] for measuring hardness and elastic modulus by indentation technique. Because of the Oliver & Pharr method, nanoindentation has widely been adopted to determine the hardness and elastic modulus of materials at small scales. Although the method has verified for numerous materials and extensively applied into commercial indentation instruments, certain aspects of it have always been interested to understand. The method was developed from fitting the unloading load-displacement data obtained during one cycle of indentation consisting of loading and unloading. *It is designed for the monolithic materials that can be described as a semi-infinite, elastic-plastic half space, in which there are no rate-dependent deformation mechanics such as viscoelasticity* [65, 66]. In particular, the method is recalled here in order to get advances in the understanding of some problems:

- Why can the unloading curves be well described by a power law function?

- How can we determine the correction factor β?

- Why is the geometric parameter ϵ 0.75 for the Berkovich indenter, rather than 0.72 similar to the conical indenter?

- How can we correct the pile-up effect?

Pharr and Bolshakov [68] did finite element (FE) simulations of indentation of elastic-plastic materials by a rigid conical indenter with loading, unloading and reloading processes. A key observation was that the unloaded deformed surface was not a perfectly conical shape, but exhibited a subtle convex curvature. The contact area increased continuously until the full load was again achieved during the reloading. Because both processes were elastic, a process must be the reverse of what happened during unloading. It is this continuous change in the contact area that produces the nonlinear unloading curve. The mathematical form of the curve can be understood by a concept of an effective indenter shape, which produces the same normal surface displacements on a flat surface that would be produced by the indenter on the deformed surface of the hardness impression during unloading [68]. As such, the effective indenter shape is able to describe Sneddon's solution [77] for an axisymmetric indenter of arbitrary profile

$$z = B\,r^n, \tag{I.15}$$

where B is a fitting constant and the exponent n varies in the range of $2 \sim 6$ depending on the material properties. Using Sneddon's formula of the total load F [77], Pharr and Bolshakov [68] gave the load-displacement response for an indenter with arbitrary profile as:

$$F = \frac{2E^*}{(\sqrt{\pi}B)^{1/n}} \frac{n}{n+1} \left(\frac{\Gamma(n/2+1/2)}{\Gamma(n/2+1)} \right)^{1/n} h_{\mathrm{e}}^{1+1/n}, \tag{I.16}$$

where Γ is the gamma function[1], h_{e} is the elastic part of the penetration depth and related with h_{t} through $h_{\mathrm{e}} = h_{\mathrm{t}} - h_{\mathrm{p}}$, h_{p} is the depth of the residual impression. Therefore, the unloading curve is best represented by a power law function of the form:

$$F = \gamma\,(h_{\mathrm{t}} - h_{\mathrm{p}})^m, \tag{I.17}$$

where m is the exponent to be determined by fitting with the experimental data. The contact stiffness $S = d\mathrm{F}/dh$ is defined as the slope of the initial part of the unloading curve during the first stage of unloading. The elastic properties can be determined from the relationship between measured contact stiffness S and the contact area A by the solution

$$S = \beta\,\frac{2}{\sqrt{\pi}}\,E^*\,\sqrt{A}. \tag{I.18}$$

---

[1]$\Gamma(1) = 1$, $\Gamma(3/2) = 1/2\,\pi^{1/2}$, $\Gamma(2) = 1$, $\Gamma(1/2) = \pi^{1/2}$

β is a correction factor that accounts for deviations in stiffness caused by the lack of axial symmetry for pyramidal indenters. β plays an important role if accurate properties measurements are desired. In the case of small deformation (*note that small deformation is achieved only if the half-included angle of the indenter is close to* $90°$ *[66]*) of an elastic material by a rigid axisymmetric indenter with smooth profile, β is exactly 1. However, because most of the real indentation experiments are performed with a non-axisymmetric indenter (Berkovich indenter) and involve large strains, an appropriate value of $\beta \neq 1$ is required. Numerical methods have been used to evaluate β and to explore the factors that influence it. For the purely elastic material, Larsson et al. [52] found that β is slightly dependent on Poisson's ratio ν by the formula

$$\beta = 1.2304 \left(1 - 0.21\nu - 0.01\nu^2 - 0.41\nu^3\right). \tag{I.19}$$

Hay et al. [33] developed a correction for the effect involving the half-included angle θ of the indenter

$$\beta = \pi \frac{\left[\frac{\pi}{4} + 0.1548 \cot\theta \frac{(1-2\nu)}{4(1-\nu)}\right]}{\left[\frac{\pi}{2} + 0.8312 \cot\theta \frac{(1-2\nu)}{4(1-\nu)}\right]^2}. \tag{I.20}$$

Oliver and Pharr [66] reviewed the values of β for the Berkovich indenter in literature and made a conclusion that the values fell in the range $1.0226 \leq \beta \leq 1.085$. They suggested that $\beta = 1.05$ was a good choice, with a potential error of approximately ± 0.05. If more accurate evaluation of β is desired, a scheme combining carefully performed experiments and 3D FE simulations could be helpful to resolve this issue.

The determination of the contact area is described by an area function given by Oliver & Pharr [65]

$$A = \sum_{n=0}^{8} C_n (h_{\mathrm{c}})^{2-n} = C_0 h_{\mathrm{c}}^2 + C_1 h_{\mathrm{c}} + ... + C_8 h_{\mathrm{c}}^{1/128}. \tag{I.21}$$

h_{c}, the contact depth, is defined in the Oliver & Pharr method with the assumption that the pile-up is negligible

$$h_{\mathrm{c}} = h_{\mathrm{t}} - h_{\mathrm{s}} = h_{\mathrm{t}} - \epsilon \frac{F_{\max}}{S}, \tag{I.22}$$

ϵ is a constant that depends on the geometry of the indenter. The value of ϵ is normally defined from Eq. (I.22) as

$$\epsilon = S \frac{h_{\mathrm{s}}}{F_{\max}} = 2E^* a_{\max} \frac{h_{\mathrm{s}}}{F_{\max}}. \tag{I.23}$$

It is able to compute values of ϵ for simple indenter geometries from Hertz's and Sneddon's solutions; specifically, $\epsilon = 1.0$ for a flat cylindrical punch, $\epsilon = 0.75$ for a parabola of revolution, and $\epsilon = 0.72$ for a conical indenter. Because a Berkovich indenter is geometrically more like a cone than a parabola of revolution or a flat punch, one might expect the value $\epsilon = 0.72$ to be most applicable. However, supported by a large number of experimental data, Oliver & Pharr concluded that the best value for ϵ is 0.75 [65]. This could be explained by the effective indenter shape concept, again. The elastic unloading process of indentation with a Berkovich indenter can be described by an effective indenter shape that is more like a parabola of revolution than a cone [68]. Therefore, the value $\epsilon = 0.75$ is more applicable than $\epsilon = 0.72$. Pharr and Bolshakov [68] provided a more precise estimate of ϵ using Eq. (I.23) in conjunction with Sneddon's method for determining the surface displacement at the contact perimeter

$$\epsilon = m \left(1 - \frac{2\Gamma\left(\frac{m}{2(m-1)}\right)}{\sqrt{\pi}\Gamma\left(\frac{1}{2(m-1)}\right)} (m-1) \right). \tag{I.24}$$

Hence, the value of ϵ varies mildly between 0.74 and 0.79 over the range of most experimental observations, i. e., $1.2 \leq m \leq 1.6$ [65]. However, since m depends not only on the indenter geometry but also on the elastic and plastic behavior of the specimen, a more appropriate value of ϵ might be obtained by experimentally measuring m and then substituting it into Eq. (I.24).

As discussed in Eq. (I.22), one significant problem with the Oliver & Pharr method is that it does not take into account the pile-up of the material around the contact impression. Pile-up, which is observed in many indentations of elastic-plastic materials, leads to a larger contact area than that estimated by this method. As a consequence, both the determined hardness and elastic modulus are overestimated, sometimes as much as 50% [5]. The fundamental material parameters, affecting the pile-up, are the ratio of the effective modulus to the yield stress, E^*/σ_y, and the work hardening behavior [66]. In general, the pile-up is greatest in materials with large E^*/σ_y and with little or no capacity for work hardening. The capacity for work hardening inhibits the pile-up because if the material at the surface adjacent to the indenter hardens during deformation, it constrains the upward flow of material to the surface. Bolshakov and Pharr [5] found that a convenient, experimentally measurable parameter can be used to identify the pile-up behavior in a indentation with conical and Berkovich indenters. The parameter is the ratio of the residual depth, h_p, to the total depth of penetration, h_t. The natural limits for h_p/h_t is $0 \leq h_p/h_t \leq 1$. The lower limit refers to fully elastic deformation and the upper limit to the rigid plastic behavior. The pile-up is only large if h_p/h_t is close to 1 and the degree of the work-hardening is small. If $h_p/h_t < 0.7$, the pile-up is negligible and independent from the work-hardening behavior of the material. Therefore, materials deforming elastically always sink in, pile-up occurs seldom.

Some methods have been developed that can be used to correct for pile-up. A good example proposed by Cheng et al. [19] is based on the work of indentation, which

can be measured from the area under the indentation loading curve, the total work of indentation W_tot, the unloading curve and the work recovered during unloading W_u. They found that the ratio of the irreversible work to the total work appears to be a unique function of E^*/H, independent of the work-hardening behavior

$$\frac{W_\mathrm{tot} - W_\mathrm{u}}{W_\mathrm{tot}} \cong 1 - 5\frac{H}{E^*}, \qquad (\mathrm{I}.25)$$

where H is the hardness of the specimen defined by the relation

$$H = \frac{F_\mathrm{max}}{A}. \qquad (\mathrm{I}.26)$$

Combining the Eqs. (I.18) and (I.26) leads to another equation involving H and E^*:

$$\beta^2 \frac{F_\mathrm{max}}{S^2} \frac{4}{\pi} = \frac{H}{(E^*)^2}. \qquad (\mathrm{I}.27)$$

Because W_tot, W_u, F_max and S are all measurable from the force-displacement curve, Eqs. (I.25) and (I.27) represent two independent relations that can be used to solve H and E^* directly. Additionally, the contact area, which includes the effects of pile-up, could be computed from the derived hardness H by means of Eq. (I.26). With the development of the advanced topographic techniques, it is possible to check the profile of the impression in nanoindentation, e. g. by using the in situ SPM Imaging model of the indenter, the scanning electron microscope (SEM), the atomic force microscope (AFM) and the surface profilemeter. In this way, the appearance and the extent of pile-up could be clearly understood and the true contact area could be determined. As a consequence, the effects of pile-up on the calculation of hardness and elastic modulus can be eliminated.

2.3   Viscoelastic analytical solutions

Generally in instrumented indentation, the analysis is developed to determine mechanical properties from measured load-displacement data for elastic and elasto-plastic materials, for which rate-dependent behavior is normally ignored. The characterization of viscoelastic behavior with indentation has been achieved by viscoelastic analytical solutions to boundary value problems of indentation based on the elastic contact theory.

The contact problem of a smooth rigid spherical indenter of radius R pressed into a linear viscoelastic half-space has been firstly studied by Lee and Radok [55]. First of

all, the stress-strain relations for linear isotropic viscoelasticity used in this study can
be expressed in the form:

$$P\, s_{ij} = Q\, e_{ij}, \tag{I.28}$$

$$P'\, \sigma_{ij} = Q'\, \epsilon_{ij},$$

where

$$s_{ij} = \sigma_{ij} - \frac{1}{3}\sigma_{kk}\,\delta_{ij} \quad \text{and} \quad e_{ij} = \epsilon_{ij} - \frac{1}{3}\epsilon_{kk}\,\delta_{ij}$$

are the stress and strain deviators, σ_{ij} and ϵ_{ij} are stress and strain components, respectively, and where P, Q and P', Q' are pairs of linear operators in the time variable. The
Hertz solutions Eqs. (I.2) and (I.10) of the elastic problems give the contact pressure,
$p(r,t)$, in terms of the shear modulus, the Poisson's ratio ν of the elastic half-space and
time t as:

$$p(r,t) = \frac{4}{\pi R}\,\frac{G}{1-\nu}\,f(r,t), \tag{I.29}$$

where

$$f(r,t) = \text{Re}\left\{[a(t)^2 - r^2]^{1/2}\right\}, \tag{I.30}$$

Re indicates the real part of $[a(t)^2 - r^2]^{1/2}$ in the case of $r > a(t)$, that means if $r > a(t)$,
$f(r,t) = 0$. For simplicity the case of incompressible material is considered, $\nu =$
0.5. The shear modulus is replaced by $Q/2P$ according to Eq. (I.28). Eq. (I.29) is an
appropriate form of the elastic solution to substitute the linear viscoelastic operators in
place of the elastic constants, non-linearity occurs only in the geometry of the boundary
conditions. Hence, the determination of the pressure distribution associated with the
indentation of a smooth rigid spherical indenter on an incompressible viscoelastic half-
space is given by

$$P[p(r,t)] = \frac{4}{\pi R}\,Q\,f(r,t), \tag{I.31}$$

The application of the Laplace-transform and its inverse transform gives the relation
of the total load $F(t)$ and the penetration $h(t)$ of indentation associated with the
viscoelastic half-space as

$$P[F(t)] = \frac{8}{3}\sqrt{\pi}\,Q\left\{[h(t)]^{3/2}\right\}, \tag{I.32}$$

P, Q are arbitrary linear viscoelastic operators. They may be the differential op-
erators associated with the common viscoelastic models of springs and dashpots, or
the integral operators associated with the hereditary-function approach, or any of the
other equivalent means of expressing viscoelastic behavior [55]. An important issue is
that the solutions eq. (I.31) and eq. (I.32) are valid only in which the radius $a(t)$ is a
monotonically increasing function of time t. The reason is that if $a(t)$ passes through
a maximum $a_{\max}$ and decreases, $f(r,t)$ in eq. (I.30) passes through a maximum and
retures to zero for $r > a(t)$, but $p(r,t)$ determined by eq. (I.31) usually passes through

zero and takes on negative or tensile values [55]. For example, if P is a differential operator, $p(r,t)$, which is given by its complementary function, is non-zero because of the non-zero value of p when $f(r,t)$ first reduces to zero at $r = a(t)$. The non-zero value of $p(r,t)$ violates the contact condition requiring that outside the contact region the surface traction should be zero. This paradoxical result does not arise with non-decreasing $a(t)$, because the zero initial conditions and zero right-hand side of eq. (I.31) for all ealier times gurantee zero surface traction outside the contact region [55].

A different approach developed by Ting [80, 81] yields an explicit solution of an integral equation which arises in indentation on a viscoelastic half-space. This more general solution is valid for contact problems if the time-dependent contact area is an arbitrary function of time. Firstly, it is assumed that the viscoelastic half-space is bounded by the horizontal plane $x_3 = 0$ of the Cartesian coordinates (x_1, x_2, x_3). $\mathbf{x} = (x_1, x_2)$ denotes the position of a point on the free surface $x_3 = 0$. Secondly, the distribution of the surface pressure $p(\mathbf{x}, t)$ over the area of the contact region $D(t)$ and the vertical downward displacement of the free surface $w(\mathbf{x}, t)$ satisfy the function proposed by Yang [89]

$$w(\mathbf{x}, t) = \int_{0^-}^{t} \phi(t - \tau) \frac{\partial}{\partial \tau} \int_{D(\tau)} K(\mathbf{x}, \boldsymbol{\xi}) \, p(\boldsymbol{\xi}, \tau) d\boldsymbol{\xi} d\tau \,, \qquad (I.33)$$

where

$$K(\mathbf{x}, \boldsymbol{\xi}) = \frac{1}{2\pi |\mathbf{x} - \boldsymbol{\xi}|} = \frac{1}{2\pi \left[(x_1 - \xi_1)^2 + (x_2 - \xi_2)^2\right]^{1/2}}$$

and $\phi(t)$ represents the viscoelastic properties of the half-space with an inverse $\psi(t)$. Thirdly, the surface function $f(x)$ of the rigid indenter and the contact area $D(t)$ are given. A continuous arbitrary contact region $D(t)$ is considered as shown in Fig. I.2 to illustrate the solutions derived by Ting [80, 81]. A time interval t is devided as

$$0 < t_1 < t_2 < ... < t_n < t, \qquad (I.34)$$

where n is the largest integer for the division. Thus, if n is an odd integer $n = 2k + 1$, $t_{n-1} < \tau < t_n$ is in the interval where $D(t)$ is monotonically increasing, cf. Fig. I.2 (left). If n is an odd integer $n = 2k$, $t_n < \tau < t_{n+1}$ is in the interval where $D(t)$ is monotonically decreasing, cf. Fig. I.2 (right). Suppose that the solutions $p(\mathbf{x}, t)$ and
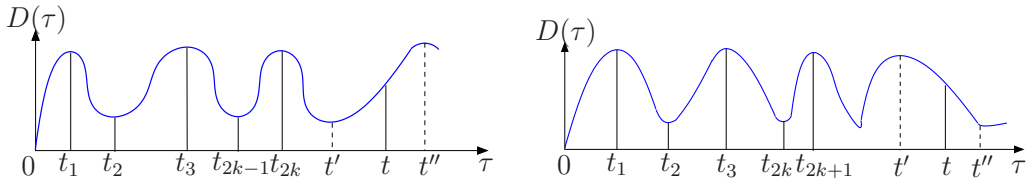
Figure I.2: Schematics illustration of $D(\tau)$, the area of the contact region or regions as a function of time [81]

$w(\mathbf{x}, t)$ have been found up to the time t'. It will proceed to find the solutions $p(\mathbf{x}, t)$ and $w(\mathbf{x}, t)$ for $t' < t < t''$ until n changes its value at t''. For $t > t'$ in the region where $D(t)$ is monotonically increasing, the solutions for $w(\mathbf{x}, t)$ and $p(\mathbf{x}, t)$ for $t \geq t'$, until n changes its value, are given by

$$w(\mathbf{x}, t) = w(\mathbf{x}, t_{2k}) - \sum_{i=1}^{k} \int_{t_{2i-1}}^{t_{2i}} F_{2k,2i}(t, \tau) \frac{\partial}{\partial \tau} w(\mathbf{x}, \tau) d\tau, \qquad (\text{I.35})$$

and

$$p(\mathbf{x}, t) = p(\mathbf{x}, t') - \int_{t'}^{t} \psi(t - \tau) \frac{\partial}{\partial \tau} A(\mathbf{x}, \tau) d\tau, \qquad (\text{I.36})$$

respectively, with

$$A(\mathbf{x}, t) = \int_{t_{2k}}^{t'} \phi(t - \tau) \frac{\partial}{\partial \tau} p(\mathbf{x}, \tau) d\tau + \sum_{i=1}^{k} \int_{t_{2i-2}}^{t_{2i-1}} F_{2k,2i-1}(t, \tau) \frac{\partial}{\partial \tau} p(\mathbf{x}, \tau) d\tau,$$

$$F_{2k,2k}(t, \tau) = \int_{t_{2k}}^{t} \phi(t - \tau^1) \frac{\partial}{\partial \tau^1} \psi(\tau^1 - \tau) d\tau^1,$$

$$F_{2k,2k-1}(t, \tau) = \int_{t_{2k}}^{t} \phi(t - \tau^1) \frac{\partial}{\partial \tau^1} \times \int_{t_{2k-1}}^{\tau^1} \psi(\tau^1 - \tau^2) \frac{\partial}{\partial \tau^2} \phi(\tau^2 - \tau) d\tau^2 d\tau^1.$$

If n changes its value before $D(t)$ becomes a maximum, Eqs. (I.35) and (I.36) are applicable with a new value for t'. Similarly, if $t \geq t'$ is in the region where $D(t)$ is monotonically decreasing as shown in Fig. I.2 (right), $w(\mathbf{x}, t)$ and $p(\mathbf{x}, t)$ are expressed by

$$w(\mathbf{x}, t) = w(\mathbf{x}, t') - \int_{t'}^{t} \phi(t - \tau) \frac{\partial}{\partial \tau} C(\mathbf{x}, \tau) d\tau, \qquad (\text{I.37})$$

and

$$p(\mathbf{x}, t) = p(\mathbf{x}, t_{2k+1}) - \sum_{i=0}^{k} \int_{t_{2i}}^{t_{2i+1}} F_{2k+1,2i+1}(t, \tau) \frac{\partial}{\partial \tau} p(\mathbf{x}, \tau) d\tau, \qquad (\text{I.38})$$

repectively, with

$$C(\mathbf{x}, t) = \int_{t_{2k+1}}^{t'} \psi(t - \tau) \frac{\partial}{\partial \tau} w(\mathbf{x}, \tau) d\tau + \sum_{i=1}^{k} \int_{t_{2i-1}}^{t_{2i}} F_{2k+1,2i}(t, \tau) \frac{\partial}{\partial \tau} w(\mathbf{x}, \tau) d\tau,$$

$$F_{2k+1,2k+1}(t,\tau) = \int_{t_{2k+1}}^{t} \psi(t-\tau^1)\frac{\partial}{\partial\tau^1}\,\phi(\tau^1-\tau)d\tau^1\,,$$

$$F_{2k+1,2k}(t,\tau) = \int_{t_{2k+1}}^{t} \psi(t-\tau^1)\frac{\partial}{\partial\tau^1}\times\int_{t_{2k}(t)}^{\tau^1} \phi(\tau^1-\tau^2)\frac{\partial}{\partial\tau^2}\,\psi(\tau^2-\tau)d\tau^2 d\tau^1\,.$$

If n changes its value before $D(t)$ becomes a minimum, Eqs. (I.37) and (I.38) are suitable to be used with a new value for t'.

The contact problem of a rigid axisymmetric indenter pressed into a viscoelastic half-space was studied by e. g. Lee and Radok [55] and Ting [80, 81], as summarized above, whose work motivated the interest of later workers and set a foundation for later research. The general corresponding solutions have been recast into various viscoelastic constitutive equations. In recent years, experimental scrutiny of these theories and attempts at applying them into the nanoindentation characterization of viscoelastic materials, have been also conducted.

The indentation of standard viscoelastic solids modeled with a three-element Voigt-Kelvin model by an axisymmetric, flat-punch indenter has been investigated theoretically using the correspondence principle by Cheng et al. [18]. The corresponding solutions cover different loading histories: single step change in load, multiple step load and arbitrary load history. Its applicability on the polyurethane (**PU**) coatings and bulk polystyrene (**PS**) have been verified experimentally. Analytical solutions of indentation on the same standard viscoelastic solids with a spherical indenter, were developed later by Cheng et al. [17]. The experimental verification of the solutions was conducted by nanoindentation relaxation and creep tests on bulk **PS** and by the creep tests on drying semicrystalline polyvinyl alcohol (**PVOH**). The results indicate that the derived three-element analytical model of spherical indentation into the considered two polymers is suitable.

Sakai and Shimizu [74] evaluated theoretically the time-dependent viscoelastic properties and the flow during indentation by a flat-ended, spherical, conical or a pyramidal indenter into glass-forming materials at temperatures near the glasstransition. The concept of representative stress and strain combined with the hereditary integral leads to principal constitutive equations for linear viscoelastic indentation. An experimental as well as theoretical study of the viscoelastic behavior of **soda-lime silica glass** have been conducted by the use of a Berkovich indenter. Later in [73], Sakai recast the analytical solutions for elastic contact of an axisymmetric indenter into the associated viscoelastic solutions via Boltzmann's hereditary integral. Relations between the time-dependent indentation load $F(t)$ versus the penetration depth $h(t)$ have been developed for simple viscoelastic liquids and solids.

A model based on the contact between a rigid indenter and a linear viscoelastic material was developed in [84] to calculate the creep compliance and stress relaxation modulus for two glassy polymeric materials, **epoxy** and polymethyl methacrylate (**PMMA**), and two polydimethyl siloxane (**PDMS**) elastomers. Jäger et al. [41] obtained a solu-

tion to identify viscoelastic properties from the nanoindentation test data taking the real tip geometry into account. This analytical solution is specialized for the case of a trapezoidal load history. Three deviatoric creep models, the single dash-pot, the Maxwell element, and the three-parameter model were considered. The approach has been illustrated by the identification of short-term viscoelastic properties of **bitumen** from nanoindentation.

In the past decades, modifications or applications of the viscoelastic indentation theory constructed by Lee and Radok [55] or by Ting [80, 81] to characterize time-dependent properties of polymers from indentation, have been published in a huge number of articles. The readers can find some additional literature in paper B. As a short conclusion, since these analytical solutions are obtained based on the classical elastic contact theory using mathematical transformations, e. g. the correspondence principle or the Laplace transform, they have limitations. Most of the analytical solutions yield accurate results only for linear viscoelastic models under fixed experimental processes. The non-linear rate- and temperature-dependent properties are fail to capture. Besides, effects such as friction, adhesion and surface roughness, which may be sensitive in nanoindentation tests, are not taken into account in the solutions. Therefore, efforts have to made to construct more general analytical solutions. Very recently, Ding et al. [23] constructed a viscoelastic solution for the stress and displacement fields by the analysis of the elasticity-viscoelasticity corresponding theory taking the temperature-dependency into account. The temperature- and time-dependent viscoelastic recovery of **PMMA**, which was measured by AFM nanoindentation experiments, was predicted by this model in a numerical way based on the Boussinesq elastic theory.

2.4   FEM based inverse method

The inverse method is a general framework that is used to convert observed measurements into information about a physical object or system that we are interested in. The experimental responses of a physical object or system, which is a prior information on a mathematically described model about this physical object or system, is treated as reference source to determine the model parameters in the inverse method. Hence, it is common in the engineering analysis to involve the determination or prediction of a new material or a new structure to use the inverse method. It is one simple way to fit the experimentally determined responses to the theoretical or analytical solutions in order to determine the material or structure parameters. However, the available analytical solutions are restricted to physical structures with relatively simple geometry and loading conditions. In this case, the finite element method (FEM) based inverse method is popular to use because it allows specimens with arbitrary shapes and physical processes with nonlinear nature and arbitrary loading conditions. This method is especially powerful when the material or structure properties are complex,
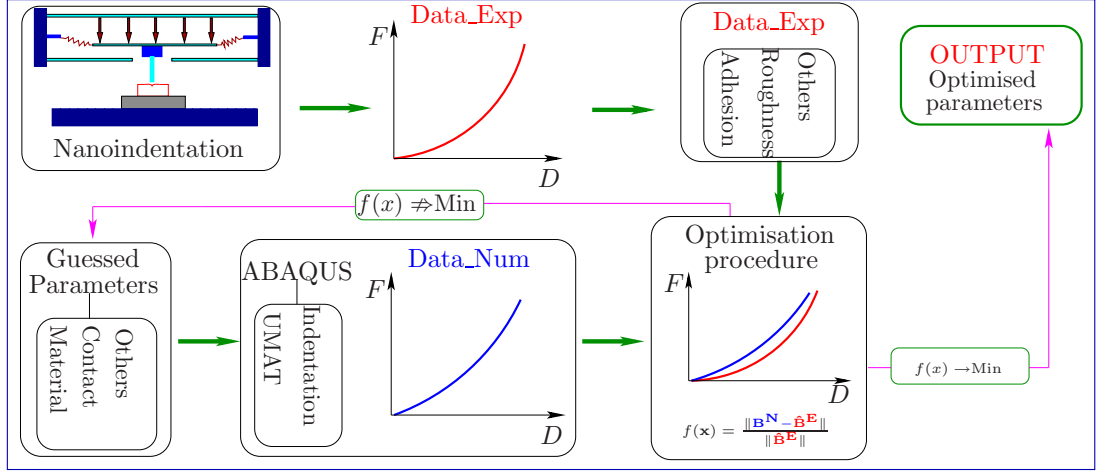
Figure I.3: Flow-chart of the developed analysis procedure using FE based inverse method

e. g. nonlinear, heterogeneous and anisotropic. Since the indentation process on polymers involves strongly nonlinear contact mechanics as well as nonlinear time-dependent material properties, the FE based inverse method is chosen to develop a robust analysis procedure in this study.

Fig. I.3 represents the flow-chart of the developed analysis procedure using the FEM based inverse method, which is a mixed experimental and numerical optimization problem. First of all, the force-displacement data obtained from nanoindentation experiments are used as reference source and are imported into an optimization procedure. The error contributions such as adhesion effects, surface roughness and other process associated factors are involved in the experimental data. The optimization procedure is developed combining the FEM code ABAQUS [®] with the mathematics tool MATLAB [®]. In the optimization procedure, the boundary value problem of nanoindentation is simulated in ABAQUS [®] taking into account the real geometry and real boundary conditions as same as in the experiments. In the numerical model, it is important to choose a suitable contact model between the tip and the surface, a material model for the specimen and models predicting other affecting responses. It is the goal to determine the corresponding parameters of these models by this procedure. The principle of the method is to compare experimental force-displacement data with the computed results from the finite element model. Starting with guessed initial values, the models' parameters are iteratively updated by an optimization algorithm. The identification can then be formulated as an optimization problem where the objective function $f(x)$ to be minimized is an error function of the least squares type that expresses the difference between experimental measurements and the numerical predictions. The argument represents all model parameters, which have to be determined.

The choice of the optimization-based method for minimizing an objective function is a topic of interest. It is generally advised to use globally convergent optimization algorithms whenever possible. These algorithms are simulated annealing [47, 27] or genetic algorithms [75, 20], such as evolutionary algorithms, or deterministic algorithms like the Simplex method [53, 50]. The gradient based algorithm is full of troublesome gradient calculation and the further drawback of local convergence. Genetic or evolutionary algorithms are globally convergent and are the only useful choice in a multi-objective optimization.

3 Error contributions affecting nanoindentation

As mentioned at the beginning, nanoindentation has a considerable advantage to determine local properties from continuously measured force-displacement data with high resolution. Unfortunately, there are various problems that influence the actual material response during indentation, e. g. friction, adhesion, surface roughness and the indentation process associated factors. These problems result in a systematic error between the numerical and the experimental results that often leads to even larger errors in the parameter identification [71, 15, 16, 6, 60, 83]. Therefore, a certain knowledge about the influence of these factors and basic investigations are indispensable to characterize the material accurately by the inverse method.

3.1 Thermal drift

The thermal drift in nanoindentation generally refers to a change in dimensions of the instrument due to thermal expansion or contraction of the apparatus. An other source of thermal drift is the heat generation of the electronic devices or within the plastic zone of indentation. This change in depth imposes a thermal drift error onto the real depth of the displacement readings.

To correct the thermal drift, it is common to measure the displacement increment during a hold series of the load. A linear regression to the displacement-time curve within this hold period allows to obtain the thermal drift rate. Then the thermal drift rate is considered in all the displacement readings according to the testing time. However, for the most of polymeric materials creep may be prominent when the load is held constant and the depth readings increase due to the superposition of creep and thermal drift. The creep response should be as full as possible included in the force-displacement data in order to characterize accurately the viscoelasticity from nanoindentation. At the same time the thermal drift effects should be eliminated.

Therefore, in the nanoindentation of polymers, the thermal drift rate is calculated during a hold period at the final unload increment because the creep within the material is less likely to occur at a low value of the load. This thermal drift correction procedure works fine for short-term indentation. But it is not clear if it is reasonable to apply such a correction for long-duration testing like creep or relaxation tests since a linear relation is assumed.

3.2 Initial contact point

In a nanoindentation test, the indentation depth is ideally measured from the level of the specimen's free surface. However, in practice, it is necessary that the indenter makes actual contact with the specimen's surface to achieve the threshold for the indentation depth measurements. Therefore, in all nanoindentation experiments, a pre-load
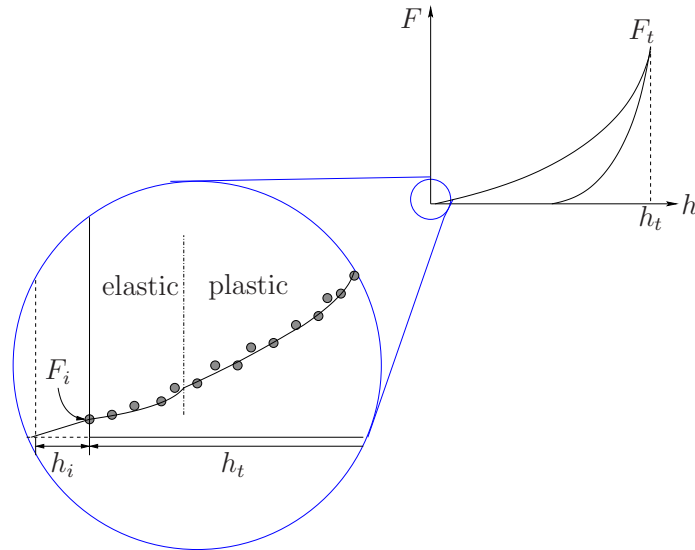
Figure I.4: Schematic illustration of the effect of initial indentation depth on the force-displacement data [26]: the initial contact force F_i results in an initial indentation depth h_i

which is often set to be the smallest obtainable force of the instrument, is usually applied to detect the initial contact point. The free surface of the specimen is identified by setting the measured indentation depth and the contact area to zero at this smallest force. For most commercially available nanoindentation instruments, the theoretical load resolution is better than 1 nN. Hence, it is theoretically capable to detect the exact

initial contact point. However, in practice, for the Hysitron TriboIndenter® used in this study for example, the achievable load resolution is limited by external influences to no better than $100\,\text{nN}$. If the indentation with this pre-load is made on the surface of metals or ceramics, the corresponding penetration beneath the undisturbed specimen's free surface may be negligible. However, due to the high compliance, a small amount of pre-load can cause a considerable indentation in soft polymers as shown schematically in Fig. I.4. As a result the initial contact point is uncertain and results from indentation testing are in error [64, 11, 22]. For instance, for the PDMS material with a tensile modulus of $1\,\text{MPa}$, the difference in the detected surface position leads to deviations in the resulting modulus which vary as high as 400% [22].

Therefore, as shown in Fig. I.4, the initial indentation depth, h_i, has to be calculated and to be added to all measured displacements, h, to correct for this initial contact point. Fischer-Cripps [26] supplied a method to calculate the initial indentation depth, h_i, with an assumption that the first few loading points result in purely elastic deformation of the specimen. So it is possible to fit this initial data points using the Hertz equations predicting that the relationship between the load and displacement for an elastic response

$$h + h_i \propto F^m, \tag{I.39}$$

where $m = 2/3$ for a spherical indenter, $m = 1$ for a cylindrical flat punch indenter, and $m = 1/2$ for a conical indenter. Alternatively,

$$h = k\,F^m - h_i = k\,F^m - k\,F_i^m, \tag{I.40}$$

where k is a constant whose value depends upon the shape of the indenter. The easiest way to adjust the variables m and k for a linear response is to plot the logarithm of both sides of Eq. (I.40) to obtain a slope equal to a unity. Thus,

$$\log h = \log k + A \log\left(F^m - F_i^m\right). \tag{I.41}$$

A plot of $\log h$ versus $\log\left(F^m - F_i^m\right)$ should have a slope $A = 1$ if m and k are chosen correctly.

A nonlinear least squares fitting procedure can also be used to fit the initial loading data point according to a power law relationship

$$F = (h + h_i)^n, \tag{I.42}$$

where n and h_i are the unknowns to be identified, and F and h are the experimental data. Care must be exercised with the choice of the initial data points of F and h that these data should be within the pure elastic response. In [82], the initial indentation depth h_i is treated as an additional parameter that is identified by a neural network. As an advantage, no assumption on the form of the initial loading curve has to be

made.

Detecting the initial contact point is also required to exclude the influence of the surface roughness on the force-displacement data in nanoindentation. According to the numerical calculation in [15], the surface roughness, which contains very sharp asperities, has an effect resulting in much lower contact stiffness especially at the very beginning of the indentation. In this case, the surface roughness effect can be removed if a new initial contact point is re-defined to throw off the contact part in which the contact stiffness is nearly zero.

3.3   Surface roughness

It is tacitly assumed in the classic contact theory, discussed in section 2, that the surface of contacting bodies are topographically smooth. In consequence contact between them is continuous within the nominal contact area. However, in reality, such circumstances are extremely rare and the real area of contact is a discontinuous small fraction of the nominal contact area. Since the contact area is measured indirectly from the indentation depth, the surface roughness is a very important issue in nanoindentation. The natural roughness of real surfaces causes errors in the determination of the contact area between the indenter and the specimen.

There is a large variety of literature on experimental as well as numerical investigation of the surface roughness effects in nanoindentation. It is known by the experiments and simulations that the surface roughness impacts the Young's modulus and the hardness measurements [4, 3, 49, 69]. The surface roughness can considerably disturb the indentation curves [45], and may, at least, be one of the main reasons for the indentation size effect [46]. The criteria to remove the surface roughness effects are found by experiments for some special materials. Johnson [43] quantified the surface roughness by a roughness parameter α:

$$\alpha = \frac{\sigma_s R}{a_0^2} \, , \tag{I.43}$$

where σ_s is equal to the maximum asperity height, R is the indenter radius and a_0 is the contact radius that would be obtained under the same F for smooth surface. Johnson [43] found that the effects of surface roughness on the validity of the elastic contact equations were of significance for $\alpha > 0.05$. The results in [4] reveal that the surface irregularities or the roughness which are characterized by fractal dimension and RMS height of asperity, play a role in the scatter in hardness measurements. Later, Bobji et al. [3] formulated a general framework to deconvolve genuine property variation by normalizing the measured hardness with the surface roughness effect for the indentation depth larger than 3 times the RMS roughness. Miller et al. [63] presented a criterion for the roughness of cement paste surfaces for nanoindentation. The material properties obtained from nanoindentation converge to a unique set of values when the

average indentation depth of the first peak is greater than 5 times the RMS roughness, where the roughness is measured over a scanning size of 200 times the average indentation depth. Donnelly et al. [24] examined the effects of surface roughness and the maximum nanoindentation load on the measured mechanical properties in two cancellous bones with different surface roughnesses using maximum loads ranging from 250 to 3000 μN. The results indicated that the variability in material properties increases substantially if the ratio of indentation depth to surface roughness decreases below 3:1. It is difficult to control the roughness of a specimen in the real experiment and to interpret the measured results. In contrast, the numerical simulation allows to supply flexible roughness geometry and to display the involved physical process. Finite element calculations are widely used to investigate and to interpret the surface roughness effects in nanoindentation. In 2007, Walter et al. [85] incorporated the measured surface topography of CrN thin films into a 2D finite element model. The Oliver & Pharr method was used to evaluate the Young's modulus from the simulated load-displacement curves. The results show that the surface roughness leads to an underestimation of the Young's modulus, but the amount of this deviation seems to be independent of the actual value of the arithmetic roughness R_a. Further simulations indicate that the mean value of a sufficiently large number of indents can give a good approximation of the Young's modulus of the films, even if the surface is rough and the data scatter is high. Two years later, Walter et al. [86] compared the simulation results from a true 3D model and from a 2D axisymmetric model [85] of nanoindentation taking the surface roughness effects into account. The comparison indicated that both models predict a significant underestimation of the evaluated Young's modulus due to the effect of surface roughness. The axisymmetric setup of the 2D model leads to increasing scatter of the force-displacement data and on average to a higher stiffness compared to the 3D model and therefore a 3D simulation seems preferable. The results obtained in [7] show also that, in order to exclude the roughness effect, an average of an appropriate number of nanoindentations must be considered, depending on the roughness magnitude. Jiang et al. [42] pointed out that in order to rule out the influence of the surface morphology, the indentation depth should be much greater than the characteristic size of the surface roughness. Moreover, an indenter with a sufficiently large diameter could also be a good choice. A numerical study was conducted in [2] to understand the coupled influence of friction and surface roughness in the nanoindentation of pure nickel. Results have shown a strong interaction between these two contributions of surface effects and their cumulative effects lead to significant variations in the force-displacement curves.

The surface roughness of the bulk sample can be altered by various mechanical or electrochemical methods of polishing. However, an excessive polishing could influence the mechanical properties of soft and thin polymer films. Therefore, in practical experiments, the surface roughness of thin films can reach an average height of asperities about 30-60 nm [49, 25, 78]. Because of that, the surface roughness is comparable to the imposed indentation depth limited by the thin layer's thickness and the influence of the substrate. In this case, some of the criteria using a deeper indentation depth

compared with the surface roughness documented in literature, cannot longer be used. A quantified evaluation of the surface roughness effect is still required. Furthermore, if an inverse optimization method is used, it is essential to decrease the system errors between the experimental settings and the numerical models. For this reason, more attention is paid on the numerical model of the realistic surface roughness profile. For most real surfaces, for example those produced by grinding or molding, the heights and the wave lengths of the roughness asperities vary in a random way. It is argued in [43] that most man-made surfaces have a pronounced "lay", which may be modeled to a first approximation by one-dimensional roughness. Therefore, Johnson established the simplest model of a rough surface in [43], which is a regular wavy surface with a sinusoidal profile. If an elastic half-space with a flat surface is brought into contact with an elastic solid having a one-dimensional wave of asperity height H and wave length λ, the gap between the surfaces can be expressed by

$$g(x) = H \left[1 - \cos(2\pi x/\lambda) \right]. \tag{I.44}$$

In the two-dimensional configuration, the gap between a flat surface and one which has a regular orthogonal waviness can be expressed as

$$g(x, y) = H_1 + H_2 - H_1 \cos(2\pi x/\lambda_1) - H_2 \cos(2\pi x/\lambda_2). \tag{I.45}$$

The three-dimensional multi-asperity contact of an indenter with a rough simulated surface was studied in [4]. The rough surface was simulated using a self-affine fractal function. The asperity height $H(x)$ of an isotropic and homogeneous rough surface in any arbitrary direction, along a straight line, can be represented by the Weierstrass-Mandelbrot relationship

$$H(x) = G^{(D-1)} \sum_{n=n_1}^{\infty} \frac{\cos(2\pi\gamma^n x)}{\gamma^{(2-D)n}}; \quad 1 < D < 2; \; \gamma > 1, \tag{I.46}$$

where, G is a scaling constant, D is the fractal dimension of the profile and $\gamma = 1/\lambda$ is the frequency mode corresponding to the reciprocal of the wave length λ of the rough surface, and n_1 is the lower cutoff frequency of the profile which depends on the length of the sample L through the relation $\gamma^{n_1} = 1/L$, γ is chosen to be 1.5 for phase randomization and high spectral density.
The finite element method is often used to simulate the effect of surface roughness. In [85] the surface roughness of sputter-deposited CrN thin films for the axisymmetric 2D model was taken from experimental AFM scanning data. Line scans of the AFM surface profile were then interpolated at the top surface node positions of the surface mesh and these nodes were re-positioned in axial direction according to the measured surface roughness [85]. However, because the model does not resemble 3D surface

roughness due to its symmetry, it is necessary to keep the model size within feasible limits. Latter Walter et al. [86] simulated the surface roughness of sputter-deposited CrN coatings with a true 3D model. A section of the measured surface profile with AFM was selected and interpolated at the node positions of the sample mesh and then introduced as top layer into the FEM model of the sample. The challenge of 3D modeling is to keep the number of degrees of the freedom (DOF) small and taking the computational cost into account. Since the size of the elements has to be small in order to represent the actual roughness profile sufficiently well, the viable overall dimensions of the model are limited too. Pre-existing straight grooves defects were introduced on the film surface in 2D FE models in [42] in order to simulate the surface roughness. The included geometric parameters are the height of the defects, the spacing between the neighboring defects and the hight of the defects. Berke et al. [2] described the roughness with a protuberance-on-protuberance profile approximated by a sine function using axisymetric 2D FE models. The surface roughness was chosen to have the simplest representation considering only the first level of a sine profile. A more realistic rough surface was modeled by the sum of four sine functions with different amplitudes, wave lengths and phase shifts.

3.4 Adhesion effects

In surfaces interaction, as a result of the competing force attraction and repulsion between individual atoms or molecules in both bodies, two ideally flat solid surfaces will have an equilibrium separation g_0. At a separation less than g_0 they will repel each other and at a separation greater than g_0 they will attract. At small scales, such as the case of tip-sample interaction in nanoindentation, the adhesion arising from attractive forces is generally not negligible and must be taken into account [43]. Several continuum mechanic models have been developed to predict the contact force between two elastic bodies as discussed before. The classic model is due to Hertz and concerns two elastic spheres in the absence of adhesion. There are three adhesive contact models available, namely JKR (Johnson-Kendall-Roberts) [44], DMT (Derjaguin-Muller-Toporov) [21] and MD (Maugis-Dugdale) [61]. JKR considers the contact when the surface forces, which only act inside the contact area, are short range in comparison to the elastic deformations during contact (i.e., compliant materials, strong adhesion forces, large tip radii). DMT which applies well in the case of long-range surface forces acts only outside the contact area (i.e., stiff materials, weak adhesion forces, small tip radii). The transition between JKR and DMT models is presented in the MD model, which studies the periphery of the tip-sample interface modeled as a crack failing at its theoretical strength. The adhesive force F_{ad} or "pull-off force", at which the surfaces separate

when being pulled apart, are given in the JKR and DMT theories by

$$F_{\text{ad(JKR)}} = 2\pi\,\gamma\,R, \tag{I.47}$$

$$F_{\text{ad(DMT)}} = \frac{3}{2}\pi\,\gamma\,R, \tag{I.48}$$

where, γ is the interfacial energy and R is the curvature radius of the spherical indenter. The models also give the functions of the contact radius a and the indentation depth

$$a_{\text{(JKR)}} = \left(\frac{R}{K}\left(\sqrt{F_{\text{ad(JKR)}}} + \sqrt{F_{\text{H}} + F_{\text{ad(JKR)}}}\right)^2\right)^{1/3}, \tag{I.49}$$

$$a_{\text{(DMT)}} = \left(\frac{R}{K}\left(F_{\text{H}} + F_{\text{ad(JKR)}}\right)\right)^{1/3}, \tag{I.50}$$

$$h_{\text{(JKR)}} = \frac{a_{\text{(JKR)}}^2}{R} - \frac{4}{3}\sqrt{\frac{a_{\text{(JKR)}}\,F_{\text{ad(JKR)}}}{R\,K}}, \tag{I.51}$$

$$h_{\text{(DMT)}} = \frac{a_{\text{(DMT)}}^2}{R}, \tag{I.52}$$

where F_{H} is the contact force evaluated according to the Hertz contact theory i.e. Eq. (I.9), K is a factor related with the reduced elastic modulus, given by $K = 4/3\,E^\star$. As illustrated in Fig. I.5, in the Maugis Dugdale case, the adhesion force is assumed
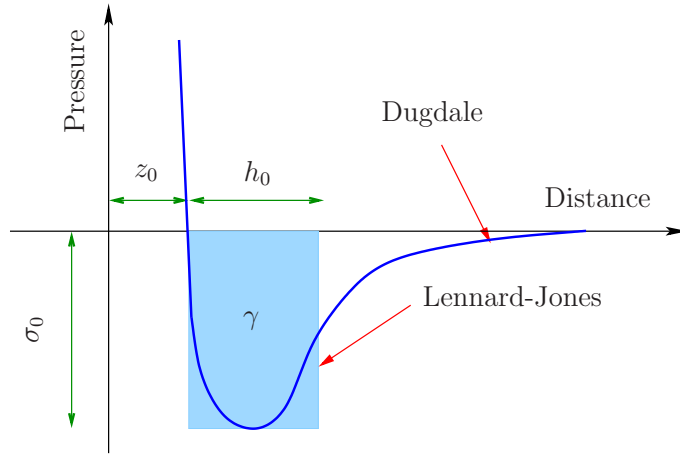
Figure I.5: Schematics illustration of effect of Lennard-Jones and Dugdale surface force laws

to have a constant value σ_0 until a separation h_0 is reached, where it falls to zero. The value of h_0 is chosen in order to match the work of adhesion of a Lennard-Jones

potential, i. e., $\gamma = \sigma_0 \, h_0$. Maugis [61] defined a nondimensional parameter

$$\lambda = 2 \, \sigma_0 \left(\frac{R}{\pi \, K^2 \, \gamma} \right)^{1/3}, \qquad (I.53)$$

and suggested that, for $\lambda < 0.1$, the DMT model is applied and for $\lambda > 5$, the JKR model is applied. Three equations are needed to evaluate F, a and h:

$$\begin{aligned} 1 &= \frac{\lambda \, \bar{a}^2}{2} \left((m^2 - 2) \tan^{-1} \sqrt{m^2 - 1} + \sqrt{m^2 - 1} \right) \\ &+ \frac{4 \lambda^2 \, \bar{a}}{3} \left(\sqrt{m^2 - 1} \tan^{-1} \sqrt{m^2 - 1} - m + 1 \right), \qquad (I.54) \\ \bar{F} &= \bar{a}^3 - \lambda \, \bar{a}^2 \left(\sqrt{m^2 - 1} + m^2 \tan^{-1} \sqrt{m^2 - 1} \right), \qquad (I.55) \\ h &= \bar{a}^2 - \frac{4 \lambda \, \bar{a}}{3} \sqrt{m^2 - 1}, \qquad (I.56) \end{aligned}$$

where, $m = c/a$, c is the radius of a circular region, over where the constant attractive force σ_0 continues to act. $\bar{a}$, $\bar{F}$, $\bar{h}$ are nondimensional parameters defined as

$$\begin{aligned} \bar{a} &= a \left(\frac{K}{\pi \, \gamma \, R^2} \right)^{1/3}, \qquad (I.57) \\ \bar{F} &= \frac{F}{\pi \, \gamma \, R} \qquad (I.58) \\ \bar{h} &= h \left(\frac{K^2}{\pi^2 \, \gamma^2 \, R} \right)^{1/3}. \qquad (I.59) \end{aligned}$$

In practice, the MD model is rather troublesome for fitting experimental data because there is no direct relationship between force and indentation depth. It is necessary to use a numerical calculation to obtain the value of λ and then values of $\bar{a}$ and m can be further evaluated.

The adhesive behavior discovered in nanoindentation experiments has been reported to be visible as negative forces in the force-displacement curve [11, 13, 56, 9], residual displacement or non-zero contact area when the load is reduced to zero [29, 9, 14]. These observations suggest that the adhesion energy at the tip-sample interface is a significant parameter for soft materials and should be taken into account for a consistent determination of the mechanical properties by nanoindentation. Including adhesive forces in the analysis of nanoindentation data can elucidate the difference of the determined modulus and the contact area at different peak loads [91, 29]. The three adhesive models such as JKR, DMT and MD have been used to evaluate analytically the adhesion effects on the contact area and, additionally, on the determined hardness

and modulus. For example, Gupta [29] evaluated analytically the elastic modulus of soft polydimethylsiloxane (PDMS) from nanoindentation with the JKR model taking the adhesive pull-off force into account. The difference in elastic modulus evaluated by the Hertz contact theory at different peak loads could be explained. Liao [56] applied a hybrid model that combines the Hertzian theory and the JKR model to evaluate the elastic modulus and the adhesion work by fitting the experimental data. All three adhesive contact models were compared with the Hertz model by Zhao et al. [91], who suggested that the MD model was the most suitable theory to deal with adhesive forces in contact problems at the nano-scale. In order to quantify the adhesion effects using the inverse method as described above, it is necessary to include an adhesive contact mechanics into the numerical modeling. Wang [88] incorporated adhesive interactions with FE computations in ABAQUS® by user-defined elements. A bilinear force-separation relationship was applied to simulate the adhesive contact behavior between a tungsten tip and an organic film. A typical contact between a sphere and a flat substrate was simulated in ANSYS® [90] with the presence of adhesion forces. The general FE simulation model of the investigated contact processes was modified and the interfacial interactions of the Lennard-Johns potential were incorporated into the contact cells. To quantify the adhesion force and its influence on the characterization in nanoindentation of polymers, the inverse method combining the FEM calculation and the numerical optimization is a new but robust method. In this method, the adhesion force can be expressed with the user defined adhesive models with the corresponding identified parameters.

3.5   Influence of friction

In the majority of nanoindentation experiments, the surface effects are difficult to control and to monitor. Only an estimation of the frictional behavior is possible but its influence on the force-displacement data and the determined properties is unknown. Furthermore, the friction cannot easily be changed experimentally in a predefined range with the same material contact pair. This motivates the numerical calculation to evaluate the influence of friction and its variation in indentation problems. The main evidence of frictional effects, most commonly considered in indentation simulations, are the influence on the local variable, e. g. stress or strain distributions and on the global variables, e. g. the imprint geometry, contact areas, indentation force-displacement curves. The friction is shown to have a substantial influence on the stress and strain fields beneath the indenter [62, 51, 12] with possible implication for deformations such as crack initiation and crack growth. However, some dispersion in the conclusions of works have been presented in the literature considering the global effect of friction on the indentation results: some conclude that the global indentation behavior is unaffected by friction on the contact interface [12, 51, 87], while other findings show that

the friction can be a significant source of scatter [1, 2, 8, 10, 30, 37, 60, 67]. Larsson and Carlsson [51] performed a detailed study of the role of friction at Brinell and Boussinesq indentation of viscoelastic polymers. The conclusion drawn from the results is that global properties, such as the contact load, is more or less unaffected by friction. The results from [12] show that friction has strong influence on the global properties such as the contact area and the mean contact pressure only if the deformation of the material is in a perfectly plastic way. Friction has no significant influence on the force-displacement curve during loading in [87]. However, during loading, friction effects result in less vertical displacement and deeper residual depth. The dissipation of friction leads to significant variations in the load-displacement curves [10, 37, 2]. Friction has a substantial effect on the contact size as a function of indent depth due to pile-up [62, 60, 8, 1, 30]. The friction has the largest influence on the contact response of solids exhibiting considerable pile-up effects, whereas material developing moderate pile-up or sinking-in are less sensitive to friction [60, 79]. The pile-up height can be up to several times larger in frictional sliding than in normal indentation [1, 6, 60]. The experimental data indicated that the frictional effects in indentation intrinsically depend on the interfacial contact conditions, e. g. contact material pair, indenter shape. The friction was recognized to have the largest influence on the normal force when using sharp indenters having included angles less or equal to 50° and to have a negligible effect for relatively flat indenters (e. g. Berkovich indenter) [8, 70]. The effect of friction was reported to be significant when the indentation depths is comparable to or larger than the radius of curvature of the indenter [10]. The importance of friction also depends on the choice of the sample's material model, the indentation of an elastic perfectly plastic material with a large value of E/σ_y is rather insensitive to friction when considering a Coulomb friction model [10, 87].

4 Summaries of the appended papers

In **Paper A**, the nanoindentation of hyperelastic polymer layers at finite deformation was investigated theoretically and numerically. Three often used hyperelastic models i. e. the neo-Hooke, the Mooney-Rivlin and the Yeoh models with the chosen parameters are applied to simulate the indentation test with the finite element code ABAQUS®. A parameters re-identification procedure was developed by combining the MATLAB® optimization toolbox with the nanoindentation boundary value problem (shorted as BVP). The squared difference between the virtual experimental results and the numerical data called objective function was minimized with respect to the model parameters using numerical optimization. An artificial random noise was superimposed on the virtual experimental data to make it more realistic and to check the stability of the identification procedure.

In contrast to the traditional nanoindentation analytical method, in this paper, the penetration depth was not constrained to avoid the influence of the substrate. A parametric investigation was performed to examine the relationship between the behavior of nanoindentation at finite deformation and the geometric parameters of the BVP. The results indicated that the ratio of the displacement to the radius of a spherical indenter u/R and the ratio of the displacement to the layer thickness u/H_L were two key parameters for force-displacement behavior in nanoindentation of polymer layers on hard substrates. The non-linear elastic behavior of the Yeoh model was strongly dependent on u/H_L, which became obvious when u/H_L was larger than 0.2 and was fully represented if u/H_L increased up to 0.4.

The parameter re-identification concept was used to capture material parameters from nanoindentation based on the evolution strategy. Therefore, it was assumed that the properties of the substrate were previously known. The single parameter of neo-Hooke model was perfectly identified whether at small deformation or at finite deformation. However, for Mooney-Rivlin model, both parameters C_{10} and C_{01} of the Mooney-Rivlin model could not be accurately identified at small deformations independing on the data noise. The contribution to the force-displacement results from C_{10} and C_{01} was not possible to be divided. Such a phenomenon is called parameters coupling. Its influence on the parameter identification decreased in this study at finite deformation. For Yeoh model, the parameters C_{20} and C_{30} of the high-order terms could not be identified accurately at small deformations because of the lack of non-linear response. Nevertheless at finite deformation, all of the three parameters of the Yeoh model were able to be identified with tolerable errors even though a random noise level was superimposed up to 5%.

As an advantage, only one parameter had to be determined for the neo-Hooke model and it was also important that a parameter coupling could be avoided. The indentation behavior of the relatively complicated hyperelastic models was tried to be represented with the simple neo-Hooke model. It seemed that the behavior of the Mooney-Rivlin model under nanoindentation can be approximated with the neo-Hooke model even though at finite deformation. However, modeling the behavior of the Yeoh model with the relative simple neo-Hooke model was restrained to the deformation at which the strong non-linearity of the Yeoh model was inactive.

In **Paper B**, to characterize the viscoelastic properties of polymer layers from nanoindentation, the inverse method was used combining finite element modeling and numerical optimization. The boundary value problems of nanoindentation of polymer layers considering real geometry was simulated with the FE code ABAQUS®. A linear viscoelastic model for small strain, based on a general Maxwell rheological model, was implemented into the user material subroutine `umat` of ABAQUS®. The rate-dependent behavior of the polymer layer under nanoindentation was investigated with various loading histories: cyclic testing, single step relaxation, monotonic testing and sinusoidal oscillatory testing. A parameter re-identification strategy offered a deep in-

sight into the relationship between the accuracy of the identification and the loading history associated with the rate-dependent material model. It allowed us to investigate how accurate the parameters could be identified from the nanoindentation force-displacement response.

Firstly, a cyclic test containing a loading and an unloading stage was applied with various loading rates to investigate the rate dependent hysteresis loop in the force-displacement curve. The obvious creep during the unloading led to a negative contact stiffness according to the Oliver & Pharr method. Therefore, a suitable holding stage before unloading was necessary to apply the Oliver & Pharr method for a rate-dependent material. Secondly, a single step of relaxation and creep tests presented the force relaxation and the deformation creep, respectively. The relaxation or creep process was not only related with the maximum load but also with the loading rate and the holding time. Thirdly, a monotonic test was used to approximate the equilibrium points of the force-displacement curve. For displacement control, the approximated equilibrium points were consistent with the equilibrium curve obtained from the numerical simulation. However, in force control testing deviations appeared if the displacement is large. Finally, a sinusoidal oscillatory testing was applied too. In the displacement controled test, the force relaxed sinusoidally towards the equilibrium states. Nevertheless, the displacement had only a slight response with sinusoidal oscillations of the force. The parameters' identification of the chosen viscoelastic model from nanoindentation was performed with the different described loading histories. The accuracy of parameter identification was dependent on the chosen loading history. It was better to capture the basic elasticity using monotonic testing first. The viscoelastic parameters of the Maxwell elements in parallel could be efficiently identified by a suitable long relaxation testing. A sinusoidal oscillatory testing, performed in the present study, seemed to be useful to identify the elastic and viscoelastic parameters at one time. However, it was difficult to identify each parameter exactly for a multi-parameters model, especially if there were several parameters acting in parallel, e. g. the shear moduli μ_e^j and the relaxation times r^j of each Maxwell element. An exact match between the experimental data and the prediction of the numerical model did not guarantee the accurate identification of each parameter. In this case, the combination of several loading histories as well as different tests of various deformation forms might be taken into account. The choice of the loading history and testing method depended on the experiment and practical experience. This was the main problem needed to be solved in characterization of polymers by nanoindentation with the inverse method.

In **Paper C**, frictional nanoindentation of hyperelastic polymer layers on hard substrate has been numerically computed with ABAQUS®. Two non-linear elastic models that are Mooney-Rivlin and Yeoh models, are used to predict the hyperelasticity of the polymer layers. The formulation of non-penetration is used to impose the contact constraints in the normal direction. The friction effect between the indenter and the polymer layer is related with the tangential contact, which is described by the classical

Coulomb's law. The influence of friction on the force-displacement data of both considered models show that the friction results in a larger indentation force if the penetration depth is deeper than 10% of the layer thickness. If the ratio of displacement to the layer thickness is 40%, the required force increases about 20% compared to the frictionless case. In this case, because of the relative tangential slip in the frictional contact, the contact area increases about 19%. Unlike the indentation test with viscoelastic or plastic material, in this case, the increment of the contact area is only related to the friction dissipation. However, if the displacement is restricted to 5% of the layer thickness, the influence of the friction can be definitely neglected. A series value is employed which varies the friction coefficient from 0 to 1.0. It seems that the influence of the frictional effects do not change with a variations of μ if it is larger than 0.4. The relative dimension of the spherical indenter and the layer thickness R/H_L have a relationship with the friction effect. The indentation forces increase by 19%, 23% and 25% compared with the frictionless cases with a R/H_L of 1.0, 1.5, 2.0, respectively. Hence, a relatively smaller spherical indenter should be chosen if it is expected to decrease the influence of friction. As a conclusion, in the case of indentation of soft layers on hard substrates, it seems that enlarging the indented deformation plays a double-edged role. On the one hand, the identified results from a large deformation are better than the results obtained from a small displacement indentation. The parameters coupling of the Mooney-Rivlin model is reduced largely and all of the three parameters of the Yeoh model can be accurately identified at large deformation. On the other hand, the investigation of friction shows that the large deformation also increases the influence of friction on the measured force-displacement data.

In **Paper D**, the characterization of two often used soft hyperelastic polymers, PDMS and silicone rubber, was investigated by nanoindentation taking into account effects of the surface roughness. The boundary value problems of the nanoindentation of two polymers were modeled with the FE code ABAQUS®. The model parameters were re-identified by using an evolution strategy based on the concept of the numerical optimization. The influence of the surface roughness was quantified as a function of the sine parameters as well as of the indentation parameters. Moreover, it was verified that the real surface topography can be characterized by using multi-level or simple one-level of protuberance-on-protuberance sinusoidal roughness profiles.
At first, the parametric investigation of the surface roughness effects was performed by indentation on a regular surface roughness described by a one-level sine function. The surface roughness effects strongly depended on the roughness shape, namely the wave length λ and the asperity height H. The indentation on a very sharp asperity with a low ratio λ/H led to a decreased contact stiffness compared to a flat surface especially at the initial indentation. The identified values of the parameters C_{10} and D_1 of the neo-Hooke model were about 60% lower than the chosen values due to the effects of surface roughness with λ/H of 0.25 ($5\,nm/20nm$). Nevertheless, the surface roughness effect on the force-displacement curve could be avoided if a new initial indentation

point was defined by a certain threshold of the resulting contact force. In this case, the re-identified parameters had only an acceptable deviation from the chosen values. The surface roughness effect resulted in a higher contact stiffness of an indentation in the roughness valley and a lower one for an indentation on an asperity top, if the wave length was larger than 50 nm. If the experimental data was replaced by the mean value of the indentation results on different positions, C_{10} and D_1 were exactly identified compared with the chosen values. It was suggested to take the mean data of a sufficiently large number of indentations to decrease the error contribution of roughness. The surface roughness effect on the force-dependent data also depended on the ratio H/u. The indentation model with a perfectly flat surface could still be used to approximate the force-displacement data indented on a rough surface if H/u was below 1:3. The parameter coupling existed if the two parameters C_{10} and C_{01} of the Mooney-Rivlin model were identified using experimental data with surface roughness effects. In this case, the initial shear modulus μ_0 evaluated from the identified parameters C_{10} and C_{01} was a suitable choice to quantify the surface roughness effects. In a second step, a more realistic surface roughness profile was modeled with irregularly various serrations. It was verified that a multi-level protuberance-on-protuberance sine profile can be used to simplify this serration surface model. Furthermore, this realistic surface model was simplified by using a one-level sinusoidal profile model described with the arithmetic average roughness R_{a}. The identified parameters of the two models had large deviations because of the surface roughness effects, which were considered in the numerical model. Nevertheless, the parameters were accurately identified if a surface roughness described by a simple one-level sine function was taken into account. In this case, the statistic parameters of the realistic surface roughness, e. g. the arithmetic average roughness R_{a}, should be used to describe the simple roughness profile.

In **Paper E**, a procedure was developed to identify the viscoelasticity and to quantify the adhesion effect in nanoindentation experiments of polymers by the inverse method. A soft polymer, i. e. a silicone rubber, was chosen considering that this material was isotropic and mainly hyperelastic with only slightly viscous behavior. The surface roughness of the specimen was characterized by scanning electron microscopy and the in situ SPM Image mode. The results implied two side-effects that the roughness influence could be neglected but the adhesion force might be large. Different testing protocols were used to demonstrate the viscoelasticity and adhesion effects in nanoindentation experiments. A rate dependent hysteresis loop in the cyclic tests and the relaxation or creep behavior in the relaxation or creep tests showed an obvious viscous dissipation. The adhesion effects were observed by the negative force at zero displacement and the residual displacement after completely withdrawing the load. A viscoelastic constitutive model with a linear evolution equation at finite strain, which is called finite viscoelasticity, was used to describe the viscoelastic behavior of the silicone rubber. The finite elastic response of the silicone rubber under nanoindentation was assumed to be characterized by the neo-Hooke model. Two Maxwell elements were expected to

represent sufficiently the relaxation spectrum. The real geometry of the Berkovich tip was considered in order to minimize the systematic errors between the numerical model and the experiments. In the numerical model, the default contact pressure-clearance relationship used in ABAQUS® was modified and a surface-based adhesive behavior in the traction-separation law was incorporated into the contact pairs. The parameters of the chosen viscoelastic constitutive model and the adhesive contact model were identified by matching the response of the numerical model with the experimental data. Good agreement between all experimental curves and corresponding numerical predictions containing the identified parameters, was obtained. Therefore, the finite viscoelastic constitutive model and the used adhesion contact model allowed to describe the viscoelastic behavior containing adhesion effects in nanoindentation. The computational model containing the surface adhesion with the identified parameters has been verified to show better reproducible results regarding the experiments than the analytical solution. Several drawbacks to the used analytical solution were discussed. The developed procedure is capable to characterize the viscoelasticity of the polymer and to quantify the adhesion effects. According to our best knowledge, it is until now the first time to identify simultaneously finite viscoelasticity and adhesion in nanoindentation experiments of polymers.

In **Paper F**, it is our goal to investigate the ability to identify the hyperelastic constitutive parameters from load-depth curves obtained from indentation. Firstly, the macro indentation which uses a spherical indenter with a diameter of 5 mm, was chosen to eliminate the error contributions in nanoindentation, especially the surface effects. In order to limit the micro structure and the viscous effects, the considered material was an unfilled silicone rubber which exhibits a behavior very close to hyperelasticity. Three hyperelastic models that means the neo-Hooke, the Mooney-Rivlin and the Yeoh model were considered to predict the finite elasticity of the rubber-like elastomer. The inverse method combining a finite element simulation with an optimization procedure was applied to identify the constitutive parameters. Secondly, uniaxial tensile tests were performed to compare with the indentation. The experimental stress-strain curves were fitted with the analytical solutions corresponding to the three hyperelastic potentials to obtain the constitutive parameters. Thirdly, the constitutive parameters obtained from the indentation were used in the numerical prediction of uniaxial tensile tests and vise versa. Finally, the identified results were validated by the biaxial tensile tests and the comparing results are discussed.
Summarizing, the differences of the elastic modulus approximated from the macroindentation and the uniaxial test are so small that the maximum deviation is less than 6.5%. Therefore, for the purpose of engineering application, the macroindentation can be used to get the isotropic elastic modulus of the elastomers in service by the Sneddon's solution as well as by the Oliver & Pharr method. The correlation between the macroindentation and the uniaxial tensile test depends not only on the chosen hyperelastic model but also on the strain level. For the one-order polynomial form, e. g. the

neo-Hooke and Mooney-Rivlin models, the obtained correlation is very good. It is validated that the parameters identified from macroindentation can be relevant to predict the uniaxial tensile behavior of unfilled silicone rubber and vice versa, even for a wide range of strain, which can represent the one encountered in most of the industrial application. However, it is not the case for higher order polynomial forms, e. g. the Yeoh model. The parameters identified in macroindentation are not able to simulate the tensile behavior at large strain $B_{11} \geq 3$. In the biaxial test, both reaction forces of the horizontal and the vertical axes match the experimental measurements very well using the neo-Hooke and Mooney-Rivlin models with parameters identified from indentation and uniaxial tensile tests. However, the one calculated using the Yeoh model presents deviations at larger deformation, not depending on the parameters identified by indentation or uniaxial tensile tests. It seems that the second invariant in the biaxial test has only a slight contribution to the force-displacement behavior in this studied case. The neo-Hooke model with only one parameter or the Mooney-Rivlin model with a small coefficient associated with the second invariant, which can characterize the indentation and uniaxial data very well, are still able to describe the force-displacement behavior in the biaxial test. It is also recognized that the Yeoh model shows larger stiffness than the neo-Hooke and Mooney- Rivlin models, but they present almost the same stiffness in the indentation and uniaxial tests. Therefore, it could be assumed that the deformation in the biaxial test is much larger than the one obtained in the indentation and uniaxial tests.

5 Conclusion remarks and outlook

In the work of this thesis, an analysis procedure to characterize polymers from nanoindentation has been developed using the finite element based inverse method. The hyperelastic as well as viscoelastic properties of polymers have been evaluated from the obtained force-displacement data taking into account the influence of friction, surface roughness and adhesion effects.

According to the numerical computation, a geometrical parametric investigation of nanoindentation of polymer layers on hard substrate has been performed conveniently. The force-displacement behavior of the three considered hyperelastic layers depends on geometry-associated factors, i.e. the ratio of displacement to tip radius u/R, and the ratio of displacement to layer thickness u/H_{L}. Compared with neo-Hooke and Mooney-Rivlin models, the non-linear behavior of the Yeoh model becomes obvious when $u/H_{\mathrm{L}} > 0.2$ and it is fully represented if $u/H_{\mathrm{L}} \geq 0.4$. The parameters identification is also dependent on the deformation in a way that larger deformation leads to a more accurate identification. One should note that, if the properties of the substrate are known, the penetration depth is not necessary to constrain in order

to avoid the influence of the substrate. It is the most important advantage of this developed inverse procedure to capture properties of thin layers or coatings from nanoindentation taking into account the influence of the substrate. The strategy of a virtual experiment and the parameters re-identification has been further used to evaluate viscoelasticity of polymer layers from nanoindentation at small deformation. It is found that the accuracy of parameters identification in this case is dependent on the used loading history. Considering the viscoelastic model with small deformation, it is better to split the identification into two steps. The first step is to capture the basic elasticity using multi-stepwise monotonic testing, containing loading and unloading cycles. The second step is to identify the parameters of Maxwell elements in parallel by some single step relaxation tests with a suitable loading time. A sinusoidal oscillatory testing seems to be useful to identify elastic and viscoelastic parameters at one time. An exact match between the experimental data and the numerical prediction does not guarantee the accurate identification of each parameter. Thus the combination of several loading histories as well as different tests with various deformation forms may be taken into account.

The friction between the indenter and the polymer layers has been modeled with the classical Coulomb's law. The friction leads to a higher indentation force if the penetration depth becomes deeper. It seems that the influence of the friction does not change with variations of the friction coefficient if it is larger than 0.4. However, if the penetration is shallow enough to avoid the influence of the substrate, the friction effect is negligible. The surface roughness effects have been investigated numerically by explicitly taking into account the roughness profile in the model. The influence of the surface roughness is quantified as a function of the sine parameters as well as of the indentation parameters. The surface roughness profiles are modeled using a one-level and multi-level protuberance-on-protuberance sine function. It is found that the roughness effects strongly depend on the surface profile shape, namely the wave length and the asperity height. The influence on the force-displacement curve can be excluded if a new initial indentation point is defined by a certain threshold of the resulting contact force. A more realistic surface roughness profile is modeled with irregularly various serrations. It is verified that a multi-level protuberance-on-protuberance sine profile can be used to simplify this serration surface model. Furthermore, this realistic surface model is simplified by using the one-level sinusoidal profile model described with the arithmetic average roughness R_a. The adhesion effect has been investigated with real nanoindentation experiments as well as numerical computation. The developed FE based inverse analysis procedure has been applied in a real experiment of silicone rubber to identify the finite viscoelasticity and to quantify simultaneously the adhesion effects. A surface-based adhesive behavior in the traction-separation law is incorporated into the contact model. The present model containing the surface adhesion with the identified parameters is verified by comparing the computational results and an analytical solution. Therefore, the developed procedure is capable to characterize the viscoelasticity of the polymer and to quantify the adhesion effects.

Finally, the data from macroindentation tests and uni/biaxial tensile tests, which

involve different deformation states, have been taken into account. The hyperelasticity of silicone rubber is firstly characterized by indentation and uniaxial tests. The results are compared to each other. If this unfilled isotropic polymer is modeled by a one-order polynomial form, e. g. the neo-Hooke and the Mooney-Rivlin models, the correlation between the macroindentation and the uniaxial test is very good. However, for higher order polynomial forms, e. g. the Yeoh model, which is characterized from macroindentation, it is not able to reproduce the uniaxial data at large strain, i. e. $B_{11} \geq 3$. The characterization results are further verified by experimental data from the biaxial tensile test. The neo-Hooke model with only one parameter or the Mooney-Rivlin model with a small coefficient associated with the second invariant, which can characterize the indentation and uniaxial data very well, are still able to describe the force-displacement behavior in the biaxial test. It is also recognized that the Yeoh model shows a larger stiffness but all three models present almost same stiffness in the indentation and uniaxial tests.

As for the future work, firstly, it is meaningful to quantify the influence of surface roughness on the force-displacement data in a more explicit way, which is practical to apply into the experiment or numerical computation as a calibration source. In the real experiment, 3D local roughness data of the real surface is possible to obtain through the in situ scanning probe microscopy (SPM) mode of the nanoindenter. On the one hand, the surface roughness effect is able to calibrate in the numerical model by using a so called effective 2D surface profile, which contains smooth multiple sine or cosine functions obtained from the Fast Fourier transform (FFT). Hence, huge computational cost of a 3D model of an inhomogeneous roughness profile in this presented inverse method is avoided. On the other hand, the contribution of roughness to the indentation force is able to be explicitly expressed as a function of the indentation depth and the statistical roughness parameters, e. g. R_{a}, RMS, R_{v} and R_{p} etc. This quantified function provides a way to calibrate the original experimental data. Of course, various well known samples with various rough surfaces and smooth surface at the measured scale are required in order to develop the quantified functions.

Secondly, further comparing work has to be done in order to verify the ability to characterize polymers from nanoindentation. One comparison will be made between the characterization of polymers from indentation performed on different scales, i. e. macro- and nanoindentation, leading to a quantification of the effects related to adhesion and surface roughness, which are sensitive in nano-scale but unimportant in macro-scale. Another comparison between indentation and other macroscopic tests of different deformation states will be performed in the characterization of polymers with pronounced viscoelasticity, e. g. EPDM. It is expected to allow deep insight into the effects of the local rheological behavior on the global rate-dependent response.

Thirdly, it is necessary to take into account not only the time-dependent but also the

temperature-dependent behavior in order to widely adopt nanoindentation in iden-
tification of polymers' properties. Determination of nano- or micro-scale thermovis-
coelasticity of polymers is essential to understand the local rheological behavior in
nano-scale with the degradation phenomena affecting moldability, formability, worka-
bility, adhesion and other properties. A high temperature indentation technique has
to be developed that facilitates viscoelastic measurements from room temperature up
to 200°C in air. In this case, the main question is how we can lower the thermal drift
and load noise floor.

Finally, nanoindentation experiments are typically carried out on multiple spatial
scales, i.e. atomic-scale, nano-scale, micro-scale and continuum scale. Because
the global force-displacement data are measured from the local and inhomogeneous
deformation, which leads to some discontinuities on the force-displacement curves.
It is complicated to interpret the experimental results due to the involved multiple
scales especially for heterogeneous material, e. g, polymer composites with multiple
interphases and polymers with fine-scale (nano- or micro-) structures. The most often
used FEM is able to model macroscopic physics based on continuum theory. But it
fails to predict the material behavior on atomic scale such as crack formation, material
transformation, dislocation emission and atomic adhesive behavior. A fully atomistic
treatment is impossible in the simulation due to its limitations of computational
power and long-range mechanical interaction. In this case, multiscale simulations
combining the greatest advantage of both atomistic and continuum approaches have
to be developed in the field of nanoindentation of polymers.

Bibliography

[1] BELLEMARE, S., M. DAO & S. SURESH [2007]. 'The frictional sliding response of elasto-plastic materials in contact with a conical indenter.' *Int. J. Solids Structures*, **44**, pp. 1970–1989.

[2] BERKE, P., F. E. HOUDAIGUI & T. J. MASSART [2010]. 'Coupled friction and roughness surface effects in shallow spherical nanoindentation.' *Wear*, **268**, pp. 223–232.

[3] BOBJI, M. S. & S. K. BISWAS [1999]. 'Deconvolution of hardness from data obtained from nanoindentation of rough surfaces.' *J. Mater. Res.*, **14**, pp. 2259–2268.

[4] BOBJI, M. S., K. SHIVAKUMAR, H. ALEHOSSEIN, V. VENKATESHWARLU & S. K. BISWAS [1999]. 'Influence of surface roughness on the scatter in hardness measurements-a numerical study.' *Int. J. Rock Mech. Min. Sci.*, **36**, pp. 399–404.

[5] BOLSHAKOV, A. & G. M. PHARR [1998]. 'Influences of pileup on the measurement of mechanical properties by load and depth sensing indentation techniques.' *J. Mater. Res.*, **13**, pp. 1049–1058.

[6] BOLZON, G., G. MAIER & M. PANICO [2004]. 'Material model calibration by indentation, imprint mapping and inverse analysis.' *Int. J. Solids Structures*, **41**, pp. 2957–2975.

[7] BOUZAKIS, K. D., N. MICHAILIDIS, S. HADJIYIANNIS, G. SKORDARIS & G. ERKENS [2003]. 'The effect of specimen roughness and indenter tip geometry on the determination accuracy of thin hard coatings stress-strain laws by nanoindentation.' *Materials Characterization*, **49**, pp. 149–156.

[8] BUCAILLE, J. L., S. STAUSS, E. FELDER & J. MICHLER [2003]. 'Determination of plastic properties of metals by instrumented indentation using different sharp indenters.' *Acta Mater.*, **51**, pp. 1663–1678.

[9] CAKMAK, U. D., T. SCHÖBERL & Z. MAJOR [2012]. 'Nanoindentation of polymers.' *Arch. Rat. Mech. Anal.*, **42**, pp. 707–718.

[10] CAO, Y., X. QIAN & N. HUBER [2007]. 'Spherical indentation into elastoplastic materials: indentation-response based definitions of the representative strain.' *Mat. Sci. Eng. A*, **454–455**, pp. 1–13.

[11] CAO, Y., D. YANG & W. SOBOYEJOY [2005]. 'Nanoindentation method for determining the initial contact and adhesion characteristics of soft polydimethysiloxane.' *J. Mater. Res.*, **20**, pp. 2004–2011.

[12] CARLSSON, S., S. BIWA & P. L. LARSSON [2000]. 'On friction effects at inelastic contact between spherical bodies.' *Int. J. Mech. Sci.*, **42**, pp. 107–128.

[13] CARRILLO, F., S. GUPTA, M. BALOOCH, S. J. MARSHALL, G. W. MARSHALL, L. PRUITT & C. M. PUTTLITZ [2005]. 'Nanoindentation of polydimethylsiloxane elastomers: Effect of crosslinking, work of adhesion, and fliud environment on elastic modulus.' *J. Mater. Res.*, **20**, pp. 2820–2830.

[14] CHARITIDIS, C. [2011]. 'Nanoscale deformation and nanomechanical properties of soft matter study cases: Polydimethylsiloxane, cells and tissues.' *ISRN Nanotechnology*, **doi:10.5402/2011/719512**, pp. 1–13.

[15] CHEN, Z. & S. DIEBELS [2012]. 'Modelling and parameter re-identification of nanoindentation of soft polymers taking into account effects of surface roughness.' *Comp. Math. Appl.*, **64**, pp. 2775–2786.

[16] CHEN, Z., S. DIEBELS, N. J. PETER & A. S. SCHNEIDER [2013]. 'Identification of finite viscoelasticity and adhesion effects in nanoindentation of a soft polymer by inverse method.' *Comp. Mat. Science*, **72**, pp. 127–139.

[17] CHENG, L., X. XIA, L. E. SCRIVEN & W. W. GERBERICH [2005]. 'Spherical-tip indentation of viscoelastic material.' *Mech. Mater.*, **37**, pp. 213–226.

[18] CHENG, L., X. XIA, W. YU, L. E. SCRIVEN & W. W. GERBERICH [2000]. 'Flat-punch indentation of viscoelastic material.' *J. Polym. Sci., Part B: Polym. Phys.*, **38**, pp. 10–22.

[19] CHENG, Y. T. & C. M. CHENG [1998]. 'Relationships between hardness, elastic modulus, and the work of indentation.' *Appl. Phys. Lett.*, **73**, pp. 614–616.

[20] DEB, K. [2000]. 'An efficient constraint handling method for genetic algorithms.' *Computer Methods in Applied Mechanics and Engineering*, **186**, pp. 311–338.

[21] DERJAGUIN, B. V., V. M. MULLER & Y. P. TOPOROV [1975]. 'Effect of contact deformations on the adhesion of particles.' *Journal of Colloid and Interface Science*, **53**, pp. 314–325.

[22] DEUSCHLE, J. [2008]. *Mechanics of soft polymers indentation*. Doctoral Thesis, Universität Stuttgart.

[23] DING, Y. H., X. H. DENG, X. JIANG, P. ZHANG, J. R. YIN & Y. JIANG [2013]. 'Nanoscale mechanical characterization of pmma by afm nanoindentation: A theoretical study on the time-dependent viscoelastic recovery.' *J. Mat. Sci.*, **48**, pp. 3479–3485.

[24] DONNELLY, E., S. P. BAKER, A. L. BOSKEY, M. C. H. VAN DER MEULEN & J. BIOMED [2006]. 'Effects of surface roughness and maximum load on the mechanical properties of cancellous bone measured by nanoindentation.' *Journal of Biomedical Materials Research - Part A*, **77**, pp. 426–435.

[25] FANG, T. H., W. J. CHANG & C. M. LIN [2007]. 'Nanoindentation characterization of zno thin films.' *Mat. Sci. Eng. A*, **452–453**, pp. 715–720.

[26] FISCHER-CRIPPS, A. C. [2004]. *Nanoindentation*. Springer, New York.

[27] GOFFE, W. L., G. D. FERRIER & J. ROGERS [1994]. 'Global optimization of statistical functions with simulated annealing.' *Journal of Econometrics*, **60**, pp. 65–99.

[28] GUESSASMA, S., M. SEHAKI, D. LOURDIN & A. BOURMAUD [2008]. 'Viscoelasticity properties of biopolymer composite material determined using finite element calculation and nanoindentation.' *Comp. Mat. Science*, **44**, pp. 371–377.

[29] GUPTA, S., F. CARRILLO, C. LI, L. PRUITT & C. PUTTLITZ [2007]. 'Adhesive forces significantly affect elastic modulus determination of soft polymeric materials in nanoindentation.' *Materials Letters*, **61**, pp. 448–451.

[30] HABBAB, H., B. G. MELLOR & S. SYNGELLAKIS [2006]. 'Post-yield characterisation of metals with significant pile-up through spherical indentations.' *Acta Mater.*, **54**, pp. 1965–1973.

[31] HARTMANN, S. [2002]. 'Computation in finite-strain viscoelasticity: finite elements based on the interpretation as differential-algebraic equations.' *Comp. Meth. Appl. Mech. Eng.*, **191**, pp. 1439–1470.

[32] HARTMANN, S., J. GIBMEIER & B. SCHOLTES [2006]. 'Experiments and material parameter identification using finite elements. uniaxial tests and validation using instrumented indentation tests.' *Exp. Mech.*, **46**, pp. 5–18.

[33] HAY, J. L., A. BOLSHAKOV & W. C. OLIVER [1999]. 'A critical examination of the fundamental relations used in the analysis of nanoindentation data.' *J. Mater. Res.*, **14**, pp. 2296–2305.

[34] HERTZ, H. [1881]. 'Über die Berührung fester elstischer körper.' *J. f. reine u. angew. Math.*, **92**, pp. 156–171.

[35] HOLZAPFEL, G. A. [1996]. 'On large strain viscoelasticity: Continuum formulation and finite element applications to elastomeric structures.' *Int. J. Numer. Meth. Eng.*, **39**, pp. 3903–3926.

[36] HOLZAPFEL, G. A. & J. C. SIMO [1996]. 'A new viscoelastic constitutive model for continuous media at finite thermomechanical changes.' *Int. J. Numer. Meth. Eng.*, **33**, pp. 3019–3034.

[37] HUANG, X. & A. A. PELEGRI [2007]. 'Finite element analysis on nanoindentation with friction contact at the film/substrate interface.' *Composites Science and Technology*, **67**, pp. 1311–1319.

[38] HUBER, N., W. D. NIX & H. GAO [2002]. 'Identification of elastic-plastic material parameters from pyramidal indentation of thin films.' *Proc. R. Soc. Lond. A*, **458**, pp. 1593–1620.

[39] HUBER, N. & C. TSAKMAKIS [2000]. 'Finite deformation viscoelasticity laws.' *Mech. Mater.*, **32**, pp. 1–18.

[40] HUBER, N. & E. TYULYUKOVSKIY [2004]. 'A new loading history for identification of viscoplastic properties by spherical indentation.' *J. Mater. Res.*, **19**, pp. 101–113.

[41] JÄGER, A. & R. LACKNER [2007]. 'Identification of viscoelastic properties by means of nanoindentation taking the real tip geometry into account.' *Meccanica*, **42**, pp. 293–306.

[42] JIANG, W. G., J. J. SU & X. Q. FENG [2008]. 'Effect of surface roughness on nanoindentation test of thin films.' *Eng. Fract. Mech.*, **75**, pp. 4965–4972.

[43] JOHNSON, K. L. [1985]. *Contact mechanics*. Cambridge University Press, Cambridge.

[44] JOHNSON, K. L., K. KENDALL & A. D. ROBERTS [1971]. 'Surface energy and the contact of elastic solids.' *Proc. R. Soc. Lond. A*, **8**, pp. 301–313.

[45] KIM, J. Y., S. K. KANG, J. J. LEE, J. JANG, Y. H. LEE & D. KWON [2007]. 'Influence of surfaceroughness on indentation size effect.' *Acta Mater*, **55**, pp. 3555–3562.

[46] KIM, J. Y., J. J. LEE, Y. H. LEE, J. JANG & D. KWON [2007]. 'Surface roughness effect in instrumented indentation: A simple contact depth model and its verification.' *Acta Mater.*, **55**, pp. 3555–3562.

[47] KIRKPATRICK, S., C. D. GELATT JR. & M. P. VECCHI [1983]. 'Optimization by simulated annealing.' *Science*, **220**, pp. 671–680.

[48] KLÖTZER, D., C. ULLNER, E. TYULYUKOVSKIY & N. HUBER [2006]. 'Identification of viscoplastic material parameters from spherical indentation data. part II: Experimental validation of the method.' *J. Mater. Res.*, **21**, pp. 677–684.

[49] KUMAR, A. K. N., M. D. KANNAN, S. JAYAKUMAR, K. S. RAJAM & V. S. RAJU [2006]. 'Investigations on the mechanical behaviour of rough surfaces of TiNi thin films by nanoindentation studies.' *Surf. Coat. Technol.*, **201**, pp. 3253–3259.

[50] LAGARIAS, J. C., J. A. REEDS, M. H. WRIGHT & P. E. WRIGHT [1999]. 'Convergence properties of the nelder-mead simplex method in low dimensions.' *SIAM Journal on Optimization*, **9**, pp. 112–147.

[51] LARSSON, P. L. & S. CARLSSON [1998]. 'On microindentation of viscoelastic polymers.' *Polymer Testing*, **17**, pp. 49–75.

[52] LARSSON, P. L., A. E. GIANNAKOPOULOS, J. R. E. SÖDERLUND, D. & R. VESTERGAARD [1996]. 'Analysis of Berkovich indentation.' *Int. J. Solids Structures*, **33**, pp. 221–248.

[53] LAWITTS, J. A. & J. D. BIGGERS [1991]. 'Optimization of mouse embryo culture media using simplex methods.' *Journal of reproduction and fertility*, **91**, pp. 543–556.

[54] LE SAUX, V., Y. MACRO, G. BLES, S. CALLOCH, S. MOYNEA, S. PLESSISA & P. CHARRIERB [2011]. 'Identification of constitutive model for rubber elasticity from micro-indentation tests on natural rubber and validation by macroscopic tests.' *Mech. Mater.*, **43**, pp. 775–786.

[55] LEE, E. H. & J. R. M. RADOK [1960]. 'The contact problem for viscoelastic bodies.' *J. Appl. Mech.*, **30**, pp. 438–444.

[56] LIAO, Q., J. HUANG, T. ZHU, C. XIONG & J. FANG [2010]. 'A hybrid model to determine mechanical properties of soft polymers by nanoindentation.' *Thin Solid Films*, **16**, pp. 1043–1047.

[57] LION, A. [1996]. 'A constitutive model for carbon black filled rubber: Experimental investigations and mathematical representation.' *Continuum Mech. Therm.*, **8**, pp. 153–169.

[58] LION, A. [1998]. 'Thixotropic behaviour of rubber under dynamic loading histories : Experiments and theory.' *J. Mech. Phys. Solids*, **46**, pp. 895–930.

[59] LUBLINER, J. [1985]. 'A model of rubber viscoelasticity.' *Mech. Res. Commun.*, **12**, pp. 93–99.

[60] MATA, M. & J. ALCALÁ [2004]. 'The role of friction on sharp indentation.' *J. Mech. Phys. Solids*, **455**, pp. 145–165.

[61] MAUGIS, D. [1992]. 'Adhesion of spheres: The jkr-dmt transition using a dugdale model.' *Journal of Colloid and Interface Science*, **150**, pp. 243–269.

[62] MESAROVIC, S. D. & N. A. FLECK [1999]. 'Spherical indentation of elastic-plastic solids.' *Proc. R. Soc. Lond. A*, **455**, pp. 2707–2738.

[63] MILLER, M., C. BOBKO, M. VANDAMME & F. J. ULM [2008]. 'Surface roughness criteria for cement paste nanoindentation.' *Cement and Concrete Research*, **38**, pp. 467–476.

[64] ODEGARD, G. M., T. S. GATES & H. M. HERRING [2005]. 'Characterization of viscoelastic properties of polymeric materials through nanoindentation.' *Society for Exprerimental Mechanics*, **45**, pp. 130–136.

[65] OLIVER, W. C. & G. M. PHARR [1992]. 'An improved technique for determining hardness and elastic modulus using load and displacement sensing indentation experiments.' *J. Mater. Res.*, **7**, pp. 1564–1583.

[66] OLIVER, W. C. & G. M. PHARR [2004]. 'Measurement of hardness and elastic modulus by instrumented indentation: Advance in understanding and refinements to methodology.' *J. Mater. Res.*, **19**, pp. 3–20.

[67] PELLETIER, H., C. GAUTHIER & R. SCHIRRER [2009]. 'Friction effect on contact pressure during indentation and scratch into amorphous polymers.' *Materials Letters*, **63**, pp. 1671–1673.

[68] PHARR, G. M. & A. BOLSHAKOV [2002]. 'Understanding nanoindentation unloading curves.' *J. Mater. Res.*, **17**, pp. 2660–2671.

[69] QASMI, M. & P. DELOBELLE [2006]. 'Influence of the average roughness rms on the precision of the young's modulus and hardness determination using nanoindentation technique with a berkovich indenter.' *Surf. Coat. Technol.*, **201**, pp. 1191–1199.

[70] QIN, J., Y. HUANG, K. C. HWANG, J. SONG & G. M. PHARR [2007]. 'The effect of indenter angle on the microindentation hardness.' *Acta Mater.*, **55**, pp. 6127–6132.

[71] RAUCHS, G. & J. BARDON [2011]. 'Identification of elasto-viscoplastic material parameters by indentation testing and combined finite element modelling and numerical optimization.' *Finite Elem. Anal. Des.*, **47**, pp. 653–667.

[72] RAUCHS, G., J. BARDON & D. GEORGES [2010]. 'Identification of the material parameters of a viscous hyperelastic constitutive law from spherical indentation tests of rubber and validation by tensile tests.' *Mech. Mater.*, **42**, pp. 961–973.

[73] SAKAI, M. [2002]. 'Time-depdendent viscoelastic relation between load and penetration for an axisymmetric indenter.' *Phil. Mag.*, **82**, pp. 1841–1849.

[74] SAKAI, M. & S. SHIMIZU [2001]. 'Indentation rheometry for glass-forming materials.' *Journal of Non-Crystalline Solids*, **282**, pp. 236–247.

[75] SCHWEFEL, H. P. [1995]. *Evolution and optimum seeking*. Wiley, New York.

[76] SNEDDON, I. N. [1948]. 'Boussinesq's problem for a rigid cone.' *Proc. Cambridge Philos. Soc.*, **44**, pp. 492–507.

[77] SNEDDON, I. N. [1965]. 'The relation between load and penetration in the axisymmetric Boussinesq problem for a punch of arbitrary profile.' *Int. J. Engng. Sci.*, **3**, pp. 47–57.

[78] DE SOUZA, G. B., C. E. FOERSTER, S. L. R. DA SILVA, F. C. SERBENA, C. M. LEPIENSKI & C. A. DOS SANTOS [2006]. 'Hardness and elastic modulus of ion-nitrided titanium obtained by nanoindentation.' *Surf. Coat. Technol.*, **191**, pp. 76–82.

[79] TALJAT, B. & G. M. PHARR [2004]. 'Development of pile-up during spherical indentation of elastic-plastic solids.' *Int. J. Solids Structures*, **117**, pp. 3891–3904.

[80] TING, T. C. T. [1966]. 'The contact stresses between a rigid indenter and a viscoelastic half-space.' *J. Appl. Mech.*, **33**, pp. 845–854.

[81] TING, T. C. T. [1968]. 'Contact problems in the linear theory of viscoelasticity.' *J. Appl. Mech.*, **35**, pp. 248–254.

[82] TYULYUKOVSKIY, E. & N. HUBER [2006]. 'Identification of viscoplastic material parameters from spherical indentation data. part I: Neural networks.' *J. Mater. Res.*, **21**, pp. 664–676.

[83] TYULYUKOVSKIY, E. & N. HUBER [2007]. 'Neural networks for tip correction of spherical indentation curves from bulk metals and thin metal films.' *J. Mech. Phys. Solids*, **55**, pp. 391–418.

[84] VANLANDINGHAM, M. R. & N. K. CHANG [2005]. 'Viscoelastic characterization of polymers using instrument indentation. Quasi-static testing.' *J. Polym. Sci., Part B: Polym. Phys.*, **43**, pp. 1794–1811.

[85] WALTER, C., T. ANTRETTER, R. DANIEL & C. MITTERER [2007]. 'Finite element simulation of the effect of surface roughness on nanoindentation of thin films with spherical indenter.' *Surf. Coat. Technol.*, **202**, pp. 1103–1107.

[86] WALTER, C. & C. MITTERER [2008]. '3d and 2d finite element simulation of the effect of surface roughness in nanoindentation of hard coatings.' *Surf. Coat. Technol.*, **203**, pp. 3286–3290.

[87] WANG, T. H., T. H. FANG & Y. C. LIN [2007]. 'A numerical study of factors
      affecting the characterization of nanoindentation on silicon.' *Mat. Sci. Eng. A*,
      447, pp. 244–253.

[88] WANGA, M., K. M. LIECHTIA, J. M. WHITEB & R. M. WINTERC [2004].
      'Nanoindentation of polymeric thin force microscope.' *J. Mech. Phys. Solids*, **52**,
      pp. 2329–2354.

[89] YANG, W. H. [1966]. 'The Contact Problem for Viscoelastic Bodies.' *J. Appl.
      Mech.*, **88**, pp. 395–401.

[90] ZHANG, X. J., X. H. ZHANG & S. WEN [2011]. 'Finite element modeling of the
      nano-scale adhesive contact and the geometry-based pull-off force.' *Tribol. Lett.*,
      41, pp. 65–72.

[91] ZHAO, Y. P., X. H. SHI & W. J. LI [2003]. 'Effect of work of adhesion on
      nanoindentation.' *Reviews on Advanced Materials Science*, **5**, pp. 348–353.

II

APPENDED PAPERS A-F

Nanoindentation of Hyperelastic Polymer Layers at Finite Deformation and Parameter Re-identification

Zhaoyu Chen · Stefan Diebels

Nanoindentation of hyperelastic polymer layers at finite deformation and parameter re-identification

Abstract Thin polymer layers on substrates have a wide range of application in important areas. However, it is impossible to measure the mechanical properties with the traditional testing methods. Recently, nanoindentation became a new but primary testing technique of thin layers. In the present work, based on a finite element model of contact mechanics and hyperelastic materials, nanoindentation of polymer layers is simulated with the finite element code ABAQUS®. Three often used hyperelastic models, that is, the neo-Hookean, Mooney–Rivlin and Yeoh models are investigated. The behaviour of these three models is compared to each other in different boundary value problems of nanoindentation in order to get some feeling of the different behaviour of various hyperelastic models under nanoindentation. In contrast to the traditional analytical method, the penetration depth is not restrained to avoid the influence of the substrate. A parameter re-identification strategy is employed to extract the parameters of the material models at small and finite deformation based on the principle of biological evolution. Furthermore, it is investigated how large the penetration depth has to be chosen in order to distinguish different models in reference to the load–displacement curves. Finally, the possibility is discussed of describing the data obtained by a non-linear complex model using the relatively simple approach based on the neo-Hookean model.

Keywords Numerical modelling of nanoindentation · Hyperelastic polymer layer · Finite deformation

1 Introduction

Thin polymer layers such as polymer coatings and thin films have a wide range of application in important industrial areas, for example, the production of plane, automobile and the equipment of solar power energy. Usually, the substrates can be metals like aluminium and steel. The polymer can be chosen in a large range, for example, polyurethane (PU), polyamidoamine (PAMAM), epoxy and so on. The mechanical properties of these polymer layers cover a greater scope due to omnigenous microchemical structure. However, as these films are very thin, soft and usually fixed on a substrate, it is impossible to measure the mechanical properties using the traditional tension, compression or shear testing. A new testing technique is required. In this case, nanoindentation can be used and increasingly became the primary testing technique of the thin layers. As

Z. Chen (✉) · S. Diebels
Chair of Applied Mechanics, Saarland University, Saarbrücken, Germany
E-mail: zh.chen@mx.uni-saarland.de
Tel.: +49-681-3022169
Fax: +49-681-3023992

S. Diebels
E-mail: s.diebels@mx.uni-saarland.de
Tel.: +49-681-3022169
Fax: +49-681-3023992

the advantages of this technique, the layers can be tested without removing the substrate and it is suitable to nanoscale materials yielding a high spatial resolution.

According to the elastic properties, for some polymer layers on metal substrate, linear elastic models cannot accurately describe the observed behaviour [17]. Non-linear elastic models based on a hyperelastic approach with particular strain energy provide a means of modelling the stress–strain behaviour of such elastomeric materials. Most of these approaches are based on a strain energy function for incompressible media proposed by Mooney, Ogden, Rivlin, and Yeoh [23,25,30,38], such as the neo-Hookean model, the Mooney–Rivlin model and the Yeoh form, etc. As far as we know, research on the elastic behaviour of a polymer under indentation is still at its first stage, the published results [3–5,7,8,31,32] focus on only some simple model, for example, neo-Hooke or Mooney–Rivlin, and leave an important dilemma: which hyperelastic model should be used to extract the elastic behaviour regarding the spherical indentation of a polymer substance by a rigid sphere of radius R? In the present work, based on a finite element model of contact mechanics and hyperelastic materials, nanoindentation of polymer layers is simulated by using the finite element code ABAQUS®. Three often used hyperelastic models, that is, the neo-Hookean, Mooney–Rivlin and Yeoh models are applied.

The behaviour of these three models under different boundary value problems of nanoindentation is compared with each other in order to get some feeling of the different behaviour between various hyperelastic models under nanoindentation. Furthermore, the obtained information can be used as a reference when we will come across the dilemma mentioned above. A purely theoretical and numerical treatment rather than the experimental method are chosen in order to vary the parameters associated with nanoindentation and to extract the different behaviour purely related to the various hyperelastic models. Therefore, the influence of the non-linearity and of the different model parameters can be studied in details. It is also important that the localised stress and strain fields can be perceived directly from the FE model.

The principle goal of most available commercial indentation instruments is to measure the hardness and elastic modulus directly from the measured force–displacement curves according to the Oliver and Pharr [26,27] method. Therefore, the influence of the substrate should be eliminated from the force–displacement measurement in order to get the properties of the pure layer when the layer material fixed on a substrate is indented. To achieve this, it is common to restrict the maximum depth of penetration to <10% of the film thickness [14,19,36]. This presents a useful criterion for hard films on soft substrates as obtained by surface treatment of metals. For polymer coatings which are soft with respect to the substrate, the maximum depth of penetration less than 5% of the layer thickness is suggested by our previous work. However, if the penetration depth is restricted to equally whether 5 or 10% of the layer thickness, the finite deformation behaviour of hyperelastic polymer layers is also very limited. In the present paper, this restriction is rejected and the effects of a large penetration depth and the influence of the substrate are investigated. In contrast to the traditional method, in the present study, the penetration depth is not restricted to avoid the influence of the substrate. As the only assumption, the properties of the substrate need to be known.

On the one hand, the measured hardness and elastic modulus are not enough to represent completely the properties of the hyperelastic material. On the other hand, a general analytical solution of the geometrically and materially non-linear indentation problem is missing. Therefore, the inverse method [20,21] became a new attempt to determine the material parameters. The main approach is using finite element computations in combination with numerical optimisation techniques [24]. In this method, the squared difference between experimental and numerical data called objective function is minimised with respect to the model parameters using numerical optimisation. And the parameters of the constitutive models are identified as the optimal solution. In contrast to the traditional inverse method, in the present paper, virtual experimental data generated by numerical simulations with a chosen parameter set replace the real experimental measurements. As an advantage, the identified parameters can be compared with the chosen values. Such a procedure is called parameter re-identification. In this case, the finite element code ABAQUS® is used as our virtual laboratory. An artificial random noise is superimposed on the virtual experimental data to make it more realistic and to check the stability of the identification procedure.

For rubber-like hyperelastic materials, the research work of parameter identification using homogeneous and inhomogeneous testing methods is documented in some literatures. The finite element method is applied to identify the parameters in a series of investigations [2,18,28,29,33]. They use a gradient-based optimisation method comparing the simulated and experimental data with the least-square method. Parameters identification of polynomial-type hyperelastic models using gradient-free procedure with tension–torsion test are discussed in the work of Hartmann et al. [9–13]. Omitting the troublesome gradient calculation for the model and the further drawback of deterministic methods of distinguishing local and global minima, in the present work, a stochastic strategy is used based on principles of biological evolution [34], for example, an evolution strategy.

The ambition of this study is to model the non-linear elastic behaviour of polymer layers based on three hyperelastic models with the various boundary value problem of nanoindentation. The friction effect between the rigid indenter and the soft polymer layer on the hard substrate is expected to have some influence on the measured results. It will be investigated in our later work. In the present research, the friction effect is not considered just to simplify the parameter identification procedure. It is studied, how large the deformation has to be chosen in order to stimulate the non-linearity of the different models. Furthermore, it is investigated if the different models can be distinguished based on the force–displacement curve only. As previously found, if the penetration depth is restricted to avoid the influence of the substrate, some of the parameters of the Mooney–Rivlin and the Yeoh model cannot be identified accurately, especially those related with the non-linearity at finite deformation. When the influence of the substrate is included in order to allow for really large deformations, we have to investigate how accurate these parameters can be identified. According to the best of our knowledge, such an investigation of nanoindentation of polymer layers is firstly documented in the present paper.

2 The FEM model

2.1 Geometry and boundary value problem

Spherical indenters show increasing popularity as this type of indenters provides a smooth transition from elastic to elastic–plastic contact. They are particularly suitable for measuring soft materials and for replicating contact damage in in-service conditions [6]. The numerical simulation of spherical nanoindentation can be modelled in an axisymmetric two-dimensional finite element model, for example, in ABAQUS® 6.9-3. The indenter is assumed to be a rigid body compared to the soft polymer layer. We define the indenter as an analytical rigid surface, in such a way that the indenter geometry can be modelled exactly with a smooth curve. In view of the contact problem, quadrilateral elements are used. Assuming linear elastic behaviour of the substrate and incompressible material behaviour of the polymer layer, the element types CAX4 and CAX4H are used for the substrate and the layer, respectively. To account for the localised deformation of the layer, it is essential that the density of nodes close to the contact region is high enough. The nodes at the axis of symmetry are fixed in the horizontal direction, while those at the bottom are constrained in the vertical direction. The geometry and boundary conditions of the spherical nanoindentation are illustrated in Fig. 1.

Concerning the numerical treatment of the contact problem, the indenter is defined as master surface, while the layer is defined as slave surface, both forming a contact pair. A contact formulation of finite-sliding
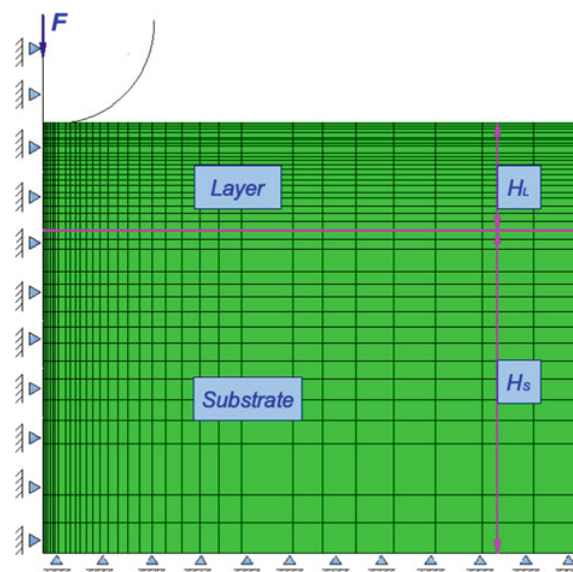
Fig. 1 Sketch of the geometry and boundary condition and the mesh of the FEM model

interaction [1] between a deformable and a rigid body in ABAQUS®/Standard is used to establish the frictionless contact model between indenter and layer. In this case, the formulation of normal contact is used as a constraint for non-penetration which treats normal contact as a unilateral constraint problem. The normal contact pressure cannot be calculated from a contact constitutive equation, but is then obtained as a reaction in the contact area and hence can be deduced from the constraint equations with the often used Lagrange multiplier method or the Penalty method, for details please see [1,37].

The FEM model is first verified by comparing the numerical force and displacement data with Sneddon's analytical solution, in which the indentation force P is given by:

$$P = \frac{4}{3} \sqrt{R} \frac{E}{1 - \nu^2} h^{\frac{3}{2}} .$$ (1)

R radius of spherical indenter, h indentation depth, E Young's modulus of layer, ν 0.5 for incompressible material.

The Sneddon's solution is only valid for small deformation and homogeneous linear elastic material. Therefore, in the numerical simulation, a homogeneous Hooke's law material model is used for both the layer and the substrate. Figure 2 shows the comparison results: the error between the numerical data and the Sneddon's solution is within 3% when the ratio u/R of the displacement to the indenter radius is less than 0.05. The accuracy of the simulation of nanoindentation is guaranteed.

2.2 Hyperelastic constitutive models

For a so-called hyperelastic material, the existence of Helmholtz free-energy function Ψ is postulated, which is defined per unit reference volume. We now restrict attention to isotropic and incompressible hyperelastic material models under isothermal regime, that is, so-called perfectly elastic material models, because such hyperelastic models can well represent the behaviour of the solid polymeric materials, for example, rubber-like materials [16,22]. For this type of ideal material, $\Psi = \Psi(\mathbf{F})$ is solely a function of the deformation gradient $\mathbf{F}$ or a strain tensor, respectively, so the Helmholtz free-energy function is referred to the strain energy function. The general format of the constitutive equation can be first derived from the Clausius–Planck form of the second law of thermodynamics which degenerates to an equality for the class of perfectly elastic materials.

$$\mathcal{D}_{\text{int}} = \mathbf{P} : \dot{\mathbf{F}} - \dot{\Psi} = \left(\mathbf{P} - \frac{\partial \Psi(\mathbf{F})}{\partial \mathbf{F}} \right) : \dot{\mathbf{F}} \geq 0$$ (2)

where $\mathcal{D}_{\text{int}}$ and $\mathbf{P}$ are the internal dissipation and the 1st Piola–Kirchhoff stress tensor, respectively. As $\mathbf{F}$ and hence $\dot{\mathbf{F}}$ can be chosen arbitrarily, the expression in parentheses must be zero. Therefore, the constitutive equation associated with $\mathbf{P}$ can be expressed as

$$\mathbf{P} = \frac{\partial \Psi(\mathbf{F})}{\partial \mathbf{F}}$$ (3)
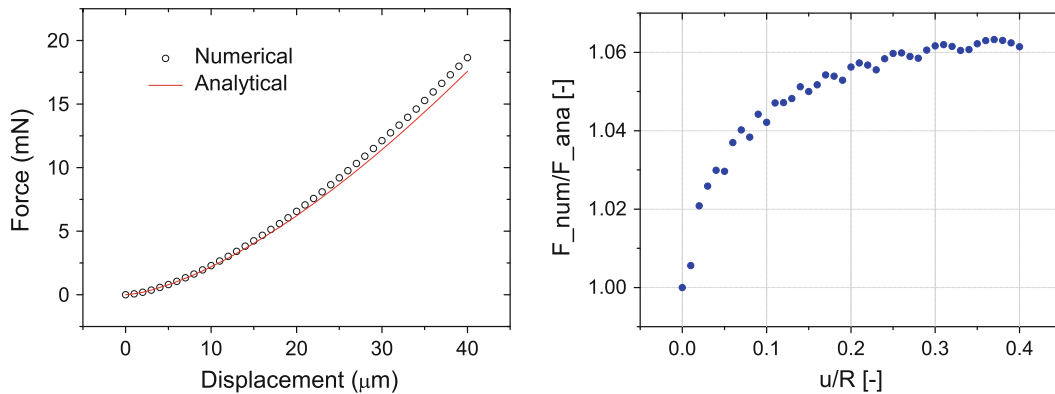
Fig. 2 The comparison of numerical data with Sneddon's analytical solution: force–displacement curve (*left*) and the force ratio as a function of the u/R (*right*)

Due to the assumption that the strain energy $\Psi(\mathbf{F})$ generated by the motion $\mathbf{x} = \widetilde{\chi}(\mathbf{X}, t)$ is objective as well as the fact that $\Psi(\mathbf{F})$ remains unchanged if a rigid-body motion is superimposed on the isotropic hyperelastic material, $\Psi(\mathbf{F})$ can also be described as

$$\Psi(\mathbf{F}) = \Psi(\mathbf{C}) = \Psi(\mathbf{B}) \tag{4}$$

with the right Cauchy Green deformation tensor $\mathbf{C} = \mathbf{F}^{\mathbf{T}} \cdot \mathbf{F}$ and the left Cauchy Green deformation tensor $\mathbf{B} = \mathbf{F} \cdot \mathbf{F}^{\mathbf{T}}$. If a scalar-valued tensor function is invariant under rotation, it may be expressed in terms of the principle invariants of its argument, for example, $\mathbf{C}$ or $\mathbf{B}$. So the strain energy Ψ of the incompressible hyperelastic material ($I_{3\mathbf{C}} = I_{3\mathbf{B}} = 1$) can be written as

$$\Psi = \hat{\Psi}(I_{1\mathbf{C}}, I_{2\mathbf{C}}) = \hat{\Psi}(I_{1\mathbf{B}}, I_{2\mathbf{B}}). \tag{5}$$

$I_i (i = 1, 2, 3)$ are the principle invariants of $\mathbf{C}$ and $\mathbf{B}$, that is,

$$I_{1\mathbf{C}} = \mathrm{tr}\mathbf{C}, \tag{6}$$

$$I_{2\mathbf{C}} = \frac{1}{2}[(\mathrm{tr}\mathbf{C})^2 - \mathbf{C} : \mathbf{C}], \tag{7}$$

$$I_{3\mathbf{C}} = \det \mathbf{C} = (\det \mathbf{F})^2 = 1. \tag{8}$$

With the relations $\overline{\mathbf{T}} = \mathbf{F}^{-1}\mathbf{P}$ and $\mathbf{T} = J^{-1}\mathbf{F}\overline{\mathbf{T}}\mathbf{F}^{\mathbf{T}}$ and the Lagrange multiplier method associated with incompressible hyperelastic materials, the 2nd Piola–Kirchhoff stress tensor $\overline{\mathbf{T}}$ and the Cauchy stress tensor $\mathbf{T}$ can be derived as (details see e.g. [16] chapter 6)

$$\overline{\mathbf{T}} = -p\mathbf{C}^{-1} + 2\frac{\partial \Psi(\mathbf{C})}{\partial \mathbf{C}} = -p\mathbf{C}^{-1} + 2\frac{\partial \Psi}{\partial I_{1\mathbf{C}}}\mathbf{I} + 2\frac{\partial \Psi}{\partial I_{2\mathbf{C}}}(I_{1\mathbf{C}}\mathbf{I} - \mathbf{C}), \tag{9}$$

$$\mathbf{T} = -p\mathbf{I} + 2\mathbf{B}\frac{\partial \Psi(\mathbf{B})}{\partial \mathbf{B}} = -p\mathbf{I} + 2\frac{\partial \Psi}{\partial I_{1\mathbf{B}}}\mathbf{B} + 2\frac{\partial \Psi}{\partial I_{2\mathbf{B}}}\mathbf{B}^{-1}. \tag{10}$$

Therefore, the constitutive equations of an isotropic and incompressible hyperelastic material under isothermal condition are given by Eqs. (9) and (10). They are split into one part governed by the hydrostatic pressure p and the other part governed by the deformation of the material. There are numerous specific forms of strain energy functions to describe the hyperelastic properties, whereas we only focus on three isotropic and incompressible hyperelastic models, namely the neo-Hookean, the Mooney–Rivlin and the Yeoh form:

$$\Psi_{\mathrm{NH}} = C_{10}(I_{1\mathbf{C}} - 3), \tag{11}$$

$$\Psi_{\mathrm{MR}} = C_{10}(I_{1\mathbf{C}} - 3) + C_{01}(I_{2\mathbf{C}} - 3), \tag{12}$$

$$\Psi_{\mathrm{Y}} = C_{10}(I_{1\mathbf{C}} - 3) + C_{20}(I_{1\mathbf{C}} - 3)^2 + C_{30}(I_{1\mathbf{C}} - 3)^3. \tag{13}$$

These forms are often used in the literature to model elastic properties of polymers. Ψ_{NH} involves only one single parameter and provides a mathematically simple and reliable constitutive model for the non-linear deformation behaviour of isotropic rubber-like materials. It is physically founded and includes typical effects known from non-linear elasticity within the small strain domain [16,22,30]. The free-energy function Ψ_{MR} of the Mooney–Rivlin model is derived on the basis of mathematical arguments with consideration of symmetry [23]. It is often employed in the description of the non-linear behaviour of isotropic rubber-like materials at moderate strain [8,16,22]. Considering a thin sheet of an incompressible hyperelastic material is subjected to a homogeneous simple deformation in the direction x_1. It could be shown that the shear stress

$$\sigma_{12} = \mu c, \quad \mu = 2\left(\frac{\partial \Psi}{\partial I_1} + \frac{\partial \Psi}{\partial I_2}\right). \tag{14}$$

where c is a parameter associated with shear deformation, and μ called the shear modulus is a measure of the resistance to distortion. According to Eq. (14)$_2$, for neo-Hookean and Mooney–Rivlin models, the shear modulus is constant. However, concerning a simple shear deformation of a filler-loaded rubber, for example, carbon-black filled rubber vulcanisates, physical observations show that the shear modulus μ varies strongly with the deformation. Therefore, the neo-Hookean and Mooney–Rivlin models are too simple to characterise the elastic properties. Yeoh made the simplifying assumption that $\partial \Psi / \partial I_2$ is zero and proposed a function Ψ_{Y} depending only on the first principle invariant. This phenomenological material model is motivated in order

to simulate the mechanical behaviour of carbon-black filled rubber showing a typical stiffening effect in the large strain domain [16,38]. With the strain energy according to Eq. (13), we calculate from Eq. $(14)_2$ that $\mu = 2C_{10} + 4C_{20} (I_1 - 3) + 6C_{30} (I_1 - 3)^2$. The effective shear modulus μ involves first- and second-order terms of $(I_1 - 3)$. It is to be mentioned that μ depends on the deformation in a significant way, and the associated relation for the shear stress is clearly non-linear.

3 Behaviour under uniaxial tension test

Comparing with nanoindentation, the uniaxial tension test is a simple test with homogeneous deformation and with simple kinematics allowing an easy interpretation of the results in the frame work of continuum mechanics. Therefore, before discussing the nanoindentation results, the behaviour of the three hyperelastic models with the parameters on the left side of Table 3 is investigated. The 1st Piola–Kirchhoff component P_{11} over the stretch in the tension direction of the three chosen models is shown in Fig. 3. As can be seen from the curves, the elastic behaviour of the Yeoh model displays the strongest non-linearity, while the neo-Hookean model exhibits slight non-linear elasticity within the small strain domain. As expected in the parameter setting, the uniaxial tension tests of the three different hyperelastic models yield the same tangent to the stress–strain curve close to the origin $0.9 \leq \lambda_1 \leq 1.1$. Otherwise, the behaviour of those models can be explicitly separated in the stretch range. The difference between the behaviour of the Yeoh model and of the other two models is huge in the large strain domain. Therefore, the behaviour of the three models under nanoindentation can be expected to be separated, too.

In order to gain confidence that the parameters can be identified from nanoindentation test, it is firstly to identify the parameters by using a simple deformation state under uniaxial tension test. The parameter identification is treated by using the procedure described in Sect. 4 with the stretch λ_1 as large as 1.5. Figure 4 shows the evolution process of the objective function $f(\kappa)$ and the guessed material parameters. The objective function $f(\kappa)$ decreases to zero as C_{10} and C_{01} approach the chosen values. The parameters are accurately identified and the values are listed in Table 1. Therefore, it is expected that the behaviour of the three hyperelastic models can be separated as well as that the parameters can be accurately identified if the deformation is large enough.

4 Nanoindentation at finite deformation

There are numerous parameters related with the nanoindentation process, such as parameters associated with the indentation instrument, temperature control, load history and indented sample, etc. Some of the parameters are proven to have strong influence on the indentation force–displacement results, theoretically and experimentally. Because the non-linear elastic behaviour of a hyperelastic material under nanoindentation at finite strain is of huge interest, we only focus on the parameters related to the geometry and to the sample's material
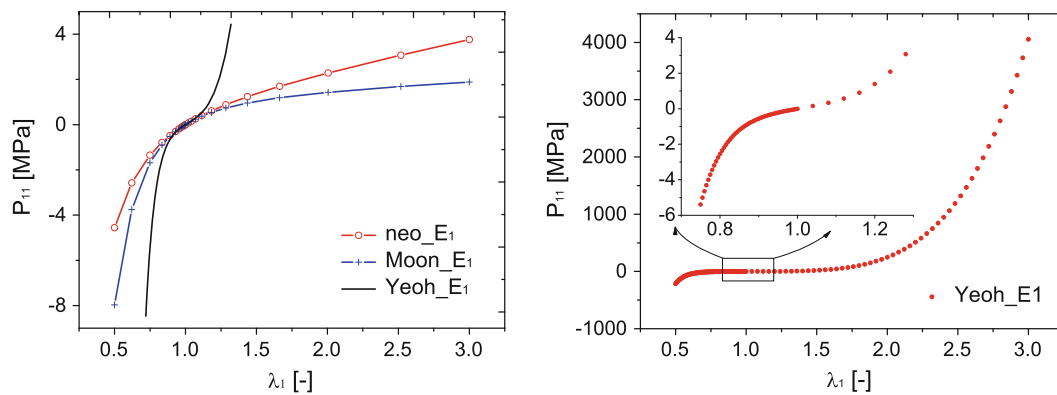
Fig. 3 The 1st Piola–Kirchhoff component over the stretch in the tension direction under uniaxial tension test: on the *left side*, the behaviour of the neo-Hookean and Mooney–Rivlin models is shown and three models are compared; on the *right side*, the behaviour of the Yeoh model is shown in the whole stretch range $0.5 \leq \lambda_1 \leq 3$
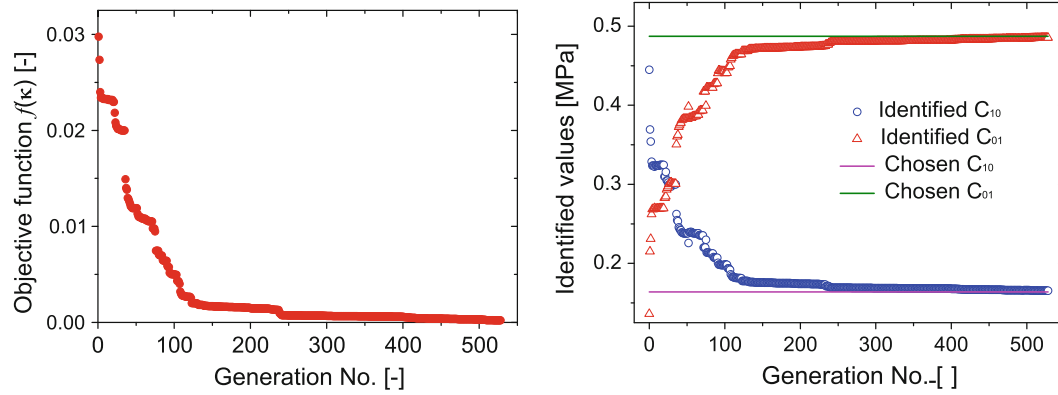
Fig. 4 The evolution process of the objective function $f(\kappa)$ (*left side*) and material parameters of the Mooney–Rivlin model (*right side*)

Table 1 The parameters are re-identified by using uniaxial tension test

Noise %	neo-Hookean	Mooney–Rivlin			Yeoh form		
	C_{10}	C_{10}	C_{01}	$C_{10} + C_{01}$	C_{10}	C_{20}	C_{30}
Chosen value	0.6513	0.1640	0.4873	0.6513	0.6513	2.5870	5.0
Bounds	(0.01; 5)	(0.01; 1)	(0.01; 1)	–	(0.1; 5)	(0.1; 20)	(0.1; 20)
0.0	0.6513	0.1655	0.4853	0.6508	0.6486	2.5987	4.9864

Table 2 Five cases with various geometry parameters

Cases	R/H_L	R (μm)	H_L (μm)	u/R	u/H_L
Case 1	0.2	100	500	0–0.4	0–0.08
Case 2	0.5	100	200	0–0.4	0–0.2
Case 3	1.0	100	100	0–0.4	0–0.4
Case 4	1.5	150	100	0–0.3	0–0.4
Case 5	2.0	200	100	0–0.2	0–0.4

keeping other parameters unchanged. Thanks to the numerical treatment in ABAQUS®, the conditions of the virtual experiments can be easily handled.

As we have shown in Fig. 1, there are four parameters related to the indentation geometry, that is, the thickness of the substrate H_S and of the layer H_L, respectively, the radius of the spherical indenter R and the indentation depth u. H_S is actually a parameter concerning about how far the stiff substrate can prevent the elastic fields from reaching the boundary condition on the bottom. So, the difference of the force–displacement data is investigated by varying H_S from 200, 400 to 1,000 μm if the layer thickness is 100 and 500 μm. No difference could be seen between the results if H_S is 400 and 1,000 μm, respectively, when the material parameters in Table 3 are used. The deviation is less than 2% comparing the results of H_S 200 μm to the results of H_S 1,000 μm. This causes in the fact that the substrate is very hard compared to the soft polymer layer. It is not the same case if the substrate is softer than the polymer layer. Therefore, in this paper, H_S is just fixed to 400 μm to reduce the computational cost during parameters identification. The indentation depth u remains to 40 μm, while the other two parameters are varied according to five cases listed in Table 2.

The parameters of the neo-Hookean, the Mooney–Rivlin and the Yeoh models listed in Table 3 are chosen in such a way that the shear moduli in Eq. (14) at the reference configuration are the same for all methods. It should be noted that the linearisation of the three models at the small strain region yields the same Young's modulus $E = 2\mu (1 + \nu)$ ($\nu = 0.5$ is chosen for incompressible material) if Hooke's law is applied, that is, the finite elasticity laws are set-up in such a way that a uniaxial tension test yields the same tangent to the stress–strain curve in the origin. Two different stiffness values E_1 and E_2 are chosen in order to get the information of various stiff materials. C_{20} and C_{30} in both cases are set to be nearly the same with the intention that if the non-linear elastic behaviour of the Yeoh model is fully developed, then the force–displacement relations of the two Yeoh models will be expected to be similar. Because the non-linear elastic behaviour at finite strain of the Yeoh model is strongly dependent on the last two terms of Eq. (13), the substrate used here is

a simple elastic metal, for example, aluminium or steel. It is assumed that the substrate is without any inelastic property just in order to simplify the model. The stiffness of the substrate is varied as 10, 100 and 1,000 times as the layer stiffness to investigate its influence. It is found that if the ratio of the stiffness of the substrate to the stiffness of the layer is larger than 100, no matter how stiff the substrate is, the force–displacement data will not change. Therefore, an arbitrary stiffness about 100 times greater than the layer stiffness is chosen for the substrate.

The friction between the indenter and the polymer layer is not taken into account in this work. Therefore, the global force–displacement data contain only the response of the material mechanical behaviour under indentation with a rigid indenter. Figures 5, 6, 7, 8 and 9 show the results of a nanoindentation test with various geometry parameters listed as case 1 to case 5 in Table 2. The diagrams on the left-hand side are the force–displacement data of the neo-Hookean, Mooney–Rivlin and Yeoh models with the material parameters listed in Table 3. The figures on the right-hand side show the difference of the behaviour between the three models with stiffness E_1. $F/F\_neo\_E_1$ represents the ratio of the force obtained from nanoindentation with the Mooney–Rivlin and the Yeoh models, respectively, to the force of the neo-Hookean model. $F/F\_neo\_E_1$ is plotted as function of the displacement as well as the values of u/R and u/H_L.

Firstly, the focus is laid on Figs. 5, 6 and 7, by which the results in case 1, case 2 and case 3 can be compared. As listed in Table 2, the value u/R is the same in case 1, case 2 and case 3. Varying H_L yields the maximum value u/H_L equals to 0.08 in case 1, 0.2 in case 2 and 0.4 in case 3, respectively. Therefore, the different behaviour of the same material in these three cases is governed by the response to different values u/H_L, that is, the distance of the indenter tip to the substrate. The non-linearity of the force–displacement curves of
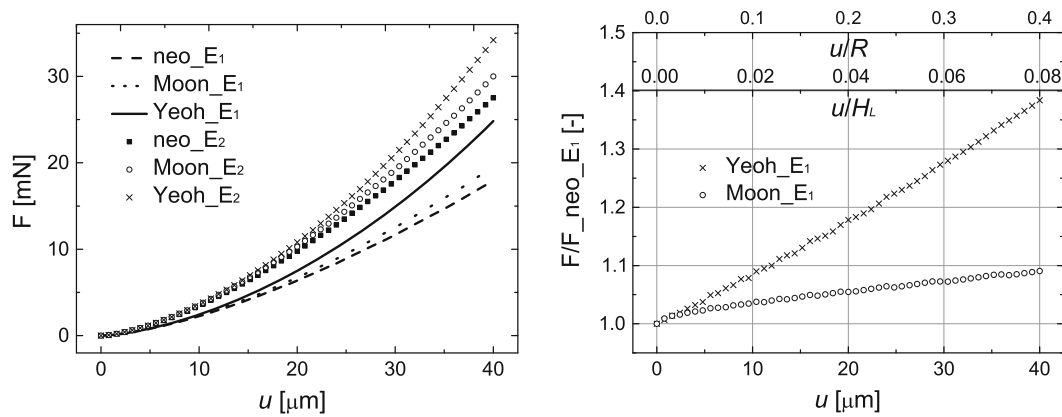
Fig. 5 The nanoindentation results of the three models with geometry parameters listed in case 1: the force–displacement data(*left*), comparison of the behaviour of the three models (*right*)
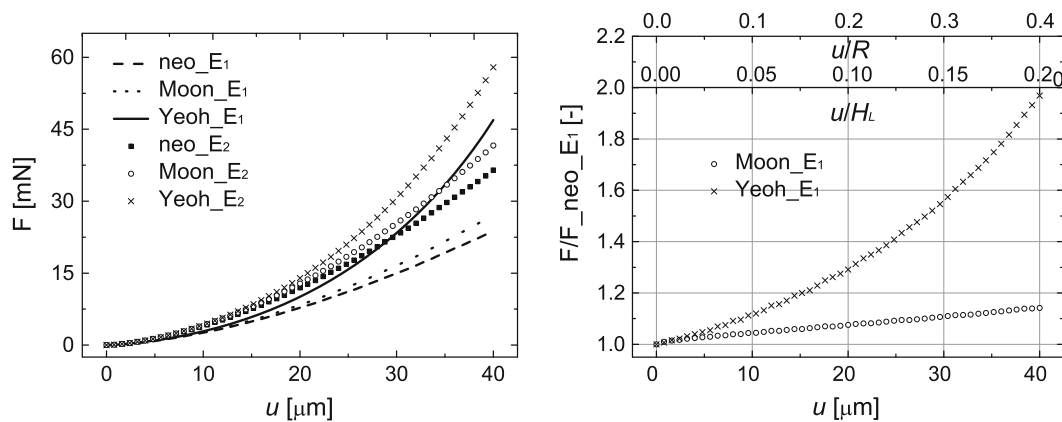
Fig. 6 The nanoindentation results of the three models with geometry parameters listed in case 2: the force–displacement data(*left*), comparison of the behaviour of the three models (*right*)
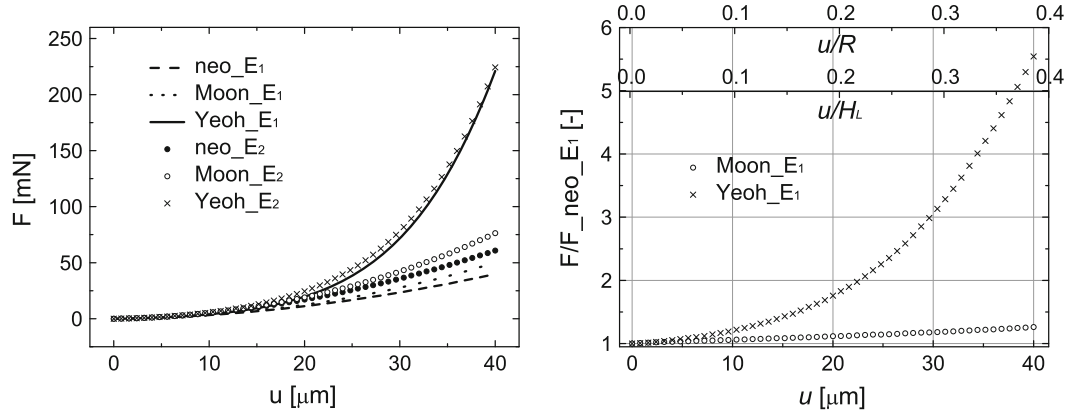
Fig. 7 The nanoindentation results of the three models with geometry parameters listed in case 3: the force–displacement data(*left*), comparison of the behaviour of the three models (*right*)
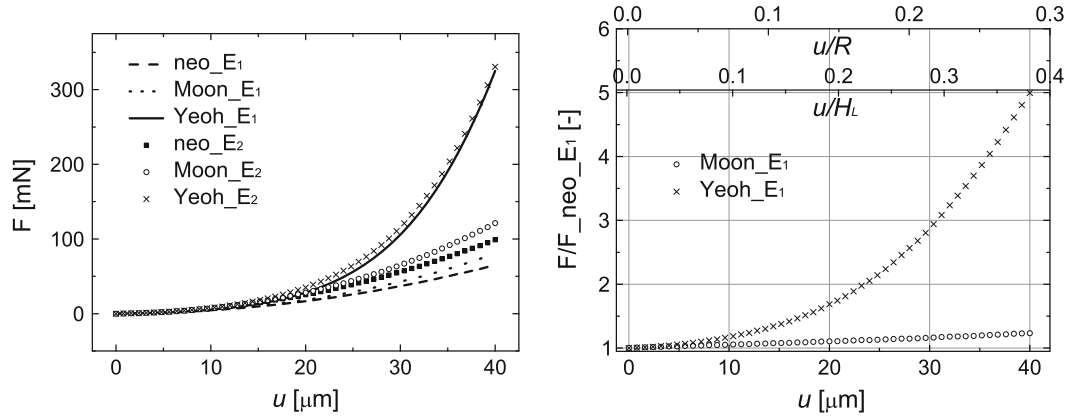
Fig. 8 The nanoindentation results of the three models with geometry parameters listed in case 4: the force–displacement data(*left*), comparison of the behaviour of the three models (*right*)
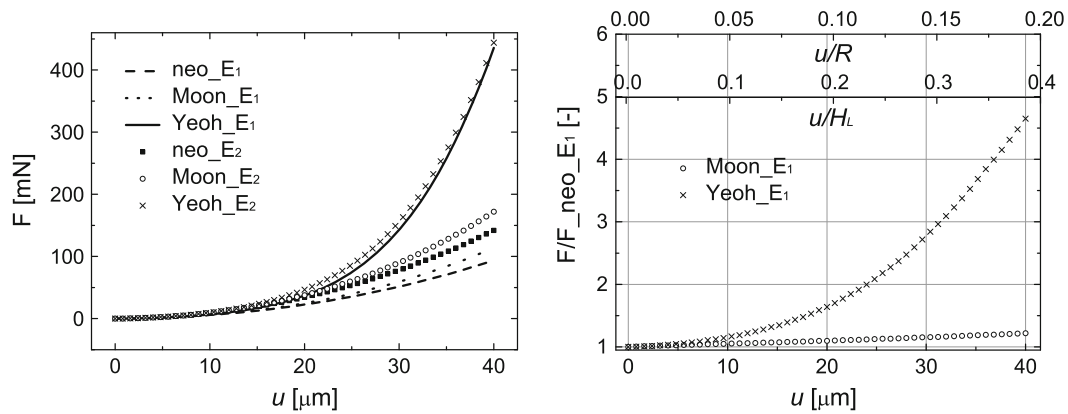
Fig. 9 The nanoindentation results of the three models with geometry parameters listed in case 5: the force–displacement data(*left*), comparison of the behaviour of the three models (*right*)

the Yeoh model with the material parameters Yeoh_E_1 and Yeoh_E_2 becomes stronger with increasing u/H_L from case 1 to case 3. At the same time, the gap between these two curves in each case becomes smaller, and finally, in case 3 they overlap each other. The potential reason stems from the constitutive equation Eq. (13) of

Table 3 Material parameters

Layers							
Hook_E_1	E_1 3.9078 MPa	ν 0.5		Hook_E_2	E_2 6.0 MPa	ν 0.5	
neo_E_1		C_{10} 0.6513 MPa		neo_E_2		C_{10} 1.0 MPa	
Moon_E_1	C_{10} 0.1640 MPa	C_{01} 0.4873 MPa		Moon_E_2	C_{10} 0.2560 MPa	C_{01} 0.7440 MPa	
Yeoh_E_1	C_{10} 0.6513 MPa	C_{20} 2.5870 MPa	C_{30} 5.0 MPa	Yeoh_E_2	C_{10} 1.0 MPa	C_{20} 2.0 MPa	C_{30} 5.0 MPa
Substrate	$E = 450$ (MPa)	$\nu = 0.3$					

the Yeoh model. As discussed above, the non-linear elastic behaviour is strongly dependent on C_{20} and C_{30}, while C_{10} controls the initial linear behaviour. In the parameters sets Yeoh_E_1 and Yeoh_E_2, the value C_{10} is different and the values C_{20} and C_{30} are almost the same. That is the reason why, in case 1 and case 2, the linear elastic behaviour is of most importance, so the gap exists. In case 3, the gap disappears when the non-linear behaviour is prominent. The interesting result is that the non-linearity of the force–displacement curve in case 3 is in the same tendency with the non-linearity of the stress–stretch curve in Fig. 3 (right). Therefore, the non-linear elastic behaviour of the Yeoh model in nanoindentation with u/H_L is as big as 0.4 can be compared with the non-linear elastic response in uniaxial tension test with large stretch. The influence of the substrate is very strong if the indenter tip comes close to the substrate, for example, u/H_L is as big as 0.4. This influence does not only increase the required force to reach the predetermined maximum displacement but also yields strong non-linear elastic behaviour at finite deformation. For the neo-Hookean and the Mooney–Rivlin models with the material parameters neo_E_1, neo_E_2, Moon_E_1 and Moon_E_2, respectively, the differences in case 1 to case 3 only originate from the increased force due to the influence of the substrate.

Secondly, in case 3 to case 5, u/H_L is fixed to 0.4, while the range of u/R is 0–0.4 in case 3, 0–0.3 in case 4 and 0–0.2 in case 5. So the difference of the force–displacement data of the same materials in Figs. 7, 8 and 9 is due to the various scale of u/R. The status of the corresponding force–displacement curves in the three cases is more or less the same, just the required force increases with increasing R. These results are consistent with the conclusion that $F \propto \sqrt{R}$ in the classical contact theories [15,35].

The separability of the elastic behaviour of the three models with the same constant stiffness E_1 in case 1 to case 5 can be quantified from the right side of Fig. 5, 6, 7, 8, 9. The values of F/F_neo_E_1 of Mooney–Rivlin and Yeoh models in the five cases are close to 1.0 if the displacement is smaller than 5 µm. In other words, the behaviour of the three models cannot be explicitly separated if the indentation depth is small compared with the layer thickness and the indenter size. This result is equivalent to the result of uniaxial tension test with small stretch shown in Fig. 3 (left). With the increment of the scale of u/H_L, shown on the right side of Figs. 5, 6 and 7, the separability of the Yeoh model from the neo-Hookean and the Mooney–Rivlin models increases strongly. The F/F_neo_E_1 curve of the Yeoh model has a non-linear relationship with the displacement, and this non-linearity becomes stronger with an increasing ratio of u/H_L. The separability of the different models changes slightly with the variation of the scale of u/R in case 3 to case 5, shown on the right side of Figs. 7, 8 and 9. In relative terms, the F/F_neo_E_1 of Mooney–Rivlin model remains <1.2, and it is a linear function of the indentation depth u.

In few words, as two important geometry-associated factors u/R and u/H_L, for nanoindentation of soft polymer layers on hard substrate, the variation of u/H_L has stronger influence on the force–displacement curves, especially if the indented material has a strong non-linear behaviour at finite strain. It is suggested to take the parameter u/H_L into account if we quantify the representative strain of indentation of thin polymer film, as that the classical representative strain is only a function of the contact radius and the indenter size [6]. Conclusively, if u/H_L is smaller than 0.05, the difference of the force–displacement data of the considered three models is not more than 10%.

5 Parameters re-identification

The parameter re-identification strategy is performed based on the concept of numerical optimisation. Therefore, the MATLAB® optimisation toolbox is used in combination with the nanoindentation boundary value problem solved by the finite element analysis with ABAQUS®. The principle behind can be explained with the following mathematical description, details are described in, for example [24]: Find the vector κ of involved parameters so that

$$f(\kappa) := \frac{\|\mathbf{F}^{num} - \mathbf{F}^{exp}\|}{\|\mathbf{F}^{exp}\|} \longrightarrow \min f(\kappa). \tag{15}$$

The vector of material parameters $\kappa := \{C_{ij}, i = 0, 1, 2, 3; j = 0, 1\}$ has to be modified until a good match between the virtual experimental data and the prediction of the numerical model is achieved. For that reason, the distance function $f(\kappa)$ has to be minimised. $f(\kappa)$ is called objective function of the least squares type. The function represents the quality of the approximation between the model's response governed by the parameter vector κ and the virtual experimental data. In Eq. (15)

$$\mathbf{F}^{exp} = [F_{d1}^{exp}, F_{d2}^{exp}, F_{d3}^{exp}, \ldots]^{T} \tag{16}$$

is the virtual experimental data superimposed with random noise, and for a displacement-controlled indentation, it is the vector of the reaction force obtained at each displacement increment with a chosen set of material parameters. The force vectors obtained for the models with an arbitrary set of material parameters are called

$$\mathbf{F}^{num} = [F_{d1}^{num}, F_{d2}^{num}, F_{d3}^{num}, \ldots]^{T}. \tag{17}$$

The applied evolution strategy is based on the principle of biological evolution in order to find the best parameters minimising the objective function. It performs with a Genetic Algorithm which selects different parameter vectors based on a starting vector κ_0 as population individuals $\kappa_\lambda^{(g)}$ at generation $g = 0$. The selection operator produces the parent population $\kappa_\mu^{(g)}$ of the next generation $g = g + 1$ through a deterministic procedure. The procedure chooses the best individuals from the set of λ individuals $(\kappa_1, \ldots, \kappa_\lambda)$ according to their objective function value $f(\kappa)$.

$$(\kappa_{1;\lambda}, \kappa_{2;\lambda}, \ldots, \kappa_{\mu;\lambda}) := Selection_{f(\mu)}(\kappa_1, \ldots, \kappa_\lambda), \lambda \geq \mu \tag{18}$$

$$f_{1;\lambda} \leq f_{2;\lambda} \leq \cdots \leq f_{m;\lambda} \leq \cdots \leq f_{\lambda;\lambda} \tag{19}$$

The symbol $(.)_{m;\lambda}$ stands for the individual with the mth smallest objective function values. The descendants $\kappa_\lambda^{(g)}$ are generated by recombination and by random mutations of selected parents.

5.1 Identification at small and finite deformations

The parameters of the three material models with the stiffness E_1 are re-identified from the nanoindentation boundary value problem of case 3 in Table 2. Two maximum displacements, 5 and 40 µm, are chosen to investigate whether the accuracy of the identified parameters of the non-linear elastic models is dependent on the magnitude of the deformation under indentation. According to our former work, the influence of the substrate is excluded if the maximum displacement is set to 5 µm, that is, u/H_L is smaller than 5%. In Table 3, the parameters of the three non-linear models are chosen in such a way that the linearisation of the three models at small strain regime yields the same Young's modulus E. Therefore, as shown in Fig. 7 case 3, the relations of the force–displacement of the three models are more or less the same if the maximum displacement is restricted to 5 µm. This case can be considered as small deformation. If the maximum displacement is increased to 40 µm, that is, $u/H_L = 40\%$, the non-linear behaviour of the hyperelastic models especially of the Yeoh form is fully developed under such finite deformation without excluding the influence of the substrate. The parameter identification is performed assuming that the properties of the substrate are known.

The algorithm requires bounds for each parameters. The computational cost can be reduced if narrow bounds are chosen. In general, the choice of the bounds depends on the problem and the experience of the user. Also the choice of the starting vector κ_0 has influence on the convergent speed to the optimal results. Figure 10 shows the evolution process of the material parameters of the Yeoh model with different starting vectors κ_0. We can see that the identified parameters with two different sets of κ_0, that is, [0.1, 0.5, 1] and [0.1, 1, 1], are more or less the same. But the number of the generations used in the first case ([0.1, 0.5, 1]) is much fewer than the number used in the second case ([0.1, 1, 1]). In this work, the starting vector [0.1, 0.5, 1] is used.

The re-identified parameters are listed in Table 4. Compared to the chosen values, the parameter C_{10} of the neo-Hookean model is identified perfectly at the maximum displacement equally, whether of 5 µm or of 40 µm even if the noise level is raised up to 5%. For the Mooney–Rivlin model, a difference of the identified results at a maximum displacement of 5 and of 40 µm appears. Except if the virtual experimental data are free of noise, C_{10} and C_{01} cannot be identified accurately at small deformations, but the sum $C_{10} + C_{01}$ is
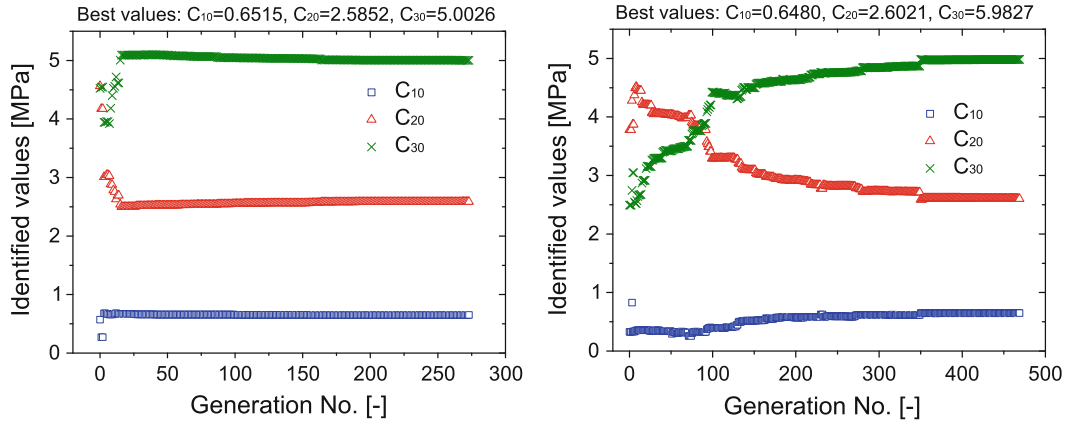
Fig. 10 The evolution process of the material parameters of Yeoh model with different starting vector κ_0: κ_0 is set to [0.1, 0.5, 1] in the case of the *left side*, κ_0 is set to [0.1, 1, 1] in the case of the *right side*

Table 4 The re-identified parameters with maximum displacement 5 and 40 μm

Noise %	neo-Hookean	Mooney–Rivlin			Yeoh form		
	C_{10}	C_{10}	C_{01}	$C_{10}+C_{01}$	C_{10}	C_{20}	C_{30}
Chosen value	0.6513	0.1640	0.4873	0.6513	0.6513	2.5870	5.0
Bounds	(0.01;5)	(0.01;1)	(0.01;1)	—	(0.1;5)	(0.1;20)	(0.1;20)
Maximum displacement 5 μm							
0.0	0.6513	0.2060	0.4483	0.6509	0.6517	2.4920	7.7901
0.5	0.6533	0.2243	0.4316	0.6559	0.6733	0.9107	8.8551
2.0	0.6581	0.4375	0.2323	0.6698	0.6801	1.1695	1.4284
5.0	0.6640	0.5814	0.1097	0.6911	0.7096	0.1001	0.1022
Sensitivity	3.045e4	3.048e4	3.157e4	—	3.052e4	3.377e2	7.290
Maximum displacement 40 μm							
0.0	0.6513	0.1602	0.4903	0.6505	0.6515	2.5852	5.0026
0.5	0.6528	0.1845	0.4728	0.6573	0.6557	2.6019	4.9607
2.0	0.6578	0.2125	0.4547	0.6672	0.6721	2.6498	4.9230
5.0	0.6640	0.4722	0.2692	0.7414	0.7716	2.7291	4.5014
Sensitivity	1.099e6	1.100e6	1.362e6	—	1.054e6	2.989e5	1.305e5

always identified exactly. The reason is associated with the parameters' coupling. These findings also agree well with the theoretical analysis and experimental results reported in [7,8,29]. The effect of parameters' coupling decreases if the maximum displacement increases to 40 μm. In the second case, C_{10} and C_{01} are identified accurately in the case that the superimposed noise is <5%. For higher noise levels, the quality of the identification decreases.

Now, the focus lies on the identified results of the Yeoh model. For this model, huge differences arise at small and finite deformation. At small deformation, except the first two parameters C_{10}, C_{20} are identified exactly when the virtual experimental data are free of noise. The identification of C_{30} is worse. If some noise is superimposed, C_{20} and C_{30} are worse to identify and finally they tend to the lower bounds. However, C_{10} can always be identified accurately. Attention should be paid to the results at large deformation, where all of the three parameters are identified exactly when the virtual experimental data are free of noise. In spite of the noise level is increased up to 5%, the biggest deviation of the identified parameters from the chosen parameters is <20%, which is still tolerable.

The reason for this behaviour is related to the sensitivity of the indentation reaction force **F** with respect to the parameters [21]. The sensitivity $\partial \mathbf{F}/\partial \kappa_i$ can be identified mathematically as follows:

$$\mathbf{F} := \mathbf{F}(\Re, \kappa_1, \dots, \kappa_i, \dots, \kappa_n) \tag{20}$$

$$\frac{\partial \mathbf{F}}{\partial \kappa_i} \approx \frac{\|\mathbf{F}(\Re, \kappa_1, \dots, \kappa_i + \delta\mu, \dots, \kappa_n) - \mathbf{F}(\Re, \kappa_1, \dots, \kappa_i, \dots, \kappa_n)\|}{|\delta\mu|} \tag{21}$$

Herein, $\Re$ is the model of interest, $\delta\mu$ is the mutation step size or an increment of the parameter κ_i. Here, we choose $\delta\mu$ as a relative value that is 10% of κ_i. The sensitivities with respect to κ_i are listed in Table 4:
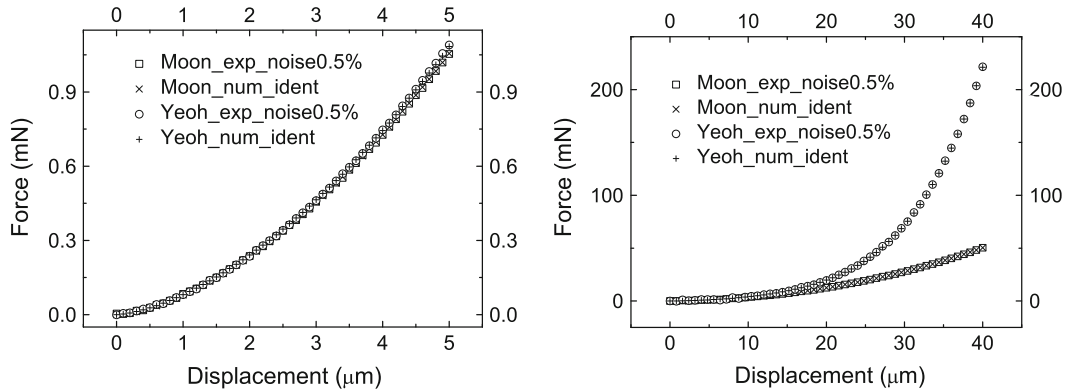
Fig. 11 Comparison of virtual experimental data with 0.5% noise and numerical data with identified parameters: at small deformation (*left*), at finite deformation (*right*)

It shows that the more exactly re-identified parameters have a higher sensitivity than the parameters that are worse to identify. Although some parameters are not identified accurately, Fig. 11 shows good consistency of the virtual experimental data with 0.5% noise and the numerical data obtained with the re-identified parameters of Mooney–Rivlin and Yeoh models at both small and finite deformation. It should be pointed out that, even though the objective function is convergent to a minimum, the accuracy of each identified parameters of the polynomial-type hyperelastic models is not guaranteed. Similar findings are also included in the literature, for example, [11,12], that even the objective function is convergent, the material parameters are changing. In the present work, for Mooney–Rivlin model at small deformation, the contributions from C_{10} and C_{01} to the force–displacement relation cannot be divided. Because of this fact, the force–displacement curve overlaps with the virtual experimental even though parameters coupling exists. For Yeoh model at small deformation, C_{20} and C_{30} are not identified successfully, but the reaction force is not sensitive to them as shown in Table 4. That is to say, their contributions to the force–displacement results are much less than the contribution from C_{10}.

5.2 Possibility of modelling by simpler models

On the one hand, as shown in Figs. 5, 6, 7, 8 and 9, the force–displacement curves of the three models are almost the same in some special deformation range especially before the non-linear behaviour of the Mooney–Rivlin and Yeoh model is fully developed under large deformations. On the other hand, C_{10} and C_{01} of Mooney–Rivlin and C_{20} and C_{30} of Yeoh model cannot be identified accurately at small deformations. Therefore, the question arises if it would be possible to model the indentation behaviour of the relatively complicated hyperelastic models with the simple neo-Hookean model. As an advantage, only one parameter has to be determined and it is also important that parameter coupling can be avoided. As discussed in Sect. 4, the deviation of the different force–displacement curves is strongly dependent on the geometry of the investigated problem; especially, the ratio of the penetration depth to the layer thickness u/H_L plays an important role. Therefore, a further question needs to be investigated: Is the possibility of approximating the Mooney–Rivlin and Yeoh results by the neo-Hookean approach related by the value of u/H_L? To solve these problems, the parameter of the neo-Hookean model is identified with respect to the virtual experimental data without noise obtained by the Mooney–Rivlin and by the Yeoh form, respectively, with various values of u/H_L of geometry case 3.

The re-identified parameters and the corresponding objective function values are listed in Table 5. In order to perceive directly, the global force–displacement curves as well as the local stress–strain curves are plotted in Figs. 12, 13 and 14. The data are obtained from the neo-Hookean model with the identified parameters in Table 5 and obtained from the corresponding Mooney–Rivlin and Yeoh models with the chosen parameters at maximum indentation depth 5, 15 and 40 μm, respectively. It should be noted that the stress–strain distribution in nanoindentation is highly inhomogeneous. Therefore, the local stress–strain data on the same integration point obtained from numerical treatment are plotted here. T_{22} is the Cauchy stress component, and LE_{22} is a logarithmic strain component in vertical direction. In ABAQUS®, the strain **LE** is a logarithmic function of the left stretch tensor **V**.

Figure 12 shows that if the scale of u/H_L is within 0.05, the behaviour under nanoindentation of both Mooney–Rivlin and Yeoh models can be described with a simpler hyperelastic model, for example, the neo-Hookean model.
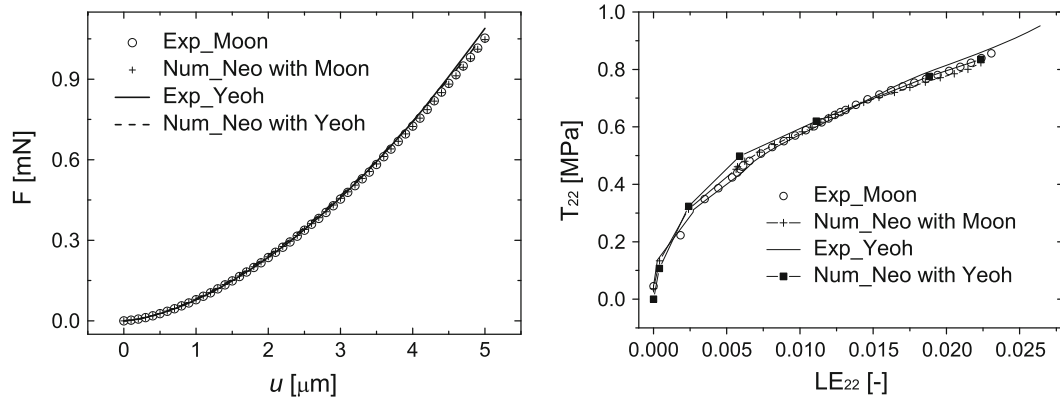
Fig. 12 The force–displacement data (*left*) and the stress–strain curves (*right*) of the neo-Hookean model with the identified parameters in Table 5 and of the corresponding Mooney–Rivlin and Yeoh models with the chosen parameters **at maximum indentation depth 5**
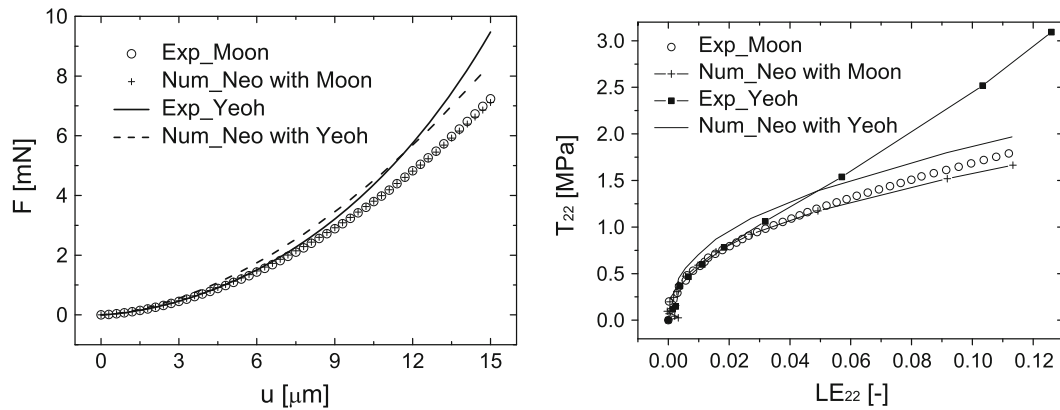
Fig. 13 It is the same like Fig. 12 but with **maximum indentation depth 15**

Table 5 Re-identified parameters of neo-Hookean model with respect to experimental data obtained from Mooney–Rivlin and Yeoh models with various displacement

Maximum displacement (μm)	u/H_L	Mooney–Rivlin		Yeoh form	
		C_{10}	$f(\kappa)$	C_{10}	$f(\kappa)$
5	0.05	0.6706	0.0047	0.6862	0.0138
10	0.10	0.6842	0.0084	0.7432	0.0377
15	0.15	0.6964	0.0125	0.8244	0.0726
20	0.20	0.7047	0.0182	0.9480	0.1179
30	0.30	0.7455	0.0268	1.374	0.2349
40	0.40	0.7762	0.0394	2.196	0.3411

In Fig. 13, if the indentation depth increases to 15 μm, the deviation between the neo-Hookean model with the parameters in Table 5 and the Yeoh model is obvious. Especially, the deviation is very large in the stress–strain curves. Only the results of the Mooney–Rivlin model are compared with the neo-Hookean model if the indentation depth increases to 40 μm. As shown in Fig. 14, the force–displacement response of Mooney–Rivlin model can be approximated with the neo-Hookean model. However, there is a distinctive difference between the stress–strain curves of these two models. The reason may be related to the inhomogeneous deformation in the indentation test; therefore, only the local stress-strain data on each integration point can be obtained.

It seems that the behaviour of the Mooney–Rivlin model under nanoindentation can be approximated with the neo-Hookean model even though at finite deformation. Of course, the errors between the results obtained with the neo-Hookean and the Mooney–Rivlin models are smaller if the penetration depth is less deep. How-
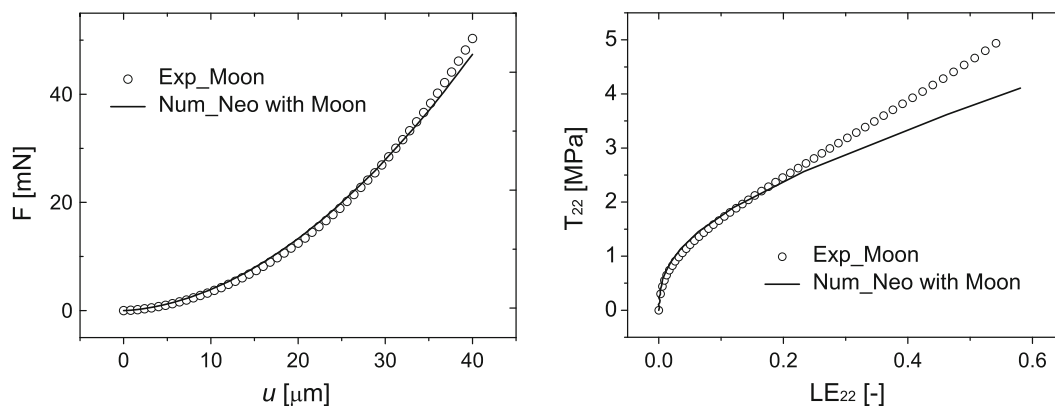
Fig. 14 The force–displacement data (*left*) and the stress–strain curves (*right*) of the neo-Hookean model with the identified parameters in Table 5 and of the corresponding Mooney–Rivlin models with the chosen parameters at **maximum indentation depth 5**

ever, modelling the behaviour of the Yeoh model with the relative simple neo-Hookean model is restrained to the deformation at which the strong non-linearity of the Yeoh model is inactive. In the present work for instance, the error between the nanoindentation results obtained with neo-Hookean and Yeoh models can be neglected if the value of u/H_L is not larger than 0.1.

6 Conclusions

In the present paper, based on a finite element model of contact mechanics and hyperelastic materials, the nanoindentation of polymer layers is studied. Three often used hyperelastic models, that is, the neo-Hookean, the Mooney–Rivlin and the Yeoh models, are applied to simulate the indentation test with the finite element code ABAQUS®. In contrast to the traditional analytical method, the penetration depth is not constrained to avoid the influence of the substrate. The behaviour of nanoindentation at finite deformation is investigated in five cases with various geometry parameters. The results show that for nanoindentation of polymer layers on hard substrates, the force–displacement behaviour of the three investigated hyperelastic models is dependent on the geometry-associated factors u/R and u/H_L. The non-linear elastic behaviour of the Yeoh model is strongly dependent on u/H_L. The non-linear behaviour becomes obvious when u/H_L is larger than 0.2 and it is fully represented if u/H_L increases up to 0.4. The parameter re-identification concept is used to capture material parameters from nanoindentation based on the evolution strategy. Therefore, it is assumed that the properties of the substrate are known. The parameter of neo-Hookean model can be perfectly identified whether at small deformation or at finite deformation. However, C_{10} and C_{01} of the Mooney–Rivlin model and C_{20} and C_{30} of the Yeoh model cannot be identified accurately at small deformations. The reason of the former is that the contribution to the force–displacement results from C_{10} and C_{01} which cannot be divided. Such phenomenon is called parameters coupling, and its influence on the parameter identification decreases in the present case at finite deformation. The latter is due to the lack of non-linearity at small deformations which depends heavily on the values of C_{20} and C_{30}. All of the parameters of the Yeoh model can be identified with tolerable errors at finite deformations even though a random noise level is superimposed up to 5%. Finally, the behaviour of the Mooney–Rivlin model under nanoindentation can be well approximated by the neo-Hookean model even though at finite deformation. However, approximating the behaviour of Yeoh model with the neo-Hookean model is restrained to the deformation at which the strong non-linearity of the Yeoh model is inactive.

References

1. Abaqus Analysis User's Manual. https://www.sharcnet.ca/Software/Abaqus610/Documentation/docs/v6.10/books/usb/default.htm 2011

2. Bertram, A., Han, J., Olschewski, J., Sockel, H.G.: Identification of elastic constants and orientation of single crystals by resonance measurements and fe analysis. Int. J. Comput. Appl. Technol. **7**, 284–291 (1994)
3. Busfield, J.J.C., Thomas, A.G.: Indentation test on elastomer blocks. Rubber Chem. Technol. **75**, 876–894 (1999)
4. Chang, W.V., Sun, S.C.: Non-linear elastic analysis of the hardness test on the rubber-like materials. Rubber Chem. Technol **64**, 202–210 (1991)
5. Choi, I., Shield, R.T.: Second order effects in problems for a class of elastic materials. J. Appl. Math. Phys. (ZAMP) **32**, 361–381 (1981)
6. Fischer-Cripps, A.C.: Nanoindentation. Springer-Verlag New York (2004)
7. Giannakopoulos, A.E., Panagiotopoulos, D.I.: Conical indentation of incompressible rubber-like material. Int. J. Solids Struct. **46**, 1436–1447 (2009)
8. Giannakopoulos, A.E., Triantafyllou, A.: Spherical indentation of incompressible rubber-like material. J. Mech. Phys. Solids **55**, 1196–1211 (2007)
9. Hartmann, S.: Numerical studies on the identification of the material parameters of rivlin's hyperelasticity using tension-torsion tests. Acta Mech. **148**, 129–155 (2001)
10. Hartmann, S.: Parameter estimation of hyperelasticity relations of generalized polynomial-type with constraint conditions. Int. J. Solids Struct. **38**, 7999–8018 (2001)
11. Hartmann, S., Haupt, P., Tschöpe, T.: Parameter identification with a direct search method using finite elements. In: Besdo, D., Schuster, R.H., Ihlemann, J. (eds.) Constitutive Models for Rubber II, pp. 249–256. Balkema Publ, Lisse (2001)
12. Hartmann, S., Tschöpe, T., Schreiber, L., Haupt, P.: Finite deformations of a carbon black-filled rubber. Experiment, optical measurement and material parameter identification using finite elements. Eur. J. Mech. A/Solids **22**, 309–324 (2003)
13. Hartmann, S., Gibmeier, J., Scholtes, B.: Experiments and material parameter identification using finite elements. uniaxial tests and validation using instrumented indentation tests. Exp. Mech. **46**, 5–18 (2006)
14. Hay, J.L., Hern, M.E.O., Oliver, W.C.: The importance of contact radius for substrate-independent properties measurement of thin films. MatER. Res. Soc. Symp. Proc. **522**, 27–32 (1998)
15. Hertz, H.: Über die Berührung fester elstischer körper. J F Reine U Angew Math **92**, 156–171 (1881)
16. Holzapfel, G.A.: Nonlinear solid mechanics: a continuum approach for engineering. Wiley, England (1985)
17. Johlitz, M., Diebels, S., Batal, J., Steeb, H., Possart, W.: Size effects in polyurethane bonds: experiments, modelling and parameter identification. J. Mater. Sci. **43**, 4768–4779 (2008)
18. Kreissig, R.: Auswertung inhomogener Verschiebungsfelder zur Identifikation der Parameter elastisch-plastischer Deformationsgesetze. Forschung Im Ingenieurwesen **64**, 99–109 (1998)
19. Lichinchi, M., Lenardi, C., Haupt, J., Vitali, R.: Simulation of berkovich nanoindentation experiments on thin films using finite element method. Mech. Mater. **42**, 278–286 (1998)
20. Mahnken, R.: An inverse finite-element algorithm for parameter identification of thermoelastic damage models. Model. Simul. Mater. Sci. Eng. **48**, 1015–1036 (2000)
21. Mahnken, R., Stein, E.: The identification of parameters for visco-plastic models via finite-element methods and gradient methods. Model. Simul. Mater. Sci. Eng. **2**, 597–616 (1994)
22. Marckmann, G., Verron, E.: Comparison of hyperelastic models for rubber-like materials. Rubber Chem. Technol. **79**, 835–858 (2005)
23. Mooney, M.: A theory of large elastic deformation. J. Appl. Phys. **11**, 582–592 (1940)
24. Nocedal, J., Wright, S.J.: Numerical Optimization. Springer-verlag, New York (1999)
25. Ogden, R.W.: Large deformation isotropic elasticity: on the correlation of theory and experiment for incompressible rubberlike solids. Proc. R. Soc. Lond. A **328**, 565–584 (1972)
26. Oliver, W.C., Pharr, G.M.: An improved technique for determining hardness and elastic modulus using load and displacement sensing indentation experiments. J. Mater. Res. **7**, 1564–1583 (1992)
27. Oliver, W.C., Pharr, G.M.: Measurement of hardness and elastic modulus by instrumented indentation: Advance in understanding and refinements to methodology. J. Mater. Res. **19**, 3–20 (2004)
28. Rauchs, G.: Optimization-based material parameter identification in indentation testing for finite strain elasto-plasticity. ZAMM Zeitschrift Fur Angewandte Mathematik Und Mechanik **86**, 539–562 (2006)
29. Rauchs, G., Bardon, j., Georges, D.: Identification of the material parameters of a viscous hyperelastic constitutive law from spherical indentation tests of rubber and validation by tensile tests. Mech. Mater. **42**, 961–973 (2010)
30. Rivlin, R.S.: Large elastic deformations of isotropic materials. iv. further developments of the general theory. Phil. Trans. R. Soc. Lond. A **241**, 379–397 (1948)
31. Sabin, G.C.W., Kaloni, P.N.: Contact problem of a rigid indentor in second order elasticity. J. Appl. Math. Phys. **34**, 370–386 (1983)
32. Sabin, G.C.W., Kaloni, P.N.: Contact problem of a rigid indentor with notational friction in second order elasticity. Int. J. Eng. Sci. **27**, 203–217 (1989)
33. Scheday, G., Miehe, C.: Parameteridentifikation finiter Elastizität bei inhomogenen Deformation. Z. Angew. Math. Mech. Suppl. **81**, S425–S426 (2001)
34. Schwefel, H.P.: Evolution and Optimum Seeking. Wiley, New York (1995)
35. Sneddon, I.N.: The relation between load and penetration in the axisymmetric Boussinesq problem for a punch of arbitrary profile. Int. J. Eng. Sci. **3**, 47–57 (1965)
36. Wang, H.F., Bangert, H.: Three-dimensional finite element simulation of vickers indentation on coated systems. Mater. Sci. Eng. A **163**(1), 43–50 (1993)
37. Wriggers, P.: Computational Contact Mechanics. Springer-verlag, Berlin (2006)
38. Yeoh, O.H.: Characterization of elastic properties of carbon-black-filled rubber vulcanizates. Rubber Chem. Technol. **55**, 792–805 (1990)

Parameter Re-identification in Nanoindentation Problems of Viscoelastic Polymer Layers: Small Deformation

Parameter re-identification in nanoindentation problems of viscoelastic polymer layers: small deformation

Zhaoyu Chen[*] **and Stefan Diebels**[**]

Chair of Applied Mechanics, Saarland University, PO Box 151150, 66041 Saarbrücken, Germany

Recently, nanoindentation became a new but all the same a primary testing technique of thin layers. A wide application of nanoindentation in polymeric layers is obstructed by the analysis method, which is used to extract the rate-dependent properties. In the present paper, the inverse method based on the finite element simulation and numerical optimisation is used to characterise the viscoelastic properties of polymers from nanoindentation. First of all, the boundary value problems using nanoindentation of polymer layers considering real geometry, is simulated with the FE code ABAQUS®. A linear viscoelastic model for small strain, based on a general Maxwell rheological model is currently applied to describe the rate-dependent material behaviour. The rate-dependent properties of the polymer layer under nanoindentation is investigated with various loading histories: cyclic testing, single step relaxation, monotonic testing, and sinusoidal oscillatory testing. A parameter re-identification strategy offers a deep insight into the relationship between the accuracy of identification and the loading history associated with the rate-dependent material model. A method to choose a suitable loading history to identify the parameters more accurately is recommended.

1 Introduction

Nanoindentation is a popular technique to determine the mechanical properties such as elastic modulus and hardness. This technique, also known as depth-sensing indentation (DSI), is widely used to investigate the behaviour of metallic or ceramic engineering material. This technique can test the materials at the micro- and nanometer scale without removing the substrate, and it offers favourable means to study the mechanical behaviour of thin films and coatings. Polymeric thin films are of increasing importance for their application in considerable industrial areas, e. g. in the production of plane and automobile, as well as in electronic, optical, medical and chemical devices. However, because these films are very thin, soft and usually fixed on a substrate, it is impossible to measure the mechanical properties using the traditional tension or bending testing. A new testing technique is required. In this case nanoindentation can be used and it increasingly became a primary testing technique of thin layers.

Usually, the substrates could be metals like aluminium and steel. The polymer can be chosen from a wide range, e. g. polyurethane (PU), polyamidoamine (PAMAM), epoxy and many more. Many polymeric materials simultaneously show elastic and viscous material behaviour. In the past decades, the investigations of viscoelastic or rate-dependent effects of polymeric materials using experimental testing, constitutive modelling and numerical computation have been published in e. g. [21, 25, 27, 30, 36, 41, 42, 45, 54, 55, 61]. Incorporating the phenomenological method in the framework of continuum mechanics one can describe the viscous behaviour with strain-like internal variables. The internal variables can be obtained by solving a series of differential evolution equations. Based on the theory of hyperelasticity, the free energy of a viscoelastic solid is split into two parts: one part describes the rate-independent material behaviour and the other part incorporates the rate-dependent effects. Concerning large strain viscoelasticity, a multiplicative decomposition of the deformation gradient into elastic and inelastic parts is further assumed [45]. In this present work, in order to get some experience about parameter identification from the force-displacement response of nanoindentation, a linear viscoelastic model for small strain is considered based on the work of Schwarzl [56], Ferry [15], Tobolsky [61], and Kaliske [36].

The analysis procedure, which is designed in most available commercial indentation instruments, is used to measure the hardness and the elastic modulus according to the Oliver & Pharr (O & P) method [47, 48]. This procedure has two limitations: On the one hand, it is designed for hard and stiff materials, so the usage of nanoindentation on soft materials makes it extremely difficult to obtain accurate results and yields questions which still need to be answered like in [3,5,9,11,13,62,63].

---

[*]   Corresponding author   E-mail: zh.chen@mx.uni-saarland.de, Phone: +49 681 302 2169, Fax: +49 681 302 3992

[**]   E-mail: s.diebels@mx.uni-saarland.de, Phone: +49 681 302 2887, Fax: +49 681 302 3992

On the other hand, the measured hardness and elastic modulus are rare to represent the rate-dependent properties. Therefore, two main ways of characterisation of viscoelastic materials by nanoindentation have been documented in the publications. One main way, the termed inverse method, is performed by combining finite element modelling and numerical optimisation. In this method, the difference between experimental and numerical data, called objective function, is minimised with respect to the model parameters using numerical optimisation and the parameters of the constitutive models are identified as the optimised solution. This inverse method was firstly applied in indentation by Huber et al. [29, 31, 37, 64]. They used neural networks to identify material parameters from indentation of metals. But it is still a new topic to determine model parameters of polymer materials using the inverse method in nanoindentation tests. Hartmann [22] identified the viscoplastic model parameters with uniaxial tests and validated them using indentation tests. Rauchs [52, 53] employed a gradient-based numerical optimisation method to identify viscous hyperelastic and elasto-viscoplastic material parameters. Guessasma [20] determined viscoelastic properties of biopolymer composite materials using finite element calculation and nanoindentation. The other method is based on analytical or semi-analytical solutions. The parameters for a specific viscoelastic model are obtained by fitting the experimental force-displacement data with the analytical expressions for the respective viscoelastic model. The basic theory of linear viscoelastic contact problems was developed by Lee and Radok [39] in 1960. The method is called correspondence principle which extends the elastic contact theory to linear viscoelastic models by using some mathematical transformation, e. g. Laplace transformation. This method is restricted to a monotonically increasing contact area. Later Ting [59, 60] and Graham [18, 19] proposed a more general solution. In 1985, Johnson [35] summarised the correspondence analysis of spherical indentation replacing the elastic constants by the Boltzmann viscoelastic hereditary integral operators. Based on these approaches, in several contributions [2, 6, 10, 12, 17, 28, 32, 33, 38, 43, 44, 49, 50, 65] the viscoelastic analytical solutions of nanoindentation with different indenter tips were presented. The method is restricted by yielding accurate identification only for specific linear viscoelastic models under fixed experimental processes. Furthermore, the affecting factors in the nanoindentation experiment, like non-linearity friction, adhesion and surface roughness are not taken into account in the analytical solutions. However, the inverse method permits us to treat any material models with non-linear properties and to include further affecting factors in the numerical model. As a conclusion, the rate-dependent properties of polymers can be more accurately identified using the inverse method. Identifying viscoelastic properties of polymers with nanoindentation testing using the inverse method remains a large research field.

In the present study, it is our goal to offer a deep insight into the identification of the viscoelastic model parameters from nanoindentation of polymer layers with various loading histories. A 3D linear viscoelastic model for small strain is taken into account. The constitutive formulation is restricted to small perturbations away from thermodynamic equilibrium. In this present study, it is investigated how accurate the material parameters can be determined from the numerical optimisation routine. In contrast to the traditional inverse method, virtual experimental data calculated by numerical simulations with chosen parameters, replace the real experimental measurements. Such a procedure, which is called parameter re-identification was used in [51, 52] to validate the gradient-based material parameter identification routine. In this sense, the finite element code ABAQUS® is used as our virtual laboratory. An artificial random noise is superimposed on the virtual experimental data to make it more realistic and to check the stability of the identification procedure. Considering the troublesome gradient calculation for the model and the further drawback of deterministic methods of distinguishing local and global minima, the stochastic strategy is used, based on principles of biological evolution, e. g. an evolution strategy [57].

This paper contains the following: firstly, the numerical model of nanoindentation of polymer layers, considering the real geometry, is described. Secondly, the constitutive model of linear viscoelasticity is recalled and the numerical implementation into ABAQUS® is explained. Thirdly, different loading histories are considered in a virtual experiment. Finally, the procedure of parameters identification is illustrated and the results under various loading histories are discussed.

2 Simulation of nanoindentation

2.1 Numerical model of nanoindentation

The spherical indentation differs from conical or pyramidal indentation because there is no elastic singularity at the tip of the indenter to produce large stresses [48]. The contact between the indenter and the specimen at small loads and displacements is entirely elastic and then the transition to inelastic effect is continuous as the indenter is driven further into the material. As a consequent, spherical indenters have an increasing application. They are particularly suitable to measure soft materials and to replicate contact damage in in-service conditions [16]. The numerical simulation of spherical nanoindentation of polymer layers on substrate, taking into account the real geometry, can be modelled by an axisymmetric two-dimensional model with a finite element code, e. g. ABAQUS® 6.10. The indenter is assumed to be a rigid body compared to the soft polymer layer. We define the indenter as an analytical rigid surface, in such a way that the indenter geometry can be modelled exactly with a smooth curve. In view of the contact problem, quadrilateral elements are used. Assuming a
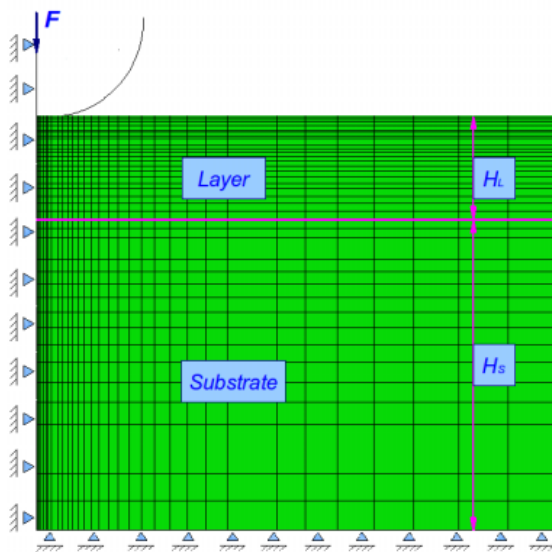
Fig. 1 (online colour at: www.zamm-journal.org) Sketch of FEM model of spherical nanoindentation.

linear elastic behaviour of the substrate and an incompressible material behaviour of the polymer layer, the element types CAX4 and CAX4H are used for the substrate and the layer, respectively. It is essential that the density of nodes close to the indenter tip is high enough to consider the localised deformation of the layer. The nodes at the axis of symmetry are fixed in the horizontal direction, while those nodes at the bottom cannot move in the vertical direction. The geometry and boundary conditions of the spherical nanoindentation are illustrated in Fig. 1. In the present work, the gradient of deformation under nanoindentation is especially restricted to the small deformation regime: the maximum displacement is only 5% of the layer thickness. The main difficulty encountered in nanoindentation of thin films is to avoid unintentional probing of properties of the substrate. To achieve this, it is common to restrict the maximum depth of penetration to less than 10% of the film thickness, e. g. [40, 66]. To determine these effects of the substrate, the contact radius is taken into account like in [6, 24]. However, in the experiment it is difficult to obtain the accurate contact radius, which depends on the penetration depth, the indenter geometry and the material properties. In this case, the effects of the substrate on the force-displacement data are determined by both the radio of the penetration depth to the indenter radius, as well as the ratio of the penetration depth to the film thickness as shown in our previous work [7]. It is found that the latter plays a more important role in determining the effects of substrate. According to [7, 8], the influence of the substrate and the friction between the indenter and the layer can be neglected.

Concerning the numerical treatment of the contact problem, the indenter is defined as master surface while the layer is defined as slave surface, both form a contact pair. A contact formulation of finite-sliding interaction [1] between a deformable and a rigid body in ABAQUS®/Standard is used to establish the frictionless contact model between indenter and layer. In this case, the formulation of the normal contact is used as a constraint for non-penetration which treats the normal contact as a unilateral constraint problem. The normal contact pressure cannot be calculated from a contact constitutive equation, but is then obtained as a reaction in the contact area, and hence can be deduced from the constraint equations with the often used Lagrange multiplier method or the Penalty method, for details please see [1, 67].

2.2 3D viscoelastic model and numerical implementation

In order to construct a phenomenological 3D viscoelastic model, a one-dimensional rheological model is introduced, as illustrated in Fig. 2. An extra spring is connected in parallel with n Maxwell elements. It is a useful model to represent quantitatively the mechanical behaviour of real viscoelastic materials. As the extra spring represents the elasticity in the relaxed state, the Maxwell elements display the viscoelastic material response considering a number of discrete relaxation times.

In this paper, we restrict ourselves to an isotropic and incompressible linear viscoelastic model for small deformation under isothermal conditions. The incompressibility is expressed by splitting the deformation of the material into a deviatoric part and a volumetric part. Experimental investigations have shown that in many cases viscoelastic behaviour is mainly related to the deviatoric part of the deformation [36]. Thus, the volume dilatation is considered as being purely elastic. The modulus of compression is assumed to be much larger than the shear modulus. Therefore, the free energy density function Ψ is split into a purely elastic part, also termed as equilibrium part, and a viscoelastic part, the so called non-equilibrium
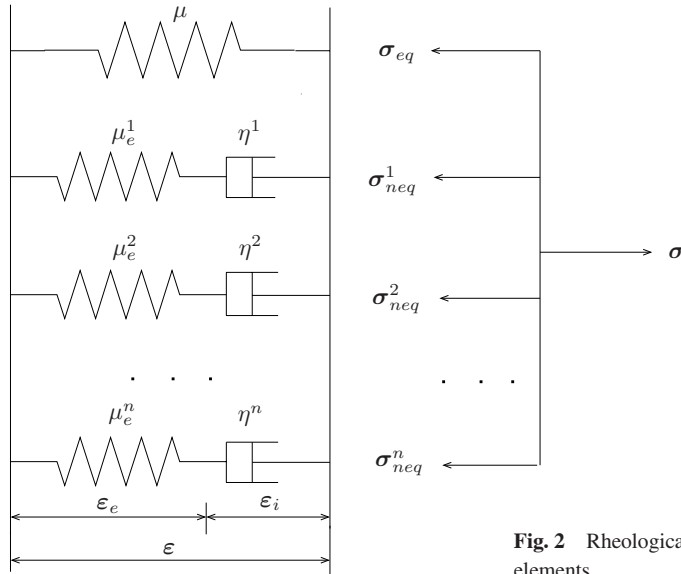
Fig. 2   Rheological model of the viscoelasticity with $j = 1, \ldots, n$ Maxwell elements.

part [45]

$$\rho_0 \Psi = \rho_0 \Psi_{eq}(\boldsymbol{\varepsilon}) + \rho_0 \sum_{j=1}^{n} \Psi_{neq}^{j}(\boldsymbol{\varepsilon}_i^{j}) = K(\boldsymbol{\varepsilon} : \mathbf{I})^2 + \mu \boldsymbol{\varepsilon}^D : \boldsymbol{\varepsilon}^D + \sum_{j=1}^{n} \mu_e^{j} \boldsymbol{\varepsilon}_e^{j^D} : \boldsymbol{\varepsilon}_e^{j^D} \tag{1}$$

with $\boldsymbol{\varepsilon}_e^{j^D} = \boldsymbol{\varepsilon}^D - \boldsymbol{\varepsilon}_i^{j^D}$. $\boldsymbol{\varepsilon}^D$ is the deviatoric strain tensor. $\boldsymbol{\varepsilon}_i^{j^D}$ is the so called deviatoric internal variable, which represents the viscous strain of the dashpot in the jth Maxwell element. The derivation of the stress-strain relation follows according to the evaluation of the entropy principle in the form of the Clausius-Planck-inequality for the isothermal case [23]

$$\boldsymbol{\sigma} : \dot{\boldsymbol{\varepsilon}} - \rho_0 \dot{\Psi} \geq 0. \tag{2}$$

After some calculations one obtains the Clausius-Planck-inequality in the form

$$\left\{ \boldsymbol{\sigma}^V - K(\mathrm{tr}\boldsymbol{\varepsilon})\mathbf{I} \right\} : \dot{\boldsymbol{\varepsilon}}^V + \left\{ \boldsymbol{\sigma}^D - 2\mu\boldsymbol{\varepsilon}^D - \sum_{j=1}^{n} 2\mu_e^{j} \boldsymbol{\varepsilon}_e^{j^D} \right\} : \dot{\boldsymbol{\varepsilon}}^D + \sum_{j=1}^{n} 2\mu_e^{j^D} \boldsymbol{\varepsilon}_e^{j^D} : \dot{\boldsymbol{\varepsilon}}_i^{j^D} \geq 0. \tag{3}$$

Herein, $\boldsymbol{\sigma}^V$ and $\boldsymbol{\varepsilon}^V$ are the volumetric stress and strain tensors, respectively, with the relations $\boldsymbol{\sigma} = \boldsymbol{\sigma}^V + \boldsymbol{\sigma}^D$ and $\boldsymbol{\varepsilon} = \boldsymbol{\varepsilon}^V + \boldsymbol{\varepsilon}^D$. Furthermore according to the classical argumentation of Coleman and Noll [14], one gets the Cauchy stress tensor $\boldsymbol{\sigma}$

$$\boldsymbol{\sigma} = \boldsymbol{\sigma}_{eq} + \boldsymbol{\sigma}_{neq} = K(\mathrm{tr}\boldsymbol{\varepsilon})\mathbf{I} + 2\mu\boldsymbol{\varepsilon}^D + \sum_{j=1}^{n} 2\mu_e^{j} \boldsymbol{\varepsilon}_e^{j^D}. \tag{4}$$

In order to satisfy the Clausius-Planck-inequality (3), the internal dissipation is set in the form

$$\sum_{j=1}^{n} \boldsymbol{\sigma}_{neq}^{j} : \dot{\boldsymbol{\varepsilon}}_i^{j^D} \geq 0. \tag{5}$$

Since the viscosity parameters satisfy $\eta^{j} \geq 0$, the model is compatible with equation (5) and a linear evolution equation can be derived

$$\dot{\boldsymbol{\varepsilon}}_i^{j^D} = \frac{1}{r^{j}} \left(\boldsymbol{\varepsilon}^D - \boldsymbol{\varepsilon}_i^{j^D} \right) \tag{6}$$

with the relaxation time of each Maxwell element $r^{j} = \eta^{j}/2\mu_e^{j}$.

The constitutive equation (4) and the linear evolution equations (6) are implemented into ABAQUS®'s user interface umat [1]. Even if ABAQUS possesses a standard implementation of a linear viscoelastic model the presented equations are implemented on the level of the user interface because further work will require the extension to the finite strain case based on the multiplicative split of the deformation gradient. In the numerical framework, the linear evolution equations (6) can be solved by an implicit Euler-backward integration scheme. Considering the time interval $[t_n, t_{n+1}]$ we define the time step $\Delta t := t_{n+1} - t_n$. By using the basic approach for a time-dependent variable one obtains the equations for each Maxwell element

$$\varepsilon_i^{j^D}(t_{n+1}) = \frac{\Delta t}{\Delta t + r^j}\varepsilon^D(t_{n+1}) + \frac{r^j}{\Delta t + r^j}\varepsilon_i^{j^D}(t_n). \tag{7}$$

These equations have to be solved for each time step Δt at each integration point of the finite elements.

In umat the stress is calculated by the Jacobian matrix of the constitutive model DDSDDE, $\partial\Delta\boldsymbol{\sigma}/\partial\Delta\boldsymbol{\varepsilon}$, where $\partial\Delta\boldsymbol{\sigma}$ are the stress increments and $\partial\Delta\boldsymbol{\varepsilon}$ are the strain increments. DDSDDE(I, J) defines the change in the I$^{\text{th}}$ stress component at the end of the time increment caused by an infinitesimal perturbation of the J$^{\text{th}}$ component of the strain increment array. The current stress is expressed as a function of the total strain and the internal variables

$$\boldsymbol{\sigma}(t_{n+1}) = K(\text{tr}\boldsymbol{\varepsilon}(t_{n+1}))\mathbf{I} + \left\{2(\mu + \sum_{j=1}^{n}\mu_e^j) - \sum_{j=1}^{n}2\mu_e^j\frac{\Delta t}{\Delta t + r^j}\right\}\varepsilon^D(t_{n+1}) - \sum_{j=1}^{n}2\mu_e^j\frac{r^j}{\Delta t + r^j}\varepsilon_i^j(t_n). \tag{8}$$

The constitutive Jacobian can be derived as the tangent matrix of the current stress with respect to the current strain

$$\mathbb{C} = \frac{\partial\boldsymbol{\sigma}(t_{n+1})}{\partial\boldsymbol{\varepsilon}(t_{n+1})} = K\mathbf{I}\otimes\mathbf{I} + \left\{2(\mu + \sum_{j=1}^{n}\mu_e^j) - \sum_{j=1}^{n}2\mu_e^j\frac{\Delta t}{\Delta t + r^j}\right\}\left(\mathbb{I} - \frac{1}{3}\mathbf{I}\otimes\mathbf{I}\right). \tag{9}$$

The constitutive Jacobian $\mathbb{C}$ is a tensor of fourth order. $\mathbb{I}$ is identified as the fourth-order unit tensor. The determination of the current variables $\varepsilon_i^j(t_{n+1})$ and $\boldsymbol{\sigma}(t_{n+1})$ requires the quantities $\varepsilon_i^j(t_n)$ of the proceeding time step and, therefore, they have to be stored in a data base.

3 Parameter re-identification

Firstly, it is our goal to develop a method to identify the material behaviour from nanoindentation based on the inverse method. The virtual experimental data and the parameters re-identification concept permit us to investigate how accurate the chosen model parameters can be identified from our developed procedure; Secondly, the real experimental data in the literature contains too much unknown details due to the complexity of nanoindentation. These unknown details can not be contained in the numerical model which may increase the system error between the numerical data and experimental results. Therefore in this part, a parameter identification routine based on the re-identification strategy is used. In this case, the boundary value problem of the FEM model of nanoindentation is calculated with the chosen material parameters. The resulting force-displacement curve is considered as virtual experimental data, which is used instead of real experimental measurements to identify the chosen parameters again.

3.1 Virtual experiment with different loading history

Usually, the substrates of polymer coatings and thin films can be metals like aluminium and steel. The polymer can be chosen in a large range, e. g. polyurethane (PU), polyamidoamine (PAMAM), epoxy and so on. The stiffness modulus of these polymer layers exhibits a greater range from several MPa to several GPa due to the micro chemical structure. In the framework of this paper, we choose a linear viscoelastic model with 3 Maxwell elements. The bulk modulus K of the extra spring should be high enough, compared with the shear modulus μ, to make sure that the material is incompressible. Hence, in this paper, it is assumed that K is a known parameter as high as 1000 times of μ. The parameters of the linear viscoelastic model are chosen according to the identified parameters of polyurethane in the work of Johlitz et al. [34]. The substrate is aluminium and it is assumed to be purely elastic. The model parameters are listed in Table 1. Because the deformation of the polymer layer is restricted to a small range, the influence of the substrate as well as the surface interactions, e. g. friction, can be neglected. Therefore, the force-displacement data, obtained from the virtual nanoindentation testing, is only the mechanical response of the indented polymer layer. The virtual experiments are performed with four kinds of loading histories with both displacement and force control. The response of the chosen model from nanoindentation BVP is investigated.

Table 1 Chosen material parameters of the used viscoelastic model.

Material	Chosen values						
Polymer	μ	μ_e^1	r^1	μ_e^2	r^2	μ_e^3	r^3
layer	1.3 MPa	0.8 MPa	0.2 s	0.4 MPa	3 s	0.1 MPa	100 s
Substrate	E = 69GPs				$\nu = 0.3$		
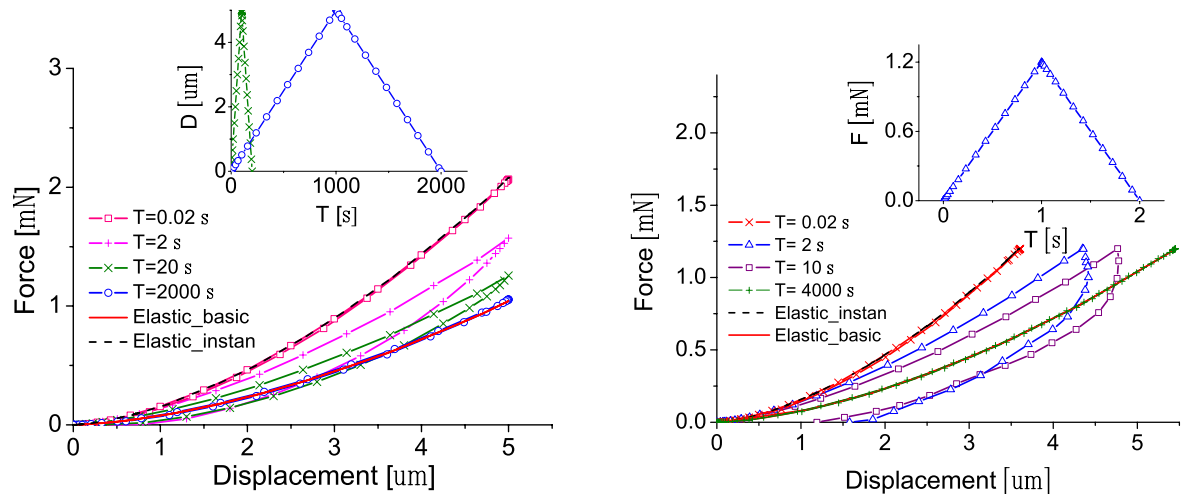
Fig. 3 (online colour at: www.zamm-journal.org) Viscous dissipation of force-displacement response obtained by a cyclic test: Displacement control (left), Force control (right).
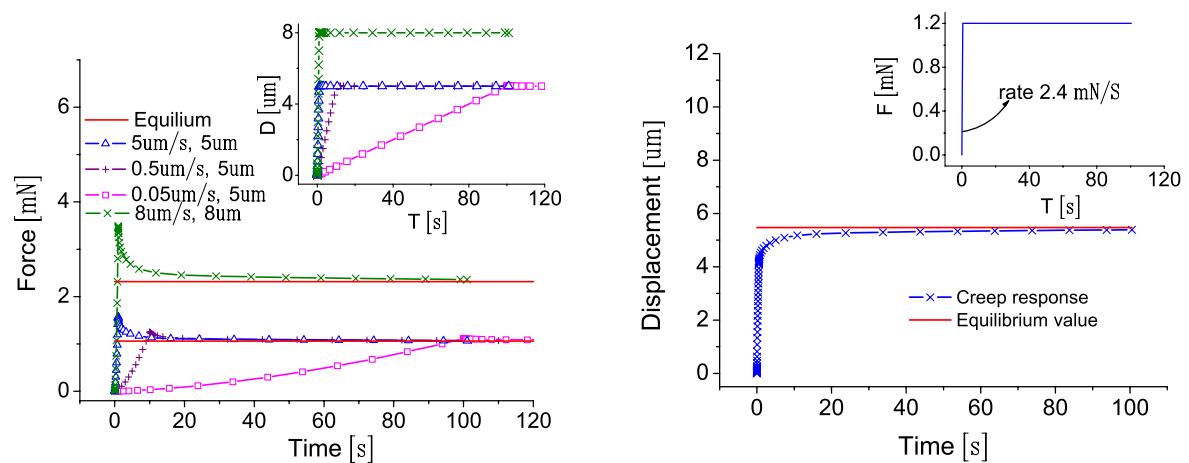
Fig. 4 (online colour at: www.zamm-journal.org) The relaxation and creep response from a single step relaxing or creeping test: Displacement control (left), Force control (right).

Firstly, a cyclic test containing a loading and an unloading stage is applied with constant loading rates. The viscoelastic properties are investigated by the rate dependent viscous dissipation, the so called hysteresis loop. A spectrum of process times results in a series of constant loading rates varying from very fast to very slow during the loading and unloading stages. Fig. 3 shows that the hysteresis loop has a maximum value for the displacement control and for the force control if the procedure time T is 2 s. It is proven in [58] that the maximum hysteresis loop depends on the radio of the process time T to the relaxation time r. The hysteresis loops disappear if the loading rate is sufficiently fast or slow and if the process time is less than 0.02 s or greater than 2000 s, as shown in Fig. 3. These two cases are the instantaneous and the equilibrium elastic
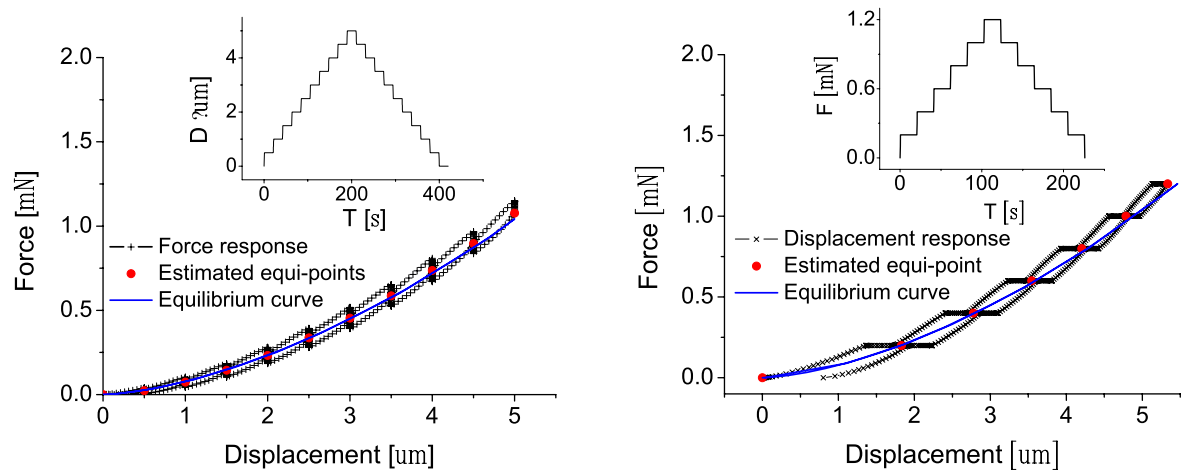
Fig. 5 (online colour at: www.zamm-journal.org) The force-displacement data obtained from a monotonic test: Displacement control (left), Force control (right).
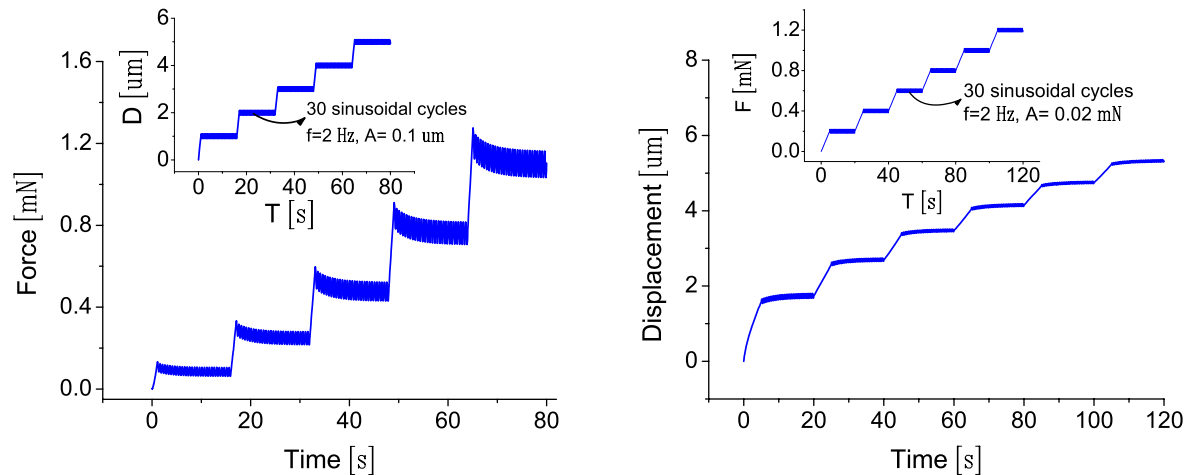
Fig. 6 (online colour at: www.zamm-journal.org) The force or displacement response obtained from a sinusoidal oscillatory test: Displacement control (left), Force control (right).

states, respectively. From the physical point of view, this phenomenon can be well explained with the rheological model shown in Fig. 2: if the loading rate is sufficient fast then the dashpots in the Maxwell elements have no time to dissipate energy, the total energy contains the maximum elastic contributions not only from springs in the Maxwell elements but also from the extra spring. Otherwise, the dashpot could dissipate the whole energy in the Maxwell elements. The total energy in the system contains only the contribution from the extra spring. For details please see [23, 26]. Attention should be paid to the obvious creep during the unloading, cf. Fig. 3, right. Similar results were observed in real experiments documented in e. g. [5, 11, 13]. In this case, the stiffness calculated according to the Oliver & Pharr method is negative. Therefore, a suitable holding stage before unloading is necessary to apply the Oliver & Pharr method for rate-dependent material. Consequently, only equilibrium properties can be determined. Secondly, a single step of relaxation and creep tests show the force relaxation and the deformation creep, respectively. The left-hand diagram in Fig. 4 shows that the equilibrium state is associated only with the maximum deformation. Nevertheless, the relaxation process is not only related with the maximum displacement but also with the loading rate and the holding time.

Thirdly, a monotonic test is used to approximate the equilibrium points of the force-displacement curve. As shown in Fig. 5, left, if the displacement is hold, the force relaxes during the loading stage but increases during the unloading stage. Similar results are also obtained from force control testing. If the holding stage is sufficiently long, the two points will

overlap each other. The cross point can be considered as the equilibrium point. However, it is impossible in a real experiment to wait several months to get the equilibrium points. Usually the average values of the static states after relaxation of loading and unloading stages could be considered as approximated equilibrium points. For both displacement and force control, the approximated equilibrium points are consistent with the equilibrium curve obtained from numerical simulation. However, because the holding time is not long enough, the deviation slightly increases with increasing penetration depth. Finally, a sinusoidal oscillatory testing is performed in this way: the displacement or force is ramped quickly then it oscillates sinusoidally with fix amplitude; such a procedure repeats with a monotonic increasing displacement or force. The loading history and the corresponding force or displacement response are shown in Fig. 6. It can be seen that, in displacement control testing, the force relaxes sinusoidally towards to the equilibrium states. Nevertheless, the displacement has only a slight response with sinusoidal oscillations of the force.

3.2 Procedure of parameter identification

The parameter re-identification strategy is performed in the MATLAB$^{®}$ optimisation toolbox combined with a spherical nanoindentation boundary value problem which is solved using the finite element analysis with ABAQUS$^{®}$. From the mathematical point of view such a process represents a numerical optimisation problem, details are described in e. g. [46]. In the present study the vector of material parameters $\boldsymbol{\kappa} := \{\mu, \mu_e^j, r^j, j = 1, 2, 3\}$ has to be modified until a close match between the virtual experimental data and the prediction of the numerical model is achieved. For that reason the distance function $f(\boldsymbol{\kappa})$ has to be minimised. $f(\boldsymbol{\kappa})$ is called objective function of the least squares type, which represents the quality of the approximation between the model response governed by the parameter vector $\boldsymbol{\kappa}$ and the virtual experimental data. Mathematically this can be formulated as follows: Find $\boldsymbol{\kappa}$ so that

$$f(\boldsymbol{\kappa}) := \frac{\|\mathbf{F}^{\mathrm{num}} - \mathbf{F}^{\mathrm{exp}}\|}{\|\mathbf{F}^{\mathrm{exp}}\|} \longrightarrow \mathrm{Minf}(\boldsymbol{\kappa}). \tag{10}$$

Herein

$$\mathbf{F}^{\mathrm{exp}} = [F_{t1}^{\mathrm{exp}}, F_{t2}^{\mathrm{exp}}, F_{t3}^{\mathrm{exp}}, \ldots]^T, \tag{11}$$

is the virtual experimental data. That is the vector of reaction force obtained at each time increment. In the present study, the indenter penetrates into the layer, and the displacement acts as the independent variable and is assumed to be noise free. The reaction force vector is superimposed with a random noise multiplied by a fixed percentage representing the levels of noise. The random noise is a vector containing normally distributed pseudorandom numbers, its average value is the same as the corresponding reaction force vector. These values represent the data which are usually obtained by experiments. The force vectors obtained for the models with an arbitrary set of material parameters are called

$$\mathbf{F}^{\mathrm{num}} = [F_{t1}^{\mathrm{num}}, F_{t2}^{\mathrm{num}}, F_{t3}^{\mathrm{num}}, \ldots]^T. \tag{12}$$

The choice of the optimisation-based method for minimising an objective function is a topic of interest. It is generally advised to use globally convergent optimisation algorithms whenever possible. These algorithms are simulated annealing or genetic algorithms, such as evolutionary algorithms, or deterministic algorithms like the Simplex method. The gradient-based algorithm is full of troublesome gradient calculation and the further drawback of local convergence. Genetic or evolutionary algorithms are globally convergent and are the only useful choice in a multi-objective optimisation. Therefore, to update the initial guessed material parameter vector $\boldsymbol{\kappa}$ the evolution strategy is employed. It works with a Genetic Algorithm which selects different parameter vectors based on a starting vector $\boldsymbol{\kappa}_0$ as population individuals $\boldsymbol{\kappa}_\lambda^{(g)}$ at generation $g = 0$. The selection operator produces the parent population $\boldsymbol{\kappa}_\mu^{(g)}$ of the next generation $g = g + 1$ through a deterministic procedure, which chooses the best individuals from the set of λ individuals $(\boldsymbol{\kappa}_1, \ldots, \boldsymbol{\kappa}_\lambda)$ according to their objective function value $f(\boldsymbol{\kappa})$.

$$(\boldsymbol{\kappa}_{1;\lambda}, \boldsymbol{\kappa}_{2;\lambda}, \ldots, \boldsymbol{\kappa}_{\mu;\lambda}) := Selection_{f(\mu)}(\boldsymbol{\kappa}_1, \ldots, \boldsymbol{\kappa}_\lambda), \lambda \geq \mu \tag{13}$$

$$f_{1;\lambda} \leq f_{2;\lambda} \leq \cdots \leq f_{m;\lambda} \leq \cdots \leq f_{\lambda;\lambda} \tag{14}$$

The symbol $(.)_{m;\lambda}$ stands in this context for the individual with the mth best objective function values. The descendants $\boldsymbol{\kappa}_\lambda^{(g)}$ are generated by recombination and by random mutations of selected parents. In details, a crossover recombination operator randomly selects genetic information from two parents as the vector entry of the descendant. Single parents generate descendants by mutation, in which a stochastic vector $\boldsymbol{\Delta\sigma}$ is added to them. Mutation is the most important ingredient for the evolution strategy [4], the choice of $\boldsymbol{\Delta\sigma}$ closely links to the convergence behaviour of the method. In order to make the algorithm efficient, it is suggested that $\boldsymbol{\Delta\sigma}$ should be modified during the minimum search [57]. Besides mutation and recombination procedures, the parents with the best fitness are guaranteed to survive in the generation $g = g + 1$ as elite individuals.

3.3   Results and discussion

On the one hand, most of the nanoindentation instruments can be performed with both displacement and force control. On the other hand, the results in Sect. 3.1 show that the force response is more sensitive with respect to the various loading histories than the displacement response. Therefore, the displacement controlled nanoindentation with three kinds of loading history is chosen to identify the model parameters, as shown in Figs. 7 and 8. It is aimed to investigate whether the multi-parameters identification of the considered viscoelastic model depends on the loading history in nanoindentation testing. A suitable bound set is useful to reduce the computational cost during the parameters identification. If smaller bounds containing the real parameter values are used, the computational cost can be strongly reduced to find the optimal parameters. However, the judgement of suitable bounds is experience dependent. Here, larger bounds which are not strongly dependent on experience are used. The lower and upper bounds are listed in Table 2.
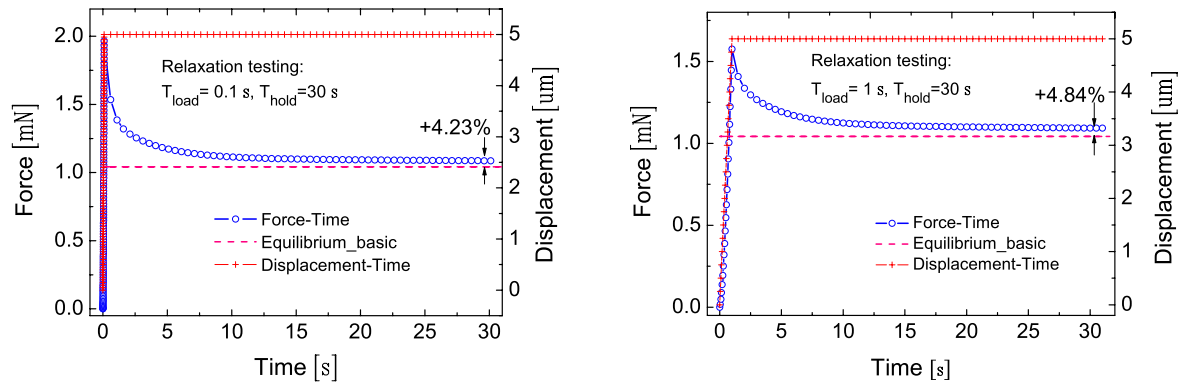
Fig. 7   (online colour at: www.zamm-journal.org) The loading history chosen for parameters identification and the corresponding force plotted at each time increment: single step relaxation with a loading time of 0.1 s (left) and with a loading time of 1 s (right).
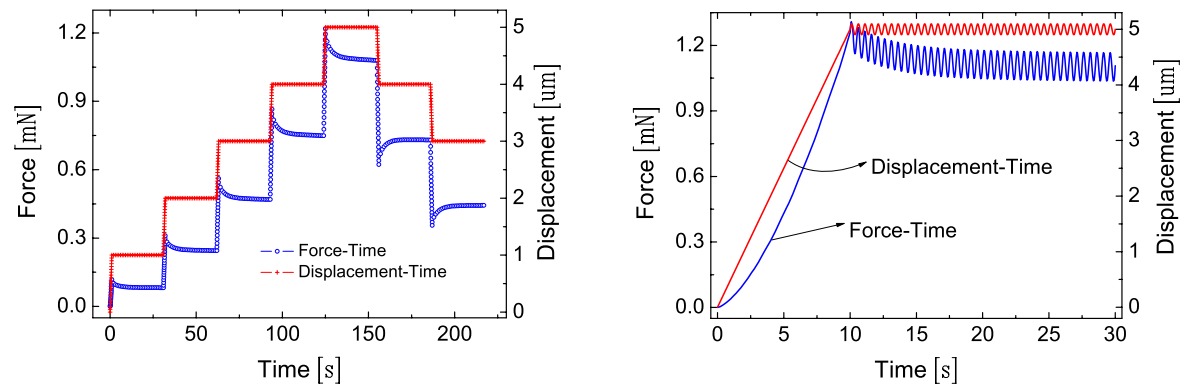
Fig. 8   (online colour at: www.zamm-journal.org) The loading history chosen for parameters identification and the corresponding force plotted at each time increment: monotonic (left) and sinusoidal oscillatory (right) testing.

First of all, we focus on the identified results with single step relaxation loading history. Two cases of a single step relaxation with the same maximum displacement are selected as shown in Fig. 7: one case with a loading time of 0.1 s and the other case with a loading time of 1 s. These two loading times are in the same decade with the relaxation time r^1 and r^2, respectively. The holding times of the two loading cases are kept the same as 30 s. Since the real model parameters are unknown in the traditional inverse method, a close match between the experimental data and the prediction of the numerical model is the only way to judge the accuracy of the parameters identification. Therefore, the comparison of the virtual experimental data and the numerical simulation results will be investigated firstly. The relative errors listed in Table 2 of the re-identified parameters with respect to the chosen values allow us to verify the most often used way of judgement. Fig. 9, left, shows the results of the single step relaxation with a loading time of 0.1 s. A close match between the experimental data and the numerical results can be seen. Indeed, the match of the numerical data obtained with the parameters identified from
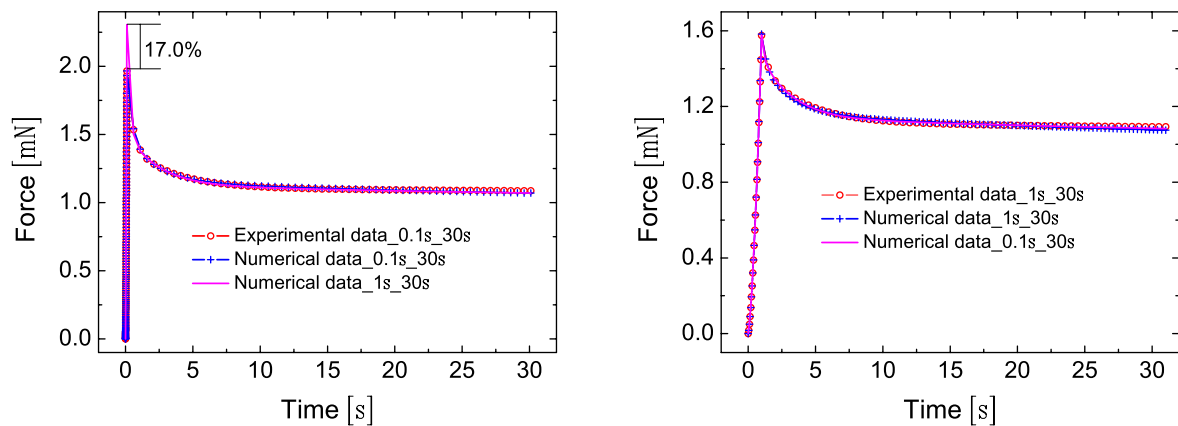
Fig. 9 (online colour at: www.zamm-journal.org) Comparison of the experimental data with numerical simulation of a single step relaxation test: with a loading time of 0.1 s (left); with a loading time of 1 s (right). **Remark**: herein, Numerical data_0.1s_30s and Numerical data_1s_30s are the numerical simulation results with the parameters identified from the single step relaxation test with a loading time of 0.1 s and 30 s, respectively.

the relaxation test with a loading time of 1 s is preferred except the force at the maximum displacement. A deviation of 17% at this point can be seen from Fig. 9. Fig. 9, right, shows the comparable results of the relaxation test with a loading time of 1 s. The matches between the virtual experimental data and the numerical data obtained with both loading cases in Fig. 7 are great. According to the traditional way of judgement, we are confident to point out that the parameters identified from the two relaxation test should be accurate. However, the relative errors of the re-identified parameters listed in Table 2 yield a contrary conclusion. In the relaxation test with a loading time of 0.1 s, the shear moduli μ, μ_e^1, and μ_e^2 and the relaxation time r^1 are perfectly identified. But the other three parameters are worse identified especially that the deviation of μ_e^3 is as high as 121.60%. In the relaxation test with a loading time of 1 s, three parameters are accurately identified: the shear moduli μ, μ_e^2, and the relaxation time r^2. The worst identified parameter is μ_e^1 in this case the re-identified value is 147.04% greater than the chosen value. Similar points can be concluded from the identified results of these two relaxation tests: a) the shear modulus μ is perfectly identified using both tests; b) the parameters of the Maxwell elements with the relaxation time in the same scale of the loading time are accurately identified, e. g. μ_e^1 and r^1 in the case with a loading time of 0.1 s, μ_e^2, and r^2 in the case with a loading time of 1 s; c) the parameters in the third Maxwell element can not be accurately identified due to the large relaxation time compared with the loading time. Therefore, it seems that the identification of the shear moduli μ_e^j and the relaxation times r^j of the Maxwell elements are strongly dependent on the loading part of the relaxation tests. The shear modulus μ of the extra spring is closely connected to the degree of the relaxation at the end of the test. It is still necessary to answer the following question: Why can the match between the virtual experimental results and the numerical data shown in Fig. 9 be so good even if the identified material parameters differ. The reason may be the sensitivity of the reaction force of nanoindentation with respect to the model parameters which are different in various loading histories [7]. These worse identified parameters have only a slight contribution to the reaction force due to a small sensitivity. Therefore, the error contribution can be neglected. In Table 2, the sum of the shear moduli in the relaxation test with a loading time of 0.1 s is nearly 40% smaller than the sum in the test with a loading time of 1 s. This should be the reason of the deviation of 17% in the left diagram of Fig. 9.

The monotonic loading history contains seven single step relaxations with a loading time of 1 s and a 20 s holding stage as shown in Fig. 8, left. Fig. 10, left shows an extremely good match between the experimental data and the numerical simulation using the same monotonic loading history. Indeed, if the simulation is performed with the parameters identified from both single step relaxation tests, the deviation is still acceptable. In contrast to that, the relative errors of the parameters identified from monotonic testing in Table 2 show absolutely not an optimistic result for all of the seven parameters compared with the chosen values. The basic elasticity is accurately captured by the monotonic testing. Although the monotonic test is composed with several single step relaxations, the identification results of monotonic testing is really different from the results of the single step relaxation. Fig. 10, left shows that the last two single step relaxation processes are strongly dependent on the basic elastic parameter μ.

The sinusoidal oscillatory test is performed with a 10 s ramping stage up to the maximum displacement 5 μm followed with a 20 s sinusoidal oscillatory loading. The sine function is designed with a frequency of 2 Hz and with an amplitude of 0.1 μm. The comparison between the experimental data and the numerical results is presented by the diagram in Fig. 10,

Table 2 Re-identified parameters and their deviations compared with the chosen values for viscoelastic model being used. **Remark**: numbers in bold and italic font are those, whose absolute value is smaller than 20%.

Parameters	μ	μ_e^1	μ_e^2	μ_e^3	r^1	r^2	r^3
Chosen	1.3 MPa	0.8 MPa	0.4 MPa	0.1 MPa	0.2s	3s	100s
Bounds	[0.01;10]	[0.01;10]	[0.01;10]	[0.01;10]	[0.01;50]	[0.01;50]	[0.01;200]
Relax ($T_{load} = 0.1$s)	1.2325	0.7435	0.4030	0.2216	0.1869	2.0467	49.2780
	-5.19%	*-7.06%*	*+0.75%*	+121.60%	*-6.55%*	-31.78%	-50.72%
Relax ($T_{load} = 1$s)	1.2596	1.9763	0.4764	0.1732	0.0461	2.7307	58.9804
	-3.11%	+147.04%	*+19.10%*	+73.20%	-76.95%	*-8.98%*	-41.02%
Monotonic	1.3238	0.3582	0.5762	0.1066	0.1857	1.6686	42.8211
	+1.83%	-55.23%	+44.05%	*+6.60%*	*-7.15%*	-44.38%	-57.18%
Oscillatory	1.2397	0.5914	0.4971	0.1536	0.2038	1.3184	64.0938
	-4.64%	-26.08%	+24.28%	+53.60%	*+1.90%*	-56.05%	-35.91%
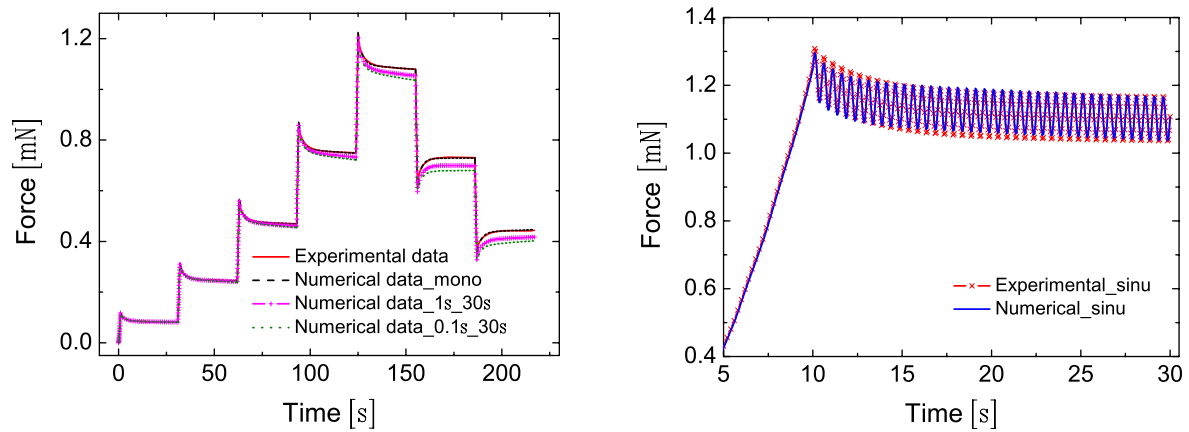
Fig. 10 (online colour at: www.zamm-journal.org) Comparison of the experimental data with numerical simulation: monotonic testing (left); sinusoidal oscillatory testing (right). **Remark**: herein, Numerical_mono and Numerical_sinu are numerical data obtained with the parameters identified from monotonic and sinusoidal oscillatory testing, respectively.

right. These two curves overlap each other. A similar good result can also be seen in Table 2 except the identified value of μ_e^3 and r^2. Compared with the single step relaxation and the monotonic testing, the identified parameters by using the sinusoidal oscillatory loading history yields more harmonious results. The identified value of the longest relaxation time r^3 is much better than the results in other loading histories.

A brief summary can be made for this subsection: The parameters to be identified of the used viscoelastic model can be split into two sets. One set contain the shear modulus μ of the extra spring governed by the basic elasticity. The other part contains the shear moduli μ_e^j and the relaxation times r^j of the Maxwell elements governed by the viscoelastic behaviour. Usually, the basic elasticity can be captured with a single step relaxation test with a sufficient long holding time. However, for the real polymers with a relaxation time of several months, it is effective to use the monotonic testing to approximate the basic elasticity. To identify the parameters of the Maxwell elements, a relaxation procedure with a suitable loading time can be chosen.

4 Conclusions

In review of the literature, nanoindentation is a powerful potential testing technique for thin films. However, its comprehensive application in viscoelastic polymer layers is restricted due to the lack of a reliable analysis method to get the rate-dependent properties. In this paper, to capture the viscoelastic properties from nanoindentation, the inverse method is

used combining finite element modelling and numerical optimisation. The concept of parameter re-identification allows us to investigate how accurate the parameters can be identified from the nanoindentation force-displacement response.

Firstly, the rate-dependent viscous dissipation is investigated by displacement and force control with various loading rates. The relaxation or creep behaviour is presented by different loading histories: single step relaxation or creep, monotonic and oscillatory testing. It is found that in the same displacement range the response of the force under displacement control is more sensitive with respect to the various loading histories. Secondly, the parameters' identification of the chosen viscoelastic model from nanoindentation is performed with various loading histories. The accuracy of parameter identification is dependent on the loading history used in the experiment and numerical modelling. Considering the viscoelastic model used here, it is better to capture the basic elasticity using monotonic testing first. The viscoelastic parameters of the Maxwell elements in parallel can be efficiently identified by some single step relaxation test with a suitable loading time. A sinusoidal oscillatory testing, performed in the present study, seems to be useful to identify the elastic and viscoelastic parameters at one time. Some questions about identification are still to be answered. It is difficult to identify each parameter exactly for a multi-parameters model, especially if there are several parameters acting in parallel, e. g. the shear moduli μ_e^j and the relaxation times r^j of each Maxwell element. An exact match between the experimental data and the prediction of the numerical model does not guarantee the accurate identification of each parameter. In this case, the combination of several loading histories as well as different tests of various deformation forms may be taken into account. The choice of the loading history and testing method depends on the experimental data and practical experience. This is the main task in our future work in nanoindentation of polymers. The parameters identification in the nanoindentation problem of polymer layers with viscoelastic model for finite deformation will be documented in an upcoming paper. The surface interactions e. g. friction and adhesion will be considered. Based on the real experimental and numerical investigation of nanoindentation, the questions which remain in this paper are expected to be answered in the upcoming paper.

References

[1] Abaqus 6.10 Analysis User's Manual (https://www.sharcnet.ca/Software/Abaqus610/Documentation/docs/v6.10/books/usb/default.htm, 2011).

[2] M. R. Ahmad, M. Nakajima, S. Kojima, M. Homma, and T. Fukuda, Methods to Measure Material Viscoelactic Properties Using Sharp, Flat and Buckling Tips Inside ESEM, in: 8th IEEE Conference on Nanotechnology, (IEEE Xplore, New York, 2008), pp. 857–860.

[3] K. Balasundaram, Y. P. Cao, and D. Raabe, Identifying the Limitation of Oliver and Pharr Method in Characterizing the Viscoelastic-Plastic Materials with Respect to Indenter Geometry, in: Nano- and Microscale Properties and Behavior under Extreme Environments, edited by A. Misra, T. J. Balk, H. Huang, M. J. Caturla, and C. Eberl, Mater. Res. Soc. Symp. Proc. Vol. 1137E, 1137-EE10-23 (Warrendale, PA, 2009).

[4] H. G. Beyer, The Theory of Evolution Strategy (Springer, Berlin, Heidelberg, 2001).

[5] B. J. Briscoe, L. Fiori, and E. Pelillo, Nano-indentation of polymeric surfaces, J. Phys. D, Appl. Phys. **31**, 2395–2404 (1998).

[6] Y. P. Cao, D. C. Ma, and D. Raabe, The use of flat punch indentation to determine the viscoelastic properties in the time and frequency domains of a soft layer bonded to a rigid substrate, Acta Biomaterialia **5**, 240–248 (2009).

[7] Z. Chen and S. Diebels, Nanoindentation of hyperelastic polymer layers at finite deformation and parameter re-identification, Arch. Appl. Mech. DOI 10.1007/s00419-012-0613-9, pp. 1–16 (2011).

[8] Z. Chen, S. Diebels, and J. Schmitt, Frictional Nanoindentation of Hyperelastic Polymer Layers: A Numerical Study, Proceedings of the 3rd ECCOMAS Thematic Conference on the Mechanical Response of Composites (Leibniz Universität Hannover, Institut of Structural Anlaysis, Hannover, Germany, 2011), pp. 229–236

[9] L. Cheng, X. Xia, L. E. Scriven, and W. W. Gerberich, Spherical-tip indentation of viscoelastic material, Mech. Mater. **37**, 213–226 (2005).

[10] L. Cheng, X. Xia, W. Yu, L. E. Scriven, and W. W. Gerberich, Flat-punch indentation of viscoelastic material, J. Polym. Sci. B, Polym. Phys. **38**, 10–22 (2000).

[11] Y. T. Cheng and C. M. Cheng, Relationships between initial unloading slope, contact depth, and mechanical properties for spherical indentation in linear viscoelastic solids, J. Mater. Res. **20**, 1046–1054 (2005).

[12] Y. T. Cheng and C. M. Cheng, Relationship between contact stiffness, contact depth, and mechanical properties for indentation in linear viscoelastic solids using axisymmetric indenters, Struct. Control Health Monit. **13**, 561–569 (2006).

[13] T. Chudoba and F. Richter, Investigation of creep behaviour under load during indentation experiments and its influence on hardness and modulus results, Surf. Coat. Technol. **148**, 191–198 (2001).

[14] B. D. Coleman and W. Noll, The thermodynamics of elastic materials with heat conduction and viscosity, Arch. Ration. Mech. Anal. **42**, 167–178 (1963).

[15] J. D. Ferry, Viscoelastic Properties of Polymers (John Wiley & Sons, New York, America, 1980).

[16] A. C. Fischer-Cripps, Nanoindentation (Springer, New York, 2004).

[17] A. E. Giannakopoulos, Elastic and viscoelastic indentation of flat surface by pyramid indenters, J. Mech. Phys. Solids **54**, 1305–1332 (2006).

[18] G. A. C. Graham, The contact problem in the linear theory of viscoelasticity, Int. J. Eng. Sci. **3**, 27–46 (1965).

[19] G. A. C. Graham, The contact problem in the linear theory of viscoelasticity when the time dependent contact area has any number of maxima and minima, Int. J. Eng. Sci. **5**, 495–514 (1967).

[20] S. Guessasma, M. Sehaki, D. Lourdin, and A. Bourmaud, Viscoelasticity properties of biopolymer composite material determined using finite element calculation and nanoindentation, Comput. Math. Sci. **44**, 371–377 (2008).

[21] S. Hartmann, Computation in finite-strain viscoelasticity: finite elements based on the interpretation as differential-algebraic equations, Comput. Methods Appl. Mech. Eng. **191**, 1439–1470 (2002).

[22] S. Hartmann, J. Gibmeier, and B. Scholtes, Experiments and material parameter identification using finite elements. Uniaxial tests and validation using instrumented indentation tests, Exp. Mech. **46**, 5–18 (2006).

[23] P. Haupt, Continuum Mechanics and Theory of Materials (Springer, Berlin, 2000).

[24] J. L. Hay, M. E. O. Hern, and W. C. Oliver, The importance of contact radius for substrate-independent properties measurement of thin films, Mat. Res. Soc. Symp. Proc. **522**, 27–32 (1998).

[25] G. A. Holzapfel, On large strain viscoelasticity: Continuum formulation and finite element applications to elastomeric structures Int. J. Numer. Methods Eng. **39**, 3903–3926 (1996).

[26] G. A. Holzapfel, Nonlinear Solid Mechanics: A Continuum Approach for Engineering (John Wiley & Sons Ltd, UK, 2001).

[27] G. A. Holzapfel and J. C. Simo, A new viscoelastic constitutive model for continuous media at finite thermomechanical changes, Int. J. Solids Struct. **33**, 3019–3034 (1996).

[28] G. Huang and H. Lu, Measurement of two independent viscoelastic functions by nanoindentation, Exp. Mech. **47**, 87–98 (2007).

[29] N. Huber, W. D. Nix, and H. Gao, Identification of elastic-plastic material parameters from pyramidal indentation of thin films, Proc. R. Soc. Lond. A **458**, 1593–1620 (2002).

[30] N. Huber and C. Tsakmakis, Finite deformation viscoelasticity laws, Mech. Mater. **32**, 1–18 (2000).

[31] N. Huber and E. Tyulyukovskiy, A new loading history for identification of viscoplastic properties by spherical indentation, J. Mater. Res. **19**, 101–113 (2004).

[32] S. A. Hutcheson and G. B. McKenna, Nanosphere embedding into polymer surfaces: A viscoelastic contact mechanics analysis, Phys. Rev. Lett. **94**, 4 (2005).

[33] A. Jäger and R. Lackner, Identification of viscoelastic properties by means of nanoindentation taking the real tip geometry into account, Meccanica **42**, 293–306 (2007).

[34] M. Johlitz, H. Steeb, S. Diebels, A. Chatzouridou, J. Batal, and W. Possart, Experimental and theoretical investigation of nonlinear viscoelastic polyurethane systems, J. Mater. Sci. **42**, 9894–9904 (2007).

[35] K. L. Johnson, Contact Mechanics (Cambridge University Press, Cambridge, 1985).

[36] M. Kaliske and H. Rothert, Formulation and implementation of three-dimensional viscoelasticity at small and finite strains, Comput. Mech. **19**, 228–239 (1997).

[37] D. Klötzer, C. Ullner, E. Tyulyukovskiy, and N. Huber, Identification of viscoplastic material parameters from spherical indentation data. Part II: Experimental validation of the method, J. Mater. Res. **21**, 677–684 (2006).

[38] M. V. R. Kumar and R. Narasimhan, Analysis of spherical indentation of linear viscoelastic materials, Curr. Sci. **87**, 1088–1095 (2004).

[39] E. H. Lee and J. R. M. Radok, The contact problem for viscoelastic bodies, J. Appl. Mech. **30**, 438–444 (1960).

[40] M. Lichinchi, C. Lenardi, J. Haupt, and R. Vitali, Simulation of Berkovich nanoindentation experiments on thin films using finite element method, Mech. Mater. **42**, 278–286 (1998).

[41] A. Lion, A constitutive model for carbon black filled rubber: Experimental investigations and mathematical representation, Contin. Mech. Thermodyn. **8**, 153–169 (1996).

[42] A. Lion, Thixotropic behaviour of rubber under dynamic loading histories: Experiments and theory, J. Mech. Phys. Solids **46**, 895–930 (1998).

[43] C. K. Liu and S. Lee, Load-displacement relations for nanoindentation of viscoelastic material, J. Appl. Phys. **100**, 503–512 (2006).

[44] H. B. Lu, B. Wang, J. Ma, G. Huang, and H. Viswanathan, Measurement of creep compliance of solid polymers by nanoindentation, Mech. Time-Depend. Mater. **7**, 189–207 (2003).

[45] J. Lubliner, A model of rubber viscoelasticity, Mech. Res. Commun. **12**, 93–99 (1985).

[46] J. Nocedal and S. J. Wright, Numerical Optimization (Springer, New York, 1999).

[47] W. C. Oliver and G. M. Pharr, An improved technique for determining hardness and elastic modulus using load and displacement sensing indentation experiments, J. Mater. Res. **7**, 1564–1583 (1992).

[48] W. C. Oliver and G. M. Pharr, Measurement of hardness and elastic modulus by instrumented indentation: Advance in understanding and refinements to methodology, J. Mater. Res. **19**, 3–20 (2004).

[49] M. L. Oyen, Analytical techniques for indentation of viscoelactic materials, Philos. Mag. **86**, 5625–5641 (2006).

[50] M. L. Oyen, Sensitivity of polymer nanoindentation creep measurements to experimental variables, Acta Mater. **55**, 3633–3639 (2007).

[51] G. Rauchs, Optimization-based material parameter identification in indentation testing for finite strain elasto-plasticity, Z. Angew. Math. Mech. **86**, 539–562 (2006).

[52] G. Rauchs and j. Bardon, Identification of elasto-viscoplastic material parameters by indentation testing and combined finite element modelling and numerical optimization, Fin. Elem. Anal. Design **47**, 653–667 (2011).

[53] G. Rauchs, J. Bardon, and D. Georges, Identification of the material parameters of a viscous hyperelastic constitutive law from spherical indentation tests of rubber and validation by tensile tests, Mech. Mater. **42**, 961–973 (2010).

[54] S. Reese and S. Govindjee, A theory of finite viscoelasticity and numerical aspects, Int. J. Solids Struct. **35**, 3455–3482 (1997).

[55] J. S. Bergström and M. C. Boyce, Constitutive modelling of the large strain time-dependent behavior of elastomers, J. Mech. Phys. Solids **46**, 931–954 (1998).

[56] F. R. Schwarzl, Numerical calculation of storage and loss modulus from stress relaxation data for linear viscoelastic materials, Rheol. Acta **10**, 165–173 (1971).

[57] H. P. Schwefel, Evolution and Optimum Seeking (Wiley, New York, 1995).

[58] K. Sedlan, Viskoelastisches Materialverhalten von Elstomerwerkstoffen: Experimentelle Untersuchung und Modellbildung (Dissertation, Universität Gesamthochschule Kassel, 2000).

[59] T. C. T. Ting, The contact stresses between a rigid indenter and a viscoelastic half-space, J. Appl. Mech. **33**, 845–854 (1966).

[60] T. C. T. Ting, Contact problems in the linear theory of viscoelasticity, J. Appl. Mech. **35**, 248–254 (1968).

[61] A. V. Tobolsky, Stress relaxation studies of the viscoelastic properties of polymers, J. Appl. Phys. **27**, 673–685 (1956).

[62] D. Tranchida and S. Piccarolo, On the use of the nanoindentation unloading curve to measure the Young's modulus of polymers on a nanometer scale, Macromol. Rapid Commun. **26**, 1880–1804 (2005).

[63] D. Tranchida, S. Piccarolo, J. Loos, and A. Alexee, Mechanical characterization of polymers on a nanometer scale through nanoindentation. A study on pile-up and viscoelasticity, Macromolecules **40**, 1259–1267 (2007).

[64] E. Tyulyukovskiy and N. Huber, Identification of viscoplastic material parameters from spherical indentation data. Part I: Neural networks, J. Mater. Res. **21**, 664–676 (2006).

[65] M. R. Vanlandingham and N. K. Chang, Viscoelastic characterization of polymers using instrument indentation. Quasi-static testing, J. Polym. Sci., Part B, Polym. Phys. **43**, 1794–1811 (2005).

[66] H. F. Wang and H. Bangert, Three-dimensional finite element simulation of vickers indentation on coated systems, Mater. Sci. Eng. A **163(1)**, 43–50 (1993).

[67] P. Wriggers, Computational Contact Mechanics (Springer-Verlag, Berlin, Heidelberg, Netherlands, 2006).

Frictional Nanoindentation of Hyperelastic Polymer Layers: A Numerical Study

Frictional Nanoindentation of Hyperelastic Polymer Layers: A numerical study

Z. Chen[1], S. Diebels[2], J. Schmitt[3]

[1] *Saarland University, Chair of Applied Mechanics, Germany; zh.chen@mx.uni-saarland.de*
[2] *Saarland University, Chair of Applied Mechanics, Germany; s.diebels@mx.uni-saarland.de*
[3] *Saarland University, Chair of Applied Mechanics, Germany; jo.schmitt@mx.uni-saarland.de*

1 Introduction

Nanoindentation became a popular and powerful testing technique in the field of thin layers such as coatings and thin films. The goal of nanoindentation is to estimate the hardness and elastic modulus from the force-displacement curve according to the Oliver & Pharr method [1, 2], which is widely employed to metals and alloys. However, to date nanoindentation is restricted to widely be used for soft polymer layers with non-linear elastic as well as viscoelastic properties. The developed semi-analytical solution has limitations such as linear elastic and plastic, rate-independent and small deformation. A reliable analysis method is still missing. Our work is to create a robust method to determine the non-linear elastic and viscoelastic properties from the indentation force-displacement curve based on an inverse method [3, 4]. Therefore, the virtual experiment of nanoindentation of polymer layers is simulated with ABAQUS®. The parameters of the chosen material models are identified using the numerical stochastic optimisation strategy based on the principle of biological evolution, e.g. an evolution strategy. In order to investigate how accurate the material parameters can be determined from the numerical optimisation routine, the numerical data obtained from the virtual experiment with the chosen parameters replace the real experimental measurements. That procedure is called parameter re-identification and is also used in [5, 6].

As shown in our earlier work [7], the nanoindentation of hyperelastic layers remains a problem in parameter identification. If the indentation depth is within 5% of the layer thickness, the influence of the substrate on the force-displacement data is negligible. Nevertheless, in this case, the parameter coupling of the Mooney-Rivlin model and Yeoh model is critical. The sensitivity of the force with respect to those parameters increases with the increment of the displacement, which motivates us to enlarge the indentation depth to identify the parameters more accurately. Because the substrate influences on the force-displacement data, we assume that the material of substrate is known. As the penetration depth approaches the substrate, the hard substrate plays a significant role as a fixed ground to the layer, leading to a relative tangential motion between the indenter and layer. In this case, the effect of friction should be noticeable. Therefore, in this work, the classical Coulomb's law is used to model the friction between the indenter and the polymer layer.

2 Virtual experiment of nanoindentation

The nanoindentation of polymer layers on a substrate is simulated numerically using ABAQUS®. The numerical implementation contains two parts: the hyperelastic material models and the finite element model of nanoindentation BVP. From this point of view, ABAQUS® can be considered as our virtual

laboratory.

2.1 Material models

The behaviour of many real polymer materials shows non-linear elasticity. Therefore, models based on a hyperelastic approach with a particular strain energy function proposed e. g. by Ogden, Rivlin, Mooney and Yeoh [8, 9, 10, 11] are often used in the literature to model finite elastic properties of polymers. Then we restrict attention to isotropic and incompressible hyperelastic material models e. g. the Mooney-Rivlin model and the Yeoh form, under isothermal regime, i. e. so called perfectly elastic material models. Such hyperelastic models can well represent the behaviour of the solid polymeric materials [13, 12]. In the present study the viscoelastic contributions are not taken into account. So the strain energy Ψ of the incompressible hyperelastic material ($I_{3C} = I_{3B} = 1$) can be written as

$$\Psi = \hat{\Psi}(I_{1C}, I_{2C}) = \hat{\Psi}(I_{1B}, I_{2B}). \tag{1}$$

$I_i (i = 1, 2, 3)$ are the principle invariants of right Cauchy Green strain tensor $\mathbf{C} = \mathbf{F}^{\mathbf{T}} \cdot \mathbf{F}$ and the left Cauchy Green strain tensor $\mathbf{B} = \mathbf{F} \cdot \mathbf{F}^{\mathbf{T}}$. With the relations $\overline{\mathbf{T}} = 2\partial \Psi(\mathbf{C})/\partial \mathbf{C}$ and $\mathbf{T} = J^{-1}\mathbf{F}\overline{\mathbf{T}}\mathbf{F}^{\mathbf{T}}$ as well as the Lagrange multiplier method associated with incompressible hyperelastic materials, the 2. Piola-Kirchhoff stress tensor $\overline{\mathbf{T}}$ and the Cauchy stress tensor $\mathbf{T}$ can be derived as (details see e. g. [12])

$$\overline{\mathbf{T}} = -p\mathbf{C}^{-1} + 2\frac{\partial \Psi(\mathbf{C})}{\partial \mathbf{C}} = -p\mathbf{C}^{-1} + 2\frac{\partial \Psi}{\partial I_{1C}}\mathbf{I} + 2\frac{\partial \Psi}{\partial I_{2C}}(I_{1C}\mathbf{I} - \mathbf{C}), \tag{2}$$

$$\mathbf{T} = -p\mathbf{I} + 2\mathbf{B}\frac{\partial \Psi(\mathbf{B})}{\partial \mathbf{B}} = -p\mathbf{I} + 2\frac{\partial \Psi}{\partial I_{1B}}\mathbf{B} + 2\frac{\partial \Psi}{\partial I_{2B}}\mathbf{B}^{-1}. \tag{3}$$

They are split into one part governed by the hydrostatic pressure p and a second part governed by the deformation of the material. The strain energy functions of the Mooney-Rivlin model and the Yeoh form are

$$\Psi_{MR} = C_{10}(I_{1C} - 3) + C_{01}(I_{2C} - 3), \tag{4}$$

$$\Psi_{Y} = C_{10}(I_{1C} - 3) + C_{20}(I_{1C} - 3)^2 + C_{30}(I_{1C} - 3)^3. \tag{5}$$

The substrate is assumed to be a stiff elastic material with Hooke's law. The chosen parameters of the polymer layers and of the substrate, respectively, are listed in Table 1.

Table 1: Material parameters

	Mooney-Rivlin model			Yeoh model		
Polymer layers	C_{10}(MPa)	C_{01}(MPa)	$C_{10} + C_{01}$(MPa)	C_{10}(MPa)	C_{20}(MPa)	C_{30}(MPa)
	0.1640	0.4873	0.6513	0.6513	0.2587	0.1275
	Substrate	E = 4516.8(MPa)		$\nu = 0.3$		

2.2 FE model of nanoindentation with friction

Spherical indenters show increasing popularity as these types of indenters are particularly suitable for measuring properties of soft materials and for replicating contact damage in in-service conditions [14]. The virtual experiment of spherical nanoindentation can be modelled in an axisymmetric two-dimensional finite element model e. g. in ABAQUS® 6.10.
We define the indenter as an analytical rigid surface, in such a way that the indenter geometry can be modeled exactly with a smooth curve. In view of the contact problem and incompressible property of the polymer layer, quadrilateral element types CAX4 and CAX4H are used for the substrate and the
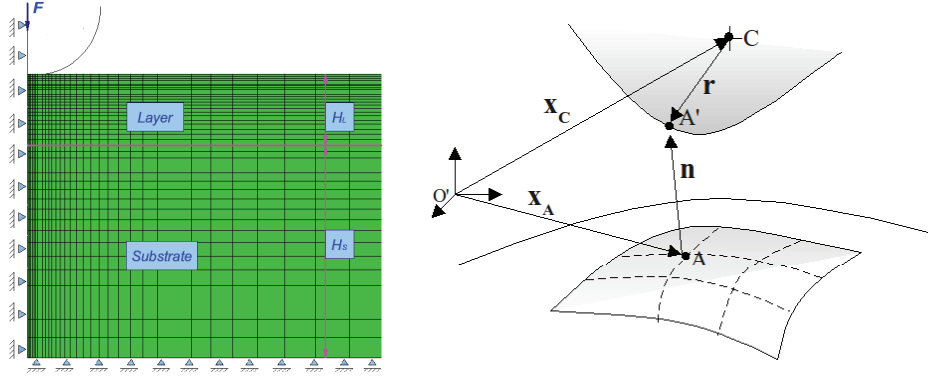
Figure 1: Sketch of the geometry and boundary condition and the mesh of the FEM model (left), a contact interface geometry between a deformable and a rigid body (right)

layer respectively. To account for the localised deformation of the layer, it is essential that the density of nodes close to the contact region is high enough. The geometry and boundary conditions of the spherical nanoindentation are illustrated in Fig. 1 left. The basic principle of this model is the same like the FEM model in [7] which has been verified with the widely accepted Sneddon's analytical solution [15] .

The BVP of indentation contains contact between a rigid body (indenter) and a deformable body (polymer layer). As shown in Fig. 1 right, A is a point on the deforming mesh with current coordinate $\mathbf{x}_A$. C is the reference point of the rigid body with current coordinates $\mathbf{x}_C$. A' is the closest point on the surface of the rigid body to A, the normal direction $\mathbf{n}$ of the rigid surface at A' passes through A. The formulation of non-penetration is used to impose the contact constraints in the normal direction, for details please see [16]. In this case, the normal contact pressure cannot be calculated from a constitutive equation. But it is then obtained as a reaction in the contact area. Hence the contact pressure can be deduced from the constraint equations with the often used Lagrange multiplier method or the Penalty method. If the point A is known, we can define the inequality constraint of the non-penetration condition

$$g_N = (\mathbf{x}_C + \mathbf{r} - \mathbf{x}_A) \cdot \mathbf{n} \geq 0. \tag{6}$$

In the case of active constraint set one has $g_N = 0$. If there is a gap between the two bodies, then the conditions $g_N > 0$ holds.

The friction effect between the indenter and the polymer layer is related with the tangential contact, for details please see [16] chapter 6. Two cases in the contact interfaces are considered. Stick holds in the case that the relative tangential velocity is zero, i. e. $\dot{\mathbf{g}}_T = 0 \Leftrightarrow \mathbf{g}_T = 0$, where $\mathbf{g}_T$ denotes the relative displacement in a tangential direction. As soon as the tangential forces are larger than a limit value then the contacting interfaces no longer stick to each other, but move relative to each other. This phenomenon is called sliding, and can be described with the Coulomb law as

$$\mathbf{t}_T = -\mu|p_N|\frac{\dot{\mathbf{g}}_T}{\|\dot{\mathbf{g}}_T\|}, \quad \text{if } \|\mathbf{t}_T\| > \mu|p_N|. \tag{7}$$

Here μ denotes the friction coefficient. It depends upon several parameters like the sliding velocity $\dot{\mathbf{g}}_T$, the normal contact pressure p_N, the surface roughness and the temperature [16].

The weak form of the contact boundary value problem is the minimisation of the total energy of the two bodies in contact

$$\Pi = \sum_{\gamma=1}^{2} \left\{ \int_{\beta^\gamma} \left[(\overline{\mathbf{T}} : \mathbf{E})^\gamma - \rho_0 \mathbf{b}^\gamma \cdot \mathbf{u}^\gamma \right] dV - \int_{\partial\beta_\sigma^\gamma} \mathbf{t}^\gamma \cdot \mathbf{u}^\gamma dA \right\} + \Pi_c \Rightarrow \text{MIN}. \tag{8}$$

Herein $\mathbf{u}^\gamma$ denotes the deformation of both bodies. The contributions due to the contact constraints are enclosed in Π_c. Once the active set of constraints of the contact interface is known, then the weak form can be written as

$$\delta\Pi = \sum_{\gamma=1}^{2} \left\{ \int_{\beta^\gamma} \left[(\overline{\mathbf{T}} \cdot \delta\mathbf{E})^\gamma - \rho_0 \mathbf{b}^\gamma \cdot \delta\mathbf{u}^\gamma \right] dV - \int_{\partial\beta_\sigma^\gamma} \mathbf{t}^\gamma \cdot \delta\mathbf{u}^\gamma dA \right\} + C_c = 0 \tag{9}$$

where C_c are the contact contributions associated with the active constraint set. $\delta \mathbf{u}^\gamma$ is the so called virtual displacement, which is zero at the boundary $\partial \beta_{\mathbf{u}}^\gamma$ where the deformations are prescribed. The contact contributions Π_c can be formulated using the Lagrange multiplier method as

$$\Pi_c^{LM} = \int_{\Gamma_c} (\lambda_N g_N + \lambda_T \cdot \mathbf{g}_T) \, dA, \tag{10}$$

where λ_N and λ_T are the Lagrange multiplier, g_N and $\mathbf{g}_T$ are the normal gap functions. The variation of Π_c then leads to the constraint formulation

$$C_c^{LM} = \int_{\Gamma_c} (\lambda_N \delta g_N + \lambda_T \cdot \delta \mathbf{g}_T) \, dA + \int_{\Gamma_c} (\delta \lambda_N g_N + \delta \lambda_T \cdot \mathbf{g}_T) \, dA. \tag{11}$$

The first integral in eq. (11) is related to the virtual work of the Lagrange multiplier along the variation of the gap function. The second one describes the enforcement of the constraints. λ_N can be identified as the contact pressure p_N, δg_N is the variation of the normal gap. In the case of pure stick, $\mathbf{g}_T$ is zero. This yields the tangential constraint formulation, then $\lambda_{\mathbf{T}}$ can be obtained as a reaction. If sliding takes place, the tangential stress vector t_T is determined by the Coulomb law i. e. eq. (7). The constraint formulation should be replaced as

$$C_c^{slid} = \int_{\Gamma_c} (\lambda_N \delta g_N + \mathbf{t}_T \cdot \delta \mathbf{g}_T) \, dA + \int_{\Gamma_c} \delta \lambda_N g_N dA. \tag{12}$$

3 The influence of friction

The friction effect between the rigid diamond indenter and the soft polymer is a topic of considerable interest. This effect is complicated, because the friction depends on various parameters such as viscosity, sliding velocity, surface roughness and the material properties [16, 17]. The reason is associated with the very low elastic modulus of the polymer and with the high internal friction exhibited by a polymer in a wide frequency range [17]. In this paper, the classical Coulomb friction law is used to simplify the numerical computation. That means the friction coefficient is assumed to be a constant value and the tangential force is proportional to the normal contact pressure. We focus on the influence of friction on the force-displacement curves. Note that in the case of indentation of a layer on a substrate, the influence of the substrate potentially increases the normal contact pressure. At the begining, the influence of the friction is investigated by varying the value of the friction coefficient. The force-displacement curves
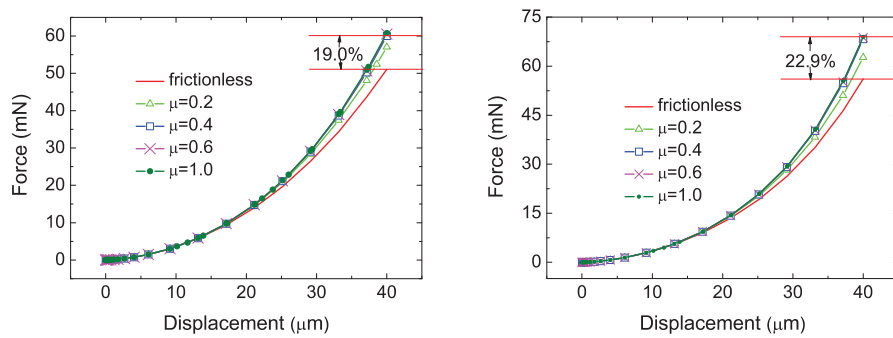
Figure 2: The influence of the friction on the force-displacement with variation of μ. Mooney-Rivlin (left), Yeoh model (right)

of the Mooney-Rivlin model (Fig. 2 left) and the Yeoh model (Fig. 2 right) show that the friction has a strong effect on force-displacement curves if the penetration depth is large. The friction increases the force more if the penetration depth becomes deeper. Fig. 2 shows that, if the ratio of displacement to the

layer thickness is 40%, the required force increases about 20% compared to the frictionless case. In the other case, if the displacement is restricted to 5% of the layer thickness, the influence of the friction can be neglected. A series value is employed which varies from 0 to 1.0 of friction coefficient is employed. It seems that the influence of the friction does not change with various value of μ if it is larger than 0.4.
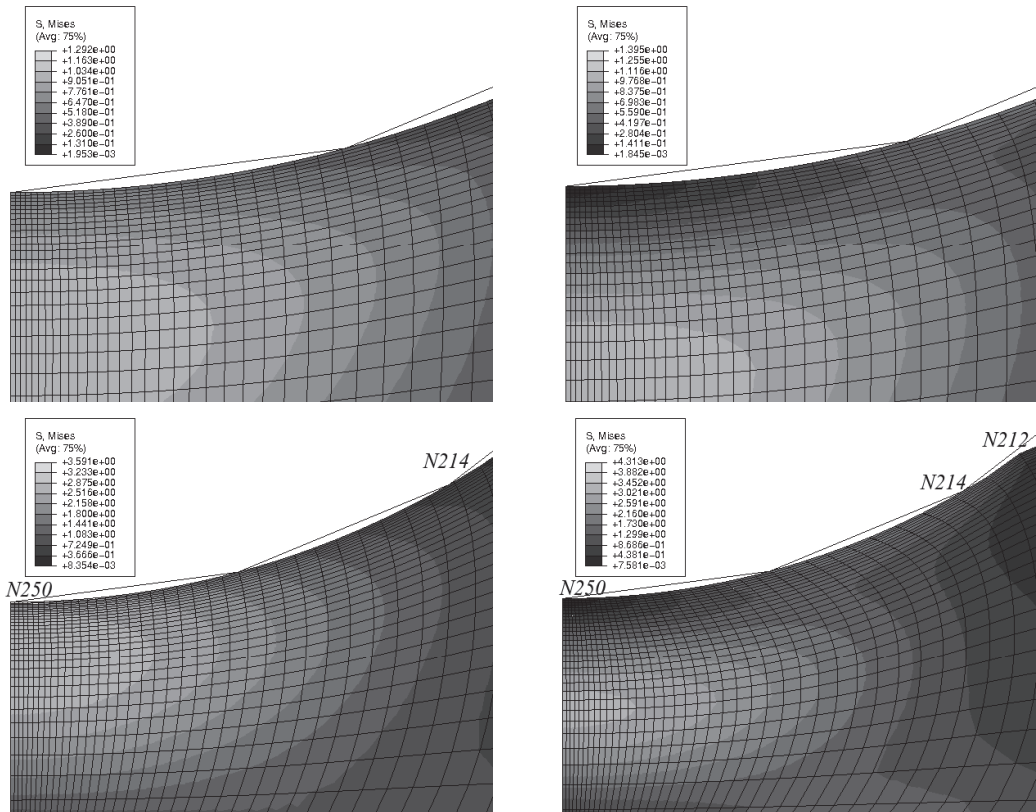
Figure 3: Plot of the deformed mesh without friction (left side) and with friction (right side) under different ratio of displacement to the layer thickness: 20% (top), 40% (bottom)

In the case of elastic frictional contact with small deformation, analytical and numerical investigations showed, that the influence of friction plays a negligible role, e. g. [21]. However, this is not true in the case of finite elastic frictional contact. The deformed mesh and the local distribution of the von Mises stress beneath the indenter obtained from finite element computation is presented in Fig 3. The results of different displacements are compared vertically, while those with or without friction are compared transversely. It is obvious that the influence of friction on the distribution of the stress increases if the penetration depth becomes deeper. Therefore, the distribution of the contact pressure on the contact interface should also be changed due to friction. Attention should be paid to the variation of the contact area, which is of great importance if the semi-analytical solutions are used to determine the hardness and the elastic modulus. Thanks to the numerical simulation, the variation of the contact area due to friction effect can be quantified explicitly. With the command "COPEN", we can obtain the contact state of the nodes during the post-processing in ABAQUS®. As shown in Fig 3 at larger displacement, the nodes beneath the indenter are numbered varying from $N250$ to $N192$ with a increment of -1. In the case of frictionless contact, the node $N214$ is in the edge of the contact area. Otherwise the node $N212$ is the last element of the contact area. Because relative tangential slip takes place in the frictional contact, a new contact area is found containing another two elements. It is easier to calculate that the contact area increases about 19% due to the friction effect, after we get the coordinates of those nodes in the current configuration. Unlike indentation test with viscoelastic or plastic material, in this case, the increment of the contact area is only related to the friction dissipation.

233
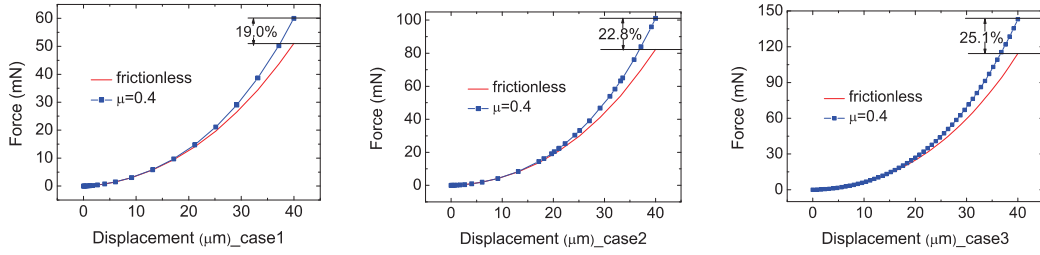
Figure 4: The influence of the friction on the force-displacement with variation of R/H_L: case 1 (left), case 2 (middle), case 3 (right)

If the dimension of the spherical indenter and the layer thickness is in the same scale, it can be expected that there should be some relations between the radius of the indenter (R) to the layer thickness (H_L) and the influence of friction. Therefore, three cases namely case 1, case 2 and case 3 are considered, their values of R/H_L are 1.0, 1.5 and 2.0 respectively. Fig. 4 shows that the influence of the friction is stronger with a larger value of R/H_L. In other words, a relatively smaller spherical indenter should be chosen if it is expected to decrease the influence of friction.

4 Parameter re-identification

If the virtual experiment of nanoindentation is displacement-controlled, the obtained experimental data $\mathbf{F}^{exp}$ is the vector of the reaction force obtained at each displacement increment with a chosen set of material parameters. The parameter re-identification is performed with MATLAB® optimisation toolbox combined with the nanoindentation BVP solved with ABAQUS®, cf. [7]. The principle behind is numerical optimisation. Details are described in e. g. [18]. We try to find the vector of material parameters κ so that

$$f(\kappa) := \frac{\|\mathbf{F}^{num} - (\mathbf{F}^{exp} + \delta\sigma)\|}{\|\mathbf{F}^{exp}\|} \longrightarrow \text{MIN}. \tag{13}$$

$\delta\sigma$ is a random noise vector, which is superimposed over the experimental data. That can make the virtual experimental data more realistic and verified the stability of the numerical optimisation process. $\mathbf{F}^{num}$ are the force vectors obtained from the models with an arbitrary set of material parameters. The distance function $f(\kappa)$ has to be minimised to find the optimal predictive parameters. $f(\kappa)$ is also called objective function of the least squares type. It represents the quality of the approximation between the model's response governed by the parameter vector κ and the virtual experimental data. The applied evolution strategy is based on the principle of biological evolution in order to obtain the optimal parameters [19, 20]. It works with a Genetic Algorithm which selects different parameter vectors based on a starting vector κ_0 as initial population individuals. The parent population κ_μ is selected through a deterministic procedure. That the best individuals are chosen from the set of individuals ($\kappa_1, ..., \kappa_\lambda$) according to their objective function value $f(\kappa)$.

$$(\kappa_{1;\lambda}, \kappa_{2;\lambda}, ..., \kappa_{\mu;\lambda}) := Selection_{f(\mu)}(\kappa_1, ..., \kappa_\lambda), \lambda \geq \mu \tag{14}$$

$$f_{1;\lambda} \leq f_{2;\lambda} \leq ... \leq f_{m;\lambda} \leq ... \leq f_{\lambda;\lambda} \tag{15}$$

The symbol $(.)_{m;\lambda}$ stands for the individual with the mth smallest objective function values. The descendants are generated by recombination and by random mutations of selected parents.

Two maximum displacements are chosen. One is constrained to 5% of the layer thickness to remove

Table 2: The re-identified parameters with small and finite deformation

Noise		Mooney-Rivlin			Yeoh form		
%		C_{10}	C_{01}	$C_{10}+C_{01}$	C_{10}	C_{20}	C_{30}
Displacement restricted to 5% of the layer thickness							
0.0	Values	0.2060	0.4483	0.6509	0.6516	0.2524	0.1406
	Errore	25.6%	8.0%	0.1%	0.0%	2.4%	10.3%
0.5	Values	0.4849	0.1938	0.6787	0.6683	0.1407	0.0856
	Errore	195.7%	60.2%	4.2%	2.6%	45.6%	32.9%
2.0	Values	0.5675	0.1231	0.6906	0.6721	0.0470	0.0156
	Errore	246.0%	74.7%	6.0%	3.2%	81.8%	87.8%
sensitivity		3.048e4	3.157e4	—	3.052e4	3.377e2	7.290
Displacement as large as 30% of the layer thickness							
0.0	Values	0.1608	0.4900	0.6508	0.6521	0.2533	0.1301
	Errore	2.0%	0.6%	0.1%	0.1%	2.1%	2.0%
0.5	Values	0.1692	0.4617	0.6579	0.6578	0.2385	0.1373
	Errore	19.6%	5.3%	1.0%	1.0%	7.8%	7.7%
2.0	Values	0.2948	0.3916	0.6846	0.6706	0.2234	0.1138
	Errore	79.8%	19.6%	5.1%	3.0%	13.6%	10.7%
sensitivity		1.100e6	1.362e6	—	1.054e6	2.989e5	1.305e5

the influence of the substrate [7], the other is as large as 30% of the layer thickness without excluding the influence of the substrate. In the case of larger displacement, the properties of the substrate and the coefficient of the friction is assumed to be known. That means the properties of the substrate as well as the friction are not included in parameters identification. The non-linear behaviour is developed by the increment of the deformation. The goal is to investigate if the parameters of the hyperelastic models can be more accurately identified by enlarging the displacement. The re-identified parameters and the relative errors corresponding to the chosen values are listed in Table 2. It shows that, as expected the identified results under large deformation are better than the results obtained from small displacement indentation. The parameters coupling of the Mooney-Rivlin is reduced largely. Attention should be paid to the progressed results at large deformation of the Yeoh model. All of the three parameters are identified exactly if the virtual experimental data is free of noise. Although the noise level is increased up to 2.0%, the biggest deviation of the identified parameters from the chosen parameters is less than 14%, which is still acceptable. The sensitivity $\partial F/\partial \kappa_i$ of the reaction force with respect to parameters can be identified mathematically as follows:

$$\mathbf{F} := \mathbf{F}(\mathfrak{R}, \kappa_1, ..., \kappa_i, ..., \kappa_n) \tag{16}$$

$$\frac{\partial \mathbf{F}}{\partial \kappa_i} = \frac{\|\mathbf{F}(\mathfrak{R}, \kappa_1, ..., \kappa_i + \delta\mu, ..., \kappa_n) - \mathbf{F}(\mathfrak{R}, \kappa_1, ..., \kappa_i, ..., \kappa_n)\|}{|\delta\mu|} \tag{17}$$

Herein, $\mathfrak{R}$ is the model of interest, $\delta\mu$ is the mutation step size or an increment of the parameter κ_i. The values of the sensitivity in Table 2 can be helpful to explain the identified results above: It shows that the more exactly re-identified parameters have a higher sensitivity than the parameters which are worse to identify. The sensitivity is relatively higher under large deformation than those under small displacement. The increment of C_{20} and C_{30} is more obvious.

5 Conclusions

This paper is the further work following [7]. In the case of indentation of soft layers on hard substrates, it seems that enlarging the indented deformation plays a double-edged role. On the one hand, the identified results from large deformation are better than the results obtained from small displacement indentation. The parameters coupling of the Mooney-Rivlin is reduced largely and all of the three parameters of

the Yeoh model can be accurately identified at large deformation. On the other hand, the investigation of friction shows that large deformation also increases the influence of friction on the measured force-displacement data. The reason is associated with the influence of the substrate. If the displacement is small enough to avoid the influence of substrate, then the influence of friction can also be neglected. Therefore, if the indented layer on the substrate is investigated with finite elasticity or viscoelasticity, the influence of the substrate and the friction effect have to be considered simultaneously.

Acknowledgements

References

[1] *An improved technique for determining hardness and elastic modulus using load and displacement sensing indentation experiments*, W. C. Oliver, G. M. Pharr, J. Mater. Res., 7:1564-1583, 1992.

[2] *Measurement of hardness and elastic modulus by instrumented indentation: Advance in understanding and refinements to methodology*, W. C. Oliver, G. M. Pharr, J. Mater. Res., 19:3-20, 2004.

[3] *An inverse finite-element algorithm for parameter identification of thermoelastic damage models*, R. Mahnken, Modelling and Simulation in Materials Science and Engineering, 48:1015-1036, 2000.

[4] *The identification of parameters for visco-plastic models via finite-element methods and gradient methods*, R. Mahnken, E. Stein, Modelling and Simulation in Materials Science and Engineering, 2:597-616, 1994.

[5] *Optimization-based material parameter identification in indentation testing for finite strain elastoplasticity*, G. Rauchs, ZAMM Zeitschrift fur Angewandte Mathematik und Mechanik, 86:539-562, 2006.

[6] *Identification of the material parameters of a viscous hyperelastic constitutive law from spherical indentation tests of rubber and validation by tensile tests*, G. Rauchs, j. Bardon, D. Georges, Int.J.Mech.Mater, 86:doi:10.1016/j.mechmat.2010.08.03, 2010.

[7] *Modelling of nanoindentation of rubber-like hyperelastic layers and parameter identification*, Z. Chen, S. Diebels, Computational Materials Science, Submittion, 2011.

[8] *Large deformation isotropic elasticity: on the correlation of theory and experiment for incompressible rubber-like solids*, R. W. Ogden, Proceedings of the Royal Society of London, A328:565-584, 1972.

[9] *Large elastic deformations of isotropic materials. iv. further developments of the general theory* R. S. Rivlin, Phil. Trans. R. Soc. Lond., A241:379-397, 1948.

[10] *A theory of large elastic deformation*, M. Mooney, Journal of Applied Physics, 11:582-592, 1940.

[11] *Characterization of elastic properties of carbon-black-filled rubber vulcanizates*, O. H. Yeoh, Rubber Chemistry and Technology, 55:792-805, 1990.

[12] *Nonlinear solid mechanics: A continuum approach for engineering*, G. A. Holzapfel, Lohn Wiley & Sons Ltd, England, 2001.

[13] *Comparison of hyperelastic models for rubber-like materials*, G. Marckmann, E. Verron, Rubber chemistry and technology, 79:835-858, 2005.

[14] *Nanoindentation*, A. C. Fischer-Cripps, Spring, 2004.

[15] *The relation between load and penetration in the axisymmetric Boussinesq problem for a punch of arbitrary profile*, I. N. Sneddon, Int. J. Engng. Sci., 3:47-57, 1965.

[16] *Computational Contact Mechanics*, P. Wriggers, Spring, Netherlands, 2006.

[17] *On the theory of rubber friction*, B. N. J. Persson, Surface Science, 401:445-454, 1998.

[18] *Numerical optimization*, J. Nocedal, S. J. Wright, Springer, 1999.

[19] *Evolution and optimum seeking*, H. P. Schwefel, Wiley, New York, 1995.

[20] *The theory of evolution strategy*, H. G. Beyer, Springer, 2001.

[21] *Hertz contact at finite friction and arbitrary profiles*, B. Storaåkers, D. Elaguine, Journal of the Mechanics and Physics of solids, 53:1422-1447, 2005.

Modelling and Parameter Re-identification of

Nanoindentation of Soft Polymers

Taking into Account Effects of Surface Roughness
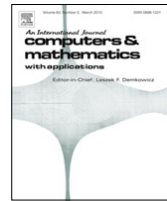
Modelling and parameter re-identification of nanoindentation of soft polymers taking into account effects of surface roughness

Zhaoyu Chen *, Stefan Diebels **

Chair of Applied Mechanics, Saarland University, PO Box 151150, 66041, Saarbrücken, Germany

A R T I C L E   I N F O

A B S T R A C T

In this paper the characterisation of polymers by nanoindentation is investigated numerically by the use of the inverse method. Effects of the surface roughness are explicitly considered. The boundary value problems of the nanoindentation of two polymers, PDMS and silicone rubber, are modelled with the FE code ABAQUS®. The model parameters are re-identified by using an evolution strategy based on the concept of the numerical optimisation. The surface roughness effects are investigated numerically by explicitly taking into account the roughness profile in the model. At first the surface roughness is chosen to have a simple representation considering only one-level of asperities described by a sine function. The influence of the surface roughness is quantified as a function of the sine parameters as well as of the indentation parameters. Moreover, it is verified that the real surface topography can be characterised by using multi-level or simple one-level of protuberance-on-protuberance sinusoidal roughness strain-energy function. profiles. The effects of the surface roughness are investigated with respect to the force–displacement data and the identified model parameters. These numerical results are expected to offer a deep insight into the influence of the real surface roughness at the results of indentation tests.

© 2012 Elsevier Ltd. All rights reserved.

1. Introduction

Over the last decades, the nanoindentation testing technique has continuously been improved. Now it is widely applied in metallic and ceramic engineering materials to determine the mechanical properties such as hardness and modulus. Since this technique is able to measure the properties of extremely small volumes with sub-μm and with sub-μN resolution, it also became one of the primary testing techniques for the mechanical characterisation of polymeric materials and biological tissues. The analysis of individual indentation tests by using the conventionally applied Oliver and Pharr method (abbreviated as O&P method) [1,2] is limited with regard to capture the hyperelastic and the rate-dependent properties of polymers and some metals. Therefore, numerical approaches in combination with the experimental testing, i.e. the finite element simulations and numerical optimisation have been used and evolved [3–13]. In this method, the difference between the experimental data and the numerical prediction is minimised with respect to the material model parameters by using numerical optimisation. The parameters are identified as the optimised solution.

Nanoindentation has the considerable advantage to measure the local properties of small volume materials from the continuously sensed force–displacement curve. However, it includes various error contributions, e.g. friction, adhesion, surface roughness and indentation process associated factors. These contributions generate the systematic errors between

---

* Corresponding author. Tel.: +49 0 681 302x2169.
** Corresponding author. Tel.: +49 0 681 302x2887.
E-mail addresses: zh.chen@mx.uni-saarland.de (Z. Chen), s.diebels@mx.uni-saarland.de (S. Diebels).

the numerical model and the experiments, and this often leads to large errors in the parameter identification [9,14–16]. Therefore, basic investigations and the certain knowledge about the influence of these factors are indispensable to characterise the materials accurately from nanoindentation based on the inverse method.

It is recognised by the use of the experimental and the numerical approaches that the surface roughness has a significant influence on the force–displacement data at a small or a moderate indentation depth, which is comparable to the height of the surface asperities [17–29]. It is known by the experimental investigation that the surface roughness impacts the Young's modulus and the hardness measurements [17,18,21,24]. The surface roughness can considerably disturb the indentation curves [22], and may, at least, be one of the main reasons for the indentation size effect [23]. The criteria to remove the surface roughness effects are found by experiments for some special materials. Miller et al. [28] found that it is possible to get a unique set of material properties if the average indentation depth is 5 times greater than the RMS roughness. For cancellous bone Donnelly et al. [29] pointed out that the variability in material properties increases substantially if the ratio of indentation depth to surface roughness decreases below 3:1. The surface roughness effects are difficult to control in an experiment, and moreover the measuring results are not easily to interpret. Nevertheless, the numerical simulation tools may help to understand the physics involved in this complex experiment. Therefore, FE simulations are widely used to interpret the experimental results if surface roughness effects are included [26,27,30,20]. The results in [26,27,30] have shown that an increasing roughness causes an increasing scatter of the data, but the mean value of a sufficiently large number of indents can still give a good approximation of the Young's modulus. Jiang et al. [20] pointed out that in order to rule out the influence of the surface morphology, the indentation depth should be much greater than the characteristic size of the surface roughness. Moreover, an indenter with a sufficiently large diameter could also be a good choice. A numerical study was conducted in [19] to understand the coupled influence of friction and surface roughness in the nanoindentation of pure nickel. Results have shown a strong interaction between these two contributions of surface effects, and their cumulative effects leads to significant variations in the force–displacement curves. The surface roughness of the bulk sample can be altered by various mechanical or electrochemical methods of polishing. However, an excessive polishing could influence the mechanical properties of soft and thin polymer films. Therefore, in practical experiments, the surface roughness of thin films can reach an average height of asperities about 30–60 nm [21,31,32]. Because of that, the surface roughness is comparable to the imposed indentation depth limited by the thin layer's thickness and the influence of the substrate. In this case, some of the criteria documented in the literature cannot be used longer. A quantified evaluation of the surface roughness effect is still required. Furthermore, it is essential to decrease the errors between the experimental settings and the numerical simulations if the inverse method is used. For this reason, more attention is paid on the numerical model of the realistic surface roughness profile. The surface roughness for the finite element models is taken from AFM data of sputter-deposited CrN within 2D and 3D in [26,27]. Pre-existing straight grooves defects are introduced on the film surface in 2D FE models in [20]. Berke et al. [19] describes the roughness with a protuberance-on-protuberance profile approximated by a sine function using axisymmetric 2D FE models.

In this present article, the behaviour of two hyperelastic soft polymers under nanoindentation is investigated numerically taking into account the effects of the surface roughness. The characterisation of the materials' properties is performed based on parameter re-identification procedure by using the inverse method. In this procedure, the virtual experimental data, which are obtained from numerical simulations with the chosen parameters, replace the real experimental measurements. In this sense, the finite element code ABAQUS® is used as a virtual laboratory. The parameter re-identification concept was used in [9,33] to validate the gradient-based material parameter identification routine. The surface roughness effects are investigated numerically based on the approach, which is mainly influenced by the work of Kumar et al. [21] and Berke et al. [19]. The surface roughness is chosen to have a simple representation considering a one-level roughness profile described in a first step by a sine function. The influence of the surface roughness is quantified phenomenological as a function of the sine curve parameters as well as of the indentation parameters. Moreover, it is verified that a real surface topography can be characterised by using a multi-level or a simple one-level of protuberance-on-protuberance sinusoidal profiles. The effects of this surface roughness are investigated with respect to the identified model parameters. The whole force–displacement curve is taken into account. The results are expected to offer a deep insight into the effects of the real surface roughness by a numerical modelling of nanoindentation.

2. FEM simulation of nanoindentation

2.1. Hyperelastic material model

In the present work we consider the nanoindentation of two nearly incompressible soft polymers by numerical simulation: polydimethylsiloxane (PDMS) 1:10 used in [34] and silicone rubber ELASTOSIL® RT 265 used in [35]. Both of the two polymers were assumed to be isotropic hyperelastic materials under isothermal conditions. Firstly in the framework of finite strain continuum mechanics, constitutive models of a nearly incompressible hyperelastic material will be recalled.

The existence of the Helmholtz free-energy function Ψ is postulated for a so-called hyperelastic material. Concerning the isotropic material under isothermal conditions, $\Psi = \Psi(\mathbf{F})$ is solely a function of the deformation gradient $\mathbf{F}$ or a strain tensor, respectively. So the Helmholtz free-energy function is referred to the strain-energy function. The general format of the constitutive equation can be derived from the second law of thermodynamics in the form of the Clausius–Planck

inequality

$$\mathcal{D}_{int} = \mathbf{P} : \dot{\mathbf{F}} - \dot{\Psi} = \left(\mathbf{P} - \frac{\partial \Psi(\mathbf{F})}{\partial \mathbf{F}} \right) : \dot{\mathbf{F}} \geq \mathbf{0}, \tag{1}$$

where $\mathcal{D}_{int}$ and $\mathbf{P}$ are the internal dissipation and the 1st Piola–Kirchhoff stress tensor, respectively. Only if $\mathbf{F}$ is chosen as a process variable influencing the free energy, $\mathbf{F}$ and hence $\dot{\mathbf{F}}$ can be chosen arbitrarily. Therefore, the expression in parentheses must be zero and the constitutive equation associated with $\mathbf{P}$ can be expressed as

$$\mathbf{P} = \frac{\partial \Psi(\mathbf{F})}{\partial \mathbf{F}}. \tag{2}$$

With the relations $\bar{\mathbf{T}} = \mathbf{F}^{-1}\mathbf{P}$ and $\mathbf{T} = J^{-1}\mathbf{F}\bar{\mathbf{T}}\mathbf{F}^T$, the 2nd Piola–Kirchhoff stress tensor $\bar{\mathbf{T}}$ and the Cauchy stress tensor $\mathbf{T}$ can be derived (details see e.g. [36, Chapter 6]). Due to the assumption that the strain-energy $\Psi(\mathbf{F})$ generated by the motion $\mathbf{x} = \widetilde{\chi}(\mathbf{X}, t)$ is objective as well as the fact that $\Psi(\mathbf{F})$ remains unchanged if a rigid-body motion is superimposed on the isotropic hyperelastic material, $\Psi(\mathbf{F})$ can also be described as

$$\Psi(\mathbf{F}) = \Psi(\mathbf{C}) = \Psi(\mathbf{B}) \tag{3}$$

with the right Cauchy–Green deformation tensor $\mathbf{C} = \mathbf{F}^T \cdot \mathbf{F}$ and the left Cauchy–Green deformation tensor $\mathbf{B} = \mathbf{F} \cdot \mathbf{F}^T$.

Since compressible materials behave quite differently in the bulk and the shear deformation, it is most useful to split the deformation locally into a so-called volumetric part and an isochoric part. In particular, we consider the multiplicative decomposition of $\mathbf{F}$, $\mathbf{C}$ and $\mathbf{B}$ into volumetric parts and isochoric parts

$$\mathbf{F} = (J^{1/3}\mathbf{I})\bar{\mathbf{F}} = (J^{1/3})\bar{\mathbf{F}}, \qquad \mathbf{C} = (J^{2/3}\mathbf{I})\bar{\mathbf{C}} = (J^{2/3})\bar{\mathbf{C}}, \qquad \mathbf{B} = (J^{2/3}\mathbf{I})\bar{\mathbf{B}} = (J^{2/3})\bar{\mathbf{B}}. \tag{4}$$

The terms $J^{1/3}\mathbf{I}$ and $J^{2/3}\mathbf{I}$ are related to volume-changing deformation, while $\bar{\mathbf{F}}$, $\bar{\mathbf{C}} = \bar{\mathbf{F}}^T\bar{\mathbf{F}}$ and $\bar{\mathbf{B}} = \bar{\mathbf{F}}\bar{\mathbf{F}}^T$ are associated with volume-preserving deformations, with the rules

$$\det \bar{\mathbf{F}} = 1, \qquad \det \bar{\mathbf{C}} = \det \bar{\mathbf{B}} = (\det \bar{\mathbf{F}})^2 = 1. \tag{5}$$

Based on the kinematic assumption above, the extension to the nearly incompressible hyperelastic behaviour is by additively decomposing the Helmholtz free-energy function Ψ into the volumetric elastic part Ψ_{vol} and the isochoric elastic part Ψ_{iso}. For isotropic materials, it is further assumed that Ψ is expressed in terms of the principle invariants of the modified Cauchy–Green tensors $\bar{\mathbf{C}}$ or $\bar{\mathbf{B}}$.

$$\Psi = \Psi_{\text{vol}}(J) + \Psi_{\text{iso}}[\bar{I}_1(\bar{\mathbf{C}}), \bar{I}_2(\bar{\mathbf{C}})] = \Psi_{\text{vol}}(J) + \Psi_{\text{iso}}[\bar{I}_1(\bar{\mathbf{B}}), \bar{I}_2(\bar{\mathbf{B}})] \tag{6}$$

The strain invariants $\bar{I}_a(a = 1, 2, 3)$ are the three modified principle invariants of $\bar{\mathbf{C}}$ and $\bar{\mathbf{B}}$, i.e.

$$\bar{I}_1 = \text{tr}\bar{\mathbf{C}} = \text{tr}\bar{\mathbf{B}}, \tag{7}$$

$$\bar{I}_2 = \frac{1}{2}[(\text{tr}\bar{\mathbf{C}})^2 - \text{tr}(\bar{\mathbf{C}}^2)] = \frac{1}{2}[(\text{tr}\bar{\mathbf{B}})^2 - \text{tr}(\bar{\mathbf{B}}^2)], \tag{8}$$

$$\bar{I}_3 = \det \bar{\mathbf{C}} = \det \bar{\mathbf{B}} = 1, \tag{9}$$

with the relationships to the principle invariants

$$\bar{I}_1 = J^{-2/3}I_1, \qquad \bar{I}_2 = J^{-4/3}I_2, \qquad \bar{I}_3 = 1. \tag{10}$$

Finally, we formulate the constitutive equation of $\bar{\mathbf{T}}$ in terms of the Jacobian J and the modified invariants $\bar{I}_1, \bar{I}_2$ (details see e.g. [36, Chapter 6])

$$\bar{\mathbf{T}} = 2\frac{\partial \Psi(\mathbf{C})}{\partial \mathbf{C}} = \bar{\mathbf{T}}_{\text{vol}} + \bar{\mathbf{T}}_{\text{iso}} \tag{11}$$

$$= J\frac{\partial \Psi_{\text{vol}}(J)}{\partial J}\mathbf{C}^{-1} + 2\frac{\partial \Psi_{\text{iso}}(\bar{I}_1, \bar{I}_2)}{\partial \bar{I}_1} : \frac{\partial \bar{I}_1}{\partial \mathbf{C}} + 2\frac{\partial \Psi_{\text{iso}}(\bar{I}_1, \bar{I}_2)}{\partial \bar{I}_2} : \frac{\partial \bar{I}_2}{\partial \mathbf{C}}. \tag{12}$$

In the framework of finite strain continuum mechanics, such formulations became popular where an additive split of the strain-energy function into isochoric parts and volumetric parts is used [37]. This type of formulation is very often used if large elastic deformations of rubber or rubber-like materials are concerned, because of the advantages in the numerical treatment of either incompressible or nearly incompressible properties. However, this formulation may lead to non-physical results if it is used without restriction to nearly incompressible materials with large volumetric deformation [37–39]. In the present study, it is reasonable to use this formulation because the investigated PDMS and silicone rubber are nearly incompressible.

Table 1
Chosen material models and parameters of the indented polymers.

Materials	Chosen models	Parameters			Shear modulus
PDMS	Neo-Hookean	C_{10} 0.662 MPa	D_1 0.255 MPa		μ_0 1.324 MPa
Silicone Rubber	Mooney–Rivlin	C_{10} 0.111 MPa	C_{01} 0.039 MPa	D_1 0.001 MPa	μ_0 0.300 MPa

There are numerous specific forms of strain-energy functions to describe the hyperelastic properties, whereas according to [34,35], the considered PDMS 1:10 and the silicone rubber can be modelled by a neo-Hookean model and a Mooney–Rivlin model [40] respectively:

$$\Psi_{\text{NH}} = \Psi_{\text{iso}}(\bar{I}_1) + \Psi_{\text{vol}}(J) = C_{10}\,(\bar{I}_1 - 3) + \frac{1}{D_1}[(J - 1)^2 + (\ln J)^2]/2, \tag{13}$$

$$\Psi_{\text{MR}} = \Psi_{\text{iso}}(\bar{I}_1, \bar{I}_2) + \Psi_{\text{vol}}(J) \tag{14}$$

$$= C_{10}\,(\bar{I}_1 - 3) + C_{01}\,(\bar{I}_2 - 3) + \frac{1}{D_1}[(J - 1)^2 + (\ln J)^2]/2. \tag{15}$$

The strain-energy function has to satisfy some physical limit conditions [41]. If the continuum is compressed to a single point, i.e. $J \to +0$, the strain energy tends to plus infinity and the volumetric stress towards to minus infinity. In the limit case if the continuum is stretched infinitely, one can obtain a plus infinite strain energy as well as a plus infinite volumetric stress. In the strainless initial state, i.e. $\bar{I}_a \to 1$ and $J \to 1$, it is a stress-free condition and no strain energy is stored. The initial shear modulus μ_0 and the initial compression modulus K_0 are related to the coefficients in the following way:

$$\mu_0 = 2\,\frac{\partial \Psi_{\text{iso}}}{\partial \bar{I}_a}\bigg|_{\bar{I}_a \to 1} = 2(C_{10} + C_{01}), \tag{16}$$

$$K_0 = \frac{\partial^2 \Psi_{\text{vol}}}{\partial J^2}\bigg|_{J \to 1} = \frac{2}{D_1}. \tag{17}$$

The compressibility parameter D_1 can be interpreted as a penalty parameter that enforces incompressibility if small values are chosen. The chosen parameters are listed in Table 1. In this study, D_1 of the silicone rubber is very small and hence it is not taken into account during the procedure of the parameter identification.

2.2. FEM model with rough surface geometry

It is our goal in this study to quantify the surface roughness effects influencing the force–displacement curve obtained from nanoindentation simulations. Hence, a numerical model of a potential real experimental setup, in which such effects play a significant role, is considered. The modelled situation is the nanoindentation with a Berkovich indenter of two soft polymer films: PDMS and silicone rubber. The indentation depth is limited to 50 nm in order to remove the influence of the hard substrates. It is found by the AFM scanning that the most commonly used three-sided Berkovich indenters are not perfectly sharp but have a tip radius in the order of 100 nm. Therefore, a spherical indenter with a radius of 100 nm is chosen to take the realistic geometry of the indenter tip into account. As explained in Section 2.1, the indented polymers PDMS and silicone rubber are assumed to be isotropic and hyperelastic. Generally speaking, a three dimensional model is necessary to represent the inhomogeneous property of the realistic surface topography. However, the computing time occupies a large part in the inverse method and is, as a consequence, a key problem of the method. This often results in a trade-off between the computing cost and the quality of the numerical model. For instance, a 2D plane model or an axisymmetric model is used most commonly to save the computing cost. In this study, the numerical nanoindentation simulation is modelled by using the finite element code, e.g. ABAQUS® 6.10. A plane strain modelling assumption is preferred, because the commonly real surface topography has a lack of axisymmetry and the position of the indenter can be set randomly on the rough surface in the plane strain model. The indenter can be assumed to be a rigid body compared to the soft polymers. We define the indenter as an analytical rigid surface in such a way that the indenter geometry can be modelled exactly with a smooth curve. The geometrical size of the polymer sample is 2 μm × 2 μm, which is sufficiently large to obtain a homogeneous stress distribution at the bottom and on the side boundaries of the model. The modelling of the surface roughness is explained in details in Section 4. Concerning the irregular geometry of the rough surface topography, 2D finite element meshes of 6 nodes triangular elements with quadratic shape function are used. For each studied configuration, the mesh convergence is checked by using more than 150,000 degrees of freedom. It shows that a refined mesh, consisting at least of 30,000 degrees of freedom, can give converged results. To account for the localised deformation of the layer, it is essential that the density of nodes under the indenter tip is high enough. The rigid indenter is fixed in the horizontal direction and a vertical displacement is applied on to its reference point. The bottom nodes of the mesh are fixed. In the present work, the deformation of the

specimen during the nanoindentation is restricted to a small deformation regime. The maximum displacement is limited to only 2.5% of the layer thickness. Therefore, the influence of the substrate and the friction between the indenter and the layer can be neglected according to [13].

3. Parameter identification

In the present study, the virtual experiments which are performed by using the FEM simulation with the chosen material models replace the real nanoindentation test for the following reasons: On the one hand, it is difficult to generate different types of surface roughness and to separate its effects from other error contributions in real-world experiments. On the other hand, in the case of virtual experiments, it is possible to investigate how accurate the model parameters can be determined from the parameter re-identification routine. In this process, the resulting force–displacement curve is considered as virtual experimental data, which is used instead of real experimental measurements to identify the chosen parameters again. The parameter re-identification strategy is performed in MATLAB® combined with the nanoindentation boundary value problem which is solved by using the finite element analysis with ABAQUS®. From the mathematical point of view such a process represents a numerical optimisation problem minimising the error between the experimental and the computed force–displacement curve with respect to the model parameters, details are described in e.g. [42]. In general, the vector of material parameters κ has to be modified to minimise the distance $f(\kappa)$ between the virtual experimental data and the prediction of the numerical model. $f(\kappa)$ is the so-called objective function of the least squares type. Mathematically this can be formulated as follows: Find κ so that

$$f(\kappa) := \frac{\|\mathbf{F}^{num} - \mathbf{F}^{exp}\|}{\|\mathbf{F}^{exp}\|} \longrightarrow \min f(\kappa). \tag{18}$$

Herein

$$\mathbf{F}^{exp} = [F_{d1}^{exp}, F_{d2}^{exp}, F_{d3}^{exp}, \ldots]^T, \tag{19}$$

is the virtual experimental data, i.e. the vector of reaction force obtained at each displacement increment. The force vectors obtained for the models with an arbitrary set of material parameters are called

$$\mathbf{F}^{num} = [F_{d1}^{num}, F_{d2}^{num}, F_{d3}^{num}, \ldots]^T. \tag{20}$$

The choice of the optimisation-based method for minimising an objective function is a topic of interest. It is generally advised to use globally convergent optimisation algorithms whenever possible. These algorithms are simulated annealing or genetic algorithms, such as evolutionary algorithms, or deterministic algorithms like the Simplex method. The gradient-based algorithm is full of troublesome gradient calculation and the further drawback of local convergence. Genetic or evolutionary algorithms are globally convergent and are the only useful choice in multi-objective optimisation. Therefore, the evolution strategy is applied in order to find the optimal vector of the material parameters and in order to minimise the objective function. This strategy is based on the principle of the biological evolution and can work with a Genetic Algorithm, which has been implemented in MATLAB® optimisation tool box, for details please see [43,44]. At the beginning, a number λ of different parameter vectors are selected as population individuals $\kappa_\lambda^{(g)}$ at generation $g = 0$ in a physically sound range based on a starting vector κ_0. The selection operator then produces the parent population $\kappa_\mu^{(g)}$ of the next generation $g = g + 1$ through a deterministic procedure, which chooses the μ best individuals from the set of λ individuals $(\kappa_1, \ldots, \kappa_\lambda)$ according to their objective function value $f(\kappa)$.

$$(\kappa_{1;\lambda}, \kappa_{2;\lambda}, \ldots, \kappa_{\mu;\lambda}) := Selection_{f(\mu)}(\kappa_1, \ldots, \kappa_\lambda), \quad \lambda \geq \mu \tag{21}$$

$$f_{1;\lambda} \leq f_{2;\lambda} \leq \cdots \leq f_{m;\lambda} \leq \cdots \leq f_{\lambda;\lambda} \tag{22}$$

The symbol $(\cdot)_{m;\lambda}$ here stands for the individual with the mth best objective function values. The descendants $\kappa_\lambda^{(g)}$ are generated by recombination and by random mutations of the selected parents. In details, a crossover recombination operator randomly selects genetic information from two parents as the vector entry of the descendant. Single parents generate descendants by mutation, in which a stochastic vector $\Delta\sigma$ is added to them. Mutation is the most important ingredient for the evolution strategy, the choice of $\Delta\sigma$ closely links to the convergence behaviour of the method. In order to make the algorithm efficient, it is suggested that $\Delta\sigma$ should be modified during the minimum search. Besides the mutation and the recombination procedures, the parents with the best fitness are guaranteed to survive in the generation $g = g + 1$ as elite individuals.

4. Results of simulation and parameter identification

To the best knowledge of the authors, in most of the papers, the O&P method is used as the post-treatment method of nanoindentation with surface roughness effects. In this method, the hardness and the elastic modulus can be computed based on the unloading segment of the load–displacement curve and the contact area. However, this method has limitations with regard to quantify the surface roughness effects. Firstly, the influence of the surface roughness is evaluated only on the obtained hardness and elastic modulus. Besides, for some shallow indentations, the loading segment of the

Table 2
The identified parameters and the deviation in % compared with the chosen values.

Materials	Chosen models	Identified parameters			Evaluated
			C_{10}	D_1/C_{01}	μ_0
PDMS	Neo-Hookean	Values	0.6614 MPa	0.2543 MPa	1.3228 MPa
		Deviation	0.06%	0.27%	0.09%
Silicone Rubber	Mooney–Rivlin	Values	0.1001 MPa	0.0495 MPa	0.2992 MPa
		Deviation	9.82%	26.92%	0.27%
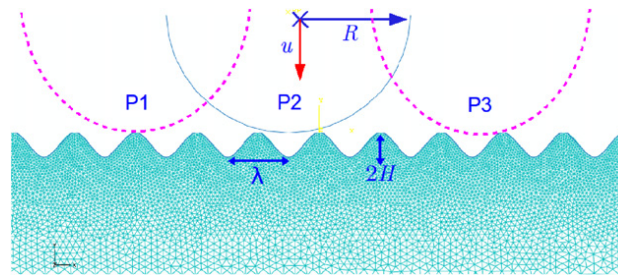
Fig. 1. The mesh configuration of the one-level protuberance-on-protuberance profile.

load–displacement curve, containing a significant influence of the surface roughness, is not used in the O&P method. Furthermore, the contact area is evaluated in this method by using the contact depth and the geometry of the indenter. A polynomial contact area function of contact depth is given by Oliver and Pharr based on the assumption of a perfectly smooth contact interface. Except the pile-up and sink-in phenomena, the surface roughness has a strong influence on the real contact area. However, it is difficult to evaluate accurately the real contact area of a rough contact interface in a real life experiment. In a numerical simulation the contact area can be obtained explicitly, but it is strongly dependent on the mesh size close to the indenter. Therefore, in the present study, the inverse method is used to quantify the influence of the surface roughness. On the one side, it is possible to evaluate the influence of the surface roughness on the identification of all model parameters not only on the hardness and the elastic modulus. On the other side, all segments of the load–displacement curve can be taken into account and the troublesome evaluation of the real contact area can be avoided.

4.1. Indentation of a flat surface

First of all, the nanoindentation of a perfectly flat surface is considered with special focus on the accuracy of the parameter identification. Moreover, the results can be used as a reference in the following discussion about the influence of the surface roughness. The identified parameters and the deviation compared with the chosen values are listed in Table 2. The parameters C_{10} and D_1 of the neo-Hookean model are exactly identified as can be seen in Table 2. This is not the case for the identified parameters C_{10} and C_{01} of the Mooney–Rivlin model. The identified C_{01} differs from the chosen value about 27%. As it is explained in [8,11], the contribution to the force–displacement results from C_{10} and C_{01} cannot be divided. Such phenomenon is called parameter coupling. It has strong influence on the parameter identification of the polynomial-type hyperelastic model. Concerned with the neo-Hookean model, D_1, not similar to C_{10}, is a compressibility parameter. Therefore, the neo-Hookean model is free of parameter coupling during the identifying procedure. Nevertheless, using the identified parameters according to Eq. (16), the evaluated shear modulus μ_0 is approximately the same as the value chosen in Table 1, i.e. the sum $C_{10} + C_{01}$ is identified correctly.

4.2. Indentation of a surface with regular roughness

The surface roughness effects are investigated numerically based on a phenomenological approach. Firstly a simple representation of the surface is chosen considering only a one-level of protuberance-on-protuberance profile described by a sine function $f(x) = H \sin \frac{2\pi}{\lambda} x$, although this simplest model is only a regular wavy surface. It is the preferred model for us to perform the parametric investigation of the surface roughness effects. Moreover, most man-made surfaces such as those produced by grinding or machining, have a pronounced "lay", which may be modelled to a first approximation by this sinusoidal profile [45]. The parameters of the sinusoidal surface profile as well as the indentation geometric parameters are illustrated in Fig. 1: the wave length λ, the roughness asperity height H, the spherical radius R and the indentation depth u. The whole indented sample surface, not only the part just under the indenter, is represented by the sinusoidal profile. This means that the influence of the interaction between the neighbouring asperities of the real surface roughness is also taken into account. It has been shown experimentally that the influence of the surface roughness is dependent on the asperity shape [19]. A large range of roughness asperity shapes from relatively sharp to smooth geometries is obtained by varying the asperity height $H = [5 \text{ nm} \cdots 50 \text{ nm}]$ and by varying the wave length $\lambda = [5 \text{ nm} \cdots 200 \text{ nm}]$.
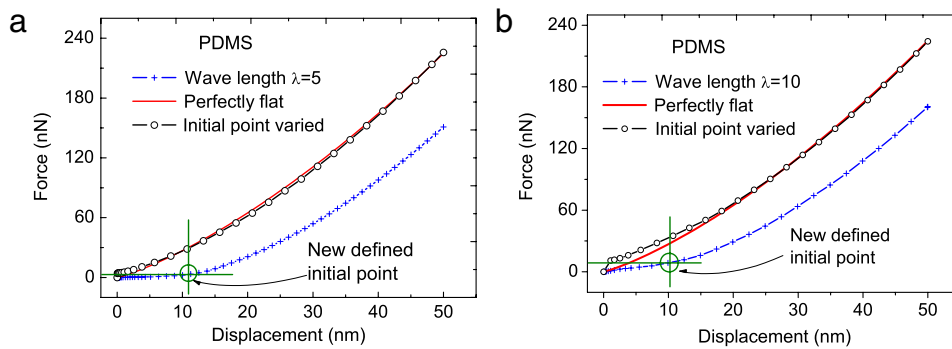
Fig. 2. The force–displacement data obtained from indentation on flat surface and regular rough surface of PDMS, with a varying wave length: (a) $\lambda = 5$ nm; (b) $\lambda = 10$ nm. **Remark**: The new initial point of the force–displacement data is defined by a threshold of the measured reaction force. This is the usual way to define the initial contact of indents and surface in real experiments.

Table 3
The identified parameters and their deviation compared with the chosen values listed in parentheses: indentation on a regular surface roughness.

Experimental data	Identified parameters		Evaluated
	C_{10}	D_1/C_{01}	μ_0
PDMS			
Wave length $\lambda = 5$	0.2941 (−55.57%)	0.1001 (−60.78%)	0.5882 (−55.57%)
Initial point varied $\lambda = 5$	0.6288 (−5.02%)	0.2182 (−14.43%)	1.258 (−5.02%)
$\lambda = 100\_P1$	0.6908 (+4.35%)	0.9818 (+285.02%)	1.382 (+4.35%)
Average_P2+P3 $\lambda = 100$	0.6740 (+1.81%)	0.2476 (−2.90%)	1.348 (+1.81%)
Silicone Rubber			
$H = 5\_P2$	0.1017 (−8.38%)	0.0429 (+10.00%)	0.2889 (−3.60%)
$H = 20\_P2$	0.0605 (−45.50%)	0.0769 (+97.18%)	0.2748 (−8.40%)
$H = 50\_P2$	0.0318 (−71.32%)	0.0265 (−32.05%)	0.1167 (−61.11%)

At first, it is focused on varying the wave length λ from 5 nm to 200 nm and keeping the asperity height fixed at 20 nm for each roughness configuration. The results show that the influence of the surface roughness depends strongly on the wave length. This dependence is the same for the PDMS and for the silicone rubber. However, the surface roughness can have a twofold effect resulting in either higher or lower contact stiffness. This twofold effect depends on the indentation position once the wave length increases to be comparable to the indenter radius. As shown in Fig. 1, the three indentation positions are noted as P1, P2 and P3, denoting the indentation performed on the top, in a roughness valley and between the valley and the top respectively. The force–displacement data of the PDMS with a very narrow wave length of 5 nm to 10 nm are shown in Fig. 2. In the two cases, the low ratio λ/H leads to a very sharp asperity. The surface roughness has an effect resulting in much lower contact stiffness especially at the very beginning of the indentation. A physically sound reason can be the response of the extremely sharp asperity, which decreases the material stiffness. The criteria to remove the surface roughness effect suggested in [20] by using a sufficiently large spherical indenter, has no use in this case. Nevertheless, the surface roughness effect on the force–displacement curve can be removed if a new initial indentation point is defined as shown in Fig. 2. The initial contact point between indenter and surface can be re-defined to throw off the contact part in which the contact stiffness is nearly zero. In practice, there are several points nearly zero. In this case, the chosen of the new initial contact point is experience dependent or a method like zero point correction [10] can be applied. The identified parameters are listed in Table 3, it can be seen that this criterion is useful to remove the surface roughness effects if the inverse method is applied based on the force–displacement data only. The surface roughness effect decreases with an increasing wave length up to 50 nm. The roughness effect depends on the indentation position if the wave length is larger than 50 nm as shown in Fig. 3. It can be seen explicitly that the surface roughness results in higher contact stiffness if the indentation is placed in a roughness valley and a decreasing stiffness if an asperity top is indented. This discovery has the same results as documented in [19]. In the real life experiments it is difficult to choose the indentation position neither in the valley or on the top. Therefore, it is reasonable to perform a sufficiently large number of indentations with arbitrary positions from the point of view of statistics. It is a good choice to take the mean value of the data with a reasonable discreteness in order to decrease the surface roughness effect. For instance, we can take the mean values "$\lambda = 100\_P2$ & P3"in Fig. 3(a) and "$\lambda = 200\_P1$ & P3"in Fig. 3(b) as the measured force–displacement data. We can also find similar conclusions in experimental as well as numerical investigations on hard metals in [26,27,30].

The dependence of the surface roughness effect on the asperity height is investigated in the second step. In this case, the wave length is firstly fixed to 50 nm while the asperity height varies in a physically sound range from 5 nm to 50 nm. As the surface roughness has the same influence for the two investigated materials, only the results of the silicone are shown in Fig. 4 in this time. The surface roughness has an effect on the force–displacement data depending on the ratio
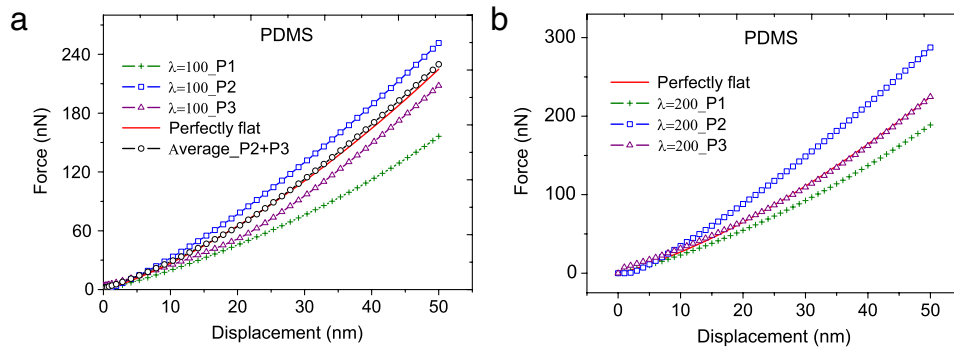
Fig. 3. The force–displacement data obtained from indentation on flat surface and regular rough surface of PDMS, with a varying wave length: (a) $\lambda = 100$ nm; (b) $\lambda = 200$ nm.
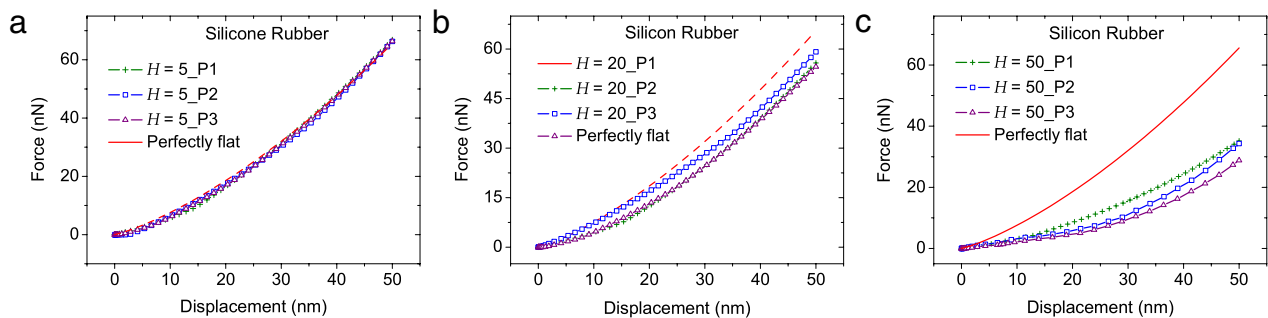
Fig. 4. The force–displacement data obtained from an indentation on a flat surface and a regular rough surface of silicone rubber with varying asperity height: (a) $H = 5$ nm; (b) $H = 20$ nm; (c) $H = 50$ nm.

of the asperity height to the indentation depth H/u. An error contribution of the surface roughness in the inverse method cannot be perceived if H/u is sufficiently small, e. g. 1:10. The indentation result on a perfectly flat surface can still be used to approximate the measuring data indented on rough surface while the ratio H/u is below 1:3. A similar finding was also obtained by Donnelly et al. [29] in an experimental investigation of the indentation on cancellous bone. Nevertheless, the surface roughness effect results in decreasing contact stiffness of approximately 50% lower if the indentation depth is identical to the asperity height.

Finally, the surface roughness effects are quantified by the parameter identification. The virtual experimental data, namely the force–displacement data shown in Figs. 2–4, represent the indentation results obtained with the regular surface roughness model and with the chosen material parameters. The numerical data are the simulation results of the indentation on a perfectly flat surface with an arbitrary set of material parameters. All of the other geometrical parameters and of the boundary value problems of the virtual experimental setup and the numerical model are identical. The comparison of the identified parameters with the chosen values can be used to quantify the surface roughness effects. The identified parameters and the corresponding deviation are compared with the chosen values as shown in Table 3. The identified parameters C_{10} and D_1 of the neo-Hookean model are about 60% lower than the chosen values due to the effects of surface roughness with a wave length of 5 nm. It is worth to note that C_{10} and D_1 are accurately identified if a new initial point is defined to remove the surface roughness effects. The effects result in a much larger identified D_1 if the experiments are performed on the top of the asperity with a wave length of 100 nm. Nevertheless, if the experimental data is replaced by the mean value of the indentation results on different positions, C_{10} and D_1 are exactly identified for the neo-Hookean model. The two parameters C_{10} and C_{01} of the Mooney–Rivlin model are accurately identified if the surface roughness possesses a low asperity height of 5 nm. The surface roughness with the asperity height of 20 nm leads to deviations of −45.50% and +97.18% for C_{10} and C_{01} respectively. But the evaluated initial shear modulus μ_0 using the identified parameters has an acceptable deviation from the reference value. The surface roughness effects can be neglected with respect to the results shown in Fig. 4(b) and w. r. t. to the evaluated shear modulus μ_0. The existing parameter coupling is the main reason to cause a big deviation to the identified C_{10} and C_{01}. The surface roughness has an effect on the evaluated μ_0 resulting in a 61.11% lower value.

4.3. Indentation on a realistic surface roughness model

In general the real surface has a roughness containing various wave lengths and asperity heights distributed irregularly if it is scanned by the AFM technique in a nano-scale. The use of a simple regular model like in Section 4.2 may has a limited domain of validity of the numerical simulation and the obtained quantified results. Moreover, in order to minimise
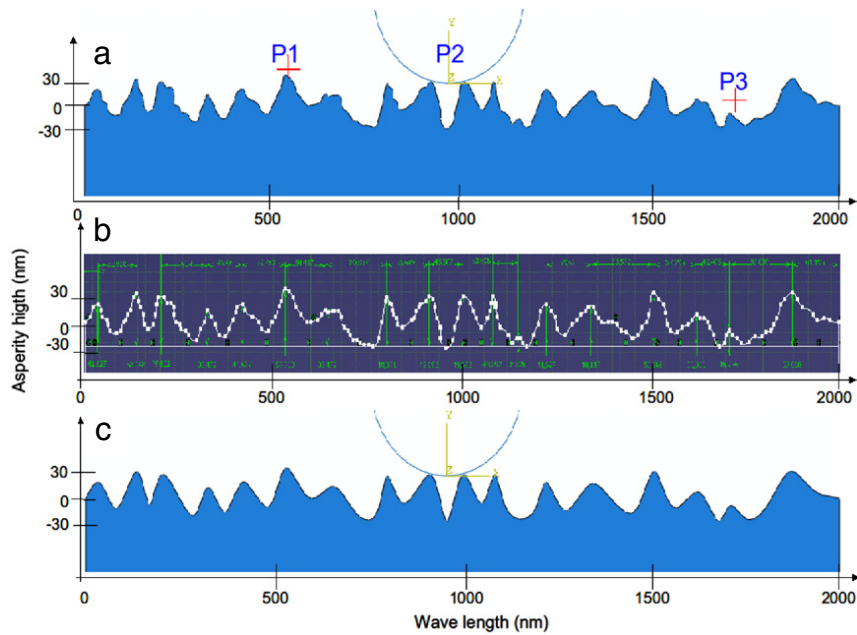
Fig. 5. The surface profile of a more realistic roughness model: (a) FEM geometry model of the realistic rough surface; (b) Measuring the random asperity; (c) Simplifying (a) with a multi-level sinusoidal curve in FEM model.
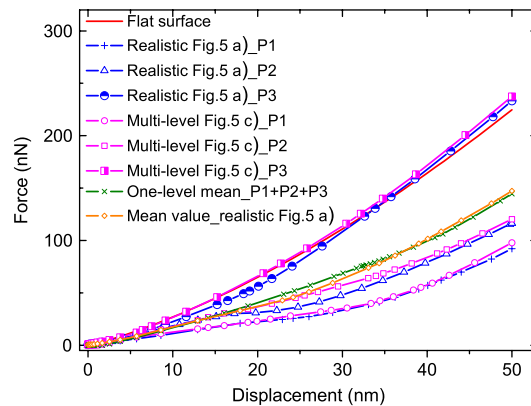
Fig. 6. Direct comparison of the force–displacement data of indentation with different positions on realistic surface roughness, multi-level sinusoidal profile model and one-level simple surface model.

the system errors due to the surface roughness effects, it is also necessary to take a realistic surface roughness model into account. A more realistic surface profile, depicted in Fig. 5(a), is modelled with irregularly various serration. Three typical indentation positions on this topography are considered with an indentation depth of 50 nm after an initial contact. A multi-level protuberance-on-protuberance sine profile is considered to simplify this serration surface model. It is measured the asperity height and the wave length of the realistic roughness by dividing the serration form into several continuous pieces, as shown in Fig. 5(b). The transformation can be performed with a CAD program and is then input into ABAQUS®. A simplified realistic surface model is plotted in Fig. 5(c). It is described by using multi-level sinusoidal functions $f_i(x) = H_i \sin\left(\frac{2\pi}{\lambda_i} x + \theta_i\right)$, with different wave length λ_i, amplitudes H_i and phase shifts θ_i. These parameters can be obtained by a Fourier transformation. Three indentations with different positions, the same as shown in Fig. 5(a), are made on this surface. The force–displacement results of the two realistic models are at first compared directly in Fig. 6. Firstly, the force–displacement data of the realistic model and the multi-level sinusoidal profile model depends strongly on the indentation position. The response to the deformation of the stochastic local topography plays an important role in the whole indentation results. Secondly, comparing the data of the same indentation position, it is found that the multi-level sinusoidal model can be used to predict the realistic surface roughness effects. The deformed configurations at the maximum displacement indented on positions P1, P2, P3 are shown in Fig. 7. They are obtained from the realistic surface roughness model as shown in Fig. 5(a) and the multi-level sinusoidal profile model as shown Fig. 5(b), respectively. These deformed configurations are able to illustrate the force–displacement results explained above. The indentation data of the
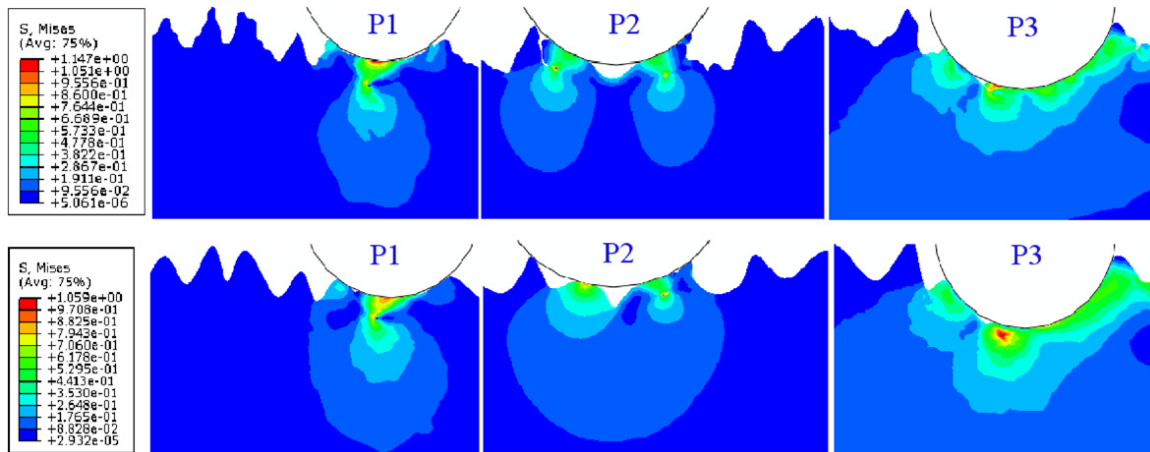
Fig. 7. The deformed configurations at the maximum displacement indented on positions P1, P2, P3 obtained from the realistic surface roughness model as shown in Fig. 5(a) (above) and the multi-level sinusoidal profile model as shown Fig. 5(b) (below).

Table 4
The identified parameters and its deviation compared with the chosen values listed in parentheses: indentation on a realistic surface roughness model.

Numerical model	Identified parameters		Evaluated
	C_{10}	D_1/C_{01}	μ_0
PDMS			
Flat surface model	0.4946 (−25.29%)	0.7494 (+193.88%)	0.9892 (−25.29%)
One-level sine profile	0.7031 (+6.21%)	0.4366 (+71.72%)	1.4062 (+6.21%)
Silicone Rubber			
Flat surface model	0.0538 (−51.53%)	0.0279 (−28.46%)	0.1634 (−45.53%)
One-level sine profile	0.0944 (−14.95%)	0.0489 (+25.38%)	0.2866 (−4.47%)

perfectly flat surface is also plotted in Fig. 6. It is worth to mention that the response of indentation on the position P3 is able to predict well the indentation behaviour of the perfectly flat surface. The local topography of the position P3 is distributed with a large wave length as well as low asperities of either a negative or a positive skew. This type of position is a good choice to decrease the error contribution due to surface roughness in a realistic experimental setup. There are many different roughness parameters in use, but R_a, called arithmetic average roughness, is the most commonly used parameter. The R_a of the realistic surface roughness model in Fig. 5 can be estimated from $R_a = 1/n \sum_{i=1}^{n} |y_i|$, y_i denote the wave length λ_i, the asperity height H_i and the phase shifts θ_i, respectively. A numerical model with the roughness of a one-level sine function of R_a is applied to predict the statistics indentation force–displacement data with effects of realistic surface roughness. It can be seen in Fig. 6 that the numerical simulation with this one-level roughness model is able to predict the statistical mean value of the force–displacement data of indentation with the effects of a realistic surface roughness.

In the second step, the model parameters of the two polymers are identified. The statistics mean force–displacement data, obtained from the realistic model Fig. 5(a) with the chosen parameters, serves as the experimental data. The FEM models with a perfectly flat surface and a one-level sine curve surface profile are used to predict the numerical data with the arbitrary set of material parameters. The identified parameters and the corresponding deviations are listed in Table 4. It shows explicitly that the identified parameters have large deviations compared with the chosen values if a numerical model with flat surface is used. The surface roughness effects which are not taken into account in the numerical model yield much big deviations of the identified parameters. Nevertheless, the parameters are accurately identified if the surface roughness described by a simple one-level sine function of the arithmetic average roughness R_a is taken into account. From this point of view, the realistic surface roughness can be modelled by using a simple one-level sine function in the process of parameter identification.

5. Conclusions and discussion

In this paper, the characterisation of two often used soft hyperelastic polymers, PDMS and silicone rubber, is investigated by nanoindentation taking into account effects of the surface roughness. The inverse method is applied to quantify the influence of the variable topography on the identified values of the model parameters.

At first, the parametric investigation of the surface roughness effects is performed by indentation on a regular surface roughness described by a one-level sine function. The surface roughness effects strongly depend on the roughness shape, namely the wave length λ and the asperity height H. The indentation on a very sharp asperity with a low ratio λ/H leads

to a decreased contact stiffness compared to a flat surface especially at the initial indentation. The identified values of the parameters C_{10} and D_1 of the neo-Hookean model are about 60% lower than the chosen values due to the effects of surface roughness with a wave length of 5 nm. Nevertheless, the surface roughness effect on the force–displacement curve can be avoided if a new initial indentation point is defined by a certain threshold of the resulting contact force. In this case, the re-identified parameters have an acceptable deviation from the chosen values. The surface roughness effect results in higher contact stiffness with an indentation in the roughness valley and a lower one with the indentation on an asperity top, if the wave length is larger than 50 nm. If the experimental data is replaced by the mean value of the indentation results on different positions, C_{10} and D_1 are exactly identified compared with the chosen values. To take the mean data of the sufficiently large number of indentations is a good choice to decrease the error contribution of surface roughness to the identification process. The surface roughness effect on the force-dependent data also depends on the ratio H/u. The indentation model with a perfectly flat surface can still be used to approximate the force–displacement data indented on a rough surface if H/u is below 1:3. The parameter coupling exists if the two parameters C_{10} and C_{01} of the Mooney–Rivlin model are identified using experimental data with surface roughness effects. In this case, the initial shear modulus μ_0 evaluated from the identified parameters C_{10} and C_{01} is a suitable choice to quantify the surface roughness effects.

In a second step, a more realistic surface roughness profile is modelled with irregularly various serrations. It is verified that a multi-level protuberance-on-protuberance sine profile can be used to simplify this serration surface model. Furthermore, this realistic surface model is simplified by using a one-level sinusoidal profile model described with the arithmetic average roughness R_a. The identified parameters of the two models have large deviations compared with the chosen values because of the surface roughness effects, which are considered in the numerical model. Nevertheless, the parameters are accurately identified if a surface roughness described by a simple one-level sine function is taken into account. In this case, the statistic parameters of the realistic surface roughness, e. g. the arithmetic average roughness R_a, should be used to describe the simple roughness profile.

The investigated results and findings in this study can be used in the polishing of the sample in real experiments and in the numerical simulation if the inverse method is applied to quantify the model parameters. It is one choice to model the realistic surface roughness in order to minimise the systematic error due to surface roughness between experimental setup and the numerical model. The surface scanning from AFM may help us to get the true local roughness shape of the sample surface. Like we did in this study, a multi-level or a one-level sinusoidal profile model described with statistics roughness parameters can be used in the numerical simulation. Moreover, the often used fast Fourier transform (FFT) in the treatment of signals can be considered to deal with the random realistic roughness. Concerned with the inhomogeneous property of the realistic surface topography, a 3D model is necessary to represent the real shape in the numerical simulation. However, the huge computational cost often results in a trade-off between the computing cost and the quality of the numerical model. In this case, a second choice can be considered to solve this problem. The idea is based on quantifying the surface roughness effects on the force–displacement data. The realistic surface roughness can be characterised by some statistics parameters: the arithmetic average roughness R_a, root mean squared roughness RMS, maximum valley depth R_v, and maximum peak height R_p. The contributions from the surface roughness to the force–displacement data can be quantified as a function of the roughness parameters based on mathematical statistical methods. The calibrated experimental force–displacement data, using these quantified functions, could be considered as experimental data without the surface roughness effects. Therefore, it is reasonable to use a 2D numerical model with flat surface if the inverse method is applied. A further investigation on the topic of surface roughness effects in nanoindentation based on this idea is the work in hand and the results will be documented in an upcoming paper.

Acknowledgements

References

[1] W.C. Oliver, G.M. Pharr, An improved technique for determining hardness and elastic modulus using load and displacement sensing indentation experiments, J. Mater. Res. 7 (1992) 1564–1583.
[2] W.C. Oliver, G.M. Pharr, Measurement of hardness and elastic modulus by instrumented indentation: advance in understanding and refinements to methodology, J. Mater. Res. 19 (2004) 3–20.
[3] N. Huber, W.D. Nix, H. Gao, Identification of elastic–plastic material parameters from pyramidal indentation of thin films, Proc. R. Soc. Lond. Ser. A 458 (2002) 1593–1620.
[4] S. Guessasma, M. Sehaki, D. Lourdin, A. Bourmaud, Viscoelasticity properties of biopolymer composite material determined using finite element calculation and nanoindentation, Comp. Mat. Science 44 (2008) 371–377.
[5] S. Hartmann, J. Gibmeier, B. Scholtes, Experiments and material parameter identification using finite elements. uniaxial tests and validation using instrumented indentation tests, Exp. Mech. 46 (2006) 5–18.
[6] N. Huber, E. Tyulyukovskiy, A new loading history for identification of viscoplastic properties by spherical indentation, J. Mater. Res. 19 (2004) 101–113.
[7] D. Klötzer, C. Ullner, E. Tyulyukovskiy, N. Huber, Identification of viscoplastic material parameters from spherical indentation data. part II: experimental validation of the method, J. Mater. Res. 21 (2006) 677–684.
[8] G. Rauchs, J. Bardon, D. Georges, Identification of the material parameters of a viscous hyperelastic constitutive law from spherical indentation tests of rubber and validation by tensile tests, Mech. Mater. 42 (2010) 961–973.

 [9] G. Rauchs, J. Bardon, Identification of elasto-viscoplastic material parameters by indentation testing and combined finite element modelling and numerical optimization, Finite Elem. Anal. Des. 47 (2011) 653–667.
[10] E. Tyulyukovskiy, N. Huber, Identification of viscoplastic material parameters from spherical indentation data. part i: neural networks, J. Mater. Res. 21 (2006) 664–676.
[11] Z. Chen, S. Diebels, Nanoindentation of hyperelastic polymer layers at finite deformation and parameter re-identification, Arch. Appl. Mech. (2011) 1–16. http://dx.doi.org/10.1007/s00419-012-0613-9.
[12] Z. Chen, S. Diebels, Numerical investigation of nanoindentation of viscoelastic polymer layers and parameters re-identification, PAMM Proc. Appl. Math. Mech. 11 (2011) 765–766.
[13] Z. Chen, S. Diebels, J. Schmitt, Frictional nanoindentation of hyperelastic polymer layers: A numerical study, in: Proceedings of the 3rd ECCOMAS Thematic Conference on the Mechanical Response of Composites, 2011, pp. 229–236.
[14] G. Bolzon, G. Maier, M. Panico, Material model calibration by indentation, imprint mapping and inverse analysis, Int. J. Solid Struct. 41 (2004) 2957–2975.
[15] M. Mata, J. Alcalá, The role of friction on sharp indentation, J. Mech. Phys. Solids 455 (2004) 145–165.
[16] E. Tyulyukovskiy, N. Huber, Neural networks for tip correction of spherical indentation curves from bulk metals and thin metal films, J. Mech. Phys. Solids 55 (2007) 391–418.
[17] M.S. Bobji, S.K. Biswas, Deconvolution of hardness from data obtained from nanoindentation of rough surfaces, J. Mater. Res. 14 (1999) 2259–2268.
[18] M.S. Bobji, K. Shivakumar, H. Alehossein, V. Venkateshwarlu, S.K. Biswas, Influence of surface roughness on the scatter in hardness measurements—a numerical study, Int. J. Rock Mech. Min. Sci. Geomech. Abstr 36 (1999) 399–404.
[19] P. Berke, F.E. Houdaigui, T.J. Massart, Coupled friction and roughness surface effects in shallow spherical nanoindentation, Wear (2010).
[20] W.G. Jiang, J.J. Su, X.Q. Feng, Effect of surface roughness on nanoindentation test of thin films, Eng. Fract. Mech. 75 (2008) 4965–4972.
[21] A.K.N. Kumar, M.D. Kannan, S. Jayakumar, K.S. Rajam, V.S. Raju, Investigations on the mechanical behaviour of rough surfaces of tini thin films by nanoindentation studies, Surf. Coat. Technol. 201 (2006) 3253–3259.
[22] J.Y. Kim, S.K. Kang, J.J. Lee, J. Jang, Y.H. Lee, D. Kwon, Influence of surfaceroughness on indentation size effect, Acta Mater 55 (2007) 3555–3562.
[23] J.Y. Kim, J.J. Lee, Y.H. Lee, J. Jang, D. Kwon, Surface roughness effect in instrumented indentation: a simple contact depth model and its verification, Acta Mater 55 (2007) 3555–3562.
[24] M. Qasmi, P. Delobelle, Influence of the average roughness rms on the precision of the young's modulus and hardness determination using nanoindentation technique with a berkovich indenter, Surf. Coat. Technol. 201 (2006) 1191–1199.
[25] S.W. Wai, G.M. Spinks, H.R. Brown, M. Swain, Surface roughness: its implications and inference with regards to ultra microindentation measurements of polymer mechanical properties, Polym. Test 23 (2004) 501–507.
[26] C. Walter, T. Antretter, R. Daniel, C. Mitterer, Finite element simulation of the effect of surface roughness on nanoindentation of thin films with spherical indenter, Surf. Coat. Technol. 202 (2007) 1103–1107.
[27] C. Walter, C. Mitterer, 3d and 2d finite element simulation of the effect of surface roughness in nanoindentation of hard coatings, Surf. Coat. Technol. 203 (2008) 3286–3290.
[28] M. Miller, C. Bobko, M. Vandamme, F.J. Ulm, Surface roughness criteria for cement paste nanoindentation, Cement and Concrete Research 38 (2008) 467–476.
[29] E. Donnelly, S.P. Baker, A.L. Boskey, M.C.H. van der Meulen, J. Biomed, Effects of surface roughness and maximum load on the mechanical properties of cancellous bone measured by nanoindentation, J. Biomed. Mater. Res. - Part A 77 (2006) 426–435.
[30] K.D. Bouzakis, N. Michailidis, S. Hadjiyiannis, G. Skordaris, G. Erkens, The effect of specimen roughness and indenter tip geometry on the determination accuracy of thin hard coatings stress–strain laws by nanoindentation, Mater. Charact. 49 (2003) 149–156.
[31] T.H. Fang, W.J. Chang, C.M. Lin, Nanoindentation characterization of zno thin films, Mater. Sci. Eng. A 452–453 (2007) 715–720.
[32] G.B. de Souza, C.E. Foerster, S.L.R. da Silva, F.C. Serbena, C.M. Lepienski, C.A. dos Santos, Hardness and elastic modulus of ion-nitrided titanium obtained by nanoindentation, Surf. Coat. Technol. 191 (2006) 76–82.
[33] G. Rauchs, Optimization-based material parameter identification in indentation testing for finite strain elasto-plasticity, ZAMM Z. Angew. Math. Mech. 86 (2006) 539–562.
[34] J. Deuschle, Mechanics of soft polymers indentation, Doctoral Thesis, Universität Stuttgart, 2008.
[35] M. Johlitz, S. Diebels, Characterisation of a polymer using biaxial tension tests. part i: hyperelasticity, Arch. Appl. Mech. (2010) 1–17. http://dx.doi.org/10.1007/s00419-010-0480-1.
[36] G.A. Holzapfel, Nonlinear Solid Mechanics: A Continuum Approach for Engineering, Lohn Wiley & Sons Ltd, England, 2001.
[37] W. Ehlers, G. Eipper, The simple tension problem at large volumetric strains computed from finite hyperelastic material laws, Acta Mech. 130 (1998) 17–27.
[38] R.W. Penn, Volume changes accompanying the extension of rubber, Trans. Soc. Rheol 14 (1970) 509–517.
[39] S. Hartmann, P. Neff, Polyconvexity of generalized polynomial-type hyperelastic strain energy functions for near-incompressibility, Int. J. Solids Struct. 40 (2003) 2767–2791.
[40] J.C. Simo, R.L. Taylor, Penalty function formulations for incompressible nonlinear elastostatics, Comput. Methods Appl. Mech. Eng. 35 (1982) 107–118.
[41] S. Doll, K. Schweizerhof, On the development of volumetric strain energy functions, J. Appl. Mech. Trans. ASME 67 (2000) 17–21.
[42] J. Nocedal, S.J. Wright, Numerical Optimization, Springer-Verlag, New York, LLC. United States of America, 1999.
[43] H.P. Schwefel, Evolution and Optimum Seeking, Wiley, New York, 1995.
[44] H.G. Beyer, The Theory of Evolution Strategy, Springer, 2001.
[45] K.L. Johnson, Contact Mechanics, Cambridge University Press, 1985.

Identification of Finite Viscoelasticity and Adhesion Effects in Nanoindentation of a Soft Polymer by Inverse Method

Identification of finite viscoelasticity and adhesion effects in nanoindentation of a soft polymer by inverse method

Zhaoyu Chen [a,*], Stefan Diebels [a,*], Nicolas J. Peter [b], Andreas S. Schneider [b]

[a] Chair of Applied Mechanics, Saarland University, PO Box 151150, 66041 Saarbrücken, Germany
[b] INM – Leibniz Institute for New Materials, Metallic Microstructures Group, Campus D2 2, 66123 Saarbrücken, Germany

ARTICLE INFO

ABSTRACT

In the present study a procedure to characterize the finite viscoelasticity and to simultaneously identify the influence of adhesion in nanoindentation experiments of soft polymers is developed. Silicone rubber, which is assumed to be an isotropic elastomer, is chosen to be examined. Different nanoindentation testing protocols are used to visualize and proof the viscoelastic properties and the adhesion behavior of a soft silicone rubber in contact with a Berkovich tip. It could be shown that the analytical solution of linear viscoelastic indentation has some limitations in order to predict the experimental data that contains finite viscoelasticity as well as adhesion effects. The inverse method is applied by using the finite element computation combined with a numerical optimization subroutine. A viscoelastic model at finite strain is chosen to represent the silicone rubber's behavior. The default contact pressure–clearance relationship used in ABAQUS® is modified; a surface-based adhesive behavior in traction–separation law is incorporated into the contact pairs. The real geometry of the Berkovich tip is considered in order to minimize the systematic errors between the numerical model and the experiments. Finally, the parameters of the chosen viscoelastic constitutive model and the adhesive contact model are identified by matching the response of the numerical model with the experimental force–displacement curves. The present model contains the surface adhesion and is verified to show better reproducibility regarding the experiments than the analytical solution. There are several drawbacks of the analytical solution that are also presented in this work.

1. Introduction

Nowadays, nanoindentation is widely applied in metallic and ceramic engineering materials to determine the mechanical properties such as hardness and modulus at the nano- and micro-scale. Since this technique has the considerable advantage to measure the local properties of extremely small volumes with sub-μm and sub-μN resolution, it also became one of the primary testing techniques for the mechanical characterization of polymeric materials and biological tissues. However, a lot of questions still need to be answered about the characterization of soft rubber-like materials by nanoindentation.

First of all, most of the rubber-like polymeric materials show high elastic and viscous material behavior at the same time, called finite viscoelasticity. In the past decades, investigations of viscoelastic effects of polymeric materials using experimental testing, constitutive modeling and numerical computation have been pub-

lished in e.g. [1–11]. Incorporating the phenomenological method in the framework of continuum mechanics, the viscous behavior can be described with strain-like or stress-like internal variables that can be obtained by solving a series of differential evolution equations. Hence, in order to characterize the rubber-like materials, an appropriate finite viscoelastic constitutive model is necessary and the model parameters have to be identified.

The analysis procedure, which is used in most indentation instruments to determine hardness and elastic modulus, is based on the Oliver & Pharr method [12,13]. This analysis method assumes that the material behaves in an elastic–plastic manner and does not exhibit any time-dependent behavior or load rate dependence. In order to identify the viscoelastic behavior of polymers by nanoindentation, two ways have been documented in literature instead of the Oliver & Pharr method. The first method is based on analytical or semi-analytical solutions. These solutions are based on parameters of the respective viscoelastic model and represent the relationship between indentation force and displacement. The model parameters are then obtained by fitting the experimental force–displacement data with the analytical functions. The viscoelastic analytical solutions with respect to different indenter tips can be found e.g. in [14–20]. They are mainly based

* Corresponding authors. Tel.: +49 (0)681 302x2169 (Z. Chen), tel.: +49 (0)681 302x2887 (S. Diebels).

E-mail addresses: zh.chen@mx.uni-saarland.de (Z. Chen), s.diebels@mx.uni-saarland.de (S. Diebels).

on the linear viscoelastic contact theory at small strain developed by Lee and Radok [21], Ting and Graham [22,23] and Johnson [24]. Since the linear viscoelastic contact solutions are derived from the Hertz elastic contact theory by the correspondence principle, this method is restricted by yielding accurate identification only for specific linear viscoelastic models under fixed experimental processes. Furthermore, effects like non-linear friction, adhesion and surface roughness in nanoindentation experiments are not taken into account in the analytical solutions. The second method, the so called inverse method, is performed by combining finite element (FE) modeling and numerical optimization. In this method, the objective function, which is the difference between experimental and numerical data, is minimized with respect to the model parameters using numerical optimization. The parameters of the constitutive models are identified as the optimized solution. Huber et al. [25–28] have been the first to apply this method in indentation. They used neural networks to identify the material parameters from indentation experiments on metals. However, the inverse method is still a new topic regarding nanoindentation problems of polymeric materials. Hartmann et al. [29] identified the viscoplastic model parameters with uniaxial tests and validated them using indentation tests. Rauchs et al. [30,31] employed a gradient-based numerical optimization method to identify viscous hyperelastic and elasto-viscoplastic material parameters. Guessasma et al. [32] determined viscoelastic properties of biopolymer composite materials using the finite element calculation and nanoindentation experiments. Le Saux et al. [33] identified the constitutive model for rubber-like elasticity from micro-indentation tests. In our previous work [34–38], the inverse method is applied to identify the hyperelastic or linear viscoelastic properties of polymers and to quantify the friction and surface roughness effects during nanoindentation in a numerical way. As the inverse method permits us to handle any material model with non-linear properties and to include additional effects in the numerical model, it is an useful new method to deal with the problems of identifying rate-dependent material properties from nanoindentation.

As mentioned at the beginning, nanoindentation has a considerable advantage to determine local properties from continuously measured force–displacement data with high resolution. Unfortunately, there are various problems that influence the actual material response during indentation, e.g. friction, adhesion, surface roughness, and the indentation process associated factors. These problems result in a systematic error between the numerical and the experimental results that often leads to even larger errors in the parameter identification [31,36,37,39–41]. Therefore, a certain knowledge about the influence of these factors and basic investigations are indispensable to characterize the material accurately by the inverse method. This work focuses on the viscoelastic properties of a silicone rubber and the adhesion between the indenter and the polymer surface. The influence of friction and surface roughness has already been investigated in our recent work [36,37].

Adhesion, as interaction between two surfaces, is size dependent and is strongly influencing nanoindentation experiments on soft materials [24]. The adhesive behavior discovered in experimental studies has been reported to be visible as negative forces in the force–displacement curve [42–45], residual displacement or non-zero contact area when the load is reduced to zero [46,45,47]. These observations suggest that the adhesion energy at the tip-sample interface is a significant parameter for soft materials and should be taken into account for a consistent determination of the mechanical properties by nanoindentation. There are three adhesive contact models available, namely JKR (Johnson–Kendall–Roberts) [48], DMT (Derjaguin–Muller–Toporov) [49] and MD (Maugis–Dugdale) [50]. JKR considers the short-range surface forces, which only act inside the contact area. DMT assumes

long-range surface forces acting only outside the contact area. MD studies the periphery of the tip-sample interface modeled as a crack failing at its theoretical strength. These models have been used to evaluate analytically the adhesion effects on the contact area and, additionally, on the determined hardness and modulus. For example, Gupta et al. [46] found that if the adhesive interaction between a conospherical tip and polydimethylsiloxane (PDMS) is analyzed with the JKR model, the difference in elastic modulus at different peak loads could be explained. Liao et al. [44] applied a hybrid model that combines Hertzian theory and the JKR model to evaluate the elastic modulus and adhesion work by fitting the experimental data. All three adhesive contact models were compared with the Hertz model by Zhao et al. [51], who suggested that the MD model was the most suitable theory to deal with adhesive forces in contact problems at the nano-scale. In order to quantify the adhesion effects using the inverse method as described above, it is necessary to include an adhesive contact mechanics into the numerical modeling. Wang et al. [52] incorporated adhesive interactions with FE computations in ABAQUS® by user-defined elements. A bilinear force–separation relationship was applied to simulate the adhesive contact behavior between a tungsten tip and an organic film. A typical contact between a sphere and a flat substrate was simulated in ANSYS® [53] with the presence of adhesion forces. The general FE simulation model of the investigated contact processes was modified, and the interfacial interactions of the Lennard–Johns potential were incorporated into the contact cells. Zhang and Zhao [54] modeled a nanowire indentation experiment by a non-linear softening spring at the adhesive contact.

In the present study it is our goal to develop a procedure to characterize the finite viscoelasticity and to identify simultaneously the influence of adhesion in nanoindentation experiments of soft polymers. Silicone rubber, which can be assumed to be an isotropic elastomer, is chosen to be investigated. The inverse method is applied using FE computation in ABAQUS® in combination with a numerical optimization subroutine. The parameters of the chosen viscoelastic constitutive model and of the adhesive contact model can then be identified by matching the response of the numerical model with the experimental force–displacement curves. The real geometry of the Berkovich tip is taken into account to minimize the systematic error between the numerical model and the experiments. This article is organized as the following: the nanoindentation experiments, the sample preparation as well as the sample surface characterization are described in Section 2. The numerical implementation and the optimization procedure are presented in Section 3, while Section 4 explains the results of the identified model parameters and the adhesion effects. Finally, the conclusions and the discussion are given in Section 5.

2. Nanoindentation experiments

2.1. Experimental device

The experiments[1] have been performed on a TI 900 TriboIndenter® of Hysitron Inc., MN, USA. The Hysitron TriboIndenter® provides quantitative testing capabilities with both normal and lateral force loading configurations. The transducer used in the TriboIndenter® is based on three-plate capacitor technology providing simultaneous actuation and measurement of force and displacement with a sub-nN and sub-nm resolution, respectively. The device uses a drift correction procedure that is very important for precise measurements at the nanoscale. In the quasi-static mode, the TriboIndenter® has

---

[1] The nanoindentation experiments were performed using the device of the chair of material science and methodology at Saarland University under the direction of Prof. H. Vehoff.
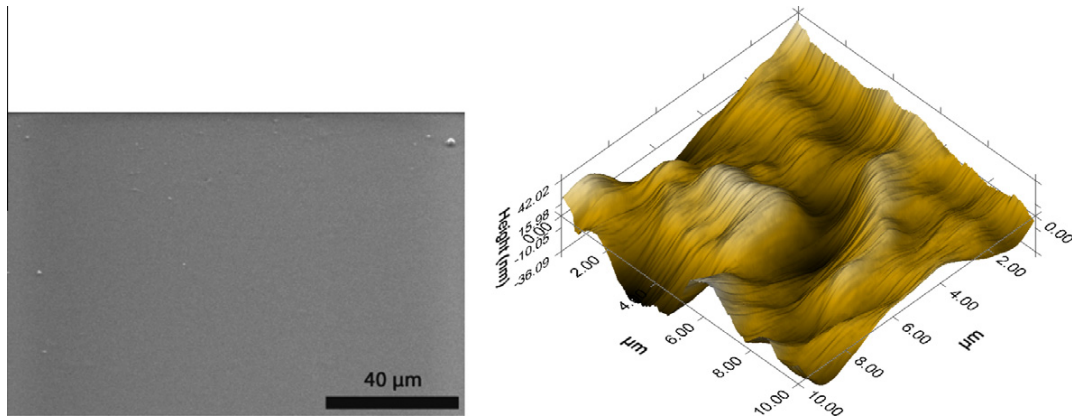
Fig. 1. The surface topography of the tested silicone rubber: 2D surface by scanning electron microscopy (left), 3D topography from in situ SPM imaging mode using a Berkovich indentation tip (right).

a force noise floor better than 100 nN and a displacement noise floor less than 0.2 nm. A three-sided pyramidal diamond tip, known as Berkovich geometry, is used in all experiments.

2.2. Sample preparation and surface characterization

The investigated material is the silicone rubber ELASTOSIL® RT 625, produced by WACKER Chemie GmbH in Germany. It consists of pourable, addition-curing two components and vulcanizes at room temperature. The two transparent and colorless components ELASTOSIL A and ELASTOSIL B are mixed together with a weight ratio of 9:1 by stirring. After degassing, the mixture is poured in a cylindrical mold and cured at room temperature for 24 h. This mixture is characterized by its high elasticity and low viscosity allowing strains up to 600%. Theoretically, the silicone rubber can be assumed to be isotropic with an experimentally determined strength of 6.5 MPa [55].

The final specimen for the testing is of cylindrical shape with a diameter of 10 mm and a thickness about 2.02 mm. It is well known from literature that a surface roughness in the range of the indentation depth or even higher has a significant influence on the force–displacement data of nanoindentation experiments [37,56,57]. Therefore, a characterization of the present roughness is necessary and was performed by scanning electron microscopy (SEM) and the in situ SPM Imaging mode of the Hysitron® indenter.[2] A FEI™ Versa 3D electron microscope is used in low vacuum mode to prevent the deposition of a conductive layer that might change the surface topography and to avoid charging effects that limit the resolution of the electron microscope. To capture the image in Fig. 1(left) at a magnification of 1500, the sample is tilted to 52° and a voltage of 10 kV is applied with a chamber pressure of 0.5 mbar. The two-dimensional optical analysis clearly shows a perfectly smooth surface in the micron range. The in situ SPM imaging mode is then used to precisely quantify the local roughness of the used sample by applying 2 μN normal force with the Berkovich tip to be sure that the tip is in contact with the surface. This force is hold constant during the imaging and the displacement is recorded in three dimensions. The local surface roughness is illustrated in Fig. 1(right) and resulted in a RMS value of around 12 nm, which is not comparable to a maximum displacement of 3 μm during indentation. The characterized smooth surface implies two side-effects: on the one hand, it guarantees that the influence of the surface roughness is negligible according to [37]; on the other hand, adhe-

sion forces are very likely to be present, as there is a contact between two very smooth surfaces. Hence, the adhesion effects may have a potential influence on the measured force–displacement data.

2.3. Nanoindentation testing protocol and results

In the present study, all experiments have been performed in a quasi-static process by either closed-loop force or displacement controlled mode with peak values of 50 μN or 3000 nm, respectively.

The first experiment is performed with a cyclic testing protocol that contains both a loading and an unloading step of the same constant loading rates. The viscoelastic properties of the silicone rubber are characterized by the rate dependent viscous dissipation, the so called hysteresis loop. Fig. 2(right) shows that the hysteresis loop is differently pronounced for the chosen rates in the load controlled mode. In contrast, the hysteresis loops obtained by the displacement controlled mode, only show slight differences. It is proven in [58] that the hysteresis loop depends on the ratio of the process time to the relaxation time r. The hysteresis loops tend to disappear if the loading rate is sufficiently "fast" or "slow". In these cases, the instantaneous elasticity and equilibrium elasticity are represented, respectively. Therefore, it can be supposed that the chosen loading rates in Fig. 2(left) are in the range of sufficiently fast or slow. If this would not be the case, the viscosity of the investigated material would have to be barely noticeable. The adhesion effects can be observed by the negative force at zero displacement and residual displacement after withdrawing the load, as shown in Fig. 2.

For the second type of protocol, a holding step of constant force or displacement is added between the loading and unloading step of the load function used in the the cyclic testing protocol. The relaxation of the applied force as well as the deformation creep can be observed from the holding stage. The resulting observations are distinctive evidences for the viscoelastic behavior of the investigated material. The relaxation protocol uses the described load function in displacement controlled mode with a holding step lasting for 60 s at the peak displacement of 3000 nm. The loading and unloading steps were performed in 20 s, respectively. At the end of the experiment, similar to Fig. 2(left), a negative force value is observed even for zero displacement. This phenomenon is an evidence that adhesion is present during the indentation process [42–45]. Fig. 3(right) only presents the relaxation behavior of the experiment. The force relaxes 6% with respect to the maximum force within 60 s towards the equilibrium state. Fig. 4 demonstrates the creep behavior of the material. The force is ramped to

---

[2] The surface scanning was performed using the device in Leibniz Institute for New Materials, Saarbrücken, Germany
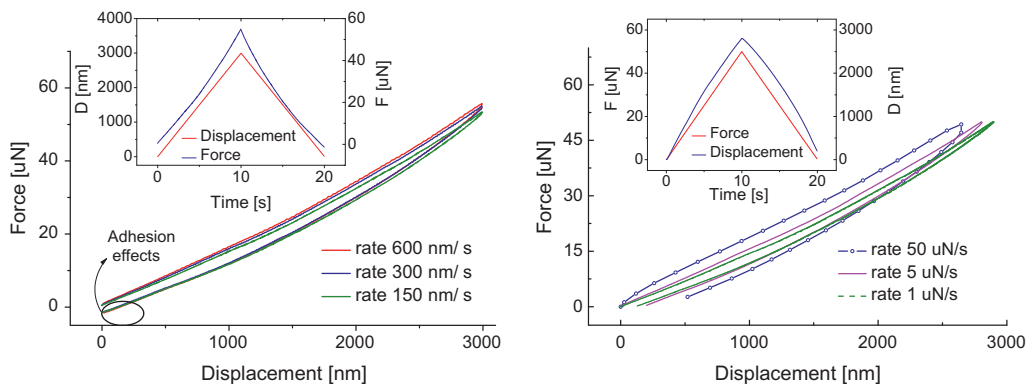
Fig. 2. The force–displacement curves of nanoindentation experiments on silicone rubber using the cyclic testing protocol: displacement controlled (DC) (left), load controlled (LC) (right).
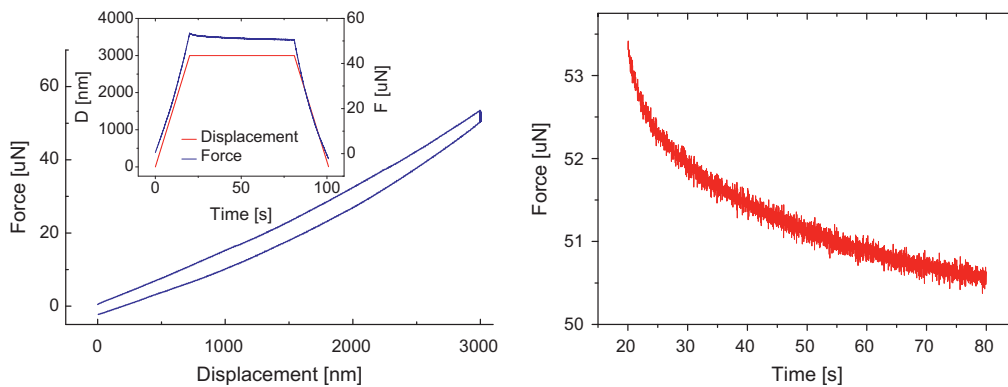
Fig. 3. The force–displacement curves of nanoindentation experiments on silicone rubber using the relaxation testing protocol: force–displacement curve (left), Relaxation behavior (right).
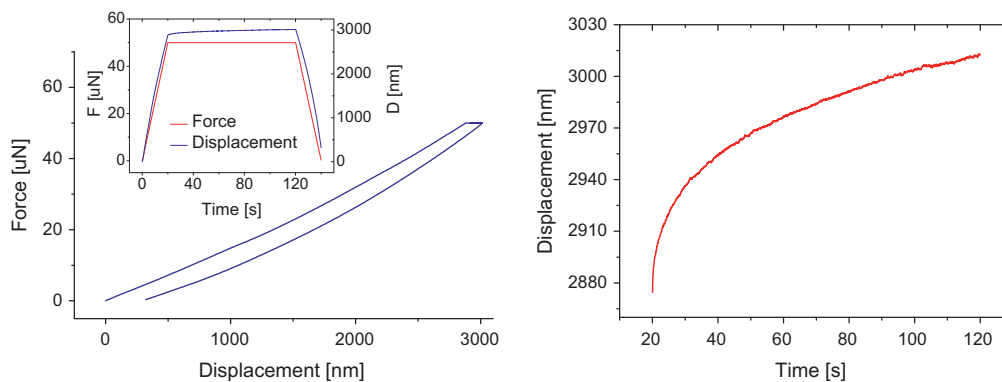
Fig. 4. The force–displacement curves of nanoindentation experiments on silicone rubber using the creep testing protocol: force–displacement curve (left), Creep behavior (right).

the peak force of 50 μN in 20 s. Subsequently it is reduced to zero with the same rate after holding the peak force for 100 s. In the force–displacement curve, it is obvious that the residual displacement is comparably large. The reasons may be viscous dissipation as well as adhesion effects [46,45,47]. The displacement increases about 5% during the holding step and could reach the equilibrium state if the holding time would be long enough. Consequently, the viscoelastic behavior and the adhesion effect could be identified in the force–displacement data of the experiments.

The third type of experiments follows the monotonic testing protocol, in which a stepwise ramping to the peak load or displacement is created by alternating loading and holding steps. It is followed by a stepwise decrease back to zero using the same steps. Displacement control mode uses a loading and unloading rate of 200 nm/s and shows holding steps at 1000 nm, 2000 nm and 3000 nm, while in force control mode the steps are performed at 20 N, 30 N, 40 N and 50 N with rates of 2 N/s. All holding steps last for 20 s. As shown in Fig. 5(left), if the displacement is held
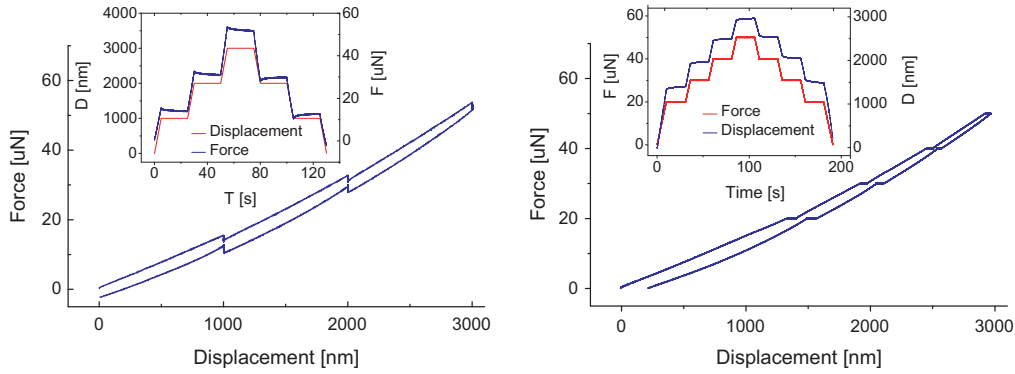
Fig. 5. The force–displacement curves of nanoindentation experiments on silicone rubber using the monotonic testing protocol: displacement controlled (DC) (left), load controlled (LC) (right).

constant, the force relaxes during the loading stage but increases during the unloading stage. Similar results are also obtained from the force controlled testing that is presented in Fig. 5(right). If the holding stage is sufficiently long, the two points should overlap each other. The cross point can be considered as the equilibrium point. Usually, if the relaxation time is extra long, the average values of the static states after the relaxation of loading and unloading stages could be considered as approximated equilibrium points. The adhesion effects are shown clearly in both the displacement and the force controlled monotonic force–displacement curves.

3. Finite viscoelasticity, FE model and inverse method

3.1. Constitutive models for viscoelasticity at finite strain of polymers

In order to construct a phenomenological 3D viscoelastic model, a one-dimensional rheological model is introduced, as illustrated in Fig. 6. An extra spring is connected in parallel with n Maxwell elements. It is a useful model to represent quantitatively the mechanical behavior of real viscoelastic materials. As the extra spring represents the elasticity in the relaxed state, the Maxwell elements display the viscous material response considering a number of discrete relaxation times $r_j \in (0, \infty), j = 1, \ldots, n$. The finite viscoelasticity is characterized explicitly by means of an internal variable model following the concept of Simo [59] and Holzapfel and Simo [3]. These internal variables can be assumed to be the strains or stresses of the Maxwell elements, like the stresses $\mathbf{Q}_j$ as shown in Fig. 6. A three-dimensional viscoelastic model suitable for finite strains and small perturbations away from the equilibrium state is postulated on the theory of compressible hyperelas-
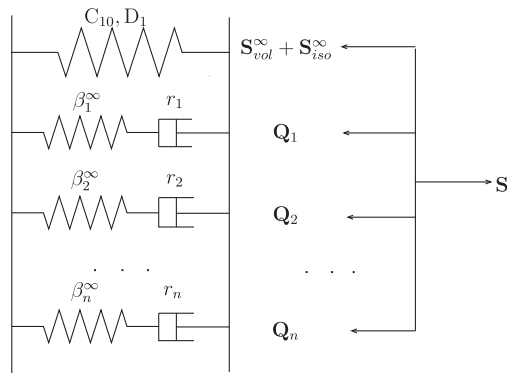
Fig. 6. Rheological model of the viscoelasticity with $j = 1, \ldots, n$ Maxwell elements.

ticity within the isothermal regime. The Helmholtz free-energy function Ψ uses the multiplicative decomposition of the deformation gradient into a so-called volumetric part and an isochoric part. Such a type of formulation is preferred for numerical realization using the finite element method considering the nearly incompressibility of the rubber-like materials. ABAQUS® modified the viscoelastic damage model created by Simo [59] to describe three-dimensional finite-strain viscoelasticity. The model implemented in ABAQUS® is a time domain generalization of either hyperelastic or hyperfoam constitutive model using the volumetric/deviatoric-split hereditary integral in the reference configuration for large strain materials and a standard push-forward operator [59,60].

At the beginning, the terms of finite strain continuum mechanics are briefly reviewed which are widely known. First, we consider the multiplicative decomposition of deformation gradient $\mathbf{F}$, the right Cauchy Green deformation tensor $\mathbf{C} = \mathbf{F}^T \cdot \mathbf{F}$ and the left Cauchy Green deformation tensor $\mathbf{B} = \mathbf{F} \cdot \mathbf{F}^T$ into volumetric parts and isochoric parts

$$\mathbf{F} = (J^{1/3}\mathbf{I})\overline{\mathbf{F}} = (J^{1/3})\overline{\mathbf{F}}, \quad \mathbf{C} = (J^{2/3}\mathbf{I})\overline{\mathbf{C}} = (J^{2/3})\overline{\mathbf{C}}, \quad \mathbf{B} = (J^{2/3}\mathbf{I})\overline{\mathbf{B}}$$
$$= (J^{2/3})\overline{\mathbf{B}}. \tag{1}$$

The terms $J^{1/3}\mathbf{I}$ and $J^{2/3}\mathbf{I}$ are related to the volume-changing deformation, $J = \det\mathbf{F}$, while $\overline{\mathbf{F}}, \overline{\mathbf{C}} = \overline{\mathbf{F}}^T\overline{\mathbf{F}}$ and $\overline{\mathbf{B}} = \overline{\mathbf{F}}\,\overline{\mathbf{F}}^T$ are associated with volume-preserving deformations leading to

$$\det\overline{\mathbf{F}} = 1, \quad \det\overline{\mathbf{C}} = \det\overline{\mathbf{B}} = (\det\overline{\mathbf{F}})^2 = 1. \tag{2}$$

The strain invariants $\bar{I}_a (a = 1, 2, 3)$ are the three modified principle invariants of $\overline{\mathbf{C}}$ and $\overline{\mathbf{B}}$, i.e.

$$\bar{I}_1 = \text{tr}\overline{\mathbf{C}} = \text{tr}\overline{\mathbf{B}}, \tag{3}$$

$$\bar{I}_2 = \frac{1}{2}[(\text{tr}\overline{\mathbf{C}})^2 - \text{tr}(\overline{\mathbf{C}}^2)] = \frac{1}{2}[(\text{tr}\overline{\mathbf{B}})^2 - \text{tr}(\overline{\mathbf{B}}^2)], \tag{4}$$

$$\bar{I}_3 = \det\overline{\mathbf{C}} = \det\overline{\mathbf{B}} = 1, \tag{5}$$

with the relationships to the principle invariants

$$\bar{I}_1 = J^{-2/3}I_1, \quad \bar{I}_2 = J^{-4/3}I_2, \quad \bar{I}_3 = 1. \tag{6}$$

The change of the free energy Ψ within an isothermal viscoelastic process from the reference to the current configuration is given as

$$\Psi(\mathbf{C}, \mathbf{\Gamma_1} \ldots \mathbf{\Gamma_n}) = \Psi_{vol}^\infty(J) + \Psi_{iso}^\infty(\overline{\mathbf{C}}) + \sum_{j=1}^n \Upsilon_j(\overline{\mathbf{C}}, \mathbf{\Gamma}_j). \tag{7}$$

It is assumed that each contribution to the free energy must satisfy the normalization condition, i.e.

$$\Psi^{\infty}_{vol}(1) = 0, \quad \Psi^{\infty}_{iso}(\mathbf{I}) = 0, \quad \Upsilon_j(\mathbf{I}, \mathbf{I}) = 0, j = 1, \ldots, n. \tag{8}$$

The first two terms in Eq. (7) are strain-energy per unit reference volume stalled in the extra spring in Fig. 6. They characterize the equilibrium state of the viscoelastic solid and they can be used to describe the volumetric elastic response and the isochoric elastic response of sufficiently slow processes, i.e. $t \to \infty$, respectively. The additional third term in Eq. (7) is responsible for the viscoelastic contribution. The scalar-valued functions Υ_j, $j = 1, \ldots, n$ represent the configurational free energy stalled in the springs of the parallel Maxwell elements in Fig. 6 and define the non-equilibrium state, i.e. the behavior of creep and relaxation. Experimental investigations have shown that in many cases the viscoelastic behavior is mainly related to the isochoric part of the deformation [5]. Thus, the volumetric response remains purely elastic and the free energies Υ_j are functions of the isochoric part of $\mathbf{C}$ and a set of strain-like internal variables $\mathbf{\Gamma}_j$, $j = 1, \ldots, n$. They are identified to be inelastic strains similar to the modified right Cauchy–Green tensor $\bar{\mathbf{C}}$. $\mathbf{\Gamma}_j$ describes the relaxation and creep behavior of the material in $j = 1, \ldots, n$ viscoelastic processes. The corresponding constitutive equations describing the viscoelastic behavior at finite strains can be obtained by using the second law of the thermodynamics in the form of the Clausius–Planck inequality. The physical expression for the second Piola–Kirchhoff stress $\mathbf{S}$ is in the form

$$\mathbf{S} = 2\frac{\partial \Psi(\mathbf{C}, \mathbf{\Gamma_1} \ldots \mathbf{\Gamma_n})}{\partial \mathbf{C}} = \mathbf{S}^{\infty}_{vol} + \mathbf{S}^{\infty}_{iso} + \sum_{j=1}^{n} \mathbf{Q}_j, \tag{9}$$

and the non-negative internal dissipation $\mathcal{D}_{int}$ is

$$\mathcal{D}_{int} = -\sum_{j=1}^{n} 2\frac{\partial \Upsilon_j(\bar{\mathbf{C}}, \mathbf{\Gamma}_j)}{\partial \mathbf{\Gamma}_j} : \frac{1}{2}\dot{\mathbf{\Gamma}}_j \geqslant 0. \tag{10}$$

The stress is split into the volumetric part $\mathbf{S}^{\infty}_{vol}$, isochoric pure elastic part $\mathbf{S}^{\infty}_{iso}$ and the viscoelastic part $\sum_{j=1}^{n}\mathbf{Q}_j$, with the definitions

$$\mathbf{S}^{\infty}_{vol} = J\frac{\mathrm{d}\Psi(J)}{\mathrm{d}J}\mathbf{C}^{-1}, \qquad \mathbf{S}^{\infty}_{iso} = J^{-2/3}\mathbb{P} : 2\frac{\mathrm{d}\Psi(\bar{\mathbf{C}})}{\mathrm{d}\bar{\mathbf{C}}}, \tag{11}$$

herein, the fourth-order projection tensor $\mathbb{P} = \mathbb{I} - \frac{1}{3}\mathbf{C}^{-1} \otimes \mathbf{C}$ is the deviatoric operator in the reference configuration. In Eq. (9), the additional internal tensor variables $\mathbf{Q}_j$, $j = 1, \ldots, n$ are introduced, which may be interpreted as non-equilibrium stresses characterized by the viscoelastic response. By the analogy with the second term of Eq. (11) and with the linear viscoelasticity, one can define the internal constitutive equations (for details, please see [61], capital 6)

$$\mathbf{Q}_j = J^{-2/3}\mathbb{P} : 2\frac{\partial \Upsilon_j(\bar{\mathbf{C}}, \mathbf{\Gamma}_j)}{\partial \bar{\mathbf{C}}} = -2\frac{\partial \Upsilon_j(\bar{\mathbf{C}}, \mathbf{\Gamma}_j)}{\partial \mathbf{\Gamma}_j}, j = 1, \ldots, n. \tag{12}$$

Hence, the internal dissipation $\mathcal{D}_{int}$ in Eq. (10) can be equivalently expressed as $\mathbf{Q}_j : \dot{\mathbf{\Gamma}}_j/2 \geqslant 0, j = 1, \ldots, n$. In the condition of thermodynamic equilibrium, i.e. for $t \to \infty$, the internal stresses $\mathbf{Q}_j$ disappear and consequently, the dissipation $\mathcal{D}_{int}$ at equilibrium is zero. In other words, general finite elasticity is recovered at the thermodynamic equilibrium state.

The evolution equations which govern the internal variables $\mathbf{Q}_j$, $j = 1, \ldots, n$ should be specified in a suitable way so that the viscous dissipation $\mathcal{D}_{int}$, i.e. the inequality Eq. (10), is satisfied. Considering the efficient time integration algorithms that are suitable for the finite element procedure, we choose linear evolution equations for each of the internal variables according to [59,3]

$$\dot{\mathbf{Q}}_j + \frac{\mathbf{Q}_j}{r_j} = \dot{\mathbf{S}}_{isoj}, \quad j = 1, \ldots, n, \tag{13}$$

herein, the tensors $\mathbf{S}_{isoj}$ characterize the isochoric second Piola–Kirchhoff stresses corresponding to the strain energy $\Psi_{isoj}(\bar{\mathbf{C}})$ which is responsible for the j-relaxation process with the relaxation time r_j, $j = 1, \ldots, n$. According to Govindjee and Simo [62]: if a viscoelastic medium such as a thermoplastic elastomer, is composed of identical polymer chains, e.g. silicone rubber, we can assume that Ψ_{isoj} is replaceable by Ψ^{∞}_{iso}

$$\Psi_{isoj}(\bar{\mathbf{C}}) = \beta^{\infty}_j \Psi^{\infty}_{iso}(\bar{\mathbf{C}}), \quad j = 1, \ldots, n, \tag{14}$$

where $\beta^{\infty}_j \in [0, \infty)$ are given as non-dimensional strain-energy factors associated with the relaxation time r_j, $j = 1, \ldots, n$. Finally, the stresses $\mathbf{S}_{isoj}$ can be replaced by $\mathbf{S}^{\infty}_{iso}$ as

$$\mathbf{S}_{isoj} = J^{-2/3}\mathbb{P} : 2\beta^{\infty}_j\frac{\partial \Psi(\bar{\mathbf{C}})}{\partial \bar{\mathbf{C}}} = \beta^{\infty}_j\mathbf{S}^{\infty}_{iso}(\bar{\mathbf{C}}), \quad j = 1, \ldots, n. \tag{15}$$

The free energy of the Neo-Hookean form involves only two parameters and provides a mathematically simple and reliable constitutive model for the non-linear deformation behavior of isotropic rubber-like materials. It is physically-founded and includes typical effects known from non-linear elasticity at slightly finite strain [63,64]. Therefore, the finite elastic response of the considered silicone rubber under nanoindentation is assumed to be characterized by using the Neo-Hookean model. In particular, the free energy of the extra spring in Fig. 6, which is responsible for the equilibrium elastic behavior, can be expressed as

$$\Psi(\mathbf{C}) = \Psi^{\infty}_{vol}(J) + \Psi^{\infty}_{iso}(\bar{\mathbf{C}}) = \frac{1}{D_1}(J - 1)^2 + C_{10}(\bar{I}_1 - 3). \tag{16}$$

The initial shear modulus μ_0 and the initial compression modulus K_0 are related to the coefficients in the following way:

$$\mu_0 = 2\frac{\partial \Psi_{iso}}{\partial \bar{I}_a}|_{\bar{I}_a \to 1} = 2C_{10}, \qquad K_0 = \frac{\partial^2 \Psi_{vol}}{\partial J^2}|_{J \to 1} = \frac{2}{D_1}. \tag{17}$$

The compressibility parameter D_1 can be interpreted as a penalty parameter that enforces incompressibility if small values are chosen. The strain energy Ψ_{isoj} can be defined according to Eq. (14)

$$\Psi_{isoj}(\bar{\mathbf{C}}) = \beta^{\infty}_j C_{10}(\bar{I}_1 - 3), \quad j = 1, \ldots, n, \tag{18}$$

The second Piola–Kirchhoff stress tensor $\mathbf{S}$ can be calculated directly with the free energy function Eq. (16). With the relations $\tau = \mathbf{F} \cdot \mathbf{S} \cdot \mathbf{F}^{\mathrm{T}}$ and $\mathbf{T} = \frac{1}{J}\tau$ the Kiochhoff stress τ and the Cauchy stress $\mathbf{T}$ can be derived as

$$\tau = \mathbf{F} \cdot \mathbf{S}^{\infty}_{vol} \cdot \mathbf{F}^{\mathrm{T}} + \mathbf{F} \cdot \mathbf{S}^{\infty}_{iso} \cdot \mathbf{F}^{\mathrm{T}} + \mathbf{F} \cdot \sum_{j=1}^{n} \mathbf{Q}_j \cdot \mathbf{F}^{\mathrm{T}}, \tag{19}$$

$$\mathbf{T} = \frac{2}{D_1}(J - 1)J + \frac{1}{J}\left(2C_{10}\bar{\mathbf{B}} - \frac{2}{3}C_{10}\bar{I}_1\mathbf{I}\right) + \frac{1}{J}\mathbf{F} \cdot \sum_{j=1}^{n} \mathbf{Q}_j \cdot \mathbf{F}^{\mathrm{T}}. \tag{20}$$

The evolution equations in the linear differential form Eq. (13) can be solved by an implicit Euler-backward integration scheme. Considering the time interval $[t_n, t_{n+1}]$ we define the time step $\Delta t := t_{n+1} - t_n$. By using the basic approach for a time-dependent variable one obtains the equations for each Maxwell element

$$\mathbf{Q}_j(t_{n+1}) = \beta^{\infty}_j \xi_j \mathbf{S}^{\infty}_{iso}(t_{n+1}) + \mathcal{H}_j(t_n), \quad j = 1, \ldots, n, \tag{21}$$

with the definition

$$\xi_j = \frac{r_j}{r_j + \Delta t}, \quad \mathcal{H}_j(t_n) = \xi_j\left\{\mathbf{Q}_j(t_n) - \beta^{\infty}_j\mathbf{S}^{\infty}_{iso}(t_n)\right\}, \quad j = 1, \ldots, n. \tag{22}$$

3.2. Finite element model with adhesive contact

Generally speaking, a three dimensional model is necessary to represent a potential real experimental setup. However, the computing time occupies a large part in the inverse method and is,

as a consequence, a key problem of the method. This often results in a trade-off between the computing cost and the quality of the numerical model. For instance, a 2D plane model or an axisymmetric model is used most commonly to save the computing cost. In this study, an axisymmetric 2D modeling assumption is preferred, because the silicone rubber is isotropic and the Berkovich indentation tip can be represented by an effective conical indenter with a half angle of 70.3°. The boundary value problem of the nanoindentation is modeled by using the finite element code, e.g. ABAQUS® 6.11.

It is hard to imagine the three pyramidal sides to end in a sharp point at the nanoscale and, additionally, the tip could have been attrited during previous experiments. Therefore, it is necessary to capture the real tip geometry in order to minimize the systematic error in the force–displacement curves. As a first step, the shape of the Berkovich tip is scanned in 3D by the in situ SPM imaging mode stalled in the TriboIndenter®. The matrix data of the 3D scanning is compiled into CATIA® to calculate the radius of the blunt tip as shown in Fig. 7(left). The effective conical edge is combined with the tip curvature by the smooth transition technique as illustrated in Fig. 7(right). The real tip geometry can then be imported into ABAQUS to create the indenter part. For the FE model, the tip can be assumed to be a rigid body compared to the soft polymer. The geometrical size of the polymer sample is 2 μm × 2 μm, which is sufficiently large to obtain a homogeneous stress distribution at the bottom and on the side boundaries of the model. For each studied configuration, the mesh convergence is checked by more than 100,000 degrees of freedom. It shows that a coarser mesh, consisting of at least 10,000 degrees of freedom, can give converged results. To account for the large localized deformation in contact, it is essential that the density of nodes under the indentation tip is high enough. The rigid tip is fixed in the horizontal direction and a vertical displacement is applied to its reference point. The bottom nodes of the mesh are fixed.

Concerning the numerical treatment of the contact problem, a contact pair is formed with the tip as the master surface and the layer as the slave surface. Friction is negligible if the indentation depth is small compared to the layer thickness according to numerical results of our previous work [36]. Hence, here we only focus on the normal contact and neglect the tangential behavior. The default contact pressure-clearance relationship used in ABAQUS®/Standard 6.11 is referred as the "hard" contact model. In this case, the formulation of the normal contact is used as a constraint for non-penetration, which treats the normal contact as an unilateral constraint problem. It only transmits pressure once the surfaces are in contact within a contact zone c, as shown in Fig. 8(left). However, this interaction model is not sufficient to simulate the real experimental behavior as adhesion is not taken into account. As a result, an adhesion zone is added to the contact zone forming an interaction area of radius $c + a$. The adhesive behavior is implemented as an interaction of the contact pair. It is defined as a surface-based cohesive behavior in ABAQUS® with a traction–separation relationship as shown in Fig. 8(right), which assumes initially linear elastic behavior followed by the initiation and the evolution of damage. The elastic behavior is written in terms of an adhesive stiffness $\mathbf{K} = [K_{nn}, K_{ss}, K_{tt}]^T$ that relates the stresses to the separation at the damage initiation $\boldsymbol{\delta}^0 = [\delta_{nn}^0, \delta_{ss}^0, \delta_{tt}^0]^T$ across the interface. The process of degradation begins when the contact separation satisfies a certain damage initiation criteria related to $\boldsymbol{\delta}^0$. A linear or exponential damage evolution law describes the rate at which the adhesive stiffness $\mathbf{K}$ is degraded once the corresponding initiation criterion is reached. The evolution laws are defined with a separation at the complete failure δ_{nn}^t and the non-dimensional exponential parameter α^E.

3.3. Optimization procedure

At the optimization procedure, the vector of containing parameters of material and adhesive contact model $\boldsymbol{\kappa} := \left\{ C_{10}, D_1, \beta_j^\infty, r^j, K_{nn}, K_{ss}, K_{tt}, \delta_{nn}^0, \delta_{nn}^t, \text{and/or } \alpha^E, j = 1, \ldots, n \right\}$ has to be modified until a close match between the experimental data and the prediction of the numerical model is achieved. For that rea-
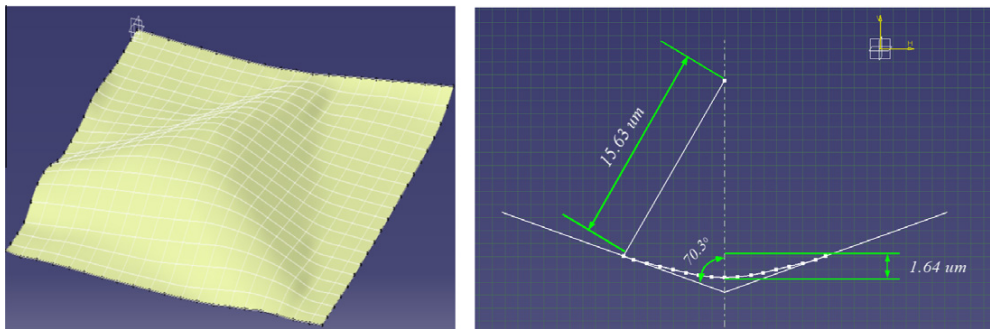
Fig. 7. 3D scanning image of the tip shape geometry (left) and the 2D effective conical indenter with a spherical tip that originated from the 3D scanning data (right).
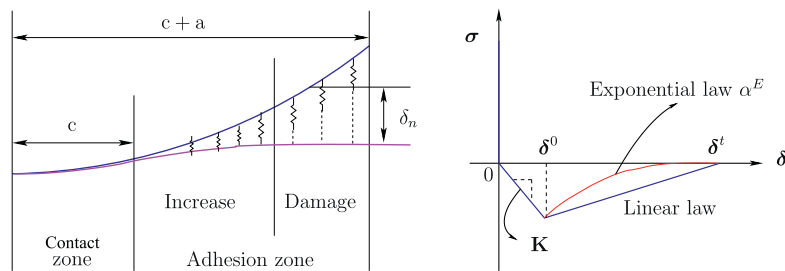
Fig. 8. Adhesive contact geometry (left), traction–separation relationship with a linear or exponential damage evolution law in adhesive contacts (right).

son the distance function $f(\boldsymbol{\kappa})$, which is called objective function of the least squares type has to be minimized to find the optimal set $\boldsymbol{\kappa}$

$$f(\boldsymbol{\kappa}) := \frac{\|\mathbf{B}^{num} - \widehat{\mathbf{B}}^{exp}\|}{\|\widehat{\mathbf{B}}^{exp}\|} \to \text{Min} f(\boldsymbol{\kappa}). \tag{23}$$

Herein

$$\widehat{\mathbf{B}}^{exp} = \mathbf{P}(\mathbf{B}^{exp}) = \left[B_{t1}^{exp}, B_{t2}^{exp}, B_{t3}^{exp}, \ldots\right]^{\mathrm{T}}, \tag{24}$$

is the vector of the experimental force or displacement data $\mathbf{B}^{exp}$ at each time increment. It is an interpolation of the experimental results by using the introduced projection operator $\mathbf{P}$, for details please see [65]. The force or displacement vectors, obtained from the models at the same time increments as the interpolated data $\widehat{\mathbf{B}}^{exp}$ with an arbitrary set of material parameters, are called

$$\mathbf{B}^{num} = \left[B_{t1}^{num}, B_{t2}^{num}, B_{t3}^{num}, \ldots\right]^{\mathrm{T}}. \tag{25}$$

The choice of the optimization-based method for minimizing an objective function is a topic of interest. It is generally advised to use globally convergent optimization algorithms whenever possible. These algorithms are simulated annealing or genetic algorithms, such as evolutionary algorithms or deterministic algorithms like the Simplex method. The gradient-based algorithm is full of the troublesome gradient calculation and the further drawback of local convergence. Genetic or evolutionary algorithms are globally convergent and are the only useful choice in a multiobjective optimization. Therefore, to update the initially guessed material parameter vector $\boldsymbol{\kappa}$, the evolution strategy based on principles of biological evolution, is employed. It works with a Genetic Algorithm, more details have been explained in [34].

4. Identified model parameters and adhesion effects

The experimental results in Section 2.3 only show slight viscoelastic behavior in both the relaxation and the creep tests. Therefore, two Maxwell-elements are expected to sufficiently represent the relaxation spectrum. It is assumed that the separa-

tion is the same for all three directions at the initial damage, in order to simplify the identification of the adhesive model. Not only the linear, but also the exponential evolution laws of damage are taken into account in the model. The force–displacement data of the relaxation and creep experiments in load and displacement controlled mode, respectively, are used as the experimental data $\mathbf{B}^{exp}$ in the identification.

Several identification procedures with different initial parameter sets lead to almost the same final optimized values. Therefore, a valid minimum is obtained according to the objective function. The reproducibility of the nanoindentation experimental data in this study are good and the maximum deviation between the three repeated experiments is less than 4.5%. It is recognized that if the noise is less than 5% of the data, the identified results are not sensitive to the data errors [34]. Table 1 shows the identified model parameters obtained by the adhesive contact model with a linear damage evolution law, while the identified parameters for the exponential evolution law are listed in Table 2. C_{10} is responsible for the equilibrium isochoric hyperelastic behavior and results in approximately the same value, regardless if the liner (Table 1) or the exponential evolution law (Table 2) is considered in both load or displacement controlled mode, respectively. The compressibility parameter D_1 is found to be about 0.005, which demonstrates that the silicone rubber is nearly incompressible. The small relaxation times r_1 and r_2 for the two Maxwell elements represent the slight rate-dependent behavior of the silicone rubber in nanoindentation experiments. The identified adhesive stiffness $\mathbf{K}$ as illustrated in Fig. 8(right) is the same for the linear evolution law and the exponential law. At the point of damage initiation, the separation is around 300 nm or 400 nm for the linear or the exponential evolution law, respectively, while the distance at complete failure is in the range of 10 μm in both adhesive models. As expected, the parameters of both material model and adhesive contact model are reproducible identified using the load controlled and displacement controlled, respectively. The identified material parameters are independent on the used evolution law in the adhesive contact model.

Table 1
The identified model parameters with a linear evolution law.

Linear evolution law for adhesive damage					
Load control	C_{10} (MPa)	D_1	β_1^∞	r_1 (s)	β_2^∞	r_2 (s)
	0.16493	0.00493	0.11293	0.47742	0.05024	9.19694
	$K_{nn}\left(\frac{\mu N}{\mu m^3}\right)$	$K_{ss}\left(\frac{\mu N}{\mu m^3}\right)$	$K_{tt}\left(\frac{\mu N}{\mu m^3}\right)$	$\delta_{nn}^0(\mu m)$	$\delta_{nn}^t(\mu m)$	
	0.01043	0.12624	0.080119	0.28962	9.63934	
Displacement control	C_{10} (MPa)	D_1	β_1^∞	r_1 (s)	β_2^∞	r_2 (s)
	0.16714	0.00486	0.11465	0.10176	0.05098	8.06892
	$K_{nn}\left(\frac{\mu N}{\mu m^3}\right)$	$K_{ss}\left(\frac{\mu N}{\mu m^3}\right)$	$K_{tt}\left(\frac{\mu N}{\mu m^3}\right)$	$\delta_{nn}^0(\mu m)$	$\delta_{nn}^t(\mu m)$	
	0.01021	0.17722	0.03147	0.31996	10.44223	

Table 2
The identified model parameters with an exponential evolution law.

Exponential evolution law for adhesive damage					
Load control	C_{10} (MPa)	D_1	β_1^∞	r_1 (s)	β_2^∞	r_2 (s)
	0.16411	0.00529	0.10513	0.12351	0.04863	8.20587
	$K_{nn}\left(\frac{\mu N}{\mu m^3}\right)$	$K_{ss}\left(\frac{\mu N}{\mu m^3}\right)$	$K_{tt}\left(\frac{\mu N}{\mu m^3}\right)$	$\delta_{nn}^0(\mu m)$	$\delta_{nn}^t(\mu m)$	α^E
	0.01006	0.15258	0.07408	0.55255	9.69328	5.06408
Displacement control	C_{10} (MPa)	D_1	β_1^∞	r_1 (s)	β_2^∞	r_2 (s)
	0.16770	0.00533	0.10286	0.11330	0.04822	6.21961
	$K_{nn}\left(\frac{\mu N}{\mu m^3}\right)$	$K_{ss}\left(\frac{\mu N}{\mu m^3}\right)$	$K_{tt}\left(\frac{\mu N}{\mu m^3}\right)$	$\delta_{nn}^0(\mu m)$	$\delta_{nn}^t(\mu m)$	α^E
	0.010531	0.17054	0.08865	0.41149	9.65793	7.25348

Figs. 9–12 present the comparisons between the experimental data and numerical prediction using the parameters that are identified by the indentation response. In Figs. 9 and 10, numerical simulations are performed using the linear evolution law of the adhesive contact model in combination with the identified parameters listed in Table 1. In contrast, Figs. 11 and 12 use the exponential evolution law of the adhesive contact in the numerical prediction with the identified model parameters from Table 2. All comparisons indicate that there is a good agreement between the experimental measurements and the numerical simulation. The relaxation and creep processes in the cyclic or monotonic holding stages are accurately predicted by the numerical simulations for nanoindentation experiments. Therefore, it can be argumented

that the viscoelastic behavior of the silicone rubber can be characterized by the chosen constitutive model together with the identified parameters from nanoindentation experiments. Adhesion effects, namely a negative force at zero displacement as well as a residual displacement after withdrawing the indenter, are also accurately calculated by the numerical simulation. Hence, the adhesive contact model illustrated in Fig. 8 can be used to quantify these adhesion effects in nanoindentation experiments. The simulation results using either a linear or exponential evolution law for the adhesive contact show no significant difference. Comparing the matches between experiments and numerical predictions on the left side and the right side, it seems that results of load controlled experiments are always better than displacement controlled
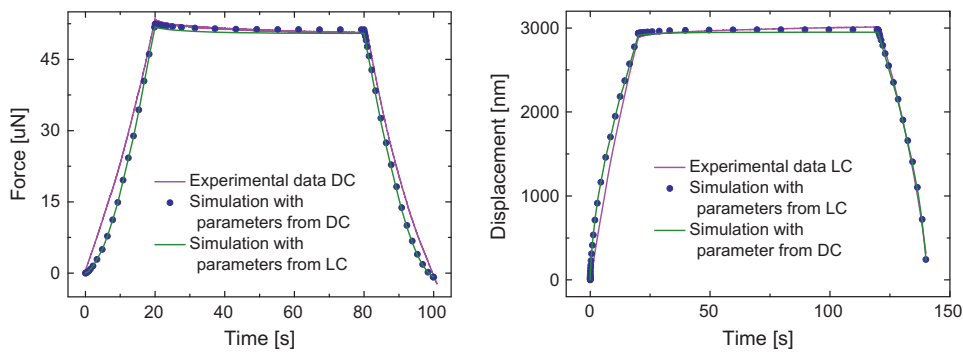
Fig. 9. Linear evolution law for adhesive damage: relaxation (left), creep (right).
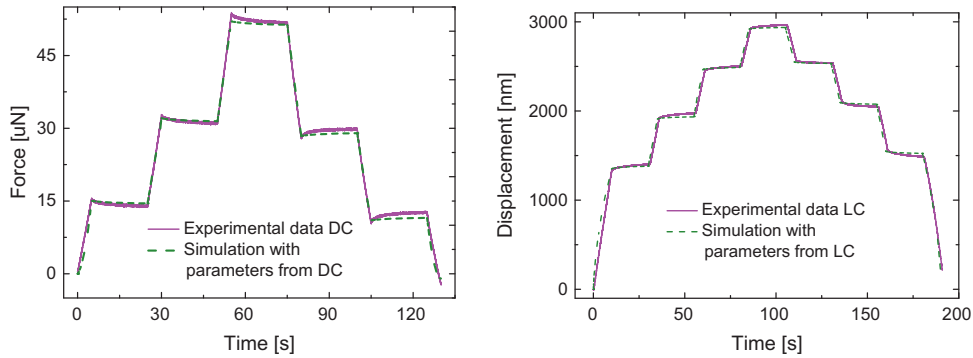
Fig. 10. Linear evolution law for adhesive damage: monotonic with DC (left) and LC (right).
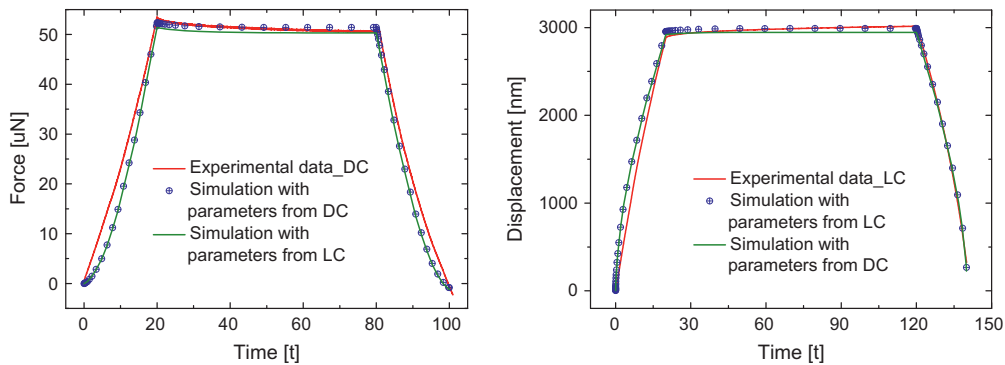
Fig. 11. Exponential evolution law for adhesive damage: relaxation (left), creep (right).
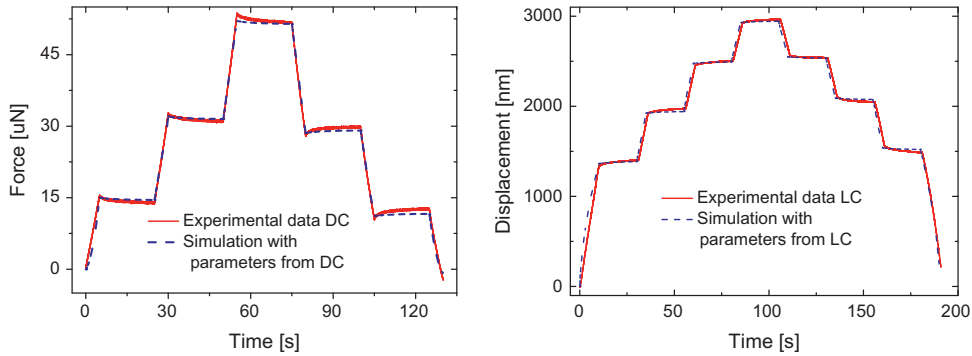
Fig. 12. Exponential evolution law for adhesive damage: monotonic with DC (left) and LC (right).

experiments. Additionally, the numerical simulation results are closer to the experimental data in the unloading part than those in the loading and holding parts in both relaxation and creep tests.

5. Theoretical analysis with linear viscoelastic solutions

In recent years, much effort has been devoted to determine the viscoelastic properties e.g. relaxation and creep functions of time-dependent materials, from indentation using the linear viscoelastic analytical solutions. However, since the linear viscoelastic contact solutions are derived based on the Hertz contact theory or Sneddon's solution using different mathematical transformations, they may have some limitations if adhesion effects or finite strains influence nanoindentation experiments. Therefore, it is interesting to predict the experimental results in the present study by the linear viscoelastic solutions to verify the used computational model.

5.1. Analytical solution for linear viscoelastic indentation

The Berkovich indenter is treated as an effective conical indenter with a half angle of 70.3°. Sneddon [66] derived an analytical solution of the axisymmetric Boussinesq problem of an indenter with arbitrary profile. The deduced simple formula for the relationship of the total load P versus penetration depth h of the rigid conical indenter is

$$P = \frac{2Eh^2}{\pi(1 - v^2)\cot \alpha}. \tag{26}$$

In this formula, E and v are Young's modulus and Poisson's ratio of the indented material, while α is the half angle of the cone. The basic integral or differential constitutive equations for linear viscoelastic materials can always be derived from the corresponding elastic constitutive equations via mathematical transformation, e.g. Laplace transformation. The relaxation function $E(t)$ and the creep compliance function $J(t)$ replace the Young's modulus E and the elastic compliance $1/E$, respectively, assuming that the Poisson's ratio is constant. The integral-type constitutive equation [21] for the time-dependent load $P(t)$ versus prediscribed h in terms of the Boltzmann hereditary integral is given by

$$P = \frac{2}{\pi(1 - v^2)\cot \alpha} \int_0^t E(t - \tau)\left\{\frac{d[h(\tau)]^2}{d\tau}\right\} d\tau, \tag{27}$$

with respect to the past time τ from $\tau = 0$ to the present time $\tau = t$. Alternatively, the solution for the time-dependent penetration depth $h(t)$ resulting from any prescribed load history P is expressed as

$$h^2(t) = \frac{1}{2}\pi(1 - v^2)\cot \alpha \int_0^t J(t - \tau)\frac{dP(\tau)}{d\tau}. \tag{28}$$

According to the one-dimensional rheological model, presented in Fig. 6, the relaxation function of the viscoelastic model has in this case the following form:

$$E(t) = E_e + \sum_{i=1}^{n} E_i e^{-t/r_i}. \tag{29}$$

The corresponding creep compliance function is given by

$$J(t) = J_e + \sum_{i=1}^{n} J_i(1 - e^{-t/r_i}). \tag{30}$$

Here E_e and J_e are the elastic modulus and compliance of the extra spring, while E_i and J_i are the elastic constants of the n springs in the parallel Maxwell elements. r_i is the relaxation or retardation time of the dashpots. The solutions given by Eqs. (27) and (28) restrict the contact area to be a monotonically increasing function of time. Two prescribed histories for the penetration depth are used, i.e. the loading state with constant loading rate $h(t) = v_0 t$ and a relaxation stage described with a Heaviside step function [67,68]

$$h(t) = \begin{cases} h_0 & (t \geqslant 0), \\ 0 & (t < 0). \end{cases} \tag{31}$$

Inserting $h(t) = v_0 t$ and Eq. (29) into Eq. (27) gives

$$P(t) = \frac{4v_0^2}{\pi(1 - v^2)\cot \alpha}\left(\frac{E_e}{2}t^2 + \sum_{i=1}^{n} E_i \tau_i(t - \tau_i) + E_i e^{-t/\tau_i}\tau_i^2\right). \tag{32}$$

For a relaxation test, while Eq. (31) should be inserted into Eq. (27). The analytical solution is then given by

$$P(t) = \frac{2}{\pi(1 - v^2)\cot \alpha}\left(E_e + \sum_{i=1}^{n} E_i e^{-t/\tau_i}\right). \tag{33}$$

Similarly, the analytical solution of the displacement for the loading stage with a constant loading rate v_0 becomes

$$h^2(t) = \frac{\pi(1 - v^2)v_0 \cot \alpha}{2}\left[\left(J_e + \sum_{i=1}^{n} J_i\right)t - \sum_{i=1}^{n} J_i \tau_i(1 - e^{-t/\tau_i})\right]. \tag{34}$$

The displacement during the creep procedure with a constant force P_0 can be expressed as

$$h^2(t) = \frac{\pi(1 - v^2)v_0 \cot \alpha}{2}P_0\left[J_e + \sum_{i=1}^{n} J_i(1 - e^{-t/r_i})\right]. \tag{35}$$

5.2. Analysis results

The relaxation and creep experimental data are fitted using the analytical solutions, i.e. Eqs. (32)–(35). The fitting curves together
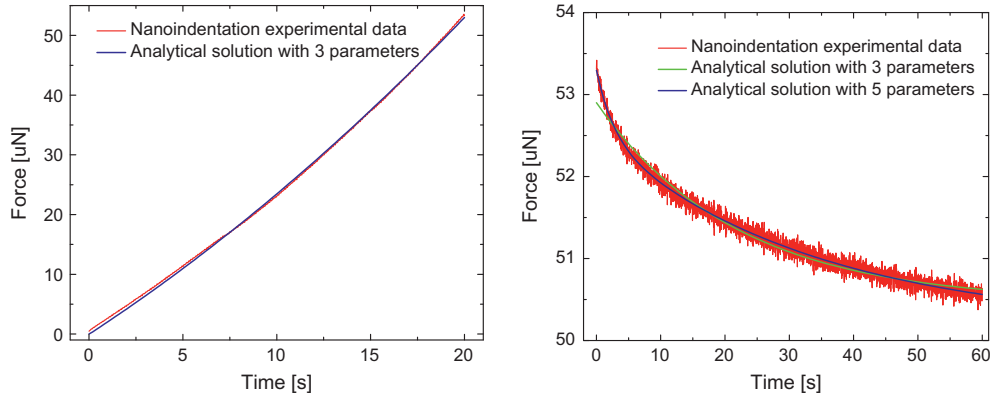
Fig. 13. The experimental force–time curves of the two displacement histories are fitted with the analytical solutions: Eqs. (32) (left) and (33) (right).
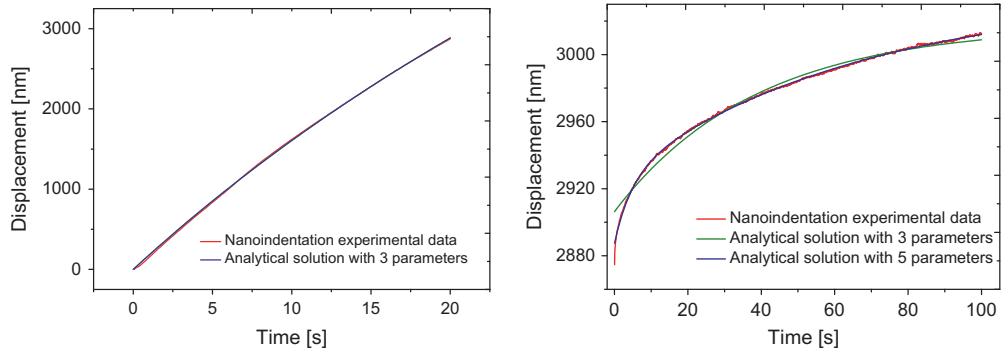
Fig. 14. The experimental displacement–time curves of the two loading histories are fitted with the analytical solutions: Eqs. (34) (left) and (35) (right).

Table 3
The identified moduli in MPa and the relaxation or retardation time in seconds using linear viscoelastic analytical solutions: Eqs. (32) and (35).

	Loading stage			Holding stage						
	Three parameters			Three parameters			Five parameters			
	E_e/J_e	E_1/J_1	r_1	E_e/J_e	E_1/J_1	r_1	E_e/J_e	E_1/J_1	r_1	E_2/J_2	r_2
Relaxation	0.57	1130.51	0.02	2.37	0.11	21.73	2.35	0.04	2.71	0.11	33.53
Creep	0.00	0.80	12.76	0.40	0.03	39.17	0.40	0.01	4.78	0.03	66.85
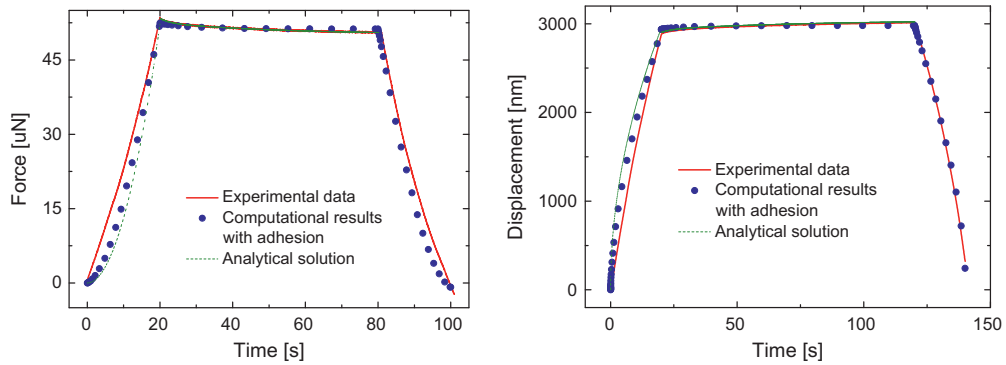
Fig. 15. The comparison between the analytical solution using two Maxwell elements model and the computational results containing adhesion effects together with the experimental data.

with the experimental data are presented in Figs. 13 and 14, while the corresponding identified parameters of the linear viscoelastic models are listed in Table 3.

It is recognized that the loading behavior in both displacement and force controlled experiments can be well described with only one Maxwell element. However, this three element model is not enough to predict the relaxation and creep response; a model containing two Maxwell elements is required. To compare the experimental data with the computational results that contain the already described adhesion model, the two Maxwell elements model with the fitted parameters are used in the analytical solutions, e.g. Eqs. (32)–(35). The comparison is presented in Fig. 15. It can be seen that the computational results are closer to the experimental response than the analytical solution. This study could verify that the used computational model is able to reproduce the viscoelastic behavior of the investigated silicone rubber in nanoindentation experiments including adhesion effects. In contrast, several drawbacks of the analytical solution are revealed. On the one hand, the hereditary integral approach requires a functional form of both the relaxation modulus and the creep compliance. They have to be selected in advance and are then fitted stepwise according to the loading histories. This procedure finally leads to different functions and parameters for the loading and holding stages, respectively, as listed in Table 3. A direct comparison of the analytical solution and the FE model is obviously not possible as completely different parameters are obtained according to Tables 1–3. On the other hand, the adhesion effect and the real geometry of the indenter could not be included in the analytical solution, which results in the slight mismatch during the loading stage.

6. Discussions and conclusions

The present work aims at developing a procedure to identify the viscoelasticity and to quantify the adhesion effect in nanoindentation experiments of polymers by the inverse method. A soft polymer, i.e. a silicone rubber, is chosen considering that this material is isotropic and mainly hyperelastic with only slightly viscous behavior. Different testing protocols are used to demonstrate the viscoelasticity and adhesion effects in nanoindentation experiments. A viscous hyperelastic constitutive model with a linear evolution equation at finite strain, which is called finite viscoelasticity, is used to describe the viscoelastic behavior of the silicone rubber. The inverse method is applied using FE computation in combination with a numerical optimization subroutine. A surface-based adhesive behavior in the traction–separation law is incorporated into the default contact model in ABAQUS® to quantify adhesion. The parameters of the chosen viscoelastic constitutive model and the adhesive contact model are identified by matching the response of the numerical model with the experimental force–displacement data. The comparisons between the experimental data and the numerical predictions containing the identified parameters show a good agreement. Therefore, the finite viscoelastic constitutive model and the used adhesion contact model can be used to describe the viscoelastic behavior and occuring adhesion effects in nanoindentation. The present model containing the surface adhesion with the identified parameters is verified by comparing the computational results and an analytical solution. Several drawbacks to the used analytical solution are presented. The developed procedure is capable to characterize the viscoelasticity of the polymer and to quantify the adhesion effects. According to our best knowledge, it is until now the first time to identify simultaneously finite viscoelasticity and adhesion in nanoindentation experiments of polymers.

Considering the identification of viscoelasticity and adhesion effects in polymers, there are still some questions remaining, which

will be faced in the proceeding work. First, the chosen silicone rubber shows no pronounced viscoelasticity resulting in only two Maxwell elements with short relaxation times that can sufficiently describe the viscous material behavior. Hence, a quasi-static mode can be used and there are neither coupling nor convergence problems during the parameter identification process. However, most other polymers show very strong viscosity and the relaxation times may be as long as months or even years. In this case, a complex viscoelastic model with nonlinear evolution equations should be used. More Maxwell elements may be necessary to describe the material's relaxation. In nanoindentation experiments, a dynamic testing mode may be required for this case. Therefore, the developed inverse procedure has to be improved to identify more parameters for dynamic conditions in nanoindentation experiments. Second, the agreement between the experimental data and the numerical simulation in load controlled mode is better than in displacement controlled mode. The reason for this observation has to be studied and it has to be investigated if this effect may be even more pronounced for other polymers. The displacement controlled mode derives from a force measurement using a feedback system, which might result in an error and, therefore, leads to the observed deviation between both modes. Furthermore, the chosen silicon rubber's adhesion is not very pronounced in nanoindentation testing. For instance, the negative force at zero displacement is very small compared to the maximum force. Hence, the applied traction–separation adhesive contact model with either a linear evolution law or an exponential evolution law for the adhesive damage can be used to quantify the adhesion effects very well. It is not clear if this is also the case for other polymers, like polydimethylsiloxane, that show strong adhesion. This will be answered in the upcoming studies. Finally, it is perceived that the responses of the numerical simulation are closer to the experimental data in the unloading part than those in the loading and holding parts. Many factors could contribute on this, e.g. thermal drift, cracks in the polymer's surface at the indentation sight or thermal influences on the material properties. The inaccurate quantification of the adhesion effects in the loading or holding stages may be also a potential reason.

References

[1] J.S. Bergström, M.C. Boyce, Journal of the Mechanics and Physics of Solids 46 (1998) 931–954.
[2] G.A. Holzapfel, International Journal for Numerical Methods in Engineering 39 (1996) 3903–3926.
[3] G.A. Holzapfel, J.C. Simo, International Journal for Numerical Methods in Engineering 33 (1996) 3019–3034.
[4] N. Huber, C. Tsakmakis, Mechanics of Materials 32 (2000) 1–18.
[5] M. Kaliske, H. Rothert, Computational Mechanics 19 (1997) 228–239.
[6] S. Hartmann, Computer Methods in Applied Mechanics and Engineering 191 (2002) 1439–1470.
[7] A. Lion, Continuum Mechanics and Thermodynamics 8 (1996) 153–169.
[8] A. Lion, Journal of the Mechanics and Physics of Solids 46 (1998) 895–930.
[9] J. Lubliner, Mechanics Research Communications 12 (1985) 93–99.
[10] S. Reese, S. Govindjee, International Journal of Solids and Structures 35 (1997) 3455–3482.
[11] A.V. Tobolsky, Journal of Applied Physics 27 (1956) 673–685.
[12] W.C. Oliver, G.M. Pharr, Journal of Materials Research 7 (1992) 1564–1583.
[13] W.C. Oliver, G.M. Pharr, Journal of Materials Research 19 (2004) 3–20.

[14] Y.P. Cao, D.C. Ma, D. Raabe, Acta Biomaterialia 5 (2009) 240–248.
[15] Y.T. Cheng, C.M. Cheng, Structural Control and Health Monitoring 13 (2006) 561–569.
[16] A.E. Giannakopoulos, Journal of the Mechanics and Physics of Solids 54 (2006) 1305–1332.
[17] G. Huang, H. Lu, Experimental Mechanics 47 (2007) 87–98.
[18] A. Jäger, R. Lackner, Meccanica 42 (2007) 293–306.
[19] C.K. Liu, S. Lee, Journal of Applied Physics 100 (2006) 503–512.
[20] M.L. Oyen, Acta Materialia 55 (2007) 3633–3639.
[21] E.H. Lee, J.R.M. Radok, Journal of Applied Mechanics 30 (1960) 438–444.
[22] T.C.T. Ting, Journal of Applied Mechanics 33 (1966) 845–854.
[23] G.A.C. Graham, International Journal of Engineering Science 3 (1965) 27–46.
[24] K.L. Johnson, Contact Mechanics, Cambridge University Press, 1985.
[25] N. Huber, W.D. Nix, H. Gao, Proceedings of the Royal Society of London. Series A. Mathematical, Physical and Engineering Sciences 458 (2002) 1593–1620.
[26] N. Huber, E. Tyulyukovskiy, Journal of Materials Research 19 (2004) 101–113.
[27] D. Klötzer, C. Ullner, E. Tyulyukovskiy, N. Huber, Journal of Materials Research 21 (2006) 677–684.
[28] E. Tyulyukovskiy, N. Huber, Journal of Materials Research 21 (2006) 664–676.
[29] S. Hartmann, J. Gibmeier, B. Scholtes, Experimental Mechanics 46 (2006) 5–18.
[30] G. Rauchs, J. Bardon, D. Georges, Mechanics of Materials 42 (2010) 961–973.
[31] G. Rauchs, J. Bardon, Finite Elements in Analysis and Design 47 (2011) 653–667.
[32] S. Guessasma, M. Sehaki, D. Lourdin, A. Bourmaud, Computational Materials Science 44 (2008) 371–377.
[33] V. Le Saux, Y. Macro, G. Bles, S. calloch, S. Moynea, S. Plessisa, P. Charrierb, Mechanics of Materials 43 (2011) 775–786.
[34] Z. Chen, S. Diebels, Archive of Applied Mechanics (2011) 1041–1056, http://dx.doi.org/10.1007/s00419-012-0613-9.
[35] Z. Chen, S. Diebels, Proceedings in Applied Mathematics and Mechanics 11 (2011) 765–766.
[36] Z. Chen, S. Diebels, J. Schmitt, Frictional nanoindentation of hyperelastic polymer layers: a numerical study, in: Proceedings of the 3rd ECCOMAS Thematic Conference on the Mechanical Response of Composites, 2011, pp. 229–236.
[37] Z. Chen, S. Diebels, Computers and Mathematics with Applications 64 (2012) 2775–2786.
[38] Z. Chen, S. Diebels, Journal of Applied Mathematics and Mechanics/Zeitschrift für Angewandte Mathematik und Mechanik (ZAMM) (2012) 1–14, http://dx.doi.org/10.1002/zamm.201100170.
[39] G. Bolzon, G. Maier, M. Panico, International Journal of Solids and Structures 41 (2004) 2957–2975.
[40] M. Mata, J. Alcalá, Journal of the Mechanics and Physics of Solids 455 (2004) 145–165.
[41] E. Tyulyukovskiy, N. Huber, Journal of the Mechanics and Physics of Solids 55 (2007) 391–418.
[42] Y. Cao, D. Yang, W. Soboyejoy, Journal of Materials Research 20 (2005) 2004–2011.
[43] F. Carrillo, S. Gupta, M. Balooch, S.J. Marshall, G.W. Marshall, L. Pruitt, C.M. Puttlitz, Journal of Materials Research 20 (2005) 2820–2830.
[44] Q. Liao, J. Huang, T. Zhu, C. Xiong, J. Fang, Thin Solid Films 16 (2010) 1043–1047.
[45] U.D. Cakmak, T. Schöberl, Z. Major, Archive for Rational Mechanics and Analysis 42 (2012) 707–718.
[46] S. Gupta, F. Carrillo, C. Li, L. Pruitt, C. Puttlitz, Materials Letters 61 (2007) 448–451.
[47] C. Charitidis, ISRN Nanotechnology (2011) 1–13, http://dx.doi.org/10.5402/2011/719512.
[48] K.L. Johnson, K. Kendall, A.D. Roberts, Proceedings of the Royal Society of London. Series A. Mathematical, Physical and Engineering Sciences 8 (1971) 301–313.
[49] B.V. Derjaguin, V.M. Muller, Y.P. Toporov, Journal of Colloid and Interface Science 53 (1975) 314–325.
[50] D. Maugis, Journal of Colloid and Interface Science 150 (1992) 243–269.
[51] Y.P. Zhao, X.H. Shi, W.J. Li, Reviews on Advanced Materials Science 5 (2003) 348–353.
[52] M. Wanga, K.M. Liechtia, J.M. Whiteb, R.M. Winterc, Journal of the Mechanics and Physics of Solids 52 (2004) 2329–2354.
[53] X.J. Zhang, X.H. Zhang, S. Wen, Tribology Letters 41 (2011) 65–72.
[54] Y. Zhang, Y. Zhao, Journal of Applied Mechanics 78 (2011) 01100701–01100712.
[55] M. Johlitz, S. Diebels, Archive of Applied Mechanics 81 (2010) 1333–1349.
[56] A.K.N. Kumar, M.D. Kannan, S. Jayakumar, K.S. Rajam, V.S. Raju, Surface and Coatings Technology 201 (2006) 3253–3259.
[57] C. Walter, C. Mitterer, Surface and Coatings Technology 203 (2008) 3286–3290.
[58] K. Sedlan, Viskoelastisches Materialverhalten von Elstomerwerkstoffen: Experimentelle Untersuchung und Modellbildung, Dissertation, Universität Gesamthochschule Kassel, 2000.
[59] J.C. Simo, Computer Methods in Applied Mechanics and Engineering 60 (1987) 153–173.
[60] Abaqus 6.11 analysis user's manual, <http://abaqus.ethz.ch:2080/v6.11/books/usb/default.htm>, 2012.
[61] G.A. Holzapfel, Nonlinear Solid Mechanics: A Continuum Approach For Engineering, Lohn Wiley & Sons, Ltd., England, 2001.
[62] S. Govindjee, J.C. Simo, International Journal of Solids and Structures 29 (1992) 1737–1751.
[63] G. Marckmann, E. Verron, Rubber Chemistry and Technology 79 (2005) 835–858.
[64] R.S. Rivlin, Philosophical Transactions of the Royal Society of London A241 (1948) 379–397.
[65] M. Johlitz, H. Steeb, S. Diebels, A. Chatzouridou, J. Batal, W. Possart, Journal of Materials Science 42 (2007) 9894–9904.
[66] I.N. Sneddon, International Journal of Engineering Science 3 (1965) 47–57.
[67] M. Sakai, Philosophical Magazine A 82 (2002) 1841–1849.
[68] Y.P. Cao, X.Y. Ji, X.Q. Feng, Philosophical Magazine 90 (2010) 1639–1655.

Macroindentation of a Soft Polymer: Identification of Hyperelasticity and Validation by Uni/Biaxial Tensile Tests

Macroindentation of a soft polymer: Identification of hyperelasticity and validation by uni/biaxial tensile tests

Zhaoyu Chen, Tobias Scheffer, Henning Seibert, Stefan Diebels *

Chair of Applied Mechanics, Saarland University, PO Box 151150, 66041, Saarbrücken, Germany

ARTICLE INFO

ABSTRACT

In the present study, macroindentation tests are performed by means of a spherical indenter on silicone rubber. The load-depth curves during the indentation process reveal only slightly viscous effects but main hyperelastic properties. The hyperelasticity is identified from the load-depth data using an inverse method. The elastic modulus is calculated according to the most often used Oliver and Pharr method in indentation from the unload stage of the monitored load-depth data. The identified material parameters of the hyperelastic constitutive laws are firstly compared with the elastic modulus obtained from this semi-analytical solution. In a second step, specimens of the considered silicone rubber are also prepared for uniaxial and biaxial tensile tests, which are performed in order to compare with the indentation. In the uniaxial tensile tests, the parameters of the three hyperelastic models: neo-Hooke, Mooney–Rivlin and Yeoh model are determined by fitting the experimental tensile stress–strain data with an analytical solution. The correlation between the identified results obtained from indentation tests and uniaxial tensile tests, is investigated. Finally, the simulation of biaxial tensile tests is performed based on the three chosen hyperelastic models and the identified parameters. Comparing the simulation results with the experimental data validates the characterization of the hyperelasticity by using macroindentation and tensile tests.

1. Introduction

Indentation testing is widely used to measure materials' local response and to describe the gradient of physical properties. Material behavior data is required to be obtained directly from the product and not from laboratory specimens in many industrial productions in order to obtain a satisfactory design. Localized tests by indentation could be used for this purpose as they could provide actual mechanical properties in the test zone and surrounding areas. High precision on force and displacement sensors expanded the application field to the micro- and nano-scales, which makes indentation testing become a main testing technique for thin films or coatings and nanocomposites.

The most common application for polymers is to measure a scalar value of hardness and modulus, based on Oliver and Pharr method (1992, 2004), which can supply access to useful qualitative information but can definitely not be used to identify local constitutive models. These constitutive models are definitely needed to describe the complex thermo-mechanical behavior, including non-linear elasticity and viscoelasticity in the numerical simulations. The inverse analysis using the accurate load–displacement data opens the way to obtain the local constitutive models from the indentation. The first way to perform this inverse analysis is based on analytical or semi-analytical solutions for some respective constitutive models. The model parameters are then obtained by fitting the experimental load-depth data with the analytical functions. Various types of viscoelastic analytical solutions with respect to different indenter tips have been reported in literature. For example, Cheng and Cheng (2006) derived

a relationship between the initial unloading slope, contact depth, and the instantaneous relaxation modulus for indentation in linear viscoelastic solids by a rigid indenter with an arbitrary axisymmetric smooth profile. The theoretical analysis results of frictionless and adhesionless contact of flat surfaces by pyramid indenters such as the Vickers, Berkovich and Knoop indenters were presented by Giannakopoulos (2006). The materials of the contacting solids were assumed to be homogeneous and isotropic, linear elastic, as well as linear viscoelastic. Cao et al. (2009) developed analytical solutions of the flat punch indentation in the time and frequency domains to determine the viscoelastic properties of a soft layer. The second way, termed inverse method, is performed by combining finite element modeling and numerical optimization. This method minimizes the difference between experimental and numerical data, called objective function with respect to the model parameters using the numerical optimization. The parameters of the constitutive models are identified as the optimized solution. This inverse method was firstly applied to the indentation of metals by Huber et al. (2002), Huber and Tyulyukovskiy (2004), Klötzer et al. (2006) and Tyulyukovskiy and Huber (2006). The inverse method is still a new topic in indentation problems of polymer materials, where time-dependent effects may have strong influence. Hartmann et al. (2006) identified the viscoplastic model parameters with uniaxial tests and validated them using indentation tests. Rauchs et al. (2010, 2011) employed a gradient-based numerical optimization method to identify viscous hyperelastic and elasto-viscoplastic material parameters. Guessasma et al. (2008) determined viscoelastic properties of biopolymer composite materials using the finite element calculation and the nanoindentation. Le Saux et al. (2011) identified the constitutive model from micro-indentation tests for rubber elasticity. The inverse method is applied to re-identify the hyperelastic or linear viscoelastic properties of polymers (Chen and Diebels, 2012, 2013) and to quantify the surface roughness (Chen and Diebels, 2012) and adhesion effects (Chen et al., 2013) in nanoindentation. Since the inverse method allows us to handle any material models with non-linear properties, it is a new but a main method to get the constitutive models from the indentation.

Experimental as well as theoretical studies on indentation, in recent research papers, mainly deal with the nano- or micro-scale rather than the macro-scale. The indentation at macro-scale is rarely used in scientific researches, even if it is preferable for bulk samples. Instead, in some cases, nanoindentation is also applied to bulk samples with the risk of poor results due to the complex testing procedure. In fact, the surface topography and surface forces in nanoindentation could affect the evaluation of bulk properties. The microindentation is generally used to measure the microhardness, e.g. the measurement of the Vickers and Knoop hardness of various polymers was performed in Amitay-Sadovsky and Wagner (1998), Flores et al. (1999) and Suwanprateeb (1998). However, macroindentation is almost unexplored even though it could be suitable to characterize bulk properties from small specimens of finished products. Only a few published papers are related to this topic. Benabdallah and Bui (2004) per-

formed the macroindentation on PA and PET using a device developed for a typical universal tensile testing machine. A range of indentation rates was considered together with three different shapes of indenter: spherical, conical and cylindrical. In 2006, a further effort in macroindentation was made by Spinks et al. (2006) who studied the indentation testing of PS using a spherical indenter with 0.5 mm radius. Afterwards, in 2008, Guglielmotti et al. (2008) performed macroindentation tests by means of a flat cylindrical indenter on HDPE and PA66. The effects of the tip roundness on the response of elastic–plastic material in macroindentation was analyzed in 2009 by Pulecio et al. (2009). Recently, Lach et al. (2012) characterized the temperature-dependent mechanical behavior (hardness, creep and relaxation, etc.) of polymers by using a newly developed macroindentation testing machine with an innovative cooling and heating device.

The tensile test is a common experiment to evaluate the mechanical properties and to determine the material parameters used in constitutive material laws. The deformation states are distincted under indentation and tensile conditions. Indentation deformations are maximized at the contact range just under the tip and radially diminish to zero with increasing distance from the contact center. It is mainly multi-compressive by nature and it is a localized deformation. Whereas, tensile-induced strains homogeneously extrude the sample which is stressed along the tension direction. Therefore, it is interesting to probe the correlation between the characterizations by instrumented indentation and tensile testing. Giannakopoulos and Triantafyllou (2007) and Rauchs and Bardon (2011) found that the constitutive parameters obtained from microindentation measurement of rubber-like elastomers were usually not suitable to describe the macroscopic tensile tests. However, Le Saux et al. (2011) identified the parameters of an Edwards–Vilgis hyperelastic model of an unfilled natural rubber from microindentation. The identified parameters are used to simulate tensile, compression and pure shear tests. The agreement with the experimental data is very good. The main reasons raised in the literature are the different stress and strain states, which are well known to be of primary influence (Rauchs and Bardon, 2011; Le Saux et al., 2011; Drozdov et al., 1996; Chevalier and Marco, 2002). The indentation test, which is localized compressive deformation by nature, does not yield the deformation modes necessary to capture the stiffening at high tensile strains. Secondly, the strain level in indentation tests used to identify the material behavior are not high enough (Rauchs and Bardon, 2011; Le Saux et al., 2011). Le Saux illustrated that these difficulties are actually clearly met for filled materials but do not seem to appear in the case of unfilled natural rubber (Le Saux et al., 2011). Anyhow, it is well known that experiments with different stress states may fit best with different expressions of the hyperelastic models (Rauchs and Bardon, 2011; Drozdov et al., 1996; Baaser and Noll, 2009; Johlitz and Diebels, 2011). It should also not be forgotten that the numerous error contributions in the complicated nano- or microindentation experiments could have a large influence on the identified constitutive parameters.

In the present study, it is our goal to investigate the ability to identify the hyperelastic constitutive parameters from load-depth curves obtained from indentation. Firstly, the macroindentation which uses a spherical indenter with a diameter of 5 mm is chosen to eliminate the error contributions in nanoindentation, especially the surface effects. In order to limit the microstructure and the viscous effects, the considered material is an unfilled silicone rubber which exhibits a behavior very close to hyperelasticity (Johlitz and Diebels, 2011). Three hyperelastic models the neo-Hooke, the Mooney–Rivlin and the Yeoh model are considered to predict the finite elasticity of the rubber-like elastomer. The inverse method deals with a finite element simulation by Abaqus® combined with an optimization procedure, which is used to identify the constitutive parameters. Secondly, uniaxial tensile tests are performed to compare with the indentation. The experimental stress–strain curves are fitted with the analytical solutions corresponding to the three hyperelastic potentials to obtain the constitutive parameters. Thirdly, the constitutive parameters obtained from the indentation are used in the numerical prediction of uniaxial tensile tests and vise versa. Finally, the identified results are validated by the biaxial tensile tests and the comparing results are discussed.

2. Macroindentation

2.1. Experimental device and specimens

The macroindentation experiments are performed using a custom-made device, which was originally designed to perform uniaxial tensile tests for polymers. Details of the device and the testing method are described in Koprowski-Theiss et al., 2011. The actuator Linos LT50ST® is able to perform the tensile as well as the compression procedure, thus it produces the compression effect required for indentation. The upper clamp in the tensile device, shown as Fig. 4 in Koprowski-Theiss et al. (2011), is replaced by a cylindrical metal rod, to which the tip of the indentation is glued. The metal rod is screwed into a central hole in the S-bracket force sensor from ME-Messsysteme®. The spherical indenter tip consists of a hardened bearing ball with a diameter of 5 mm. The flexibility of this indentation device can be neglected with respect to the compliance of the soft polymers. The displacement of the indenter is controlled and measured through the linear stage in a closed loop control of the stepper motor. The position is supplied via the integrated encoder by the number of steps of the stage. Loosing steps yields an error message of the device. The maximum displacement of 150 mm can be measured with a resolution of 1 μm. In the meantime the reaction force is measured via a sensor KD24s of ME-Messsysteme® in the range of 20 N and a linear accuracy of 0.1%. With a computer control, realized by LabVIEW®, both, the values of the force sensor and the displacement signal of the linear stage can be collected simultaneously. The experimental results are comparable with the data obtained in the Leibniz Institute for New Materials (INM), Saarland University, using a
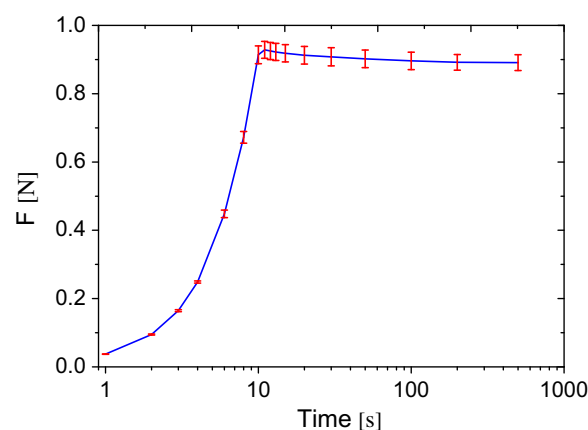
Fig. 1. Semi-log plot of a single step relaxation in macroindentation.

commercial macroindenter universal testing instrument Z 1446 produced by Zwick GmbH, Germany.

The investigated material is the silicone rubber ELASTO-SIL® RT 625, produced by the WACKER Chemie GmbH, Germany. It consists of pourable, addition-curing two components that vulcanize at room temperature. The two transparent and colorless components ELASTOSIL A and ELASTOSIL B are mixed up with a weight ratio of 9:1 by stirring. After degassing, the mixture is poured in a cylindrical mold and cured at room temperature for 24 h.[1] Theoretically, the silicone rubber can be assumed to be isotropic and incompressible, what will be validated through the performed experiments. Moreover softening effects like Mullins-effect do not occur, which makes a preconditioning unnecessary. The final specimen is of cylindrical shape with a diameter of 25 mm and a thickness about 23 mm. Considering the size of the indenter as well as the maximum displacement of 0.5 mm, the boundary effects and the substrate influence can be neglected (Hay et al., 1998). The specimen is positioned directly under the actuator on a flat substrate of hard metal. The whole setup is located on an assembling board which isolates from external vibrations.

2.2. Macroindentation testing protocol and results

The macroindentation testing is performed with displacement control. The load is continuously monitored in order to obtain the load–displacement curves. For each testing, three experiments are performed at different positions on the sample surface. In a first step, a single step relaxation is performed to investigate the viscous effects. A displacement of 0.5 mm is applied to the indenter within 10 s. Afterwards, the indenter is hold at the maximum displacement lasting for 500 s. The reaction force is monitored to evaluate the relaxation behavior of the silicone rubber. The reaction force along with the logarithm of real testing time is plotted in Fig. 1. The relaxation during 200 s is slight as shown in the semi-log plot. As a second step, a cyclic test containing a loading and an unloading stage

---

[1] The samples' preparation by the Chair for Adhesion and Interphases in Polymers at Saarland University is gratefully acknowleged.
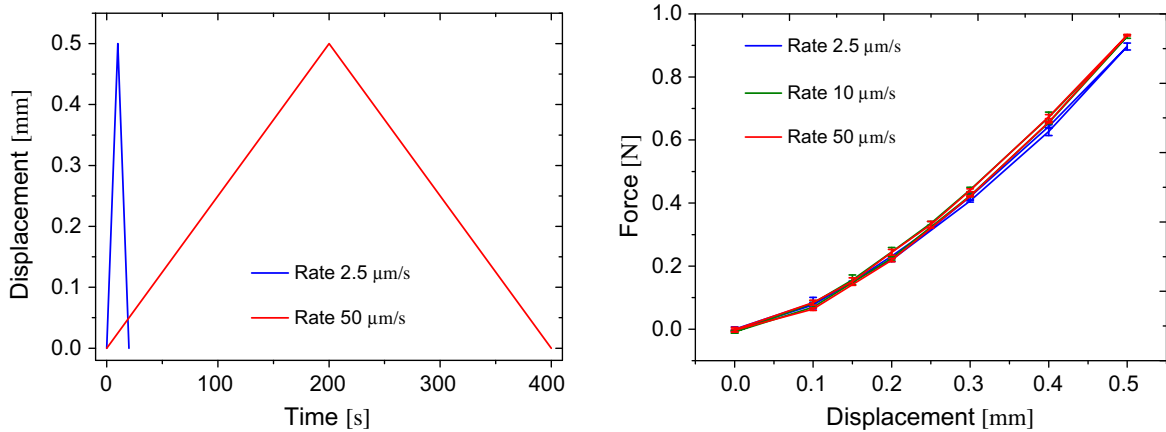
Fig. 2. Macroindentation with a cyclic testing by various loading rates.

with various rates is performed in order to investigate the rate-dependent viscous hysteresis effects. Three different rates 2.5 µm/s, 10 µm/s and 50 µm/s are chosen, cf. Fig. 2 (left). The force–displacement curves obtained from the three rates are overlapping each other as shown in Fig. 2 (right). It is not possible to observe any hysteresis loop in the loading and unloading process. In addition, in contrast to the nanoindentation, there is no negative force when the indenter completely withdrew from the sample. So the adhesion effects are not observable in the macro-scale indentation as expected.

It is important to note that the experimental scattering is very low from one experiment to another (errorbars in Fig. 1 and Fig. 2 (right) are very small), which confirms the low influence of the inhomogeneity of the material. Therefore, as a conclusion from the experiments, the chosen material exhibits a behavior close to perfect isotropic hyperelasticity. Furthermore, the effects of adhesion and surface roughness, which are prominent in indentation at the nano-scale, can be neglected at the macro-scale.

2.3. Analysis based on contact theory

The elastic contact theory, which plays a key role in the analysis procedure, was originally considered in the late 19th century by Hertz (1881) and Boussinesq (1885). Hertz analyzed the elastic contact between two spherical bodies with different ratios and elastic constants. The Hertz contact theory forms the basis of many experimental and theoretical work in the field of contact mechanics. Boussinesq developed a method for computing the stress and displacements in the contact between an elastic body and a rigid, axisymmetric indenter. Based on this method, subsequently, Sneddon derived general relationships among the load, the displacement and the contact area for any indenter which can be described as a solid of revolution of a smooth function (Sneddon, 1965). Another major contribution was made by Oliver and Pharr. They developed a method to measure hardness and elastic modulus by instrumented indentation techniques (Oliver and Pharr, 1992; Oliver and Pharr, 2004). The Oliver & Pharr method has widely been adopted in the determination of mechan-

ical behavior of materials at small scales and has become a primary analysis technique in nanoindentation of thin films and small structural features.

In this study, the Sneddon's solution and the Oliver and Pharr method are chosen to determine the elastic modulus of a silicone rubber, which will be compared with the identified results using the inverse method. As a first step, the uniaxial tests are used to prove the assumption of incompressibility of the considered material. The volume strain in terms of the Jacobian J can be computed from the stretches λ_1, λ_2 and λ_3 by $J = \det\mathbf{F} = \lambda_1 \lambda_2 \lambda_3$. Therefore, not only the elongation of the specimen but also the transverse deformation has to be measured. The values of J at different displacements for four individual tensile tests are shown in Fig. 3. On average, the assumption of incompressibility $\det\mathbf{F} = 1$ is fulfilled quite well. Hence, the Poisson's ratio v will be assumed as 0.5 in the following analysis using the Sneddon's solution and the Oliver and Pharr method. The load–displacement curves containing the load and unload parts in Fig. 2 are fitted with the Sneddon's solution (Please see Appendix A). The non-linear
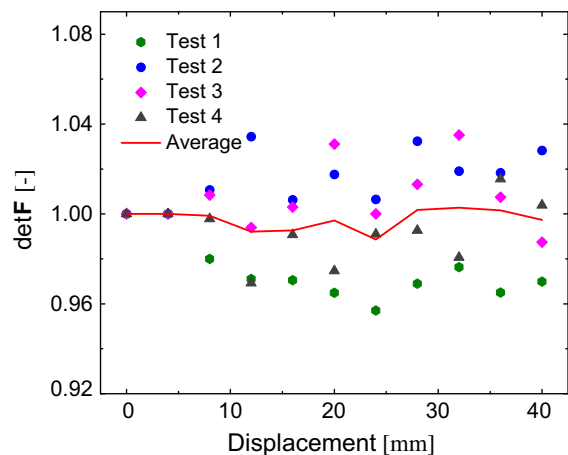
Fig. 3. Verification of the incompressibility, volume strain along the displacement.
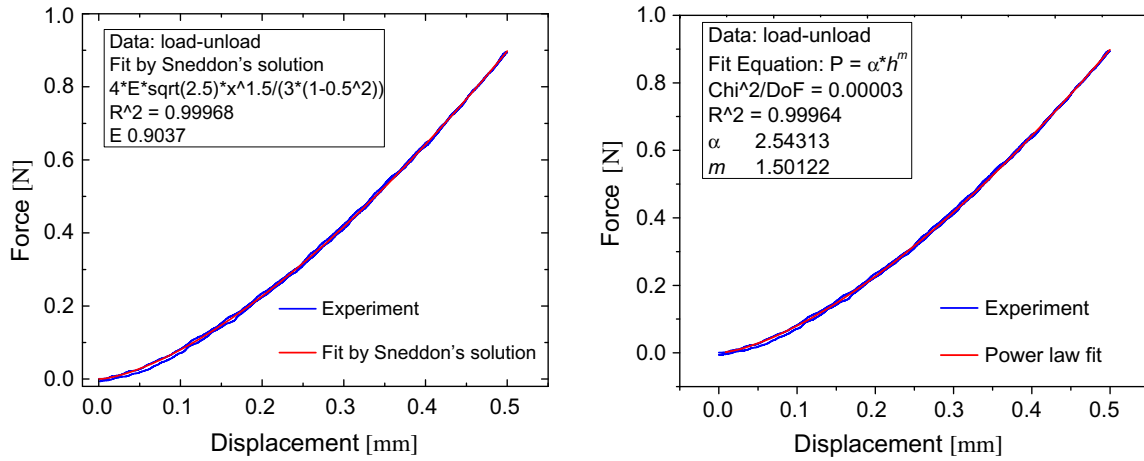
Fig. 4. The curve in Fig. 2 is fitted with the Sneddon's solution (left) and the unloading part is fitted by a power law function (right) in the Oliver and Pharr method.

Table 1
The parameters and measured elastic modulus from the Oliver and Pharr method.

Parameters	α	m	S (N/mm)	h_s (mm)	h_c (mm)	A (mm²)	E^* (MPa)	E (MPa)
Values	2.543	1.501	2.697	0.2497	0.2503	3.735	1.237	0.9277

least squares regression is used to capture the Young's modulus E while the Poisson's ratio v is defined to be 0.5. As shown in Fig. 4 (left), the Young's modulus is determined to be 0.9037 MPa for the used silicone rubber.

The Oliver and Pharr method (Please see Appendix B) was developed to determine the hardness and elastic modulus of a material from indentation load–displacement data obtained during one cycle of loading and unloading. If this method is applied, attention should be paid on the behavior of the material, which is limited to be described as a semi-infinite, elastic–plastic half space. As shown in Fig. 4 (right), the load–displacement curve in Fig. 2 is fitted by a power law function Eq. (B.1). Since only the elastic displacement can be read out of Fig. 2, h_f is 0. The fitted exponent m is close to 1.5, which is the value suggested by Oliver and Pharr method for an indenter behaving more like a paraboloid of revolution. The calculated parameters and the measured elastic modulus from the Oliver and Pharr method are listed in Table 1. Compared to Sneddon's solution the identified value of the Young's modulus is 2.6% larger.

3. FE simulation and inverse method

3.1. Hyperelastic constitutive model

First of all, in the framework of finite strain continuum mechanics, constitutive models of a nearly incompressible hyperelastic material will be recalled. The existence of the Helmholtz free-energy or strain-energy function Ψ is postulated for a so-called hyperelastic material. The nearly incompressible hyperelastic behavior is treated by additively decomposing the Helmholtz free-energy function

Ψ into the volumetric elastic part Ψ_{vol} and the isochoric elastic part Ψ_{iso}. This type of formulation is very often used if large elastic deformations of rubber or rubber-like materials are concerned, because of the advantages in the numerical treatment of either incompressible or nearly incompressible properties. There are numerous specific forms of strain-energy functions to describe the hyperelastic properties, whereas we only focus on three isotropic and nearly incompressible hyperelastic models, namely the neo-Hooke (NH), the Mooney–Rivlin (MR) and the Yeoh form (YE):

$$\Psi_{NH} = \Psi_{iso}(\bar{I}_1) + \Psi_{vol}(J)$$
$$= C_{10}(\bar{I}_1 - 3) + \frac{1}{D_1}[(J-1)^2 + (\ln J)^2]/2, \quad (1)$$

$$\Psi_{MR} = \Psi_{iso}(\bar{I}_1, \bar{I}_2) + \Psi_{vol}(J) = C_{10}(\bar{I}_1 - 3) + C_{01}(\bar{I}_2 - 3)$$
$$+ \frac{1}{D_1}[(J-1)^2 + (\ln J)^2]/2, \quad (2)$$

$$\Psi_{YE} = \Psi_{iso}(\bar{I}_1) + \Psi_{vol}(J) = C_{10}(\bar{I}_1 - 3) + C_{20}(\bar{I}_1 - 3)^2$$
$$+ C_{30}(\bar{I}_1 - 3)^3 + \frac{1}{D_1}[(J-1)^2 + (\ln J)^2]/2. \quad (3)$$

In all cases the same volumetric part Ψ_{vol} is chosen depending on the Jacobian J and compressibility parameter D_1. These forms are often used in the literature to model elastic properties of polymers. The isochoric part Ψ_{NH} involves only one single parameter C_{10} and provides a mathematically simple and reliable constitutive model for the non-linear deformation behavior of isotropic rubber-like materials. It is physically-founded and includes typical effects known from non-linear elasticity within the small

strain domain (Holzapfel, 2001; Marckmann and Verron, 2005; Rivlin, 1948). The isochoric free energy function Ψ_{MR} of the Mooney–Rivlin model is derived on the basis of mathematical arguments with consideration of symmetry (Mooney, 1940). It is often employed in the description of the non-linear behavior of isotropic rubber-like materials at moderate strain (Giannakopoulos and Triantafyllou, 2007; Holzapfel, 2001; Marckmann and Verron, 2005) and depends on two constants C_{10} and C_{01}.

The strain-energy function has to satisfy some physical limit conditions (Doll and Schweizerhof, 2000). If the continuum is compressed to a single point, i.e. $J \rightarrow +0$, the strain energy tends to plus infinity and the volumetric stress towards minus infinity. In the limit case if the continuum is stretched infinitely, one can obtain a plus infinite strain energy as well as a plus infinite volumetric stress. In the strainless initial state, i.e. $\bar{I}_a \rightarrow 1$ and $J \rightarrow 1$, it is a stress-free condition and no strain energy is stored. The initial shear modulus μ_0 and the initial compression modulus K_0 are related to the coefficients in the following way:

$$\mu_0 = 2\frac{\partial\Psi_{iso}}{\partial\bar{I}_a}\Big|_{\bar{I}_a\rightarrow 1} = 2(C_{10} + C_{01}), K_0 = \frac{\partial^2\Psi_{vol}}{\partial J^2}\Big|_{J\rightarrow 1} = \frac{2}{D_1}. \tag{4}$$

The compressibility parameter D_1 can be interpreted as a penalty parameter that enforces incompressibility if small values of D_1 are chosen.

3.2. FE model of macroindentation

Since the silicone rubber is isotropic and the spherical indenter possesses rotational symmetry, an axisymmetric 2D modeling assumption is preferred to save the computational cost. The boundary value problem of macroindentation is modeled by using a finite element code, e.g. ABAQUS® 6.11. The steel indenter can be assumed to be a rigid body compared to the soft silicone rubber. The geometrical size of the sample is 10 mm × 10 mm, which is sufficiently large to obtain a homogeneous stress distribution at the bottom and on the side boundaries of the model. For each studied configuration, the mesh convergence is checked by more than 100,000 degrees of freedom. It shows that a coarse mesh, consisting of at least 8000 degrees of freedom, can give converged results. To account for the large localized deformation in contact, it is essential that the density of nodes under the indentation tip is high enough. The rigid tip is fixed in the horizontal direction and a vertical displacement is applied to its reference point. The bottom nodes of the mesh are fixed. Fig. 5 presents the geometry, boundary value problem and the mesh of the FEM model of macroindentation.

Concerning the numerical treatment of the contact problem, the indenter is defined as master surface while the specimen is defined as slave surface, both forming a contact pair. In the macroindentation experiment, the maximum displacement is less than 5% of the specimen's thickness. In this case, the effects of the substrate and the friction between the indenter and the polymer surface is negligible according to Chen and Diebels (2012) and Chen et al. (2011). A contact formulation of finite-sliding inter-

action between a deformable and a rigid body in ABAQUS®/Standard is used to establish the frictionless contact model between indenter and specimen. In this case, the formulation of the normal contact is used as a constraint for non-penetration which treats the normal contact as a unilateral constraint problem. The normal contact pressure cannot be calculated from a contact constitutive equation, but is then obtained as a reaction on the contact surfaces, and hence can be deduced from the constraint equations with the often used Lagrange multiplier method or the Penalty method, for details please see Wriggers (2006).

3.3. Numerical optimization procedure

The material parameters are obtained by inverse method dealing with numerical optimization. In the optimization procedure, the vector of material parameters $\boldsymbol{\kappa} := \{C_{ij}, i = 0, 1; j = 0, 1, 2, 3\}$ has to be modified until a close match between the experimental data and the prediction of the numerical model is achieved. For that reason the distance function $f(\boldsymbol{\kappa})$, which is called objective function of the least squares type has to be minimized to find the optimal $\boldsymbol{\kappa}$

$$f(\boldsymbol{\kappa}) := \frac{\|\mathbf{B}^{num} - \hat{\mathbf{B}}^{exp}\|}{\|\hat{\mathbf{B}}^{exp}\|} \longrightarrow \text{Min }(f(\boldsymbol{\kappa})). \tag{5}$$

Herein

$$\hat{\mathbf{B}}^{exp} = P(\mathbf{B}^{exp}) = [B_{t1}^{exp}, B_{t2}^{exp}, B_{t3}^{exp}, \ldots]^T \tag{6}$$

is the vector of the experimental force or displacement data $\mathbf{B}^{exp}$ at each time increment. It is an interpolation of the experimental results by using the introduced projection operator P, for details please see Johlitz et al. (2007). The force or displacement vectors, obtained from the models at the same time increments as the interpolated data $\hat{\mathbf{B}}^{exp}$ with an arbitrary set of material parameters, are called

$$\mathbf{B}^{num} = [B_{t1}^{num}, B_{t2}^{num}, B_{t3}^{num}, \ldots]^T. \tag{7}$$

The choice of the optimization-based method for minimizing an objective function is a topic of interest. It is generally advised to use globally convergent optimization algorithms whenever possible. These algorithms are simulated annealing or genetic algorithms, such as evolutionary algorithms or deterministic algorithms like the Simplex method. The gradient-based algorithm is full of the troublesome gradient calculation and the further drawback of local convergence. Genetic or evolutionary algorithms are globally convergent and the only useful choice in a multi-objective optimization. Therefore, to update the initially guessed material parameter vector $\boldsymbol{\kappa}$, the evolution strategy based on principles of biological evolution, is employed. It works with a Genetic Algorithm, more details have been explained in Beyer et al. (2001).

The algorithm requires bounds for each parameters. The computational cost can be reduced if narrow bounds are chosen. In general, the choice of the bounds depends on the problem and the experience of the user. Furthermore, the choice of the initial values of the parameters has
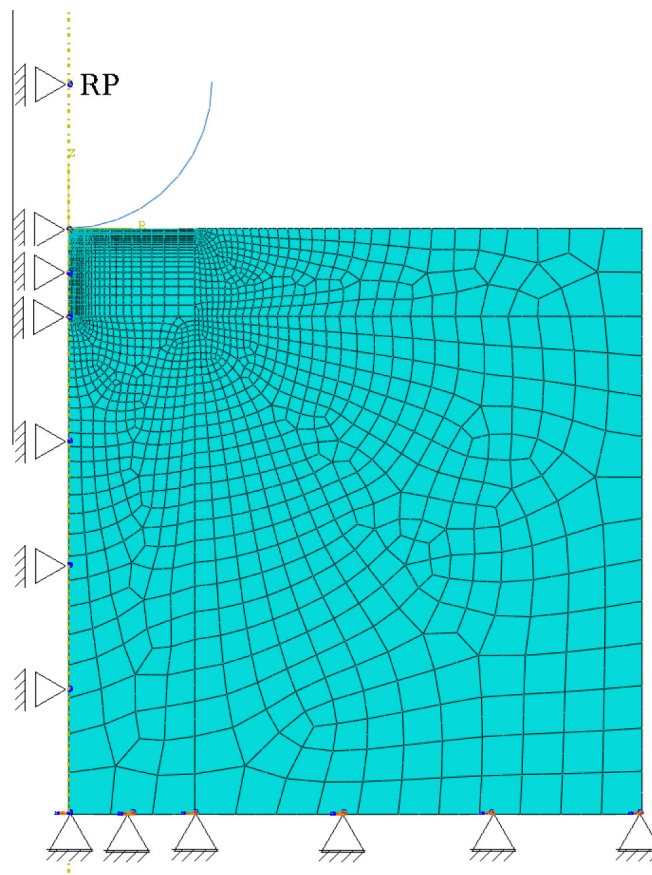
Fig. 5. Sketch of the geometry, boundary value problem and the mesh of the FEM model of macroindentation.

influence on the convergence speed to the optimal results. In Table 2 the identified results as well as the set bounds and the initial values are listed. Because of a negative value of C_{20}, the Yeoh form is able to describe the up-turn in the stress–strain curve at large deformation. The comparison between the experimental measurement and the numerical simulations using the identified parameters will be discussed in Section 5.

4. Tensile tests

In order to investigate the correlation of the characterization using different type of mechanical testing, both uniaxial and biaxial tensile tests are performed for the considered silicone rubber.

4.1. Experimental setup

The device shown as Fig. 4 in Koprowski-Theiss et al. (2011), is used to perform the uniaxial tensile tests. Dog-bone specimens according to DIN EN ISO 527 are die cut from the silicone rubber sheet with a thickness of about 2 mm. The deformation of the specimen is measured based on an optical technique with a pixel size of 1024×1024 pixels. More details about this tensile device and testing methods are described in Koprowski-Theiss et al. (2011). The stretches, not only in the tensile direction (λ_1) and transverse direction (λ_2), but also in the thickness direction (λ_3) can be measured optically. The isotropic assumption is proved that there is no significant difference between the measured values of λ_2 and λ_3. The incompressibility can then be verified by the Jacobian J, which is computed by

Table 2
The identified parameters from macroindentation.

Models	neo-Hooke	Mooney–Rivlin		Yeoh form		
Parameters	C_{10}	C_{10}	C_{01}	C_{10}	C_{20}	C_{30}
Bounds	(0.0001;0.5)	(0.0001;0.5)	(0.0001;0.5)	(0.0001;0.5)	(−0.5;0)	(0.0001;0.5)
Initial	0.05	0.05	0.05	0.05	−0.05	0.05
Identified	0.150	0.146	0.004	0.150	−0.004	0.004
$f(\kappa)$	0.00458	0.00463		0.00449		

$J = \det \mathbf{F} = \lambda_1 \lambda_2 \lambda_3 = \lambda_1 \lambda_2^2$ and its value has been shown in Fig. 3. The component of Cauchy stress T_{11} can be calculated from the force F_1 and the stretch in tensile direction λ_1 through $T_{11} = \frac{F_1}{A_0} \lambda_1$, wherein A_0 stands for the initial cross section of the specimen.

The biaxial tensile testing device consists of four actuators driven by stepper motors MDrive34® of the company Intelligent Motion Systems Inc.®, which are arranged in a cruciform manner, see Fig. 6 (left). Both motors, which form an axis, move ahead symmetrically as shown in Fig. 6 (middle). The four arms of the specimen (see Fig. 6 (right)) are fixed in the clamps with a dimension of 12.5 mm × 12.5 mm. The symmetric motion ensures that the center of the specimen does not move during the experiment and stays stationary, which makes it possible to use the optical method to measure the deformation in the center (Johlitz and Diebels, 2011). The biaxial tensile device is also performed by displacement control, with a resolution of 1 μm and a maximum value of 300 mm. The force on each axis is measured by an independent force sensors. The whole device is computer controlled, realized by the real-time system Compact Rio® of the company National Instruments®. A high sampling rate (50 kS/s) allows to average a bundle of force values immediately to reduce the noise.

This biaxial tensile device was firstly used and described in Johlitz and Diebels (2011). They used a cruciform specimen composed by two dogbone forms. A small square mark of silk screen color was placed on the center of the cruciform specimen like in the uniaxial tensile test. Only the deformation of this square was measured using an optical method. Problems were found during the experiments that not enough homogeneous deformation in the middle of the specimen as required was obtained. In addition to that, the deformation and force were measured at different positions of the sample. Therefore, the geometrical shape of the specimen is optimized to make the deformation in the middle of the specimen as homogeneous as possible. A specimen's shape shown in Fig. 6 (right) with a quite large radius from one axis to the other one is chosen as an optimized geometry (Melchior, 2012). Specimens of such a shape are die cut from the silicone rubber sheet with a thickness of about 2 mm. The local deformation measurement used in Johlitz and Diebels (2011) is replaced by a field measurement technique based on the

evaluation of speckle patterns. The sample is firstly marked with a stochastic pattern by spraying color, see Fig. 7 (left). A digital image correlation (DIC) is applied, with which the displacement of the speckles over the whole specimen can be measured. The pattern fields which are correlated in the software Vic2D® have a size of 15 pixels × 15 pixels in this case. Whereby, as presented in Fig. 7 (right), in each of these fields at least 3 spraying dots have to be included. Hence, during the experiment Vic2D® is able to calculate the deformation at continuous level of the speckles based on the correlated solutions obtained from DIC (Sutton et al., 2009). Following (Johlitz and Diebels, 2011) the evaluation of the biaxial test is treated as an inverse problem, i. e. in a numerical simulation of the test, the measured forces are applied to the specimen. The resulting deformation in the center part is compared to the measured deformation.

4.2. Fitting with analytical solutions

Similar to macroindentation test, firstly, a single step relaxation testing is performed to display the viscous effects. A maximum displacement of 40 mm is applied to the tensile tester within 10 s. Hereafter, the specimen is hold at this maximum deformation lasting for 300 s. A semi-log plot of the measured force along with testing time is displayed in Fig. 8. Like in the macroindentation, the silicone rubber behaves mainly in an elastic way. Therefore, for the following analysis, the viscous part is not taken into account. We focus only on the basic elasticity. Four different maximum displacements of 10 mm, 20 mm, 30 mm and 40 mm are considered secondly in order to represent a spectrum of stress–strain curves with the maximum strains about 1.6, 2.3, 3.1, 4.1 as shown in Fig. 9. For the homogeneous case of the uniaxial tensile test, analytical solutions of the stress–strain relationship can be derived for an incompressible material. In order to be comparable with the macroindentation results, the three classical models, neo-Hooke, Mooney–Rivlin and Yeoh, are chosen in the uniaxial test, too. The analytical solutions for the Cauchy stress component T_{11} in tensile direction as function of the component B_{11} of the left Cauchy strain are shown in Appendix C. These analytical solutions are fitted to the experimental $T_{11} - B_{11}$ data using the non-linear least squares regression. As can be seen in Fig. 9,
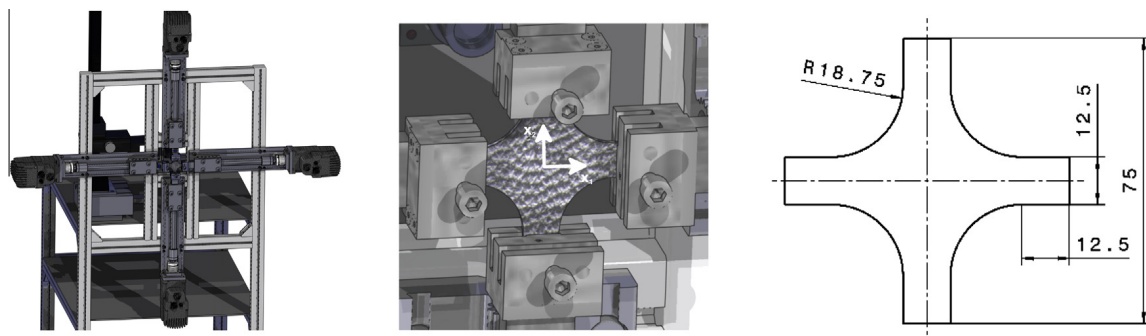
Fig. 6. Overview of the biaxial tensile test (left) with built-in specimen in detail (middle) and dimensions of specimen (right).
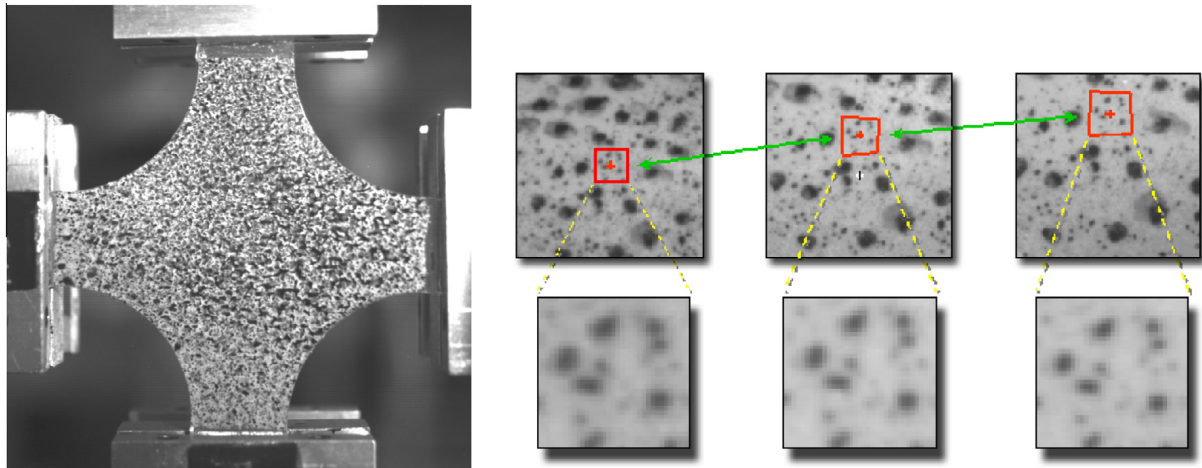
Fig. 7. Left: stochastic pattern on the specimen; right: pattern recognition for different deformation levels.
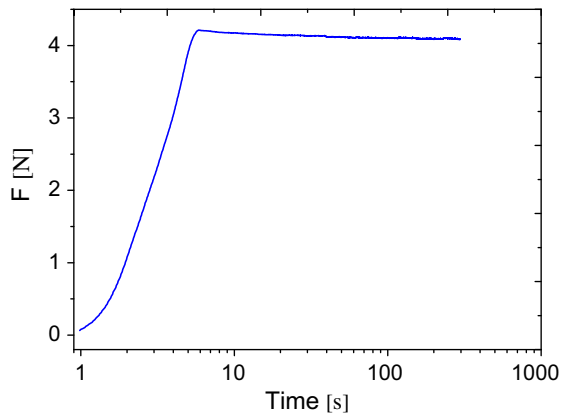
Fig. 8. Semi-log plot of a single step relaxation in uniaxial tensile test.
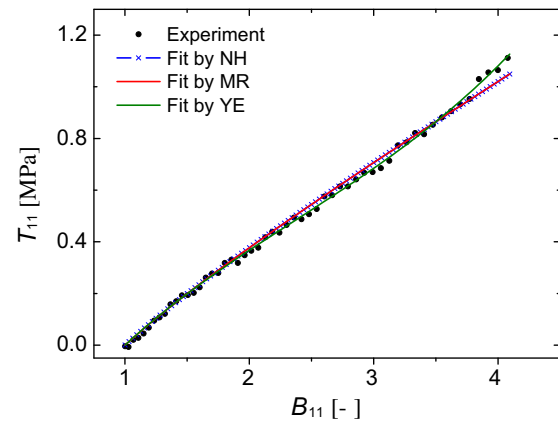
Fig. 9. The $T_{11} - B_{11}$ curves are fitted by the analytical solutions.

the black points represent the experimental data and the colored lines are the fits by different models. First of all, the fitting curves of the neo-Hooke model and the Mooney–Rivlin models overlap in every single case. This could be explained by the fitted parameters listed in Table 3 the parameter, i. e. C_{01} of the Mooney–Rivlin model is close to zero, and the contribution made by the second invariant in the Mooney–Rivlin model (cf. Eq. (2)) is negligible. Secondly, one should note that the difference of the three models is detectable until the strain increases up to 3. The Yeoh model is able to describe the elastic behavior in the large strain domain precisely (Yeoh, 1990). As can be seen in Table 3, if the strain B_{11} is larger than 3 (cf. of the load cases u = 30 mm, u = 40 mm), the parameters C_{20} and C_{30} related with the second-order and the third-order terms can be identified. The contribution due to these two terms allows the Yeoh model to be able to describe the up-turn in the stress–strain curve leading to a deviation from the other two models at large deformations. In the first case, cf. u = 10 mm, C_{20} is determined to be a larger value but C_{10} is fitted with a much smaller value compared with

other cases. An explanation to these results could be the parameters' coupling, which is a typical problem in the determination of the hyperelastic models' parameters (Rauchs et al., 2010; Giannakopoulos and Triantafyllou, 2007; Giannakopoulos and Panagiotopoulos, 2009).

5. Comparisons and discussion

5.1. Comparison of the obtained Young's modulus

The Young's modulus E is a measurement of the stiffness of an elastic material and is an important quantity used to characterize materials. As analyzed in Section 2.3, the elastic modulus is able to be determined by the Sneddon's solution and the Oliver and Pharr method in the instrumented indentation tests. Since the incompressibility of the used silicone rubber has been proven, the elastic modulus can also be evaluated from the tensile measurements. Table 4 contains the elastic modulus determined from the macroindentation and the uniaxial tensile tests. The elastic modulus evaluated from the three hyperelastic

Table 3
The model parameters fitted from uniaxial tensile tests.

Models	neo-Hooke	Mooney–Rivlin		Yeoh form		
Parameters	C_{10}	C_{10}	C_{01}	C_{10}	C_{20}	C_{30}
u = 10 mm, B_{11} = 1.6	0.147	0.146	0.000	0.139	−0.038	0.000
u = 20 mm, B_{11} = 2.3	0.146	0.146	0.000	0.147	−0.000	0.000
u = 30 mm, B_{11} = 3.1	0.147	0.147	0.000	0.148	−0.007	0.004
u = 40 mm, B_{11} = 4.1	0.146	0.146	0.000	0.148	−0.009	0.004

Table 4
Comparison of the determined Young's modulus E.

Macroindentation					Determined by uniaxial tensile[b]	
Sneddon's solution	Oliver and Pharr	Identified				
0.90[a]	0.93[a]	NH	0.90[a]	NH	0.88[a]	
		MR	0.90[a]	MR	0.88[a]	
		YE	0.90[a]	YE	0.87[a]	

[a] The standard deviation of the Young's modulus E in this table is 0.0184.
[b] The average value of each model parameters in Table 3, taken from the four different displacements, is used to evaluate the elastic modulus.

models are the same not only for the macroindentation but also for the uniaxial tensile tests. In the macroindentation, the elastic modulus determined by the Oliver & Pharr is about 3% larger than the values calculated by the other two methods. Such a deviation is really small and is acceptable and arise because the loading part and the unloading part of the same force–displacement curve measured from indentation are used in the Sneddon's solution and the Oliver and Pharr method, respectively. The reason could be the slightly viscous effect in the unloading curve, which leads to a slight larger contact stiffness. The elastic modulus approximated from the fitted parameters in uniaxial tensile tests are less than those values obtained from macroindentation. This difference may be due to the different stress and strain states between the indentation and the tensile tests, which will be discussed further in the following section. Anyway, the differences between the modulus obtained by various methods are so small that the deviation of the maximum and the minimum is less than 6.5%. Therefore, for the purpose of engineering application,

macroindentation can be used to get the elastic modulus of the elastomers in service by the Sneddon's solution as well as the Oliver and Pharr method. Or the modulus could be also approximated from the model parameters if the inverse method is used.

5.2. Comparison of macroindentation and uniaxial tensile tests

Fig. 10 (left) presents the comparison between the experimental force–displacement curve obtained from macroindentation and the simulated ones using the parameters (in Table 2) identified based on the indentation response. The agreements of all three models are actually perfect, which could be also judged according to the objective functions given in Table 2. Besides, the same experimental force–displacement curve is compared to the simulated one using the parameters (in Table 3) fitted by the analytical constitutive solutions on the uniaxial tensile measurements. The tensile responses of the considered
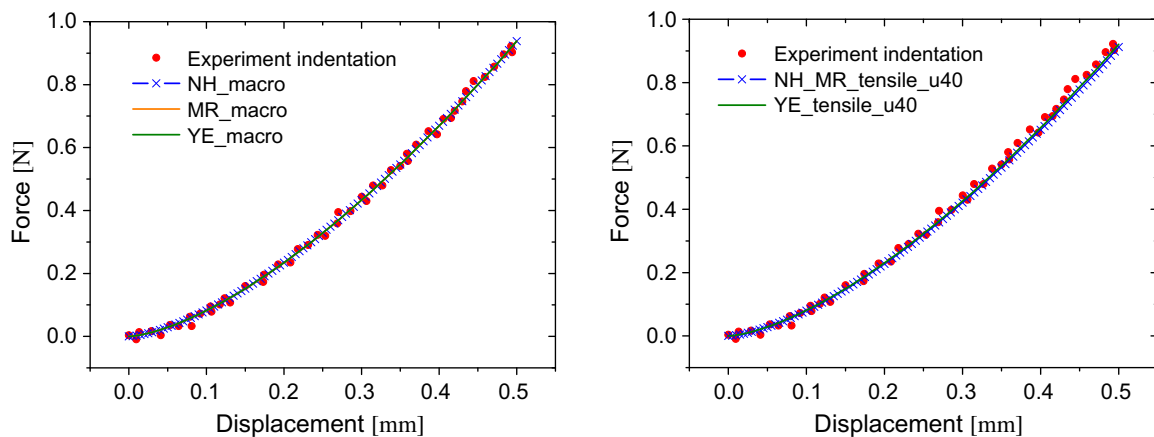
Fig. 10. Comparison of indentation experimental force–displacement curve with numerical simulations using obtained parameters: left, in Table 2 (macroindentation); right, in Table 3 (tensile).
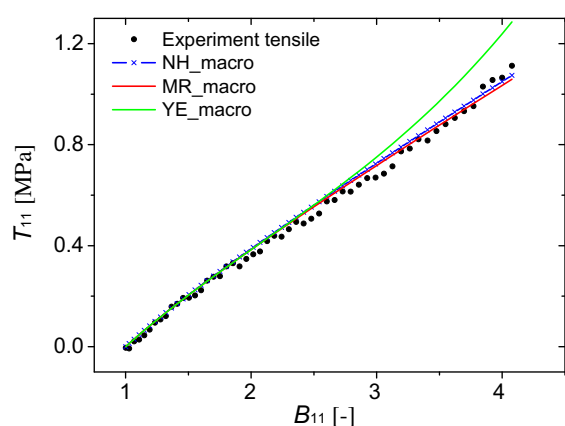
Fig. 11. Comparisons between the experimental stress–strain curves in uniaxial tensile tests and the analytical predictions with the parameters obtained from macroindentation.

material at various displacements from 10 to 40 mm are taken into account. The matches between the experiment and the simulations are very good except the Yeoh model with the parameters fitted at the displacement of 10 mm. In order to shorten the paper, only the result which is obtained with a displacement of 40 mm, is presented in Fig. 10 (right).

In the following, the parameters identified from the indentation tests will be used to predict the responses in the uniaxial tensile tests. Fig. 11 illustrates the comparisons between the experimental stress–strain curves and the one analytically evaluated using the constitutive functions with the parameters given in Table 2. As can be seen from Fig. 11, if the strain is in the range of $1 \leqslant B_{11} \leqslant 3$, the analytical predictions of all the three models match the experimental data as good as those with the parameters obtained from the identical tests, which are shown in Fig. 9. If the strain raises up to 4, the agreements of the neo-Hooke and Mooney–Rivlin models are better compared to Fig. 9. Hence, the prediction using the neo-Hooke and Mooney–Rivlin models are closer to the responses in uniaxial tensile tests with the parameters identified from macroindentation than the evaluation with the parameters obtained from the identical tests. However, it is not the case for the Yeoh model. A pronounced gap appears and raises up with the increment of the strain.

Summarizing, the correlation between the macroindentation and the uniaxial tensile test depends not only on the chosen hyperelastic model but also on the strain level. For the one-order polynomial form, e.g. neo-Hooke and Mooney–Rivlin models, the correlation obtained is very good. It is validated that the parameters identified from macroindentation can be relevant to predict the uniaxial tensile behavior of unfilled silicone rubber and vice versa, even for a wide range of strain, which can represent the one encountered in most of the industrial application. These partial results are similar to the findings in Le Saux et al. (2011). However, it is not the case for higher order polynomial forms, e.g. Yeoh model, which is motivated to simulate the mechanical behavior showing a typical stiffening effect in the large strain domain. In the uniaxial tensile

tests, if the strain is smaller than 1.6, parameters of the Yeoh model cannot be accurately identified. The parameters identified in uniaxial tensile tests at larger strains are able to describe the behavior in macroindentation in this study. Conversely, the parameters identified in macroindentation are not able to simulate the tensile behavior at large strain $B_{11} \geqslant 3$. A similar conclusion stated in Rauchs and Bardon (2011) and Giannakopoulos and Triantafyllou (2007) that the constitutive parameters obtained from microindentation measurement of filled rubber-like elastomers were usually not suitable to describe the macroscopic tensile tests. Le Saux et al. argued that the reasons in Rauchs and Bardon (2011) and Giannakopoulos and Triantafyllou (2007) could be the stiffening effect at large strain for the filled rubber and the numerous error contributions in the nano- or microindentation experiments (Le Saux et al., 2011). These two aspects are avoided in our study. Therefore, the different stress and strain state, which are well known to be of primary influence, could be the potential reason and will be further discussed. Fig. 12 presents the obtained strain state from numerical simulation of the macroindentation experiment in this study at the maximum displacement of 0.5 mm. A Mooney–Rivlin model with the parameters identified from indentation is used. B_{11} represents the component of the left Cauchy strain in the direction of indentation. The strains are maximized at the contact range just under the spherical tip and radially diminish to zero with increasing distance from the contact center. The circular strain zones with the various value shown in the color bar validate that the deformation in indentation is mainly multi-axial and locally compressive by nature. Only slight tensile effects ($B_{11} < 1$) exist outside the contact zone. In addition to that, the stress–strain behaviors in the uniaxial compression and in tensile tests are compared in Fig. 13. The three models with the parameters identified on the response of indentation and tensile tests at displacement of 40 mm are taken into account. There is no difference in the five curves if the strain is smaller than 3, which contains the strain range in macroindentation as shown in Fig. 13. This could be the most likely explanation that the models with the identical parameters show the same behavior in indentation but the Yeoh model shows higher stiffness in the tensile response.

5.3. Further verification by biaxial tensile tests

A phenomenon can be seen in the identified results discussed above, that the parameter associated with the second invariant of the Mooney–Rivlin cannot be absolutely identified from uniaxial tensile tests but could be identified with a small value from macroindentation. Concerning hyperelastic models, a well known explanation is that experiments with different stress or strain states may fit best with different expressions of the hyperelastic potential (Drozdov et al., 1996; Baaser and Noll, 2009; Johlitz and Diebels, 2011). An invariant plane as presented in Fig. 14, can be normally used to express the deformation states for incompressible material behavior (Baaser and Noll, 2009; Johlitz and Diebels, 2011; Treloar, 1975; Baaser et al., 2013). It is recognized that the uniaxial tensile and
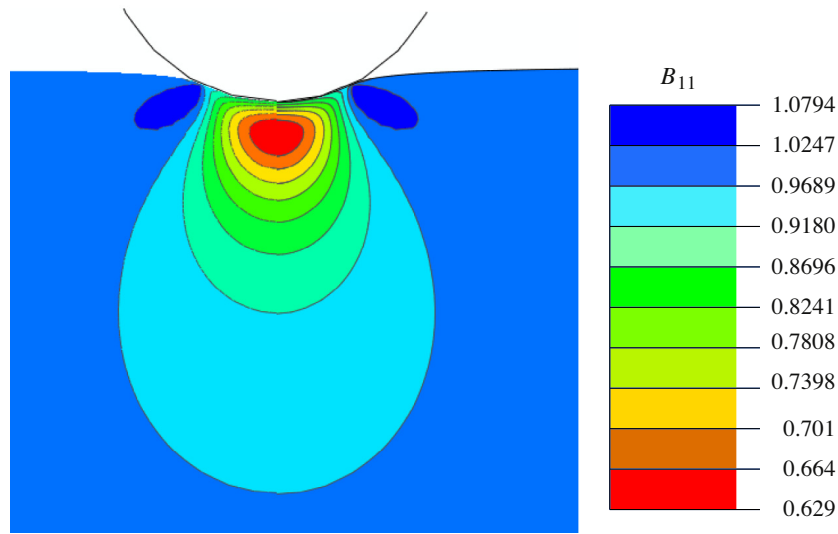
Fig. 12. The strain state of the deformed specimen under macroindentation with maximum displacement of 0.5 mm.

compression tests as well as the shear test only represent one curve in the invariant plane. The indentation test covers a small area close to the curve of compression in the invariant plane taking into account different shapes of indenter. In the case of a spherical indenter, a stronger compressive deformation phenomenon takes place, while the shearing deformation state is more predominant with sharper indenter. The biaxial tensile test is able to capture a larger area in the invariant plane. Not only all deformation states contained in the testing types mentioned above but also new states are possible in biaxial tensile test. Hence, it is interesting to verify the characterization of the silicone rubber using the uniaxial tensile test and macroindentation by the biaxial tensile test. (see Fig. 13)

As a first step, the biaxial tensile test is performed on the same material with the loading set presented in Fig. 15 (left). The vertical arms are stretched 40 mm in the x_2-direction within 90 s and hold at this deformation. Subsequently, the horizontal arms are stretched stepwisely 40 mm in the x_1-direction including relaxation so that the arms are stretched 1 mm within 20 s and are hold for about 300 s at each step. The holding time is chosen in such a way that the measured force achieves a stationary value at the end of the step. The unloading is performed for all arms in short time when a displacement of 40 mm on both horizontal arms is reached. The numerical simulation of the biaxial tensile experiments are done using a similar loading set as shown in Fig. 15 (right). Because the chosen three hyperelastic models are used, not a stepwise but a ramp loading is used.

The verification is dealt by comparing the obtained force from experiments and simulations. Firstly, a comparison of the Lagrangian strain state is performed to guarantee the suitable boundary condition and loading settings in the FEM simulation. The Mooney–Rivlin model with the identified parameters from macroindentation is used. Fig. 16 presents the Lagrangian strain E_{11} in x_1-direction calculated by DIC at the step when the maximum displace-

ments in both directions is reached. The Lagrangian strain in x_1-direction at the same step calculated by FEM is shown in Fig. 17 (left). It is recognized that the covered range and the distribution of the Lagrangian strain in x_1-direction are almost the same in the experiment and in the simulation. The slight difference of the strain state in the middle and at the arms may be due to the used material model that the second invariant makes only a slight contribution. Besides, the applied DIC technique has a limitation to measure the deformation of the fringes and of the areas near the clamps, which could also make some difference compared to the numerical calculation. Furthermore, the stress state as shown in Fig. 17 (right) makes a further validation that, if such a geometrical shape (see Fig. 6 (right)) of specimen is used, a larger area in the middle with homogeneous deformation can be obtained.

The reaction forces of the horizontal and the vertical axes calculated by simulation, F_1 and F_2, are compared to
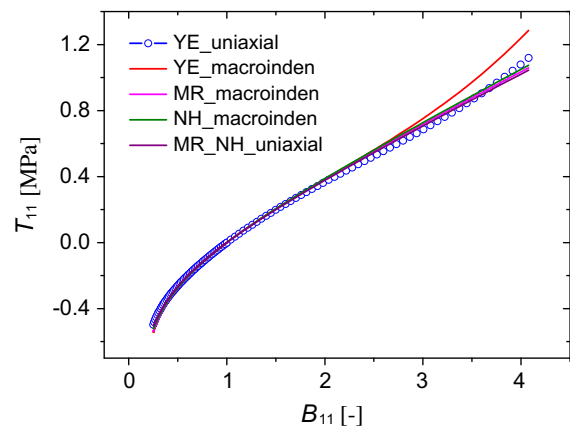
Fig. 13. The stress–strain curve of the used hyperelastic model with the identified parameters in compression and tensile tests.
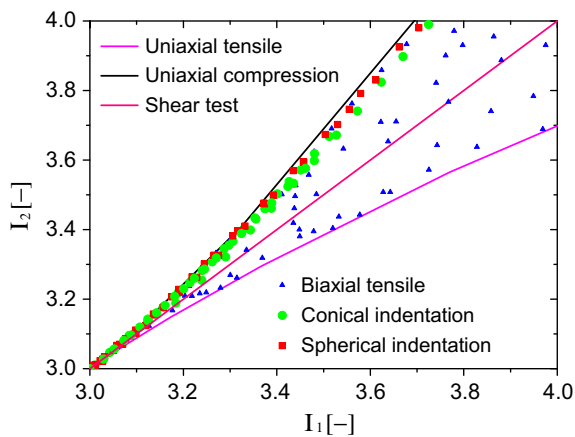
Fig. 14. Deformation states of Uni/Biaxial tensile tests, shear test and indentation tests described in the invariant plane for incompressible material behavior.

Fig. 16. Lagrangian strain in x_1-direction calculated by DIC in biaxial tensile test before unloading.

the measurements at each axes, respectively. Both reaction forces match the experimental measurements very well using the neo-Hooke and Mooney–Rivlin models with parameters identified from indentation and from uniaxial tensile tests, as can be seen in Fig. 18. However, the one calculated using Yeoh model presents deviations at larger deformation, not depending on the parameters identified by indentation or uniaxial tensile tests. It seems that the second invariant in the biaxial test has only slight contribution to the force–displacement behavior in this studied case. The neo-Hooke model with only one parameter or the Mooney–Rivlin model with a small coefficient associated with the second invariant, which can characterize the indentation and uniaxial data very well, are still able to describe the force–displacement behavior in the biaxial test. It is also recognized that the Yeoh model shows larger stiffness than the neo-Hooke and Mooney–Rivlin models, but they present almost the same stiffness in the indentation and uniaxial tests. Therefore, it could be assumed that the deformation in the biaxial test is much larger than the one obtained in the indentation and uniaxial tests.

6. Conclusions

In the present study, we performed macroindentation tests by means of a spherical indenter on silicone rubber using a device originally developed for a typical universal tensile testing machine. Specimens of the considered material are also prepared for uniaxial and biaxial tensile tests. The hyperelasticity is characterized by the inverse method from the experimental data of indentation and uniaxial tests and compared to each other. The characterization is then verified further by the biaxial test. Firstly, it shows that the differences of the elastic modulus approximated from the macroindentation and the uniaxial test are so small that the maximum deviation is less than 6.5%. Therefore, for the purpose of engineering application, macroindentation can be used to get the isotropic elastic modulus of the elastomers in service by the Sneddon's solution as well as the Oliver and Pharr method. Secondly,
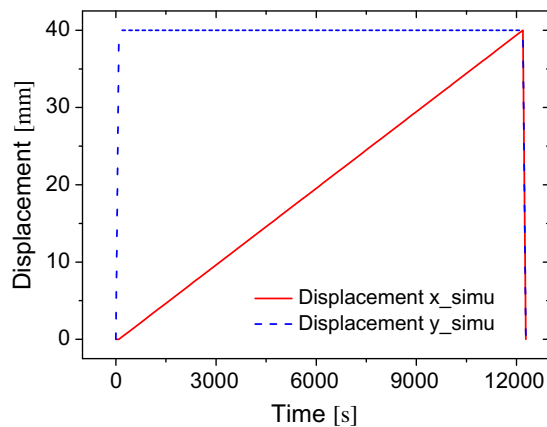
Fig. 15. The loading set of the biaxial tensile tests: Experiment (left); Simulation (right).
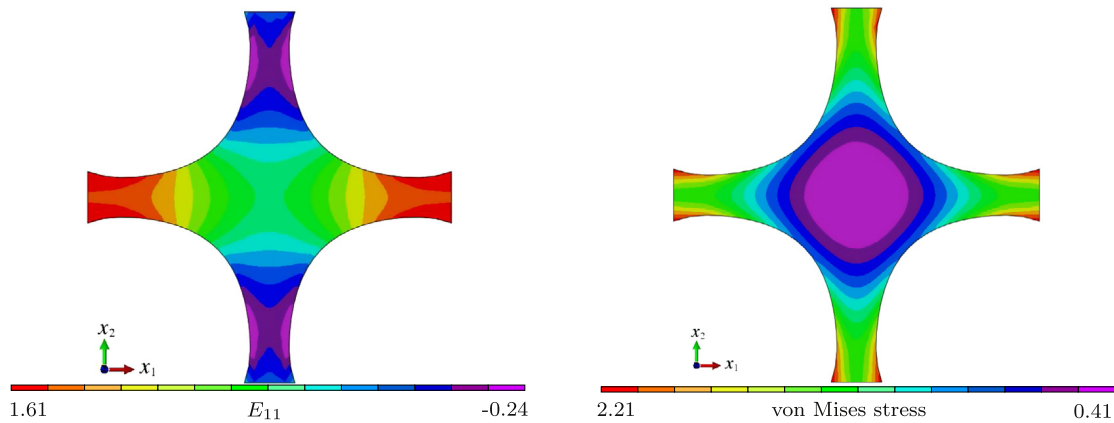
Fig. 17. The visualized plots obtained from simulation of biaxial tensile test before unloading: Lagrangian strain in x_1-direction (left); Von Mises stress (right).
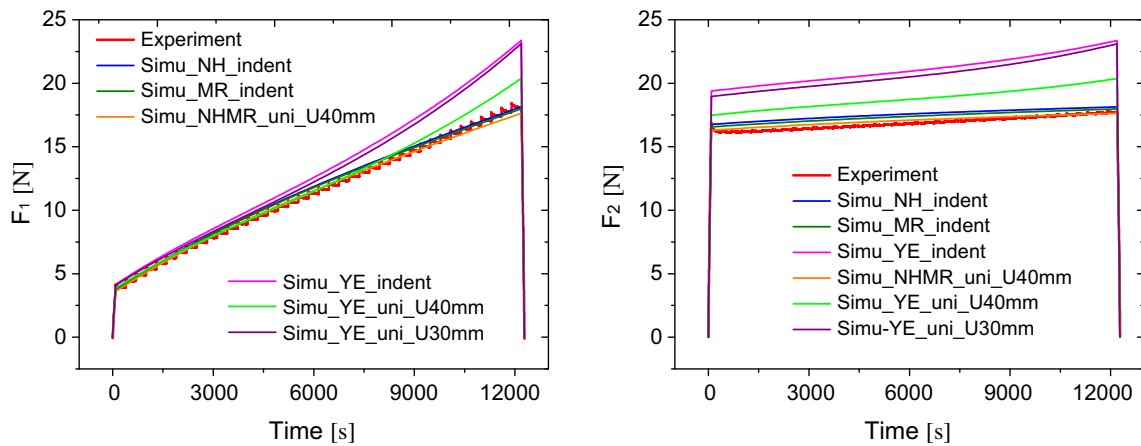
Fig. 18. Comparison of the obtained forces in x_1- and x_2-directions from experiments and simulations.

if the unfilled isotropic polymer is characterized by a one-order polynomial form, e.g. neo-Hooke and Mooney–Rivlin models, the correlation between the macroindentation and the uniaxial test is very good. However, for higher order polynomial forms, e.g. the Yeoh model, which is characterized from macroindentation, it is not possible to reproduce the uniaxial data at large strain $B_{11} \geqslant 3$. Thirdly, the neo-Hooke model with only one parameter or the Mooney–Rivlin model with a small coefficient associated with the second invariant, which can characterize the indentation and uniaxial data very well, are still able to describe the force–displacement behavior in the biaxial test. It is also recognized that the Yeoh model shows a larger stiffness than the neo-Hooke and Mooney–Rivlin models, but they present almost same stiffness in the indentation and uniaxial tests.

Acknowledgment

Appendix A. Sneddon's solution

At the beginning, the Hertz theory of elastic contact will be briefly reviewed. Hertz studied Newton's optical interference fringes in the gap between two lenses and concerned at the influence of the elastic deformation of the surfaces of the lenses due to the contact pressure (Hertz, 1881). Guided by his observation of the interface during experiments, Hertz first pointed out that the contact area is in general elliptical. He then introduced the assumptions
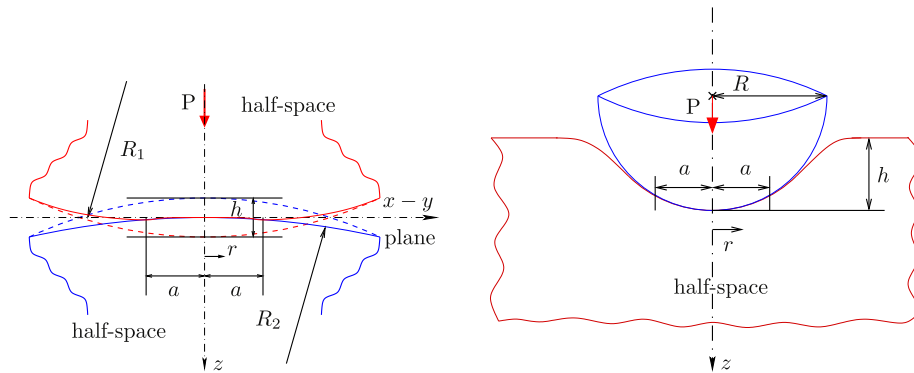
Fig. A1. Schematics of contact between two elastic deformable half-spaces (left) and indentation on a elastic half-space by a rigid spherical indenter (right).

for the purpose of calculating the local deformation (Hertz, 1881; Johnson et al., 1985):

1. Each solid in contact can be considered as an elastic half-space;
2. The dimensions of the contact area must be small compared with the dimensions of each solid body and the relative radii of curvature of the surfaces;
3. The surfaces in contact are frictionless.

A distribution of pressure, proposed by Hertz based on the assumptions above, leads to the displacement

$$p = p_0\{1 - (r/a)^2\}^{1/2}, \tag{A.1}$$

where p_0 is the maximum pressure, r ($0 \leqslant r \leqslant a$) is the lateral coordinate along the contact area, as shown in Fig. A1. The radius a of the contact circle is given by

$$a = \frac{\pi p_0 R}{2E^*}. \tag{A.2}$$

The effective elastic modulus E^* is defined as

$$\frac{1}{E^*} = \frac{(1 - v_1^2)}{E_1} + \frac{(1 - v_2^2)}{E_2}, \tag{A.3}$$

E_1, v_1, E_2, v_2 are the Young's modulus and the Poisson's ratio of the first and the second body, respectively. R is the relative curvature, which is expressed by $1/R = (1/R_1 + 1/R_2)$. The mutual approach of corresponding points, also called total displacement in the two bodies, is formulated by

$$h = \frac{\pi a p_0}{2E^*}. \tag{A.4}$$

The total load P compressing the solids is calculated from the pressure by

$$P = \int_0^a p(r) 2\pi r \, dr = \frac{2}{3} p_0 \pi a^2. \tag{A.5}$$

The relationship between the total load and the displacement can be written as

$$P = \frac{4}{3} E^* \sqrt{R} h^{3/2}. \tag{A.6}$$

For the Boussinesq problem of a rigid axisymmetric body indenting into a half-space composed of a homogeneous, linearly elastic and isotropic material, Sneddon derived an expression for the indentation load with an axisymmetric indenter arbitrary shape $f(x)$ (Sneddon, 1965)

$$P = \frac{4\mu a}{1 - v} \int_0^1 \frac{x^2 f\prime(x)}{\sqrt{1 - x^2}} \, dx, \tag{A.7}$$

where μ is the shear modulus, v is the Poisson's ratio of the indented half-space and $f(x)$ is the smooth shape function of the indenter with dimensionless coordinate $x = r/a$ ($0 \leqslant x \leqslant 1$), as defined in Fig. A1 (right). The Sneddon's solution of the displacement is given by

$$h = \int_0^1 \frac{f\prime(x)}{\sqrt{1 - x^2}} \, dx. \tag{A.8}$$

For a spherical indenter, the shape function is $f(x) = (ax)^2/(2R)$ under the assumption $ax \ll R$, The relationship between load and displacement can be derived as

$$P = \frac{4}{3} \frac{E}{1 - v^2} \sqrt{R} h^{3/2}, \tag{A.9}$$

where the shear modulus $\mu = \frac{E}{2(1+v)}$ is replaced by the Young's modulus E. Sneddon's contact is a special case of Hertz's contact with further assumptions, as shown in Fig. A1 (left), the upper spherical body is a rigid body with a finite radius R_1 as well as the lower half-space has an infinite large radius R_2. Therefore, the reduced modulus E^* in Eq. (A.6) is only related to the elastic constants of the lower half-space E_2 and v_2, the relative curvature R is consistent with R_1. In this case, the relationships between the load and the displacement expressed by Eq. (A.6) and (A.9) are the same.

Appendix B. Oliver and Pharr method

The Oliver and Pharr method was developed to determine the hardness and elastic modulus of a material from indentation load–displacement data obtained during one cycle of loading and unloading. If this method is applied, attention should be paid on the behavior of the material, which is limited to be described as a semi-infinite, elastic–plastic half space.
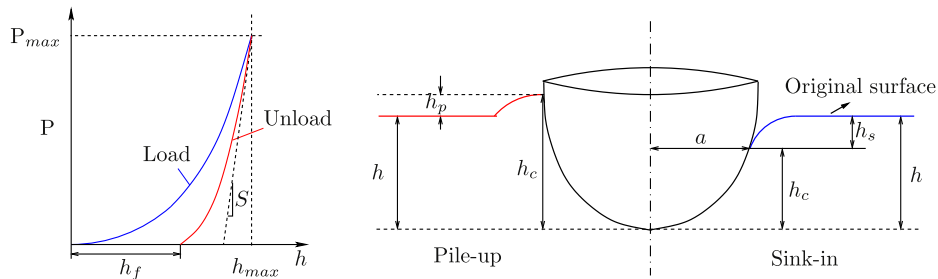
Fig. A2. Schematics illustration of indentation load–displacement data (left) and of the contact geometry (right).

There are three important quantities that must be measured from the force–displacement curves, as defined in Fig. A2 (left): the maximum load P_{max}, the maximum displacement h_{max} and the contact stiffness $S = \frac{dP}{dh}$, which is defined as the slope of the initial part of the unloading curve during the first stage of unloading. Another important quantity for the plastic behavior is the final depth h_f, the permanent depth of penetration after the indenter is fully unloaded. With the assumption that during the unloading, only the elastic displacements are recovered, the unloading curves are usually well approximated by the power law relation:

$$P = \alpha (h - h_f)^m, \tag{B.1}$$

where α and m are power laws fitting constants. The elastic properties can be determined from the relationship between measured contact stiffness S and the contact area A through the solution

$$S = \beta \frac{2}{\sqrt{\pi}} E^* \sqrt{A}. \tag{B.2}$$

Herein the effective elastic modulus E^* as expressed in Eq. (A.3) takes into account the elastic displacements that occur not only in the specimen, but also in the indenter. β is a correction factor that accounts for deviations in stiffness caused by the lack of axial symmetry for pyramidal indenters. β plays an important role if accurate properties measurements are desired. It is difficult to set a single preferred value of β due to its dependence on many factors, e.g. the indenter geometry, the radial displacements of the indenter surface and the complex elastic–plastic deformation with pyramidal indenters. The values obtained from experiments and finite element simulations lie in the range of $1.0226 \leqslant \beta \leqslant 1.085$ (Oliver and Pharr, 1992, 2004). For a perfect spherical rigid indenter, β usually takes the value of 1. The other tricky problem in the Oliver & Pharr method is the determination of A which is the projected contact area described using an area function given by Oliver and Pharr (1992)

$$A = \sum_{n=0}^{8} C_n (h_c)^{2-n} = C_0 h_c^2 + C_1 h_c + \cdots + C_8 h_c^{1/128}. \tag{B.3}$$

Eq. (B.3) is also called shape function of the indenter, where $C_0 \ldots C_8$ are constants determined by curve-fitting in the instrumented indentation analysis procedure. A perfect spherical indenter of radius R is represented by the first two terms with $C_0 = -\pi$ and $C_1 = 2\pi R$. As defined in

Fig. A2 (right), h_c is the depth along the contact line. h_c is defined in the Oliver & Pharr method with the assumption that the pile-up is negligible. It accounts only the amount of sink-in h_s, as shown in Fig. A2,

$$h_c = h_{max} - h_s = h_{max} - \epsilon \frac{P_{max}}{S}. \tag{B.4}$$

ϵ is a constant that depends on the geometry of the indenter. Again, with $\epsilon = 0.75$ for a spherical indenter with a small indentation depth. In the course of an experimental study, Oliver and Pharr found that the amount of pile-up or sink-in depends on the ratio h_f/h_{max} and the work-hardening behavior. The pile-up is only large if h_f/h_{max} is close to 1 and the degree of the work-hardening is small. If $h_f/h_{max} < 0.7$, the pile-up is negligible and independent from the work-hardening behavior of the material.

Appendix C. Constitutive analytical solutions

The analytical solutions for the Cauchy stress component T_{11} in uniaxial tensile direction as function of the component B_{11} of the left Cauchy strain are derived as Johlitz and Diebels (2011)

$$T_{11}^{NH} = 2 C_{10} \left(B_{11} - \frac{1}{\sqrt{B_{11}}} \right), \tag{C.1}$$

$$T_{11}^{MR} = 2 C_{10} \left(B_{11} - \frac{1}{\sqrt{B_{11}}} \right) + 2 C_{01} \left(\sqrt{B_{11}} - \frac{1}{B_{11}} \right), \tag{C.2}$$

$$T_{11}^{YE} = \left(2C_{10} + 4C_{20} \left(B_{11} + \frac{2}{\sqrt{B_{11}}} - 3 \right) + 6C_{30} \left(B_{11} + \frac{2}{\sqrt{B_{11}}} - 3 \right)^2 \right) \left(B_{11} - \frac{1}{\sqrt{B_{11}}} \right). \tag{C.3}$$

References

Oliver, W.C., Pharr, G.M., 1992. An improved technique for determining hardness and elastic modulus using load and displacement sensing indentation experiments. Journal of Materials Research 7, 1564–1583.

Oliver, W.C., Pharr, G.M., 2004. Measurement of hardness and elastic modulus by instrumented indentation: advance in understanding and refinements to methodology. Journal of Materials Research 19, 3–20.

Cheng, Y.T., Cheng, C.M., 2006. Relationship between contact stiffness, contact depth, and mechanical properties for indentation in linear viscoelastic solids using axisymmetric indenters. Structural Control and Health Monitoring 13, 561–569.

Giannakopoulos, A.E., 2006. Elastic and viscoelastic indentation of flat surface by pyramid indenters. Journal of the Mechanics and Physics of Solids 54, 1305–1332.

Cao, Y.P., Ma, D.C., Raabe, D., 2009. The use of flat punch indentation to determine the viscoelastic properties in the time and frequency

domains of a soft layer bonded to a rigid substrate. Acta Biomaterialia 5, 240–248.

Huber, N., Nix, W.D., Gao, H., 2002. Identification of elastic-plastic material parameters from pyramidal indentation of thin films. Proceedings of the Royal Society of London. Series A. Mathematical, Physical and Engineering Sciences 458, 1593–1620.

Huber, N., Tyulyukovskiy, E., 2004. A new loading history for identification of viscoplastic properties by spherical indentation. Journal of Materials Research 19, 101–113.

Klötzer, D., Ullner, C., Tyulyukovskiy, E., Huber, N., 2006. Identification of viscoplastic material parameters from spherical indentation data. Part II: Experimental validation of the method. Journal of Materials Research 21, 677–684.

Tyulyukovskiy, E., Huber, N., 2006. Identification of viscoplastic material parameters from spherical indentation data. Part I: Neural networks. Journal of Materials Research 21, 664–676.

Hartmann, S., Gibmeier, J., Scholtes, B., 2006. Experiments and material parameter identification using finite elements. Uniaxial tests and validation using instrumented indentation tests. Experimental Mechanics 46, 5–18.

Rauchs, G., Bardon, J., Georges, D., 2010. Identification of the material parameters of a viscous hyperelastic constitutive law from spherical indentation tests of rubber and validation by tensile tests. Mechanics of Materials 42, 961–973.

Rauchs, G., Bardon, J., 2011. Identification of elasto–viscoplastic material parameters by indentation testing and combined finite element modelling and numerical optimization. Finite Elements in Analysis and Design 47, 653–667.

Guessasma, S., Sehaki, M., Lourdin, D., Bourmaud, A., 2008. Viscoelasticity properties of biopolymer composite material determined using finite element calculation and nanoindentation. Computational Materials Science 44, 371–377.

Le Saux, V., Macro, Y., Bles, G., calloch, S., Moynea, S., Plessisa, S., Charrierb, P., 2011. Identification of constitutive model for rubber elasticity from micro-indentation tests on natural rubber and validation by macroscopic tests. Mechanics of Materials 43, 775–786.

Chen, Z., Diebels, S., 2012. Nanoindentation of hyperelastic polymer layers at finite deformation and parameter re-identification. Archive of Applied Mechanics 82, 1041–1056.

Chen, Z., Diebels, S., 2013. Parameter re-identification in nanoindentation problems of viscoelastic polymer layers: small deformation. Journal of Applied Mathematics and Mechanics/Zeitschrift für Angewandte Mathematik und Mechanik (ZAMM) 93, 88–101.

Chen, Z., Diebels, S., 2012. Modelling and parameter re-identification of nanoindentation of soft polymers taking into account effects of surface roughness. Computers and Mathematics with Applications 64, 2775–2786.

Chen, Z., Diebels, S., Peter, N.J., Schneider, A.S., 2013. Identification of finite viscoelasticity and adhesion effects in nanoindentation of a soft polymer by inverse method. Computational Materials Science 72, 127–139.

Amitay-Sadovsky, E., Wagner, H.D., 1998. Evaluation of Young's modulus of polymers from knoop microindentation tests. Polymer 39, 2387–2390.

Flores, A., Baltá-Calleja, F.J., Bassett, D.C., 1999. Microhardness studies of chain-extended PE: I. Correlations to microstructure. Journal of Polymer Science: Polymer Physics 37, 3151–3158.

Suwanprateeb, J., 1998. A comparison of different methods in determining load- and time-dependence of vickers hardness in polymers. Polymer Testing 23, 495–506.

Benabdallah, H.S., Bui, V.T., 2004. Indentation of poly(formaldehyde), reinforced nylons and poly(ethyl terephthalate). Polymer Engineering & Science 44, 1439–1447.

Spinks, G.M., Brown, H.R., Liu, Z., 2006. Indentation testing of polystyrene through the glass transition. Polymer Testing 25, 868–872.

Guglielmotti, A., Quadrini, F., Squeo, E.A., 2008. Macroindentation of polymers. Polymer Engineering & Science 37, 1279–1288.

Pulecio, S.A.R., Farias, M.C.M., Souza, R.M., 2009. Analysis of the tip roundness effects on the micro- and macroindentation response of elasticplastic materials. Journal of Materials Reseach 24, 1037–1044.

Lach, R., Schöne, J., Bierögel, C., Grellmann, W., 2012. Instrumented macroindentation techniques for polymers and composites

mechanical properties, fracture toughness and time-dependent behaviour as a function of the temperature. Macromolecular Symposia 315, 125–131.

Giannakopoulos, A.E., Triantafyllou, A., 2007. Spherical indentation of incompressible rubber-like material. Journal of the Mechaics and Physics of Solids 55, 1196–1211.

Drozdov, A., 1996. Finite Elasticity and Visoelasticity. World Scientific Publishing.

Chevalier, L., Marco, Y., 2002. Tools for multiaxial validation of behavior laws chosen for modeling hyperelasticity of rubber-like materials. Polymer Engineering & Science 42, 280–298.

Baaser, H., Noll, R., 2009. Simulation von elastomerbauteilen-materialmodelle und versuche zur parameterbestimmung, DVM-Tag Elastomere, Berlin, pp. 1–10.

Johlitz, M., Diebels, S., 2011. Characterisation of a polymer using biaxial tension tests. Part I: Hyperelasticity. Archive of Applied Mechanics 81, 1333–1349.

Koprowski-Theiss, N., Johlitz, M., Diebels, S., 2011. Modelling of a cellular rubber with nonlinear viscosity functions. Experimental Mechanics 51, 749–765.

Hay, J.L., Hern, M.E.O., Oliver, W.C., 1998. The importance of contact radius for substrate-independent properties measurement of thin films. Materials Research Society Symposium Proceedings 522, 27–32.

Hertz, H., 1881. Über die Berührung fester elstischer körper. Journal für die reine und angewandte Mathematik 92, 156–171.

Boussinesq, J., 1885. Applications des Potentiels a létude de Équilibre et du Mouvement des Solids Élastiques. Gauthier-Villars, Paris.

Sneddon, I.N., 1965. The relation between load and penetration in the axisymmetric Boussinesq problem for a punch of arbitrary profile. International Journal of Engineering Science 3, 47–57.

Holzapfel, G.A., 2001. Nonlinear Solid Mechanics: A Continuum Approach for Engineering. John Wiley & Sons, Ltd., England.

Marckmann, G., Verron, E., 2005. Comparison of hyperelastic models for rubber-like materials. Rubber Chemistry and Technology 79, 835–858.

Rivlin, R.S., 1948. Large elastic deformations of isotropic materials. IV. Further developments of the general theory. Philosophical Transactions of the Royal Society of London A241, 379–397.

Mooney, M., 1940. A theory of large elastic deformation. Journal of Applied Physics 11, 582–592.

Doll, S., Schweizerhof, K., 2000. On the development of volumetric strain energy functions. Journal of Applied Mechanics, Transactions ASME 67, 17–21.

Chen, Z., Diebels, S., Schmitt, J., 2011. Frictional nanoindentation of hyperelastic polymer layers: a numerical study. In: Proceedings of the 3rd ECCOMAS Thematic Conference on the Mechanical Response of Composites, pp. 229–236.

Wriggers, P., 2006. Computational Contact Mechanics. Springer-Verlag, Berlin, Heidelberg, Netherlands.

Johlitz, M., Steeb, H., Diebels, S., Chatzouridou, A., Batal, J., Possart, W., 2007. Experimental and theoretical investigation of nonlinear viscoelastic polyurethane systems. Journal of Materials Science 42, 9894–9904.

Beyer, H.G., 2001. The Theory of Evolution Strategy. Springer.

Melchior, C., 2012. Optimierung der Versuchsführung beim Biaxialversuch. Universität des Saarlandes Lehrstuhl für Technische Mechanik.

Sutton, M.A., Orteu, J., Schreiter, H.W., 2009. Image Correlation for Shape, Motion and Deformation Measurements. Springer.

Yeoh, O.H., 1990. Characterization of elastic properties of carbon-black-filled rubber vulcanizates. Rubber Chemistry and Technology 55, 792–805.

Giannakopoulos, A.E., Panagiotopoulos, D.I., 2009. Conical indentation of incompressible rubber-like material. International Journal of Solids and Structures 46, 1436–1447.

Treloar, L.R.G., 1975. The Physics of Rubber Elasticity, 3rd ed. Clarendon Press, Oxford.

Baaser, H., Hopmann, C., Schobel, A., 2013. Reformulation of strain invariants at incompressibility. Archive of Applied Mechanics 83, 273–280.

Johnson, K.L., 1985. Contact Mechanics. Cambridge University Press.